



Koyroytsaltis-McQuire, Dominic (2024) *Plasmonic and all-dielectric chiral metamaterials for biomolecule detection*. PhD thesis.

<http://theses.gla.ac.uk/84378/>

Copyright and moral rights for this work are retained by the author

A copy can be downloaded for personal non-commercial research or study, without prior permission or charge

This work cannot be reproduced or quoted extensively from without first obtaining permission in writing from the author

The content must not be changed in any way or sold commercially in any format or medium without the formal permission of the author

When referring to this work, full bibliographic details including the author, title, awarding institution and date of the thesis must be given

Enlighten: Theses

<https://theses.gla.ac.uk/>
research-enlighten@glasgow.ac.uk



Plasmonic and All-Dielectric Chiral Metamaterials for Biomolecule Detection

Dominic Koyroytsaltis-McQuire

Submitted in fulfilment of the requirements for the
Degree of Doctor of Philosophy

School of Chemistry
College of Science and Engineering
University of Glasgow

November 2023

Abstract

Metamaterials have proven themselves revolutionary as a means of bestowing novel properties to materials, for use in a variety of applications. One such area of focus is the enhancement of chiral light-matter interactions. Chirality is a property observed throughout the natural world, which has important consequences in health, environmental and pharmaceutical fields, to name but a few. Metamaterials have been used to enhance the detection of chiral molecules given the inherent weakness in traditional sensing methods. In this thesis, two forms of metamaterial platforms and their optical properties are investigated through a combination of experiment and numerical simulations.

Firstly, the CD spectra of plasmonic gammadions are rationalised and the sensitivity of each resonance to ordered and disordered biomolecule deposits are explored. It is determined that the spectra exhibit localised and delocalised (periodic) resonances. Both types of resonance are shown to display enantiomeric sensitivity, however, only the localised modes show a dependence on the structure of the deposited chiral biomolecular layer. This is reconciled through electromagnetic field analysis, which indicated that the presence of birefringent (ordered) chiral layers can perturb the gammadion's chiral near fields and act as sources/sinks of optical chirality. As a result, the asymmetric perturbations to the coupling between the nanostructure's arms are reflected in the CD spectra of the metamaterials.

The second form of metamaterial investigated is composed of silicon S-shaped structures, fabricated to four different heights between 160-240 nm. Both enantiomorphic and racemic arrays are fabricated, and their reflectance and ORD spectra studied. The sources of their spectral features are determined through a numerical method known as multipole decomposition, which is also used to explain the height dependence of the silicon on the spectra. It is determined that at lower silicon thicknesses the magnetic dipole contribution dominates and at higher thicknesses, the changes to their reflectance arise from red shifting of multipole contributions and an increase in magnetic quadrupole character. In addition to traditional Stokes polarimetry, Mueller matrix polarimetry was also performed on the samples. This method allows for a full characterisation of the optical properties of the samples, which were found to be bianisotropic in nature. The MMP data confirmed that the large optical rotations observed in the ORD measurements were a result of the linear birefringence of the samples, highlighting the limitations in standard polarimetry methods which often cannot distinguish between chiral and linear effects.

The sensing capabilities of the silicon structures were also investigated, revealing their refractive index response to be weak. Significant changes to the reflectance and MMP spectra are, however, observed after a layered biomolecule deposition. Numerical simulations were performed, where the layer was approximated as a dipole, to determine if the observed behaviour was a result of the biomolecular charge. Some qualitative agreement in the simulated reflectance spectra was observed, and field analysis revealed that the presence of the charged chiral layer produced an asymmetric change in the field properties of the structures, consistent with the observed MMP data. The model, however, broke down under orthogonal light polarisation, indicating that further refinement is required to confirm the source of the experimental results.

Contents

List of Figures	5
List of Abbreviations	11
Acknowledgements	12
Author's Declaration	13
Publications	14
Introduction	15
Chapter 1: Background Theory	17
1.1 Maxwell's Equations	17
1.2 Light Polarisation	20
1.3 Chirality and Chiroptical Measurements	21
1.4 Optical Chirality	24
1.5 Metamaterials	26
1.6 Biosensors	28
1.7 Conclusions	29
1.8 References	30
Chapter 2: Metamaterial Fabrication	32
2.1 Fabrication Processes	32
2.1.1 Structure Design	32
2.1.2 Sample Cleaning	32
2.1.3 Electron Beam Lithography	33
2.1.4 Material Deposition	34
2.1.5 Silicon Sample Etching	35
2.1.6 Sample Characterisation	36
2.2 Process Summaries	39
2.2.1 Gold Gammadion Structures	39
2.2.2 Silicon S-shaped Structures	40
2.3 Conclusions	42
2.4 References	43
Chapter 3: Methodology	44
3.1 Spectroscopic Measurements	44
3.1.1 Sample Preparation	44
3.1.2 Gammadion Sample Measurements	45
3.1.3 Silicon Sample Measurements	45
3.2 Numerical Simulations	48
3.3 Conclusions	50
3.4 References	51
Chapter 4: Chiral Plasmonic Detection of an Antibody-Antigen Complex	52
4.1 Introduction to Planar Chiral Metamaterials	52
4.1.1 Plasmonics	52
4.1.2 Planar Chiral Metamaterial Sensing	53
4.2 Methodology	57
4.2.1 Experimental Procedure	57
4.2.2 Simulation Procedure	58
4.3 Results and Discussion - CD Spectra	60
4.3.1 Measured CD	60
4.3.2 Simulated CD	61
4.4 Results and Discussion - Streptavidin Depositions	63
4.4.1 Isotropic Deposition	63
4.4.2 Anisotropic Deposition	64
4.4.3 Numerical Simulations	66
4.5 Conclusions	71

4.6 References	72
Chapter 5: Stokes Polarimetry of S-shaped Silicon Nanostructures	74
5.1 Introduction to Silicon Based Metamaterials.....	74
5.1.1 Light-Matter Interactions in Silicon	74
5.1.2 Birefringence and Chirality	76
5.2 Methodology	78
5.2.1 Sample Design and Fabrication	78
5.2.2 Simulation Procedure.....	78
5.2.3 Experimental Procedure	79
5.3 Results and Discussion - Reflectance.....	81
5.3.1 Measured Reflectance.....	81
5.3.2 Simulated Reflectance	82
5.3.3 Multipolar Decomposition.....	89
5.3.4 Reflectance Summary	100
5.4. Results and Discussion - Optical Rotation	101
5.4.1 Measured ORD	101
5.4.2 Simulated ORD.....	104
5.4.3 Optical Chirality Density	106
5.5 Conclusions.....	109
5.6 References	111
Chapter 6: Mueller Matrix Polarimetry of S-shaped Silicon Metamaterials	114
6.1 Introduction to Stokes and Mueller Matrix Polarimetry	114
6.2 Methodology	118
6.2.1 Experimental Procedure	118
6.2.2 Simulation Procedure.....	119
6.3 Results and Discussion	120
6.3.1 Mueller Matrix Symmetries of Silicon Nanoarrays	120
6.3.2 Optical Properties of Silicon Nanoarrays	126
6.3.3 Numerical Simulations.....	130
6.4 Conclusions.....	132
6.5 References	133
Chapter 7: Capacitive Sensing with Silicon Metamaterials	134
7.1 Biosensing Platforms.....	134
7.1.1 Refractive Index Sensors	134
7.1.2 Capacitive Effects.....	135
7.2 Methodology	137
7.2.1 Deposition Procedure.....	137
7.2.2 Spectra Collection	138
7.2.3 Simulation Procedure.....	138
7.3 Results and Discussion - Experimental	139
7.3.1 Butanol Measurements	139
7.3.2 Streptavidin Depositions	140
7.3.3 MMP Measurements	144
7.4 Results and Discussion - Numerical Simulations	147
7.4.1 Uncharged Layer Model	147
7.4.2 Charged Layer Model	147
7.4.3 Field Plots.....	151
7.5 Conclusions.....	155
7.6 References	156
Chapter 8: Summary and Outlook.....	158

List of Figures

Figure 1.1: A visualisation of LPL, a superposition of counter rotating CPL components, passing through an optically active medium. The LCP (red) component experiences a different refractive index to the RCP (blue) component, resulting in a rotation of the plane of polarisation of the LPL wave.

Figure 1.2: A visualisation of LPL undergoing uneven absorption of CPL components, where only RCP is absorbed, after which the wave gains an elliptical polarisation.

Figure 1.3: A visualisation of the E vector for CPL (top) and a superchiral field (bottom), with projections of the fields on adjacent walls of the figure in blue. The superchiral field displays regions in which the E vector undergoes a greater sense of twist than that of the CPL wave. Figure adapted from reference [18].

Figure 1.4: Examples of some chiral geometries used elsewhere. a) A RH gammadion b) a LH shuriken and c) an achiral nanoslit (left), which supports regions of enhanced electric (red) and magnetic (blue) fields, paired in a chiral arrangement (right). Images adapted from references [21,29,32].

Figure 1.5: Examples of 2D and 3D chiral geometries. Defining the handedness of 2D chiral objects is arbitrary, as it changes depending on which side the object is viewed from. 3D chiral objects maintain their handedness regardless of how they are viewed. Figure adapted from reference [34].

Figure 1.6: The four general components of a biosensor. Analyte recognition by the bioreceptor triggers a response by the transducer, which creates a measurable signal that can be processed by the device electronics. This response is returned to the user with some display.

Figure 2.1: A visualisation of the metallisation and lift-off processes when using a resist single layer (left) and bilayer (right), post e-beam exposure and development. Non-uniform electron exposure can lead to wall sloping, an ‘overcut’, which increases the likelihood of defects upon lift-off (final removal of resist). This undesirable effect can be limited with a resist bilayer, which utilises an ‘undercut’ to improve pattern transfer. The undercut forms due to the top layer developing at a slower rate compared to the bottom layer.

Figure 2.2: SEM images of a gammadion sample dose test with a poor dose selection of $1200 \mu\text{C cm}^{-2}$ (left) and a more optimal dose of $800 \mu\text{C cm}^{-2}$ (right), in which 200 nm of PMMA 2010 was topped by a 100 nm layer of PMMA 2014. Scale bars are 5 μm (left) and 2 μm (right).

Figure 2.3: An example of AFM data collected for the silicon S structures. a) A 3D rendering of the sample scan. B) A top down 2D image of the scanned data, across which surface profiles can be obtained (measuring line shown in red). c) The height profiles obtained from the measurement line placed across the sample.

Figure 2.4: A schematic of the process steps involved for the fabrication of a gammadion sample and the materials present at each stage. 1.-3. details the initial cleaning, spinning of the PMMA bilayer and Al metallisation prior to e-beam exposure. 4.-5. shows the removal of the Al and exposed resist after e-beam exposure. 6. displays the NiCr / Au deposition and 7. the final lift-off, leaving only the gold gammadions.

Figure 2.5: A schematic of the process steps involved for the fabrication of a silicon sample and the materials present at each stage. 1.-4. includes the initial cleaning, amorphous silicon deposition, resist bilayer spin and Al deposition. 5.-6. displays the Al strip and development of exposed resist. 7. shows the NiCr etch mask metallisation and 8. the lift-off. 9. shows the dry etch to removed unprotected silicon and 10. details the wet etch that removes the remaining NiCr mask, leaving only the silicon s-structures.

Figure 3.1: An example of a gammadion sample secured in the 3D printed sample holder. The silicone seal (orange) allows for the injection of solutions over the sample. The distance between the centres of adjacent screws is 30 mm.

Figure 3.2: A schematic of the Stokes polarimeter used for reflectance and ORD measurements. The camera is used to align the sample and the analyser is rotated to obtain ORD data.

Figure 3.3: A schematic of the PL microscope used in experiment, operating with a 404 nm laser.

Figure 3.4: a) The meshed unit cell of the silicon model, with domain components labelled. b) The meshing of an AFM imported structure (top) and a COMSOL generated (idealised) structure (bottom) with the same preset element size.

Figure 4.1: The coupled oscillator model of optical activity. This arrangement of coupled electrons (coupling constant ξ) of mass m , charge e and separation d , with confined oscillations (restoring constant k), creates two distinct enantiomeric states. Figure adapted from [18].

Figure 4.2: The plasmonic extension of the Born-Kuhn coupled oscillator model. a) The corner-stacked plasmonic nanorod arrangements produce distinct enantiomeric forms. b) Incident R-/L-CPL interacts differently between the enantiomers as the electric field vector rotates. c) The respective charge distributions in the stacked rods produces hybridized states. Figure adapted from reference [18].

Figure 4.3: Transmittance (left) of a D-enantiomer when exposed to RCP, LCP and LPL. CD (right) spectra of the nanorods for the D- (purple) and L-enantiomer (green), forming mirror image bisignates. Figure adapted from reference [18].

Figure 4.4: A visualisation of the helical oscillator model of optical activity. a) An achiral metal nanoparticle interacting with a LPL wave. b) An achiral particle interacting with CPL causes the plasmon to follow a helical path. c) A chiral nanoparticle interacting with CPL of the same handedness produces a strong chiroptical response as the particle can accommodate the helical plasmon. d) A chiral particle the opposite handedness interacting with the CPL wave produces a weaker response, due to a mismatch between the two. Figure adapted from [23].

Figure 4.5: a) A visualisation of a RH gammadion, with the diameter 400nm, height 100nm and an arm width 80nm. b) SEM images of RH (top) and LH (bottom) nanostructures, upon which the model dimensions were based. Scale bar 1 μ m.

Figure 4.6: The periodic unit cell used in numerical simulation, with outer dimensions labelled. The gold gammadion (blue) is placed above quartz domains, with the remaining domains assigned as water.

Figure 4.7: a) An idealised model of a LH gammadion with 20 nm external domains, which can be given a ξ value and an isotropic or anisotropic refractive index. b) A schematic (not to scale) illustrating the surface profile of streptavidin when non-specifically (isotropic) and specifically (anisotropic) bound to the gold structures.

Figure 4.8: CD spectra for the LH (solid) and RH (dashed) samples in PBS, inclined at $\Theta=0^\circ$ (red), 4° (black) and 10° (blue). Modes used for analysis are labelled as I, II and III.

Figure 4.9: Simulated CD spectra for LH (solid) and RH (dashed) gammadion nanostructures in water, with no external layer present. Modes I, II and III are labelled.

Figure 4.10: a) E_z plots for the 3 resonance modes of figure 4.8, for LH and RH structures, when exposed to RCP and LCP incident light. b) Optical chirality density plots for LH and RH structures for each mode. Each row includes symmetry equivalent pairs between the structure handedness and incident CPL. All field plots are taken from the midpoint of the structures. Optical chirality density plots are normalised to RCP.

Figure 4.11: a) Experimental CD spectra collected in PBS buffer of LH (solid) and RH (dashed) samples (red), followed by the non-specific deposition of streptavidin (black). b) The subsequent deposition of antistrep (green) with respect to the streptavidin. The three modes used for measuring spectral shifts are highlighted with lines to aid the eye (LH solid and RH dashed).

Figure 4.12: a) Experimental CD spectra collected in PBS buffer of LH (solid) and RH (dashed) samples (red), followed by the biotin SAM binding to the surface (blue). b) The subsequent deposition of streptavidin (black) and c) antistrep (green). The three modes used for measuring spectral shifts are highlighted with lines to aid the eye (LH solid and RH dashed).

Figure 4.13: Simulated CD spectra in water of the gammadions (red) and with an isotropic external layer present (black).

Figure 4.14: Simulated CD spectra in water of the gammadions (red) and with an anisotropic external layer present (blue).

Figure 4.15: a) A comparison of the $\Delta\Delta\lambda$ asymmetry values for modes I (red), II (green), and III (blue) obtained from both experiment and simulation, for the isotropic and birefringent (anisotropic) layers. b) Tabulated $\Delta\Delta\lambda$ asymmetries. c) Asymmetries obtained for achiral reference solutions.

Figure 4.16: E_z plots for the achiral, isotropic and birefringent simulations at mode II. The white regions highlighted in achiral RCP / LH are used to calculate the average field intensities which are displayed in figure 4.17. Electric field values for the plots are between $6\text{-}12\text{ Vm}^{-1}$ to improve image contrast between the arms. Each row includes symmetry equivalent pairs between the structure handedness and incident CPL. All field plots are taken from the midpoint of the structures.

Figure 4.17: Optical chirality density plots for achiral, isotropic and birefringent simulations at mode II. As before, white regions highlighted in achiral RCP / LH were used for the intensity values in figure 4.17. Each row includes symmetry equivalent pairs between the structure handedness and incident CPL. All field plots are taken from the midpoint of the structures and are normalised against RCP.

Figure 4.18: Electric field and optical chirality density values compared for the three simulation types, each averaged from four equivalent areas (highlighted in figures 4.15 and 4.16 between the arms of the structures). The shaded rows denote one set of symmetry related pairs.

Figure 5.1: A visual representation of light passing through a higher index (spherical) cavity. Figure adapted from reference [2].

Figure 5.2: Incident EM radiation shown by its B-field vector (red) travelling in the x-axis, generates a circulating E field displayed in the leftmost arrow plot. The magnetic field arrow plot is shown in the orthogonal plane. Figure adapted from reference [2].

Figure 5.3: A comparison between metallic and dielectric dimers in terms of electric (p , red) and magnetic (m , blue) material polarisations and coupling, under E_x (top) and E_y (bottom) light polarisations. Figure adapted from [9].

Figure 5.4: Orthogonally polarised components of the light incident on the birefringent slab experience different refractive indices. The ordinary ray (O-ray) experiences the same refractive index in every direction of the medium, whilst the extraordinary ray's (E-ray) velocity is dependent on propagation direction.

Figure 5.5: a) The L-Edit design file for a single LH S-structure, with dimensions labelled. Black dots represent $10\text{ }\mu\text{m}$ intervals. b) AFM images from each array type, the RA image is taken from where four of the 19×19 arrays meet.

Figure 5.6: a) A top-down view a single RH idealised model of the silicon S structure, in a $850 \times 850\text{ nm}$ unit cell of periodic boundary conditions. The two incident light polarisations used throughout this chapter are labelled with respect to the structure's orientation b) A side-on view of the model, with domain materials labelled. c) The two variations of models used single structures (left) and four structures (right).

Figure 5.7: Dektak scan data for each of the four samples used in experiment. The profilometer tip scans across the sample's quartz glass substrate and onto the silicon array, measuring the step height between them.

Figure 5.8: Experimental reflectance spectra for LH (black), RH (red), RA (green) and RS (blue) arrays at four different heights of silicon deposition under incident y- and x-polarised light (labelled in the left-most plots of the first and third rows). Peaks A and B represent the dominant feature of the y-polarised spectra, with the RS arrays also producing a peak close to the sample periodicity, labelled C. Peaks D and E occur for x-polarised spectra, representing a sharp peak prior to a broader one, respectively.

Figure 5.9: Simulated reflectance spectra for RH single structured models (red) and 4-structured RH (red dashed) and RS (blue) models, for each sample thickness under y- (left) and x-polarisations (right).

Figure 5.10: Distributions for the electric ($|E|$) and magnetic ($|H|$) field magnitudes plotted for equivalent resonances across all sample thicknesses, under y- (top two rows) and x-polarisations (bottom two rows). Field plots here and subsequently are taken from the midpoint of the structures.

Figure 5.11: Reflectance comparison of y- (left) and x-polarised (right) illumination of a 180 nm sample between experiment (black), a 'real' AFM imported model (red) and the idealised model (blue).

Figure 5.12: $|E|$ and $|H|$ field distributions for 180 nm 'ideal and 'real' AFM structures for peaks A and D.

- Figure 5.13:** $|E|$ and $|H|$ field distributions for 180 nm 4-structured RH and RS arrays under y- and x-polarised excitation. Distributions give an indication of the degree to which resonances are localised or periodic.
- Figure 5.14:** A comparison of the RH experimental reflectance (black), simulated reflectance (blue) and the total multipole scattering cross section (orange) for the 180 nm (left column) and 240 nm (right column) structures when illuminated with y-polarised incident light.
- Figure 5.15:** A comparison between experimental reflectance (black) and the simulated sum of the scattering cross section (orange) for the 180 nm structure under y-polarised illumination. The components include the E_D (red), M_D (green), E_Q (blue) and M_Q (cyan) contributions. Note that the scale of the sum plot is double that of the contributions.
- Figure 5.16:** A comparison between experimental reflectance (black) and the simulated sum of the scattering power components (orange) for the 240 nm structure under y-polarised illumination. The components include the E_D (red), M_D (green), E_Q (blue) and M_Q (cyan) contributions.
- Figure 5.17:** E_z and H_z distributions for select peaks under y-polarisation, viewed from different planes. x-y plane images are taken from the midpoint of the structures, whilst orthogonal planes dissect the centre of the unit cell.
- Figure 5.18:** Electric field and current density arrow plots for peaks A and B of the 180 nm sample under y-polarised illumination. Arrow surfaces are taken at the midpoint of the structure.
- Figure 5.19:** A comparison of the RH experimental reflectance (black), simulated reflectance (blue) and the total multipole scattering cross section (orange) for the 180 nm (left column) and 240 nm (right column) structures when illuminated with x-polarised incident light.
- Figure 5.20:** A comparison between experimental reflectance (black) and the simulated sum of the scattering cross section (orange) for the 180 nm structure under x-polarised illumination. The components include the E_D (red), M_D (green), E_Q (blue) and M_Q (cyan) contributions.
- Figure 5.21:** A comparison experimental reflectance (black) and the simulated sum of the scattering cross section (orange) for the 240 nm structure under y-polarised illumination. The components include the E_D (red), M_D (green), E_Q (blue) and M_Q (cyan) contributions. Note that the M_Q scale is double that of the other contributions.
- Figure 5.22:** E_z and H_z distributions for select peaks under x-polarisation, viewed from different planes. x-y plane images are taken from the midpoint of the structures, whilst orthogonal planes dissect the centre of the unit cell.
- Figure 5.23:** Electric field and current density arrow plots for peaks D and E of the 180 nm sample under x-polarised illumination.
- Figure 5.24:** Experimental ORD under y- (top row) and x-polarisation (bottom row) for LH (black), RH (red), RA (green) and RS (blue) arrays for each sample thickness. Positions of experimental reflectance peaks A-E of figure 5.8 are labelled. Note that the x-polarised 240 nm ORD is on an increased scale.
- Figure 5.25:** Reflectance and ORD measurements for each array of a 210 nm sample, for forwards and backwards x- and y-polarised illumination, with peaks labelled.
- Figure 5.26:** Simulated CD (top) and corresponding KK transformed CD (bottom) spectra of LH, RH and RS arrays for the four sample heights. Dashed lines correspond to Peak A of simulated reflectance from figure 5.9.
- Figure 5.27:** Volume averaged optical chirality density values for y-(top) and x-polarised (bottom) illumination of LH, RH and RS arrays for each sample thickness. Dashed lines correspond to Peak A. Plots are normalised against RCP.
- Figure 5.28:** Optical chirality density maps for y-(top) and x-polarised (bottom) LH and RH structures, corresponding to dashed lines of figure 5.27, for each sample thickness. Plots are taken at the midpoints of the structures and are normalised against RCP.
- Figure 6.1:** The optical components of the Mueller Matrix Polarimeter at *Diamond Light Source UK*, on the B23 beamline. Figure reproduced from [9].
- Figure 6.2:** The 16 Mueller matrix elements for both the LH and RH arrays of a 210 nm sample immersed in water. The dashed blue line across the main diagonal is used to help visualise the symmetry plane between MMP element pairs, with green outlines representing predominant similarities between pairs and red showing stronger differences.

Figure 6.3: The overall symmetry of an idealised sample on the quartz substrate increases depending on the refractive index environment above the structure (relative to the substrate). The placement of the structure on the substrate is one of two major sources of dissymmetry of the structure.

Figure 6.4: The 16 Mueller matrix elements for the RA array of a 210 nm sample immersed in water, for which only the LD and LB elements are non-zero.

Figure 6.5: The 16 Mueller matrix elements for the RS array of a 210 nm sample immersed in water, where again, only the LD and LB elements are non-zero.

Figure 6.6: A comparison between the optical properties of the LH and RH arrays of a 210 nm sample immersed in water, based on MMP elements of figure 6.2.

Figure 6.7: The optical properties of the RA array of a 210 nm sample immersed in water, based on MMP elements of figure 6.4.

Figure 6.8: The optical properties of the RS array of a 210 nm sample immersed in water, based on the MMP elements of figure 6.5.

Figure 6.9: A comparison between the CD spectra obtained from simulation (top) and experimental MMP (bottom) for a 210 nm sample immersed in water. The simulated data is blue shifted 25 nm to account for the idealised model and aid comparison.

Figure 7.1: Examples of several SRR geometries. a) An open-SRR. b) An S-shaped SRR. c) An omega SRR. Material currents and capacitive coupling differ due to the arrangement of the structural features. Figure adapted from reference [7].

Figure 7.2: A schematic of the deposition process with labelled constituent layers. Positively charged poly-L-lysine binds to the silicon surface. Glutaraldehyde crosslinks between the lysine and streptavidin coated quantum dots. Ethanolamine acts as a capping layer to limit nonspecific binding. The streptavidin coated quantum dots are then free to bind with additional species.

Figure 7.3: Y-polarised experimental reflectance data of a ~210 nm sample, obtained for a) LH b) RH c) RA and d) RS arrays immersed in PBS buffer (solid) and R-S-butanol (dashed).

Figure 7.4: Photoluminescence signals obtained under y-incident polarisation for the streptavidin coated quantum dots on each array, excited at 404 nm. The signal is normalised against the number of acquisitions.

Figure 7.5: Experimental y-polarised reflectance spectra collected in PBS buffer for a) LH b) RH c) RA and d) RS arrays of a ~160nm sample (black), followed by the depositions of streptavidin (red) and antistrep antibody (blue).

Figure 7.6: AFM data collected for the sample used in figure 7.5 a) AFM image (left panel) of a RH structure and the associated height profile (right panel) across the middle arm, of a pristine structure prior to any deposition. b) Equivalent data after experiment, following the deposition of antistrep onto the streptavidin functionalised surface.

Figure 7.7: Experimental y-polarised reflectance spectra collected in PBS buffer for a) LH b) RH c) RA and d) RS arrays of a ~160 nm sample (black), followed by the depositions of streptavidin (red) and biotin (green).

Figure 7.8: LD MMP data for the ~210 nm sample. LD spectra for LH (solid) and RH (dashed) structures collected in PBS buffer with a) no biomolecule present and with b) streptavidin and c) antistrep deposited. d) LH:RH peak ratios are calculated from the peaks marked by the dashed lines and are tabulated.

Figure 7.9: LD' MMP data for the ~ 210 nm sample. LD' spectra for LH (solid) and RH (dashed) structures collected in PBS buffer with a) no biomolecule present and with b) streptavidin and c) antistrep deposited. d) LH:RH peak magnitude ratios, calculated from the peaks marked by the dashed lines, are tabulated.

Figure 7.10: CD MMP data for the ~ 210 nm sample. CD spectra for LH (solid) and RH (dashed) structures collected in PBS buffer with a) no biomolecule present and with b) streptavidin and c) antistrep deposited. d) LH:RH peak magnitude ratios are calculated from the peaks marked by the dashed line and are tabulated. The CD data is smoothed to aid analysis.

Figure 7.11: LD, LD' and CD MMP data for the racemic arrays of the ~210 nm sample. LD data for the a) RA and b) RS arrays is shown for the sample immersed in PBS with no biomolecule present (black) and with streptavidin (red) and antistrep (blue) deposited. Equivalent data is presented for c)-d) LD' and e)-f) CD. Note the scales for LD' and CD are reduced compared to the enantiomeric data. The CD data is smoothed as before.

Figure 7.12: Simulated reflectance spectrum of an ideal 180 nm structure under y-polarised illumination, with media above the structure modelling water ($n=1.33$) and 2-butanol ($n=1.397$).

Figure 7.13: A depiction of the polarisation directions of the external layers in each of the three planes for a LH structure. The external layer is partitioned in each axis. Polarisation arrows are of arbitrary scale.

Figure 7.14: Simulated y-polarised reflectance spectra of ideal 180 nm LH (left) and RH (right) structures in water with external layer given a refractive index and chirality (top) and additional polarisation (bottom).

Figure 7.15: Simulated x-polarised reflectance spectra of ideal 180 nm structures in water (black) without (top) and with (bottom) a polarisation assigned to the external layer. LH (green) and RH (blue) data is shown when polarisation is present, which should be equivalent as the layer is achiral. Only LH data for water and the layer with no polarisation (red) is shown as the RH is identical.

Figure 7.16: A comparison between the $|E|$ (top row), E_z (middle row) and optical chirality density (bottom row) plots for y-polarised illumination of a 180 nm structure without an external layer (left column), with an achiral polarised layer (middle column) and a chiral polarised layer (right column). Surface integrated values for the maps shown (taken from the midpoints of the structure) are labelled beneath the respective images. Scales for the polarised layers are altered, labelled in the top left corner of the middle column.

Figure 7.17: A comparison between the $|E|$ (top row), E_z (middle row) and optical chirality density (bottom row) plots for x-polarised illumination of a 180 nm structure without an external layer (left column) and with an achiral polarised layer (right column). Surface integrated values for the maps shown (taken from the midpoints of the structure) are labelled beneath the respective images. Scales for the polarised layer are altered, labelled in the top left corner of the right column.

List of Abbreviations

LCP	left-handed circularly polarised
RCP	right-handed circularly polarised
LPL	linearly polarised light
CPL	circularly polarised light
LH	left-handed
RH	right-handed
ORD	optical rotatory dispersion
CD	circular dichroism
CB	circular birefringence
LB	linear birefringence
JWNC	James Watt Nanofabrication Centre
CAD	computer aided design
E-beam	electron beam
AMI	acetone, methanol, isopropyl alcohol
IPA	isopropyl alcohol
PMMA	poly-methyl methacrylate
MIBK	methyl isobutyl ketone
SEM	scanning electron microscope
PECVD	plasma enhanced chemical vapour deposition
AFM	atomic force microscopy
FEM	finite element method
PL	photoluminescence
PML	perfectly matched layer
SPP	surface plasmon polaritons
LSPR	localised surface plasmonic resonance
SAM	self assembled monolayer
Antistrep	anti-streptavidin antibody
MMP	Mueller matrix polarimetry
LD	linear dichroism
PEM	photoelastic modulator
RI	refractive index
RIU	refractive index unit
SRR	split ring resonator
PLL	poly-L-lysine
QD	quantum dot

Acknowledgements

There are many people who have in some way helped me through 9 years at the University of Glasgow, before and during my Ph.D., and have made my time here special to me.

Firstly, I owe many thanks to my supervisor, Malcolm Kadodwala, who first introduced me to the field of chiral metamaterials, and whose patience and guidance throughout the last 4 years has helped me reach the end of my Ph.D. I have gained some memorable experiences during this time, being able to travel to conferences, work at state-of-the-art facilities and enjoy several group Christmas Dinners, featuring plumb vodka and some dancing (perhaps not-so-memorable in the end).

I would also like to thank Adrian Laphorn, my secondary supervisor, who has always been someone I can seek advice and support from. I am also thankful for Affar Karimullah's support, who was always quick to share his expertise.

I also thank the Kadowala group, for their valuable help, and shared knowledge during my time in the research group. Their welcoming and friendly attitudes have made my Ph.D. more rewarding. Special thanks go to Cameron Gilroy, Maryam Hajji, Stephanie Wallace and Rahul Kumar, who provided much needed help when I needed it.

My thanks go to the technical and support staff of the James Watt Nanofabrication Centre, who have always made it a pleasure to work in the facility. Also, to the staff at Diamond Light Source Ltd., in particular Giuliano Siligardi, who was very welcoming and helped me complete my work there.

I owe a huge thank you to my friends and family who have supported and encouraged me from start to finish of my studies, and who were there when it was needed most.

Finally, perhaps the biggest thanks go to two very important people. Firstly, my Mum, Audrey McQuire, who has always been there to support and encourage me towards my goals and who I owe many of my achievements to. Her belief in me was matched by my Gran, Irene McQuire, whose love, wisdom and support helped me greatly throughout my life and always inspired me to continuously push myself. I would not be where I am today without it and this thesis is dedicated to her.

Author's Declaration

I declare that, except where explicit reference is made to the contribution of others, that this dissertation is the result of my own work and has not been submitted for any other degree at the University of Glasgow or any other institution.

Printed Name: DOMINIC KOYROYTSALTIS-MCQUIRE

Signature:

Publications

The work detailed in **Chapter 4** has been published in the journal article:

“Detecting Antibody-Antigen Interactions with Chiral Plasmons: Factors Influencing Chiral Plasmonic Sensing”

D. J. P. Koyroytsaltis-McQuire, C. Gilroy, L. D. Barron, N. Gadegaard, A. S. Karimullah and M. Kadodwala, *Adv. Photonics Res.*, 2022, **3**, 2100155.

And contributed to the journal article:

“Superchiral hot-spots in ‘real’ chiral plasmonic structures”

C. Gilroy, D. J. P. Koyroytsaltis-McQuire, N. Gadegaard, A. S. Karimullah and M. Kadodwala, *Mater. Adv.*, 2022, **3**, 346-354.

The work detailed in **Chapters 5** and **6** has been published in the journal article:

“Tuning Dipolar and Multipolar Resonances of Chiral Silicon Nanostructures for Control of Near field Superchirality”

D. J. P. Koyroytsaltis-McQuire, R. Kumar, T. Javorfi, G. Siligardi, N. Gadegaard and M. Kadodwala, <https://arxiv.org/abs/2310.12639>

Introduction

Chirality is a long-studied field which dates to the early 19th century, when the French physicist Arago observed the rotation of plane polarised light during his studies with quartz crystals in 1811. Shortly after, in 1815, Biot discovered that this optical effect could also arise from organic compounds. Chirality at this time remained undefined; yet further observations by Pasteur, in which seemingly identical crystals rotated the polarisation plane of light in opposite directions, were made in 1848. This was attributed to the atomic arrangement of the molecules, a conclusion which is now known to be correct.¹

It would be almost 50 years from this discovery for the term ‘chirality’ to be put forward by Lord Kelvin in 1894, which is described as a property an object has if it is non-superimposable on its mirror image.² Chirality is now understood to be incredibly important to the fundamental interactions that support life, and perhaps even its origin.³ Chiral light-matter interactions are however limited due to the size disparity of incident light waves and chiral molecules. The fundamental aim of this thesis is to explore methods of improving this interaction. Central to this is a new class of material known as metamaterials, which possess properties that do not occur naturally and can therefore be tailored towards different applications.

This work explores the optical properties of chiral metamaterials and how they can change in the presence of biomolecules. Understanding how these properties are generated and influenced is an important step towards the production of ultrasensitive sensing platforms, which is one of the key aims within the field of chiral metamaterials.

The thesis is composed of several chapters, beginning with an introduction to the relevant background theory necessary to understand subsequent chapters; including Maxwell’s equations, the nature of light polarisation, chirality and metamaterials. This is followed by chapters 2 and 3, which detail the nanofabrication processes required to produce the metamaterials and the techniques behind the experimental and computational acquisition of data.

Chapter 4 is based upon samples of gold, plasmonic gammadion structures. It begins with an introduction to plasmonics and how gammadion structures produce their spectra. The chapter focusses on the effects of birefringent chiral layers on biomolecular sensing with planar chiral metamaterials.

Chapter 5 introduces the silicon metamaterials discussed in the remainder of the thesis. The focus of this chapter is their reflectance and optical rotation properties, which could find applications in not just biosensing, but nano-optical platforms also. The sources of the observed spectral features identified from the numerical technique of multipolar decomposition are also reviewed.

Chapter 6 includes further analysis of the silicon structures, this time using Mueller matrix polarimetry to determine the origins of the optical properties. The advantages it has over traditional Stokes polarimetry are discussed.

Chapter 7 investigates the spectral response of the silicon metamaterials when charged biomolecular layers are bound to their surface. The final chapter provides a summary of the thesis and discusses potential future work.

- 1 J. Gal and P. Cintas, *Top. Curr. Chem.*, 2013, **333**, 1-40.
- 2 W. T. Kelvin, *The molecular tactics of a crystal*, Clarendon Press, Oxford, 1894.
- 3 L. D. Barron, *Molecular Light Scattering and Optical Activity*, Cambridge University Press, 2nd edn., 2004.

Chapter 1: Background Theory

This chapter provides a general overview of the theory behind electromagnetism and chirality, relevant to the work in this thesis. More specific theoretical descriptions are included in the introductions of each of the respective chapters.

1.1 Maxwell's Equations

As this thesis focusses on the interactions of light and matter, it is necessary to provide a background on electromagnetic theory; this cannot be done without the introduction of Maxwell's equations, four of the most influential equations in all of science. Maxwell was able to complete a comprehensive description of electromagnetic theory by combining four constituent equations to produce the wave equation, which gives a complete description of the nature of electromagnetic waves. Maxwell's equations are as follows¹:

$$\nabla \cdot \mathbf{E} = \frac{\rho}{\epsilon_0} \quad [1.1] \textit{ Gauss's Law for Electric Fields}$$

$$\nabla \cdot \mathbf{B} = 0 \quad [1.2] \textit{ Gauss's Law for Magnetic Fields}$$

$$\nabla \times \mathbf{E} = \frac{-\partial \mathbf{B}}{\partial t} \quad [1.3] \textit{ Faraday's Law}$$

$$\nabla \times \mathbf{B} = \mu_0 \left(\mathbf{J} + \epsilon_0 \frac{-\partial \mathbf{E}}{\partial t} \right). \quad [1.4] \textit{ Ampere - Maxwell Law}$$

In which \mathbf{E} and \mathbf{B} are the electric and magnetic field vectors, respectively. \mathbf{J} is the current density, ρ is the charge density, ϵ_0 is the free space electric permittivity, μ_0 is the free space magnetic permeability and t is time. The equations presented above apply to electric and magnetic fields in both free space and in matter. When considering the latter, the bound charges and currents must be taken into account in addition to those that are free. Upon exposure to an external electric field, positive and negative charges can become displaced and form electric dipole moments, \mathbf{p} . For a dielectric material of N molecules per unit volume, the electric polarisation (the dipole moment per unit volume), \mathbf{P} , is given by²:

$$\mathbf{P} = N\mathbf{p}. \quad [1.5]$$

Within a dielectric medium, the volume density of bound charges, ρ_b is given by:

$$\rho_b = -\nabla \cdot \mathbf{P}. \quad [1.6]$$

Equating this to Gauss's Law for electric fields and considering the total charge as the sum of the free (ρ_f) and bound charge, $\rho = \rho_b + \rho_f$:

$$\nabla \cdot \mathbf{E} = \frac{\rho}{\epsilon_0} = \frac{\rho_b + \rho_f}{\epsilon_0}. \quad [1.7]$$

Substituting equation 1.6 for bound charges and collecting like terms yields:

$$\nabla \cdot (\epsilon_0 \mathbf{E} + \mathbf{P}) = \rho_f. \quad [1.8]$$

The term within the parenthesis is referred to as the displacement field, \mathbf{D} :

$$\mathbf{D} = (\epsilon_0 \mathbf{E} + \mathbf{P}). \quad [1.9]$$

Substituting this into equation 1.8 gives a differential form of Gauss's law that only applies to free charges:

$$\nabla \cdot \mathbf{D} = \rho_f. \quad [1.10]$$

Using the divergence theorem, which equates the flux of a vector field to the volume integral of the field's divergence, gives the integral form of Gauss's law for electric fields in terms of the flux of the displacement and enclosed free charge, $q_{\text{free,enc}}$:

$$\oint_S \mathbf{D} \cdot \hat{\mathbf{n}} da = q_{\text{free,enc}}. \quad [1.11]$$

With $\hat{\mathbf{n}}$ the unit vector normal to surface, S , where da is some increment of the surface area. Gauss's law for magnetic fields and Faraday's law do not directly involve electric charge or current and therefore do not require further derivations, which leaves the Ampere-Maxwell law. Just as external electric fields can generate electric dipole moments in a material, an external magnetic field can induce a magnetisation, or the magnetic dipole per unit volume, \mathbf{M} . The presence of bound currents, \mathbf{J}_b , can act as a source of additional magnetic fields:

$$\mathbf{J}_b = \nabla \times \mathbf{M}. \quad [1.12]$$

The total current density has further contributions from free currents, \mathbf{J}_f , and from changes in the polarisation, \mathbf{J}_p . The Ampere-Maxwell law in its differential form is:

$$\nabla \times \mathbf{H} = \mathbf{J}_f + \frac{\partial \mathbf{D}}{\partial t}. \quad [1.13]$$

Where \mathbf{H} is referred to as the magnetic field strength:

$$\mathbf{H} = \frac{\mathbf{B}}{\mu_0} - \mathbf{M}. \quad [1.14]$$

Applying Stokes' Theorem to the differential form of the Ampere-Maxwell law produces the integral form:

$$\oint_C \mathbf{H} \cdot d\mathbf{l} = I_{\text{free,enc}} + \frac{d}{dt} \int_S \mathbf{D} \cdot \hat{\mathbf{n}} da. \quad [1.15]$$

For an enclosed path, C , with some incremental segment of the path $d\mathbf{l}$ and a free enclosed charge $I_{\text{free,enc}}$.

Each of Maxwell's equations describe the fundamental behaviour of electric and magnetic fields. Employing the appropriate vector algebra and identities one can find how the four equations are intrinsically connected as they combine to generate the wave equation, a second order partial differential equation that can describe an electromagnetic wave:

$$\nabla^2 \mathbf{E} = \mu_0 \epsilon_0 \frac{\partial^2 \mathbf{E}}{\partial t^2}. \quad [1.16] \text{ The Wave Equation}$$

The wave equation can be solved through the use of a suitable form of solution, one of those being that of a plane wave:

$$\mathbf{E} = \mathbf{E}_0 e^{i(\mathbf{k} \cdot \hat{\mathbf{x}} - \omega t)}. \quad [1.17]$$

Whilst the electric field vector is shown, the solution is identical in form for a magnetic field, \mathbf{B} . Here, \mathbf{k} is the wavevector, ω is the angular frequency (related by $\omega = c|\mathbf{k}|$, with c the speed of light), $\hat{\mathbf{x}}$ is the unit vector in the x axis and \mathbf{E}_0 is known as the polarisation vector for the electric field. It is the latter term that provides an understanding on the path the \mathbf{E} field traces as it propagates. For a wave travelling in the z direction the electric field has the form:

$$\mathbf{E} = \mathbf{E}_0 e^{i\omega\left(\frac{z}{c} - t\right)}. \quad [1.18]$$

In which:

$$\mathbf{E}_0 = (E_x, E_y, 0). \quad [1.19]$$

\mathbf{E}_0 is orthogonal to \mathbf{k} and E_x , E_y , E_z are the electric field amplitudes in their respective axes and are complex, having both magnitude and phase, ϕ . These amplitudes can be defined in the form of:

$$E_x = |E_x| e^{i\phi_x}. \quad [1.20]$$

Combining equation [1.18] with [1.19] and [1.20], the full form of the \mathbf{E} field can be described as:

$$\mathbf{E} = E_x \hat{\mathbf{x}} \cos(kz - \omega t + \phi_x) + E_y \hat{\mathbf{y}} \cos(kz - \omega t + \phi_y). \quad [1.21]$$

1.2 Light Polarisation

Electromagnetic waves consist of orthogonal electric and magnetic field vectors propagating in space. The polarisation of a wave is often described in terms of its electric field vector. In the case of unpolarised light, the electric field vector is considered to propagate in an infinite number of planes. The polarisation of a light wave can be altered with optical components such as polarisers and wave-plates. A plane wave is considered linearly polarised in the y-axis if the polarisation vector [1.19] has components $E_x=0$ and $E_y \neq 0$ with no phase difference between them. From [1.21] it is clear that the resulting \mathbf{E} field would have the form:

$$\mathbf{E} = E_y \hat{y} \cos(kz - \omega t) . \quad [1.22]$$

A further type of polarisation can be produced if a phase difference of $\phi_x - \phi_y = \frac{\pi}{2}$ is introduced. With \mathbf{E}_0 components now $(E_0, iE_0, 0)$, the real part of the electric field is found to be:

$$\text{Re}[\mathbf{E}] = (E_0 \cos(kz - \omega t), -E_0 \sin(kz - \omega t), 0) . \quad [1.23]$$

This is known as left-handed circularly polarised (LCP) light, named as such due to the electric field vector tracing an anti-clockwise circle as it propagates. Similarly, right-handed circularly polarised (RCP) light is the result of a phase difference of $-\frac{\pi}{2}$. Linearly polarised light (LPL) can also be considered as a linear combination of LCP and RCP. The addition of the two yields:

$$\mathbf{E}_0 = (E_0, iE_0, 0) + (E_0, -iE_0, 0) = (2E_0, 0, 0) . \quad [1.24]$$

Which is x-polarised LPL, the subtraction of the respective waves therefore gives y-polarised LPL. As has been shown, circularly polarised light (CPL) arises from a difference in phase of the \mathbf{E}_0 vector components. If their magnitudes vary over time, such as through absorption, an ellipse rather than a circle is traced along the propagation axis, this is aptly named elliptical polarisation.

Polarisers work by limiting the axes of light that can pass through them. The first such invention was the polaroid film, which was composed of polymer molecules that were aligned in one direction on the surface. The light incident on the film could only excite the molecules in their direction of alignment, hence restricting the \mathbf{E} vectors in this orientation and allowing light perpendicular to the polymer to pass. There also exists many materials that are birefringent, meaning they have different refractive indices in different directions. Calcite is one example, where the difference in the refractive index arises from its crystal structure. The polaroid film could also be considered an example, with the refractive index, $n=\infty$, in one direction. Quartz is a common component of wave-plates, which are used to produce CPL from LPL (quarter-wave plate) or rotate the polarisation of LPL (half-wave plate). The birefringence of quartz introduces a phase shift in an incident plane wave, with the appropriate selection of quartz thickness, this phase difference can be controlled.

1.3 Chirality and Chiroptical Measurements

An object is said to be chiral if it is non-superimposable on its mirror image. This property takes its name from the Greek 'Χέρι' meaning 'hand', with hands themselves being examples of chiral entities. The term was first used by Lord Kelvin in 1894³ and has since then gone on to become a rich field of research with relevance in many areas of modern science.⁴ Chirality extends across a vast range of scales, from spiralling galaxies, to the molecules that exist within them. Molecules that are chiral possess the same atomic constituents and share many properties, it is their conformations in space that are distinct and are referred to as enantiomers. Enantiomers are often distinguished as left- (LH) or right-handed (RH), although are conventionally identified within chemistry as R (rectus, Latin for right) or S (sinistral, left) from the Cahn-Ingold-Prelog rules.⁵

It is thought that chirality could be key to one of the greatest mysteries in nature, the origin of life, given the prevalence of homochirality.⁶ This phenomenon is the observation that all naturally occurring amino acids (with the exception of achiral glycine) and sugars are exclusively LH or RH, respectively. Whilst a definitive answer to this question remains elusive, the importance of chirality in day-to-day life is still apparent. Although many chemical properties of chiral enantiomers are the same, their interaction with other chiral environments can produce drastically different outcomes. Enzymes and receptors within the human body are examples of chiral objects, highlighting the important implications in accurately identifying which enantiomers might be present in foods and pharmaceuticals.⁷ The most severe of man-made cases was that of Thalidomide, with the R enantiomer providing relief for morning sickness but the S enantiomer being a teratogenic, which causes foetal abnormalities.⁸ Not all chiral compounds have such drastic differences between enantiomers, often any variations can be as trivial as odour or taste.⁹⁻¹¹

The description of molecules can often involve the use of point groups, which describe the symmetry operations that are applicable to their structures. Each point group consists of a collection of symmetry operations, which are operations that manipulate an object or structure in space. Chiral molecules lack an improper axis of rotation (a rotation followed by a reflection), S_n , an inversion through a centre of symmetry, I , or a mirror plane, σ . For these notations, the 'n' subscript represents the degree of rotation, by angle $360^\circ/n$. Chiral molecules therefore must belong to one of the point groups C_n , D_n , O , T or I .⁴

A further convention for distinguishing between enantiomers is with d- and l-notation, which is related to the direction of in which the molecule rotates plane polarised light. Optical rotation with a clockwise rotation (+) is termed d- and anticlockwise (-) l-, from dextrorotatory (right) and laevorotatory (left). When measured across a wavelength range, optical rotation is known as optical rotatory dispersion (ORD). ORD is known as a chiroptical technique, meaning it is capable of distinguishing between enantiomers.

As shown previously, LPL can be considered a superposition of two counter rotating CPL waves. When passing through an achiral medium, the two components propagate at the same velocities and with the same phase, such that the incident LPL emerges with its polarisation unchanged. If the medium is chiral, it is said to be optically active and CPL components will experience a different refractive index and will travel at different velocities. Upon recombination, the

phase difference that arises will result in the LPL polarisation being rotated. The angle of rotation, α , is given by the equation⁴:

$$\alpha = \frac{1}{2}(\theta_L + \theta_R). \quad [1.25]$$

Where θ_L and θ_R are the angles the electric vectors of the left (E_L) and right (E_R) beams make with the incident polarisation plane. The phenomenon is depicted in **figure 1.1**. ORD is routinely used for the conformational studies of biomolecules, including the binding effects of nucleic acids with other proteins, drugs and amines.¹²

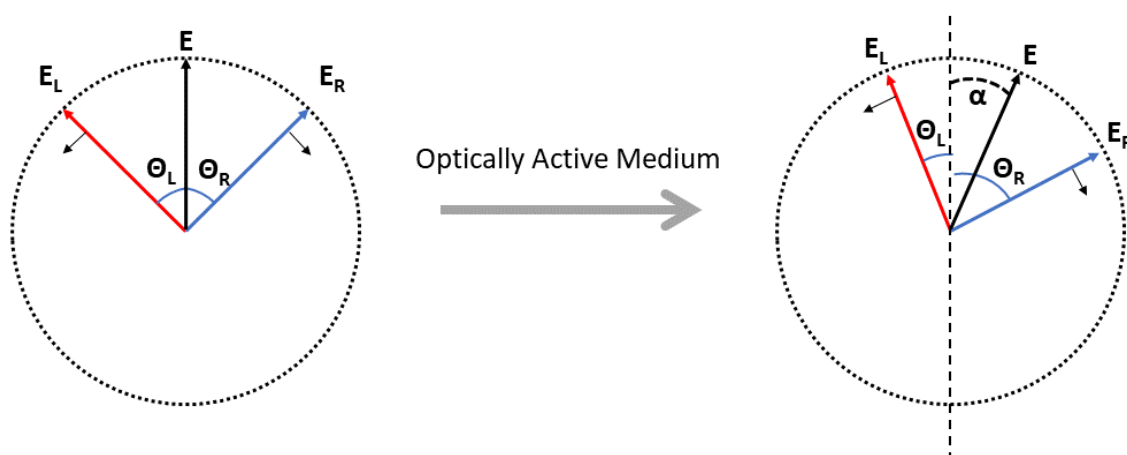


Figure 1.1: A visualisation of LPL, a superposition of counter rotating CPL components, passing through an optically active medium. The LCP (red) component experiences a different refractive index to the RCP (blue) component, resulting in a rotation of the plane of polarisation of the LPL wave.

A closely related property, known as circular dichroism (CD), is another widely used chiroptical method. It has been used extensively as a means to study biomolecular conformations, interactions and mutation effects.¹³ Rather than a difference in velocity between the CPL components, the difference in their absorption is measured. Preferential absorption of one component will result in the reduction of one of the CPL vector's magnitudes, in which case their recombination will result in the total electric field vector tracing an elliptical path rather than a circular one, visualised in **figure 1.2**. Ellipticity, ψ , is defined as the ratio between the minor and major axis of the ellipse. It is defined as the ratio of the difference and sum of the circular components⁴:

$$\tan \psi = \frac{E_R - E_L}{E_R + E_L}. \quad [1.26]$$

L- and R-CPL therefore have ellipticity values of $+45^\circ$ and -45° , respectively.

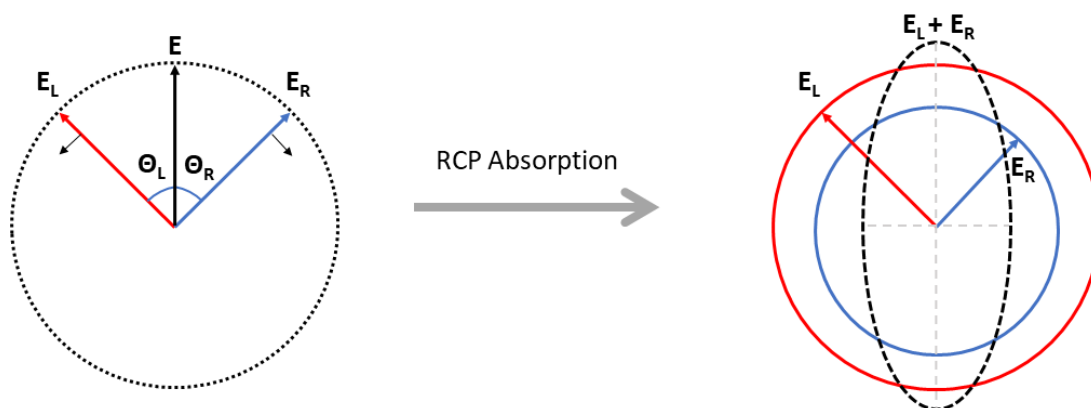


Figure 1.2: A visualisation of LPL undergoing uneven absorption of CPL components, where only RCP is absorbed, after which the wave gains an elliptical polarisation.

It must be noted that there exists a degree of confusion within the literature regarding the distinction between optical rotation and optical activity. If optical rotation occurs within a system, this does not necessarily imply that the system is optically active. Optical activity refers explicitly to CD and circular birefringence (CB), CB being the phenomenon of counter rotating CPL waves experiencing different refractive indices within a medium. Optical rotation can occur due to linear birefringence (LB), a non-chiroptical effect, which is the difference in refractive index between LPL waves of different polarisation planes (i.e. x- and y-polarised). CB and LB effects can occur separately or simultaneously, so one must be cautious when attributing optical rotation to optical activity and consider the symmetry of the medium in question and the polarimetry techniques used for measurements.

It should also be noted that the optical activity throughout this thesis refers to what is known as natural optical activity, where mirror image objects display equal and opposite optical rotation. There also exists the phenomenon of magnetic optical activity, discovered by Michael Faraday, in which achiral molecules within a static magnetic field can generate opposing optical rotations when the magnetic field is reversed. This is not a chiral effect and arises due to the particles being set into a circular motion by the surrounding magnetic field.¹⁴

A general term used to evaluate the level of chiral dissymmetry within a system is the dissymmetry factor, g . It is defined by the ratio of the circular dichroism to the absolute absorption intensities. It can provide an indication as to whether the CD in a particular absorption band is measurable based on the instrument sensitivity⁴:

$$g = \frac{A_{LCP} - A_{RCP}}{\frac{1}{2}(A_{LCP} + A_{RCP})} . \quad [1.27]$$

Where $A_{LCP/RCP}$ represents the absorption rate of RCP and LCP light. CD and ORD are said to be Kramers-Kronig related due to the way that the properties are associated with the complex refractive index. ORD is dependent on the real part and CD on the imaginary part. It is therefore possible to obtain one dataset from the other if only one is known.¹⁵

1.4 Optical Chirality

There is an intrinsic weakness in traditional chiroptical measurements that stems from the dimensional mismatch between the chiral molecules and the incident CPL. As a consequence, CPL undergoes a barely perceptible twist as it travels across the molecule, limiting the sensitivity of the measurements.¹⁶ There is therefore a clear motivation to enhance the light-matter interaction to achieve significantly greater responses between the incident light and the analyte.

CPL represents the light-based manifestation of chirality, as the circular paths traced by \mathbf{E} for RCP and LCP are non-superimposable mirror images. In 1964, Lipkin introduced ten new conservation equations for electromagnetic waves, which at the time were dismissed as having no physical meaning, and as such were named 'Zilches'.¹⁷ In 2010, Tang and Cohen were seeking to quantify the chirality of an electromagnetic wave. To do so, they needed an equation which satisfied the necessary symmetry conditions and described a wave that had field lines wrapping around a central axis as well as a component parallel to the axis. They identified that one of Lipkin's Zilches fit this description. They termed this quantity optical chirality density, C , which in its time dependent form is given by¹⁸:

$$C \equiv \frac{\epsilon_0}{2} \mathbf{E} \cdot \nabla \times \mathbf{E} + \frac{1}{2\mu_0} \mathbf{B} \cdot \nabla \times \mathbf{B}. \quad [1.28]$$

This parameter essentially describes the degree to which the electric and magnetic field vectors wrap around the axis of propagation, visualised in **figure 1.3**, from the curl of the fields. In addition, the presence of the dot product satisfies the component parallel to the propagation axis. The time averaged optical chirality is given as¹⁹:

$$\bar{C} = \frac{\epsilon_0 \omega}{2} \text{Im}(\mathbf{E}^* \cdot \mathbf{B}). \quad [1.29]$$

Here, \mathbf{E} and \mathbf{B} represent the complex electric and magnetic field amplitudes, respectively. The optical chirality can be incorporated into the dissymmetry factor to produce a general definition of g that can describe any electromagnetic field²⁰:

$$g = g_{\text{CPL}} \left(\frac{cC}{2U_e \omega} \right). \quad [1.30]$$

In which g_{CPL} is the dissymmetry factor under CPL, c is the speed of light, U_e is the local electric energy density and ω is the angular frequency. The equation implies that if the ratio within the parenthesis can be increased relative to g_{CPL} , then the overall dissymmetry of a system can be greater than when it is exposed to CPL alone. In cases where $\left(\frac{cC}{2U_e \omega} \right)$ exceeds unity (the value for CPL), then the field is termed superchiral.

Tang and Cohen demonstrated that this could be achieved by decreasing the U_e value of the electromagnetic field in a theoretical experiment. Briefly, they achieved this by creating a standing wave from two counterpropagating CPL beams of opposite handedness, reflected from an imperfect mirror. A LCP wave reflected at the mirror produced a RCP wave with the same phase and frequency, but with a slightly reduced amplitude. It is at the nodes of the standing wave that the U_e is

at its minimum, which maximises the overall dissymmetry factor for the system. Placing chiral molecules at the nodes then led to enantioselective enhancements of between one and two orders of magnitude.¹⁸ A further method that has been used to maximise the g factor, is through the fabrication of a modern class of materials, known as metamaterials.

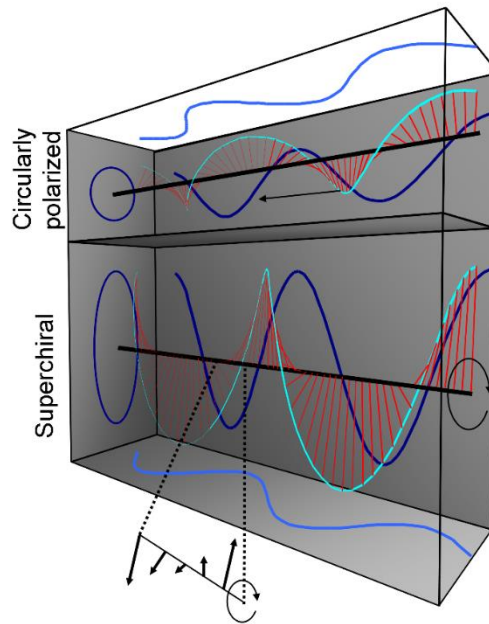


Figure 1.3: A visualisation of the E vector for CPL (top) and a superchiral field (bottom), with projections of the fields on adjacent walls of the figure in blue. The superchiral field displays regions in which the E vector undergoes a greater sense of twist than that of the CPL wave. Figure adapted from reference ¹⁸.

Optical chirality is a conserved property, meaning it remains constant over time in a given system. The flow of optical chirality, optical chirality flux, \mathbf{F} , was described by Tang and Cohen as¹⁸:

$$\frac{\partial C}{\partial t} + \frac{1}{\mu_0} \nabla \cdot \mathbf{F} = -\frac{1}{2} (\mathbf{J} \cdot \nabla \times \mathbf{E} + \mathbf{E} \cdot \nabla \times \mathbf{J}). \quad [1.31]$$

This takes a similar form to the Poynting vector, \mathbf{S} , which describes the direction of power flow in a system:

$$\frac{\partial U}{\partial t} + \frac{1}{\mu_0} \nabla \cdot \mathbf{S} = -\mathbf{J} \cdot \mathbf{E}. \quad [1.32]$$

Where U is the electromagnetic energy density. Poynting's theorem states that energy lost by electromagnetic fields can be gained by particles and energy flowing out of the system, and vice versa. By analogy, this indicates that optical chirality can be interconverted between electromagnetic fields from the incident light and the chiral currents of a material. This process is known as the dissipation of optical chirality, which occurs through loss (absorption) and at interfaces between different materials.²¹ A material's chiral currents can therefore act as a source or sink of optical chirality. Optical chirality flux can serve as an indicator of light polarisation or depolarisation and can therefore provide a measure of optical chirality dissipation in the far field.²²

1.5 Metamaterials

Metamaterials are engineered materials that possess unique properties not found naturally. These materials are designed at the nano and microscale level, their behaviour controlled by manipulating the arrangement of their constituent elements to achieve the desired properties. The concept of metamaterials was pioneered by Sir John Pendry in the late 1990s, who developed microstructures with tuneable magnetic permeability values.²³ Shortly after, the development of split ring resonators were theorised and manufactured with negative permittivity and permeability values.^{24,25} Since then, metamaterials have gone on to find applications in optics, acoustics, electronics and sensing applications.²⁶ With advances in nanofabrication techniques, by which smaller and better resolved structures can be generated, there is still much potential for metamaterials to be explored.

There has been extensive research carried out on chiral geometries^{19,27-31} in an attempt to produce high regions of optical chirality and therefore strong chiroptical responses, some of which are shown in **figure 1.4**. The ability to produce natural optical activity within these metamaterials requires the stimulation of electric dipole, magnetic dipole and electric quadrupole moments within the constituent structures and their mutual interference.⁴

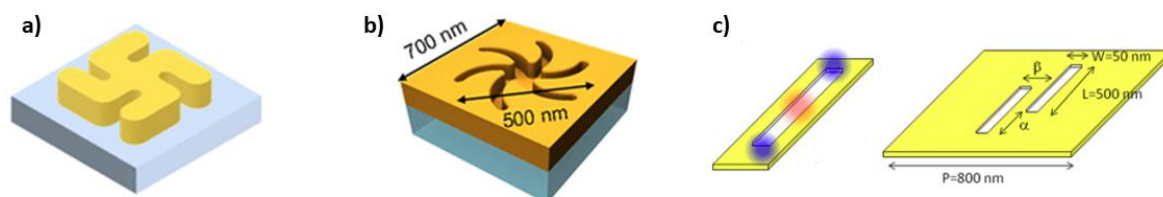


Figure 1.4: Examples of some chiral geometries used elsewhere. a) A RH gammadion b) a LH shuriken and c) an achiral nanoslit (left), which supports regions of enhanced electric (red) and magnetic (blue) fields, paired in a chiral arrangement (right). Images adapted from references ^{21,29,32}.

Gammadion structures similar to those pictured in **figure 1.4a**, have in the past been shown to be capable of distinguishing between protein conformations through asymmetries in the gammadion CD.²⁷ They are an example of a planar structure, their arms are arranged such that the local charge distributions provide favourable overlapping of dipole and multipole moments. Similarly, the shuriken patterned substrates, **figure 1.4b**, were found to show asymmetric responses between ORDs of their LH and RH forms, in the presence of a protein solutions.^{28,29} They are capable of generating equivalent electric and magnetic modes on top of each other, which can interact to produce optical activity.³³ It is also possible for achiral geometries, **figure 1.4c**, to produce chiral fields from asymmetric arrangement of the structures.³² The nanoslits possess both enhanced electric and magnetic field regions, which can be made to preferentially overlap by staggering their placement on the substrate.

The properties of chiral metamaterials can be difficult to predict, particularly whether a configuration will yield regions of higher optical chirality density. There are, however, some basic design principles that have been developed over several years of research that can be considered to maximise the likelihood of this desired property. Schäferling found that planar structures with a strong twist and without sharp corners are optimal for continuous regions of enhanced optical chirality. In

contrast, to obtain large gradients in the optical chirality, compact 3D structures should be utilised. Regardless of a structure's ability to produce strong chiral fields locally, this does not necessarily translate to the chiroptical measurement as the far-field chiral response can still be weak, adding further complexity to the problem. There remains much room for further exploration of the best structural designs, particularly with the freedom afforded by modern patterning techniques.¹⁹

Optical activity, being a reciprocal property, should not change with the direction of propagation of the incident light. Gammadions are said to possess geometric 2D chirality, in which the handedness of the structure depends on the side from which it is viewed. A 3D chiral object, shown in **figure 1.5**, will maintain its sense of twist no matter the face from which it is viewed. Its optical activity will therefore not change if the direction of light passage is reversed. For these reasons, optical activity cannot be achieved solely from geometric 2D chirality.³⁴



Figure 1.5: Examples of 2D and 3D chiral geometries. Defining the handedness of 2D chiral objects is arbitrary, as it changes depending on which side the object is viewed from. 3D chiral objects maintain their handedness regardless of how they are viewed. Figure adapted from reference ³⁴.

Many chiral metamaterial platforms rely on planar nanostructures like the gammadion and can be engineered to produce varying levels of optical activity. There is therefore an apparent contradiction, if geometric 2D chiral structures are unable to produce optical activity. There are two primary sources intrinsic to the fabrication of planar chiral metamaterials that contribute to the symmetry breaking of the structures, those being the presence of a substrate and the morphological defects that occur through the fabrication process. The presence of the substrate breaks the symmetry of the surrounding environment of the structure. This effectively makes the structure-substrate ensemble a 3D chiral system as the handedness is no longer reversed by viewing from opposite faces, due to the inequivalences in the structure's environment. One of the main fabrication defects that occurs when producing planar structures is the rounding of their outer edges. This can occur from multiple processes, such as high-aspect-ratio shading and angular dispersion of etching ions.³⁵ Even if one was to neglect the substrate and consider only fabrication defects of the sample, it is apparent that the rounding of the edges breaks the planarity of the structures, introducing asymmetry in the system and a level of optical activity.

1.6 Biosensors

A major theme of this thesis is the detection of biomolecular analytes by the metamaterial samples fabricated. This process falls under the field of biosensing, which is an essential part of many vital sectors, such as public health, environmental monitoring and largescale production of foodstuffs. These industries will only grow in importance as the world's population grows and their demands increase; metamaterials have emerged as a route towards cheaper, mass-produced and highly sensitive devices, which may help address this issue.^{27,28,36}

Biosensors are analytical devices that can produce a quantitative and specific response to the presence of a particular analyte. Their operation can generally be characterised by four components, visualised in **figure 1.6**.³⁷

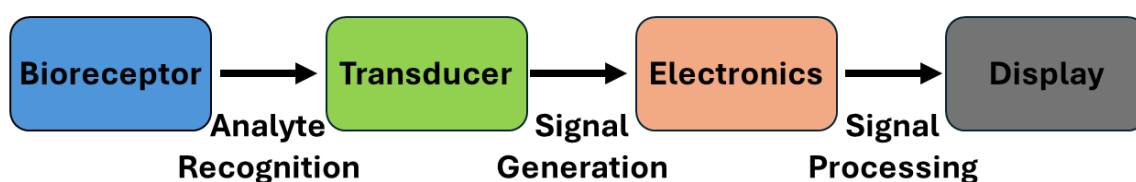


Figure 1.6: The four general components of a biosensor. Analyte recognition by the bioreceptor triggers a response by the transducer, which creates a measurable signal that can be processed by the device electronics. This response is returned to the user with some display.

A bioreceptor is immobilised on a substrate with defined properties and will interact with a target analyte in a response known as the bio-recognition event. This brings about a change in the properties of the transducer, which are components that generate a quantifiable signal from the bioreceptor-analyte interaction.³⁸ There are a variety of detection methods available, including potentiometric, impedimetric and piezoelectric.³⁹ Once the signal is generated, it is processed by the electronic components of the sensor and presented in a display which can be interpreted by the user.⁴⁰ Low-cost biosensors can operate without the need for electronics, such as the lateral flow biosensor.⁴¹

This thesis focusses on the transducer aspects of biosensing and seeks to identify novel methods of highly sensitive signal generation. As metamaterials can produce properties which can be finely controlled, they present an ideal platform for biosensing applications, in both the way they generate signals and in their sensitivity. As will be shown, both plasmonic and dielectric structures can generate measurable signals in the presence of biomolecules. Better understanding behind the processes of biomolecule detection with metamaterials will hopefully lead to the development of devices with higher throughput and lesser cost, which are important factors for wide-scale impact.

1.7 Conclusions

The fundamental theory relevant to subsequent chapters has now been introduced, alongside some general discussion regarding the field of chirality and metamaterials. Maxwell's equations represent the foundations of electromagnetic theory and are relied upon for the numerical simulations presented in this thesis. The concept of light polarisation must be understood to rationalise experimental techniques and their results, as changes to the polarisation states of light are measured through experiment. The concept of chiral molecules and enantiomers were discussed, alongside the chiroptical techniques of ORD and CD which are capable of distinguishing between them.

The phenomenon of optical activity was defined, which is a reciprocal effect in which chiral molecules produce optical rotation. It was highlighted that the presence of optical rotation alone is not sufficient to determine if an object is optically active. Properties such as LB can contribute to optical rotation and produce significant ORD signals, which has led to some confusion within the literature between optical rotation and optical activity. Such a distinction will prove important in later chapters regarding the silicon metamaterials studied.

One of the key motivations behind this work was identified as the desire to decrease the size disparity between the chiral centres of molecules and the light that probes them. The ability of electromagnetic fields to possess chirality was shown to be a potential solution to this problem, which led to the introduction of chiral metamaterials as a way to deliver platforms of enhanced sensitivity, as they are composed of nanostructures that can produce chiral fields. These fields are generated by interference between electric dipoles, magnetic dipoles and electric quadrupoles that are supported by structural features. As of yet, there is still no clear recipe for maximising the chirality of the fields they produce, and hence the strength of the chiroptical interactions they can exhibit. However, it is not just the nanostructures that can be tailored to enhance interactions; modifications to analyte properties can be performed as will be shown with the plasmonic gammadion metamaterials.

The distinction between 2D and 3D chirality was discussed. 2D geometric objects are incapable of being chiral as their handedness depends upon the face from which they are viewed through. 3D chiral object, however, maintain their handedness no matter their orientation. The ability of planar and seemingly 2D chiral nanostructures to be chiral was shown to arise from the presence of symmetry breaking perturbations; namely the substrate upon which they exist and the defects intrinsic to their fabricated process.

Finally, a general overview of a biosensor was provided, highlighting their four typical components. There are a variety of biosensor platforms that utilise different methods of signal generation, and metamaterials add a further tool in this arsenal as they offer unique optical properties with highly controllable spectra, as will be shown in this work.

1.8 References

1. Jackson, J. D. *Classical electrodynamics* . (1999).
2. Fleisch, D. *A Student's Guide to Maxwell's Equations. Student's Guides* (Cambridge University Press, 2008). doi:DOI: 10.1017/CBO9780511984624.
3. Kelvin, W. T. Baltimore Lectures. in.
4. Barron, L. D. *Molecular Light Scattering and Optical Activity*. (Cambridge University Press, 2004). doi:10.1017/CBO9780511535468.
5. Cahn, R. S., Ingold, C. & Prelog, V. Specification of Molecular Chirality. *Angew. Chemie Int. Ed. English* **5**, 385-415 (1966).
6. Barron, L. D. Chirality and Life. *Space Sci. Rev.* **135**, 187-201 (2008).
7. Nguyen, L. A., He, H. & Pham-Huy, C. Chiral drugs: an overview. *Int. J. Biomed. Sci.* **2**, 85-100 (2006).
8. Vargesson, N. Thalidomide-induced teratogenesis: history and mechanisms. *Birth Defects Res. C. Embryo Today* **105**, 140-156 (2015).
9. Gal, J. Molecular Chirality in Chemistry and Biology: Historical Milestones. *Helv. Chim. Acta* **96**, 1617-1657 (2013).
10. Schiffman, S. S., Sennewald, K. & Gagnon, J. Comparison of taste qualities and thresholds of D- and L-amino acids. *Physiol. Behav.* **27**, 51-59 (1981).
11. Brookes, J. C., Horsfield, A. P. & Stoneham, A. M. Odour character differences for enantiomers correlate with molecular flexibility. *J. R. Soc. Interface* **6**, 75-86 (2009).
12. Greenfield, N. J. Circular Dichroism and ORD, Biomacromolecular Applications. in (eds. Lindon, J. C., Tranter, G. E. & Koppenaal, D. W. B. T.-E. of S. and S. (Third E.) 263-275 (Academic Press, 2017). doi:<https://doi.org/10.1016/B978-0-12-803224-4.00109-6>.
13. Martin, S. R. & Schilstra, M. J. Circular Dichroism and Its Application to the Study of Biomolecules. in *Methods in Cell Biology* vol. 84 263-293 (Academic Press, 2008).
14. Barron, L. D. True and false chirality and absolute enantioselection. *Rend. Lincei* **24**, 179-189 (2013).
15. Collins, J. T. *et al.* Chirality and Chiroptical Effects in Metal Nanostructures: Fundamentals and Current Trends. *Adv. Opt. Mater.* **5**, (2017).
16. Mason, S. F. *Molecular optical activity and the chiral discriminations*. (Cambridge University Press, 1982).
17. Lipkin, D. M. Existence of a New Conservation Law in Electromagnetic Theory. *J. Math. Phys.* **5**, 696-700 (1964).
18. Tang, Y. & Cohen, A. E. Optical Chirality and Its Interaction with Matter. *Phys. Rev. Lett.* **104**, 163901 (2010).
19. Schäferling, M., Dregely, D., Hentschel, M. & Giessen, H. Tailoring Enhanced Optical Chirality: Design Principles for Chiral Plasmonic Nanostructures. *Phys. Rev. X* **2**, 31010 (2012).
20. Tang, Y. & Cohen, A. E. Enhanced Enantioselectivity in Excitation of Chiral Molecules by Superchiral Light. *Science* (80-.). **332**, 333 (2011).
21. Gilroy, C. *et al.* Roles of Superchirality and Interference in Chiral Plasmonic Biodetection. *J. Phys. Chem. C* **123**, 15195-15203 (2019).
22. Poulidakos, L. V *et al.* Optical Chirality Flux as a Useful Far-Field Probe of Chiral Near Fields. *ACS Photonics* **3**, 1619-1625 (2016).
23. Pendry, J. B., Holden, A., Robbins, D. J. & Stewart, W. J. Magnetism from Conductors, and Enhanced Non-linear Phenomena. *Microw. Theory Tech. IEEE Trans.* **47**, 2075-2084 (1999).

24. Smith, D. R., Padilla, W. J., Vier, D. C., Nemat-Nasser, S. C. & Schultz, S. Composite Medium with Simultaneously Negative Permeability and Permittivity. *Phys. Rev. Lett.* **84**, 4184-4187 (2000).
25. Smith, D. R., Pendry, J. B. & Wiltshire, M. C. K. Metamaterials and Negative Refractive Index. *Science* (80-.). **305**, 788 (2004).
26. Valipour, A., Kargozarfard, M. H., Rakhshi, M., Yaghootian, A. & Sedighi, H. M. Metamaterials and their applications: An overview. *Proc. Inst. Mech. Eng. Part L J. Mater. Des. Appl.* **236**, 2171-2210 (2021).
27. Hendry, E. *et al.* Ultrasensitive detection and characterization of biomolecules using superchiral fields. *Nat. Nanotechnol.* **5**, 783 (2010).
28. Karimullah, A. S. *et al.* Disposable Plasmonics: Plastic Templated Plasmonic Metamaterials with Tunable Chirality. *Adv. Mater.* **27**, 5610-5616 (2015).
29. Kelly, C. *et al.* Chiral Plasmonic Fields Probe Structural Order of Biointerfaces. *J. Am. Chem. Soc.* **140**, 8509-8517 (2018).
30. Kelly, C. *et al.* Controlling the symmetry of inorganic ionic nanofilms with optical chirality. *Nat. Commun.* **11**, 5169 (2020).
31. Gilroy, C. *et al.* Active Chiral Plasmonics: Flexoelectric Control of Nanoscale Chirality. *Adv. Photonics Res.* **2**, 2000062 (2021).
32. Hendry, E., Mikhaylovskiy, R. V, Barron, L. D., Kadodwala, M. & Davis, T. J. Chiral Electromagnetic Fields Generated by Arrays of Nanoslits. *Nano Lett.* **12**, 3640-3644 (2012).
33. Horák, M. *et al.* Limits of Babinet's principle for solid and hollow plasmonic antennas. *Sci. Rep.* **9**, 4004 (2019).
34. Arteaga, O. *et al.* Relation between 2D/3D chirality and the appearance of chiroptical effects in real nanostructures. *Opt. Express* **24**, 2242-2252 (2016).
35. Sarangan, A. *Nanofabrication: Principles to Laboratory Practice.* (CRC Press, 2016).
36. Hassan, M. M., Sium, F. S., Islam, F. & Choudhury, S. M. A review on plasmonic and metamaterial based biosensing platforms for virus detection. *Sens. Bio-Sensing Res.* **33**, 100429 (2021).
37. Bhalla, N., Jolly, P., Formisano, N. & Estrela, P. Introduction to biosensors. *Essays Biochem.* **60**, 1 (2016).
38. Yadav, S., Saini, A., Devi, R. & Lata, S. Transducers in Biosensors BT - Biomaterials-Based Sensors: Recent Advances and Applications. in (eds. Kumar, P., Dash, S. K., Ray, S. & Parween, S.) 101-125 (Springer Nature Singapore, 2023). doi:10.1007/978-981-19-8501-0_4.
39. Halilovic, A., Merdan, E., Kovačević, Ž. & Gurbeta Pokvic, L. *Review of Biosensors for Environmental Field Monitoring.* (2019). doi:10.1109/MECO.2019.8760166.
40. Mehrotra, P. Biosensors and their applications - A review. *J. Oral Biol. Craniofacial Res.* **6**, 153-159 (2016).
41. Quesada-González, D. & Merkoçi, A. Nanoparticle-based lateral flow biosensors. *Biosens. Bioelectron.* **73**, 47-63 (2015).

Chapter 2: Metamaterial Fabrication

The procedures involved in the fabrication of the two types of samples used in this work are detailed in this chapter, including the characterisation techniques used to validate the quality and effectiveness of the overall process. Summaries of both fabrication processes are given towards the end of the chapter.

Modern-day nanofabrication continues to push the limits of nanopatterned materials, as new fabrication technologies further improve the quality and reduce the scale of design features.¹ Sub-micron structures down to several nanometres in size are now routinely produced, which has ultimately been the driving force behind the technological revolution of the last century: specifically, the reduction in scale of the transistor. Similar advances have been observed in fields such as optics and biosensing, as current processes allow for the production of a vast range of structures of both 2- and 3-dimensions.² This has led to the rise of metamaterials as one of the most exciting fields of modern research, with nanofabrication providing unprecedented control over material properties.³

All fabrication procedures took place in the James Watt Nanofabrication Centre (JWNC). The JWNC hosts a cleanroom facility, which is a highly controlled environment suitable for the production of micro and nanoscale devices. Factors such as air flow, temperature, lighting and clothing are controlled to minimise the risk of contaminants coming into contact with samples. Cleanrooms like the JWNC possess state of the art equipment, which are capable of performing the precise and accurate processes necessary when manufacturing devices of such a small scale.^{4,5}

2.1 Fabrication Processes

2.1.1 Structure Design

The first step of any fabrication process is the design of the structures being produced, typically done with a computer aided design (CAD) package, in this case *L-Edit*. This software allows for the drawing of multi-layered designs which can be of particular use in the fabrication of semiconductor devices. Two types of metamaterial samples were produced for this work: gold gammadions and silicon S-shaped nanostructures. The CAD file can be imported into the software *Cjob*, in which the position of the structures on the substrate can be input along with the electron beam (e-beam) parameters.

2.1.2 Sample Cleaning

In this work, each process begins with the cleaning of a substrate which for both sample types was a square (25 x 25 mm) quartz glass slide (*Newcastle Optical Engineering*). Given the nanoscale dimensions of the structures being fabricated, the presence of excessive impurities on a substrate are likely to lead to the spoiling of a sample. It is therefore vital that substrates are cleaned thoroughly before any other procedures take place.⁶ A standard cleaning procedure, known as AMI (Acetone, Methanol, Isopropyl Alcohol), provides the starting point of the fabrication procedure. The substrate is immersed in each solution separately for

5 minutes whilst under ultrasonic agitation. Gradual displacement of the previous solution is performed, with care taken to prevent the sample from drying between steps. Acetone is a solvent capable of removing both polar and non-polar contaminants, however, if used alone it would leave a residue upon drying. Methanol is therefore used to dissolve the residual acetone, before isopropyl alcohol (IPA) removes the methanol. IPA offers the added benefit of dehydrating the surface, removing the requirement for a high temperature bake. Ultrasonic cleaning exposes the sample to high frequency waves operating at 1-2 MHz, capable of removing particles as small as 100 nm. Regions of high-pressure oscillating waves are created across the sample surface which carry away impurities. Once removed from the IPA, the samples are dried under flow of N₂.

The quartz substrates are then exposed to an oxygen plasma to remove any remaining contaminants. High energy oxygen radicals are made incident on the surface. These react with organic species on the surface to produce volatile chemical species that are pumped out of the vacuum chamber. UV radiation created by the plasma discharge also helps breakdown organic molecules on the sample. During the cleaning stage, a 100 W plasma for 5 minutes is sufficient to prepare the substrate for the following steps.

2.1.3 Electron Beam Lithography

E-beam lithography provides a highly controllable, high-resolution method of nanopatterning materials.^{7,8} A high energy beam of electrons is created under high vacuum and a combination of magnetic lenses are used to focus and move the beam. Although the theoretical wavelength of an electron at 100 keV is 4 pm, due to electron-optical and process limitations, typical resolution limits are of the 10s of nanometre scale. For both sets of samples, a *Raith EBPG 5200* electron beam tool operating at 100 kV was used.

To transfer a pattern onto the surface, an electron sensitive resist is required. This is typically done using a resist spinner, of which the rotational speed (and resist type) dictates the thickness of the layers. E-beam resists contain a photoactive compound and a solvent. For both sample types, poly-methyl methacrylate (PMMA) was used as the photoactive compound, spun at 4000 rpm for 1 minute.⁹ For optimal pattern transfer a resist bilayer is spun, a representation of which is shown in **figure 2.1**. PMMA is a positive photoresist, where upon exposure, is broken down into smaller fragments which are soluble in resist developer, which in this work was methyl isobutyl ketone (MIBK) in IPA. The resist is therefore removed in the regions that are exposed to the beam after development. This is contrary to negative photoresists, where e-beam written regions undergo a strengthening cross-linking reaction and become insoluble when placed in developer.

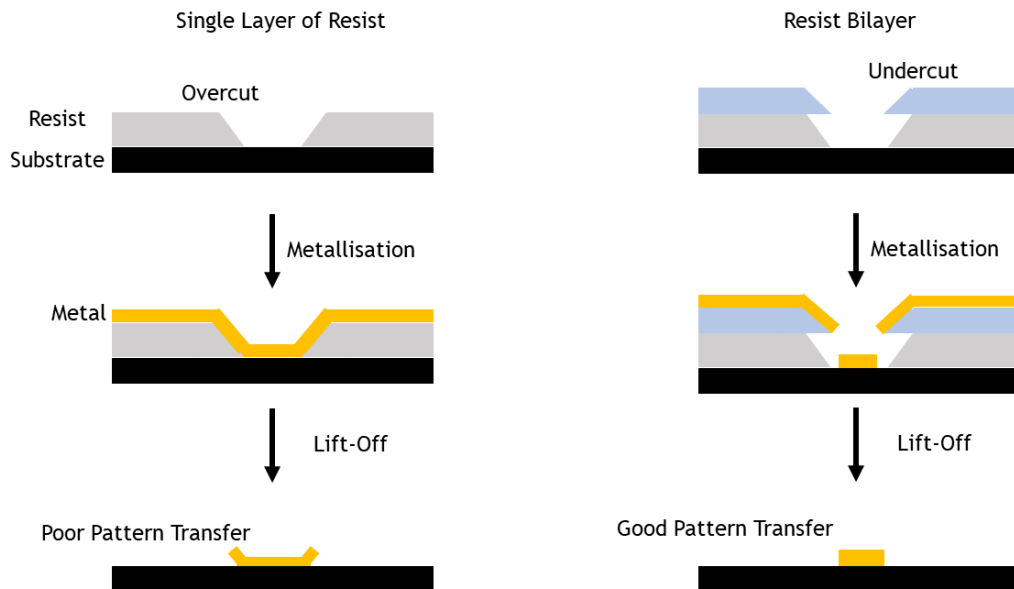


Figure 2.1: A visualisation of the metallisation and lift-off processes when using a resist single layer (left) and bilayer (right), post e-beam exposure and development. Non-uniform electron exposure can lead to wall sloping, an ‘overcut’, which increases the likelihood of defects upon lift-off (final removal of resist). This undesirable effect can be limited with a resist bilayer, which utilises an ‘undercut’ to improve pattern transfer. The undercut forms due to the top layer developing at a slower rate compared to the bottom layer.

Development of resist generally yields a sloped profile due to the exposure of the electrons not being perfectly uniform. The effects of this can be reduced with a bilayer. The use of a single layer maintains the sloped walls of resist, which can lead to artifacts from the metallisation process. In the bilayer, the top layer resist type develops at a slower rate than the bottom layer, which results in the ‘undercut’ profile shown, providing a better means of pattern transfer.

An important part of any fabrication process that involves a lithography step is the dose test. This is performed to determine the e-beam parameters for optimal pattern transfer, which includes variables such as electron dose and beam current.¹⁰ These values will vary depending on the types of resists used. Parameters are typically altered in steps across a pre-determined range. The results can be analysed by scanning electron microscope (SEM), to confirm which e-beam values are most favourable.

2.1.4 Material Deposition

2.1.4.1 Metals

Deposition of metals and dielectrics are amongst some of the most widely used procedures in nanofabrication. All metals deposited on these samples were performed with a *PLASSYS MEB 550s* electron beam evaporator. These tools operate at high vacuum, where electrons are generated from a heated tungsten filament and accelerated towards a metal target by a strong negative potential.¹¹ A combination of magnets and electromagnets are used to guide the electrons towards a crucible containing a metal target. The electrons cause the evaporation of the metal, which is directed towards the sample chamber. Slow rotation of the sample provides a controlled, uniform coverage with the desired metal for a specified depth.

Whilst most of the metallisation occurs after the resist has been developed, there is an initial 10 nm Al layer required for both sample types prior to e-beam exposure. This acts as a conducting layer to prevent charge build-up on the sample, which would negatively affect the quality of the structures. The Al layer later is removed before after e-beam writing using the chemical CD-26, which is corrosive to Al, before the sample is placed in resist developer.

After development of the exposed resist in MIBK:IPA solution for 1 minute, the next metal evaporation on the sample is performed. For the gammadion samples, a 5 nm NiCr adhesive layer is deposited under 100nm of Au. The silicon samples undergo a 50 nm NiCr deposition, required as an etch mask later. The resist development removes the regions of resist exposed under e-beam, the metal deposited in these regions is therefore in direct contact with the material upon which the resist was spun (quartz glass for the gammadions and silicon for the s-structures), in the shape of the designed structures. As the metal deposition is uniform, metal also deposits over the remaining resist, where the e-beam did not pattern. These regions, which surround the intended structures, must be removed in a process known as lift-off, which was previously shown in **figure 2.1**. This is performed in a 50°C acetone bath for several hours (overnight). The acetone acts on the resist that remains on the samples, upon which the excess metal lies. After a sufficient time period, gentle agitation of the sample in the acetone strips the resist, carrying away the excess metal. For the gammadion samples, the process would be complete upon a final cleaning of the sample. The silicon structures require further process steps, to remove the silicon beneath the NiCr etch mask.

2.1.4.2 Silicon

Whilst the gammadion samples have metals deposited directly onto the substrate surface, the s-structure samples require the deposition of amorphous silicon after the initial cleaning. The silicon layer is deposited differently to the metals, using the technique of Plasma Enhanced Chemical Vapour Deposition (PECVD). PECVD requires a mixture of gaseous precursor chemicals that react to form a vapour of the material to be deposited, which then coats the sample.¹² This is similar to traditional chemical vapour deposition, however a benefit of PECVD is the large reduction in sample temperatures, from 500-1000°C to 300°C, due to the reactive precursor radicals being produced by the low power RF plasma. The PECVD process was carried out on an *SPTS Delta* tool using SiH₄ feed gas at 300°C and a pressure of 600 mT.

2.1.5 Silicon Sample Etching

Etching is the removal of a material from a sample substrate and can be performed under 'dry' or 'wet' conditions.^{13,14} The removal of the silicon not protected by the NiCr etch mask was done via a dry etch process. Also known as plasma etching, the process is like that of PECVD, where feed gases are ionised between charged plates. The difference arises from the radicals generated reacting with surface atoms to create volatile species that are removed in the vacuum chamber. Plasma etching can be isotropic or anisotropic, where the removal of the etched material is uniform in all directions or faster in one plane over others, respectively. The crystal structure of materials such as silicon, as well as the etchant used, will determine which etch profile is obtained. When etching to create nanostructures,

etch masks are used to protect certain regions of the surface. The masks can be selected based on their etch rate relative to the target material, which is termed selectivity. A 50 nm NiCr mask was suitable for these samples. The etch feed materials used were SF₆/C₄F₈, which provided an anisotropic etch of the amorphous silicon, to provide sufficiently straight sidewalls on the structures.

Wet etching utilises etching solutions that can dissolve a given target material. Just as the Al layer was etched with CD-26, the NiCr etch mask was removed by individual exposure to both chromium etchant and nitric acid. Upon removal of the etch mask, the silicon samples were complete with a final sample cleaning.

2.1.6 Sample Characterisation

Several sample characterisation methods can be used to determine the effectiveness of the fabrication process. Optical microscopy (as well as photolithography) is limited in resolution by the wavelength of light, and while it can prove useful for the inspection of fabricated samples, it is incapable of reaching the resolution required to properly analyse the quality of nanoscale structures. A solution can be found by using electrons instead of light to view samples. Electrons can possess a much lower wavelength, allowing for the imaging of nanometre scale features. SEM provides a real-time, high-resolution view of a sample through the detection of incident electrons scattering from the surface. Deposition of a thin conducting film is required to prevent charge build up, like in e-beam lithography.

As with a lithographic tool, a high energy beam of electrons is guided towards the sample surface through magnetic interactions. Detectors surrounding the sample stage measure backscattered electrons that have impinged on the sample and are used to build an image as the e-beam is rapidly scanned across the region of the sample being viewed. A rotating sample stage allows for a view of the sample from multiple angles. SEM is first performed after the initial dose test for the lithography step. An *FEI NanoSEM 630* was used for all SEM images in this work, some of which are shown in **figure 2.2**.

The SEM images highlight the importance of finding the correct dose of electrons. Overexposure, in which the regions surrounding the target areas of the resist receive too high a dose, leads to poor resolution of the structures, in this instance producing no usable structures and rows of connected 'blotches'. At a more optimal dose, the resolution is vastly improved with a better realisation of the target structure.

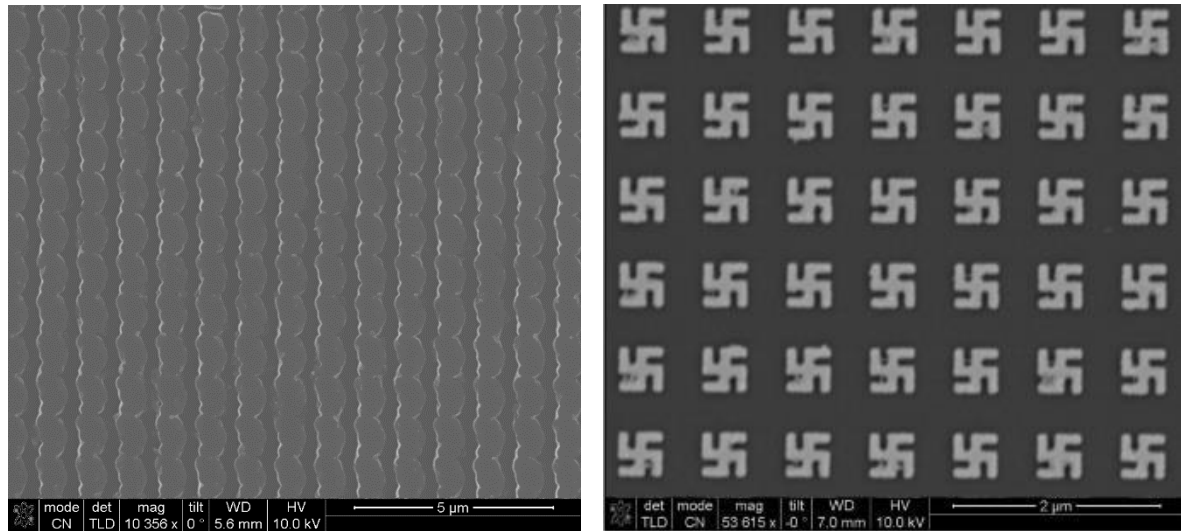


Figure 2.2: SEM images of a gammadion sample dose test with a poor dose selection of $1200 \mu\text{C cm}^{-2}$ (left) and a more optimal dose of $800 \mu\text{C cm}^{-2}$ (right), as part of a dose test, in which 200 nm of PMMA 2010 was topped by a 100 nm layer of PMMA 2014. Scale bars are 5 μm (left) and 2 μm (right).

Atomic force microscopy (AFM) is another valuable method of surface characterisation, which provides information on a sample's topography. AFM operates by moving a cantilever, oscillating at its resonance frequency, across a sample's surface. The resonance is driven by a piezoelectric material. A laser reflecting from the cantilever onto a photodiode provides the electric signal used as part of the measurement. When the cantilever tip approaches a sample surface, the interaction between the sample and tip generates a change in the signal from the reflected laser. The tip is extremely thin, often only a few atoms wide, and is therefore highly sensitive to changes in surface morphology which allows for high resolution imaging.

AFM tools can operate in contact and non-contact modes, the best method is dependent on the sample type. Non-contact tapping mode was used in this work, on a *Bruker Dimension Icon* system. Postprocessing of the AFM data was performed on *ProfilmOnline*, which enables the user to analyse specific scan regions, shown in **figure 2.3**, and obtain further data such as height and surface roughness.

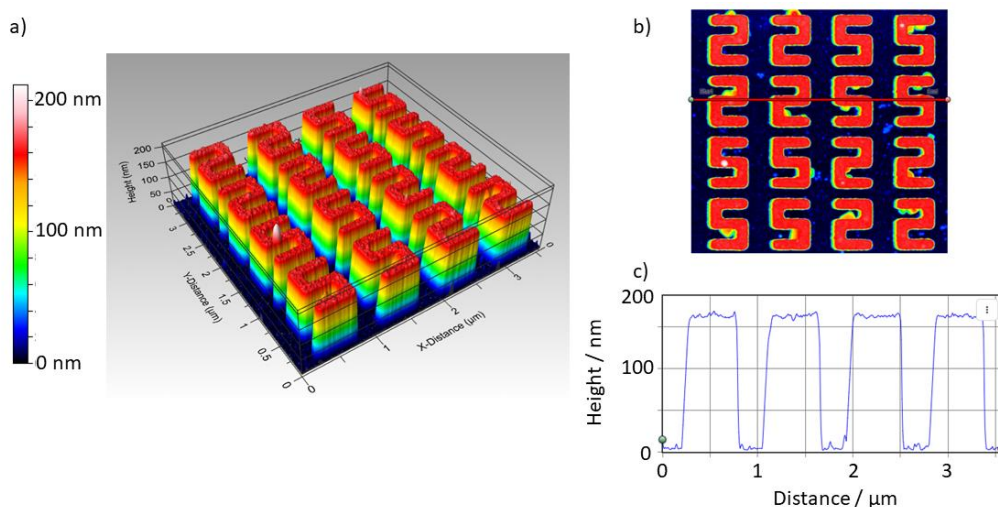


Figure 2.3: An example of AFM data collected for the silicon S structures. a) A 3D rendering of the sample scan. b) A top down 2D image of the scanned data, across which surface profiles can be obtained (measuring line shown in red). c) The height profiles obtained from the measurement line placed across the sample. Images acquired with *ProfilmOnline*.

Profilometry is a further technique used to measure the properties of a sample's surface. Operating in a similar fashion to AFM with the use of a cantilever, a significant difference lies in the tip size.¹⁵ Profilometers such as the *Dektak* used in this work possess larger tips which therefore offer a less detailed definition of the surface. They do however provide the advantage of a larger field of view and quicker scanning time and can be particularly useful in identifying areas of interest for subsequent AFM analysis. They can also provide quick information on the height of fabricated structures.

2.2 Process Summaries

2.2.1 Gold Gammadion Structures

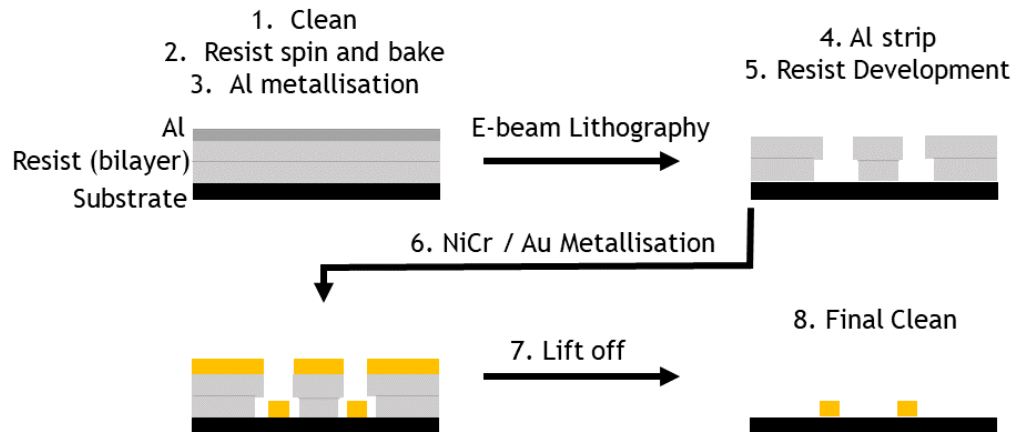


Figure 2.4: A schematic of the process steps involved for the fabrication of a gammadion sample and the materials present at each stage. 1.-3. details the initial cleaning, spinning of the PMMA bilayer and Al metallisation prior to e-beam exposure. 4.-5. shows the removal of the Al and exposed resist after e-beam exposure. 6. displays the NiCr / Au deposition and 7. the final lift-off, leaving only the gold gammadions.

1. Quartz substrate cleaned for 5 minutes each in acetone, methanol and IPA in an ultrasonic bath. Substrates dried under N₂ and subject to RIE for 5 minutes at 100 W.
2. Resist spinning at 4000 rpm for 1 minute for each resist, with a 5 minute 180°C bake after each spin. 200 nm of PMMA 2010 and 100 nm of PMMA 2014 were used.
3. 10 nm Al conductive layer deposited with metal evaporator. Sample submitted for e-beam writing.
4. After e-beam exposure, Al strip performed with CD-26 for 90 s, before rinsing with water and drying under N₂.
5. Development of exposed resist for 1 minute in 3:1 MIBK:IPA developer, then 5 s in IPA and rinsed in water. Development residue removed with 50 W, 10 s plasma clean.
6. Metallisation of sample with 5 nm NiCr adhesive layer prior to 100 nm Au.
7. Samples left in acetone at 50°C for lift-off. Agitation with pipette after several hours to aid removal of remaining resist.
8. Sample cleaned in plasma cleaner for 5 minutes at 100 W before use in experiment.

2.2.2 Silicon S-shaped Structures

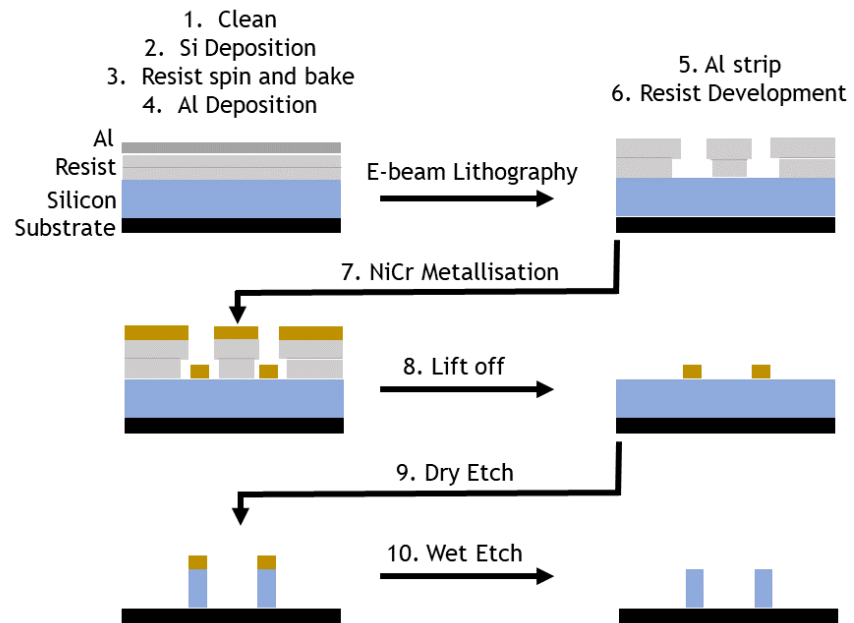


Figure 2.5: A schematic of the process steps involved for the fabrication of a silicon sample and the materials present at each stage. 1.-4. includes the initial cleaning, amorphous silicon deposition, resist bilayer spin and Al deposition. 5.-6. displays the Al strip and development of exposed resist. 7. shows the NiCr etch mask metallisation and 8. the lift-off. 9. shows the dry etch to removed unprotected silicon and 10. details the wet etch that removes the remaining NiCr mask, leaving only the silicon s-structures.

1. Quartz substrate cleaned for 5 minutes each with acetone, methanol and IPA in an ultrasonic bath. Substrates dried under N_2 and subject to RIE for 5 minutes at 100 W.
2. Silicon deposited on substrate via PECVD, using SiH_4 feed gas at $300^\circ C$ and a pressure of 600 mT.
3. Resist spinning at 4000 rpm for 1 minute for each resist, with a 5 minute $180^\circ C$ bake after each spin. PMMA 632.12 50k in anisole was used for a 300 nm initial layer, followed by PMMA 649.04 200k in ethyl lactate for a 150 nm layer.
4. 10nm Al conductive layer deposited with metal evaporator. Sample submitted for e-beam writing.
5. After e-beam exposure, Al strip performed with CD-26 for 90 s, before rinsing with water and drying under N_2 .
6. Development of exposed resist for 1 minute in 2.5:1 MIBK:IPA developer, then 5 s in IPA and rinsed in water. Development residue removed with 50 W, 10 s plasma clean.
7. Metallisation of sample with 50 nm NiCr as an etch mask.
8. Samples left in acetone at $50^\circ C$ for lift-off. Agitation with pipette after several hours to aid removal of remaining resist.
9. Sample submitted for silicon dry etching using the Marco 10 recipe (JWNC).

10. NiCr etch mask removed with 2-step wet etch in 60% nitric acid for 2 minutes and chromium etchant for 2 minutes, then rinsed in water.
11. Sample cleaned in plasma cleaner for 1 minute at 60 W before use in experiment.

2.3 Conclusions

The fabrication processes used to make the two sample types in this work have been discussed. Each stage of the fabrication protocol has been detailed, including the initial design software, the tools and methods used for pattern transfer, and the characterisation equipment available for validating the end products. The information in this chapter reveals some of the techniques available to nanofabrication engineers and gives an indication of how such a diverse range of metamaterial devices can be produced with current technologies.

The processes used for the different sample types are similar, with the silicon-based process being slightly longer. Both processes employ a PMMA resist bilayer and e-beam writing, resist development, metallisation and lift-off techniques. The gammadion samples are deposited directly onto the quartz glass substrate. In contrast, the s-structure samples require an initial deposition of silicon onto the quartz glass substrate. To form the structures, the silicon must also be etched and the etch mask removed in a final wet etch step.

2.4 References

1. Paras *et al.* A Review on Low-Dimensional Nanomaterials: Nanofabrication, Characterization and Applications. *Nanomaterials* vol. 13 (2023).
2. Franssila, S. Introduction to Microfabrication. *Introd. to Microfabr.* (2010) doi:10.1002/9781119990413.
3. Liddle, J. A. & Gallatin, G. M. Nanomanufacturing: A Perspective. *ACS Nano* 10, 2995-3014 (2016).
4. Liddle, J. A., Bowser, J., Ilic, B. R. & Luciani, V. So, You Want to Have a Nanofab? Shared-Use Nanofabrication and Characterization Facilities: Cost-of-Ownership, Toolset, Utilization, and Lessons Learned. *J. Res. Natl. Inst. Stand. Technol.* 125, 125009 (2020).
5. Candeloro, P., Panella, D., Pullano, S. A., Coluccio, M. L. & Perozziello, G. Chapter 6 - Fabrication technologies. in *Micro and Nano Technologies* (eds. Perozziello, G., Krühne, U. & Luciani, P. B. T.-M. for C. A.) 223-274 (Elsevier, 2023). doi:https://doi.org/10.1016/B978-0-12-822482-3.00006-3.
6. Sarangan, A. *Nanofabrication: Principles to Laboratory Practice*. (CRC Press., 2016).
7. Chen, Y. Nanofabrication by electron beam lithography and its applications: A review. *Microelectron. Eng.* 135, 57-72 (2015).
8. Prakash, S. & Yeom, J. Chapter 4 - Advanced Fabrication Methods and Techniques. in *Micro and Nano Technologies* (eds. Prakash, S. & Yeom, J. B. T.-N. and M.) 87-170 (William Andrew Publishing, 2014). doi:https://doi.org/10.1016/B978-1-4377-4469-9.00004-4.
9. AllResist. PMMA Datasheet. https://www.allresist.com/wp-content/uploads/sites/2/2015/12/allresist_produkinfos_ar-p630-670_englisch.pdf (2023).
10. Pala, N. & Karabiyik, M. Electron Beam Lithography (EBL) BT - Encyclopedia of Nanotechnology. in (ed. Bhushan, B.) 1033-1057 (Springer Netherlands, 2016). doi:10.1007/978-94-017-9780-1_344.
11. Bashir, A., Awan, T. I., Tehseen, A., Tahir, M. B. & Ijaz, M. Chapter 3 - Interfaces and surfaces. in (eds. Awan, T. I., Bashir, A. & Tehseen, A. B. T.-C. of N.) 51-87 (Elsevier, 2020). doi:https://doi.org/10.1016/B978-0-12-818908-5.00003-2.
12. Wang, F. & Wu, J. Chapter 10 - Plasma-enhanced chemical vapor deposition. in (eds. Wang, F. & Wu, J. B. T.-M. I. P. T.) 247-285 (Elsevier, 2023). doi:https://doi.org/10.1016/B978-0-323-90833-7.00010-3.
13. Kohler, M. Dry-Etching Methods. in *Etching in Microsystem Technology* 111-171 (1999). doi:https://doi.org/10.1002/9783527613786.ch4.
14. Kohler, M. Wet-Chemical Etching Methods. in *Etching in Microsystem Technology* 29-110 (1999). doi:https://doi.org/10.1002/9783527613786.ch3.
15. Mabilleanu, G. & Sabokbar, A. 7 - In vitro biological test methods to evaluate bioresorbability. in *Woodhead Publishing Series in Biomaterials* (ed. Buchanan, F. B. T.-D. R. of B. M.) 145-160 (Woodhead Publishing, 2008). doi:https://doi.org/10.1533/9781845695033.3.145.

Chapter 3: Methodology

Several spectroscopic techniques were performed alongside numerical simulations on the metamaterial types used in this work. Details of the sample preparation, optical setups and simulation procedures are described in this chapter.

3.1 Spectroscopic Measurements

3.1.1 Sample Preparation

Whilst different samples underwent measurements from various optical setups, the fundamental sample preparation was consistent between them. In each case, the samples were introduced to different solutions prior to being secured to sample stages. Given that both samples were based on a quartz substrate, custom 3D printed sample holders were used to hold and orient the samples, shown in **figure 3.1**. The samples were placed face-up in the bottom half of the plastic holder. Above the sample, a *Fastwell* silicone gasket is placed beneath a clear quartz slide, before the top half of the holder is tightened to secure the sample. The gasket provides a 1 mm tall cavity with a volume of ~0.2 ml, into which solutions can be injected by syringe. The silicone gasket ensures a needle can repeatedly penetrate the cavity whilst maintaining a leak free seal once removed.

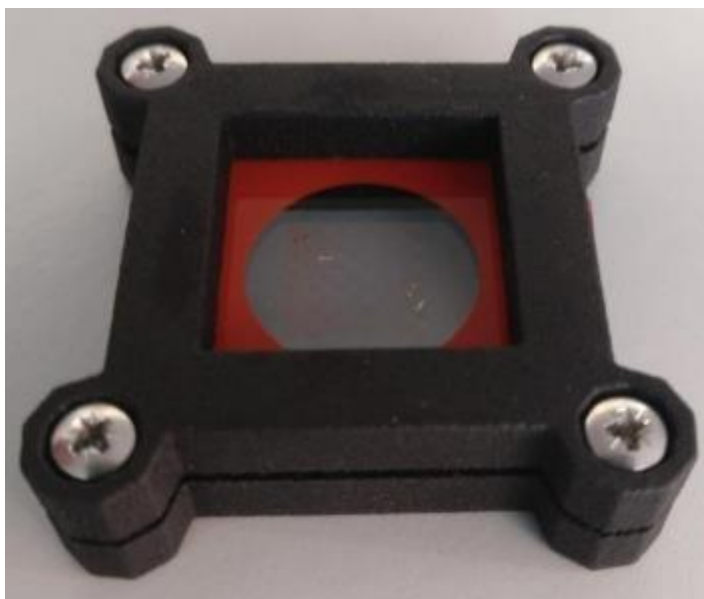


Figure 3.1: An example of a gammadion sample secured in the 3D printed sample holder. The silicone seal (orange) allows for the injection of solutions over the sample. The distance between the centres of adjacent screws is 30 mm.

3.1.2 Gammadion Sample Measurements

The gammadion sample CD measurements were performed in a *JASCO J-810* spectropolarimeter. The sample holder could be placed in the sample chamber after the desired solutions had been introduced, at which point RCP and LCP light was directed at the sample. The difference in absorption of the two forms of light are measured and the ellipticity, in degrees, of the output light is calculated by¹:

$$\theta = (A_{LCP} - A_{RCP}) \times 32.98. \quad [3.1]$$

Where $A_{LCP,RCP}$ are absorbance of LCP and RCP, respectively. Typical values of ellipticity for proteins are quoted in millidegrees (mdeg) and are of the order of 10 mdeg. Measurements were repeated twice in each instance and the average values calculated.

3.1.3 Silicon Sample Measurements

The silicon samples were subject to measurements from three different optical setups.

3.1.3.1 Stokes Polarimetry

Standard reflectance and ORD measurements were performed with a custom Stokes polarimeter, shown in figure 3.2.

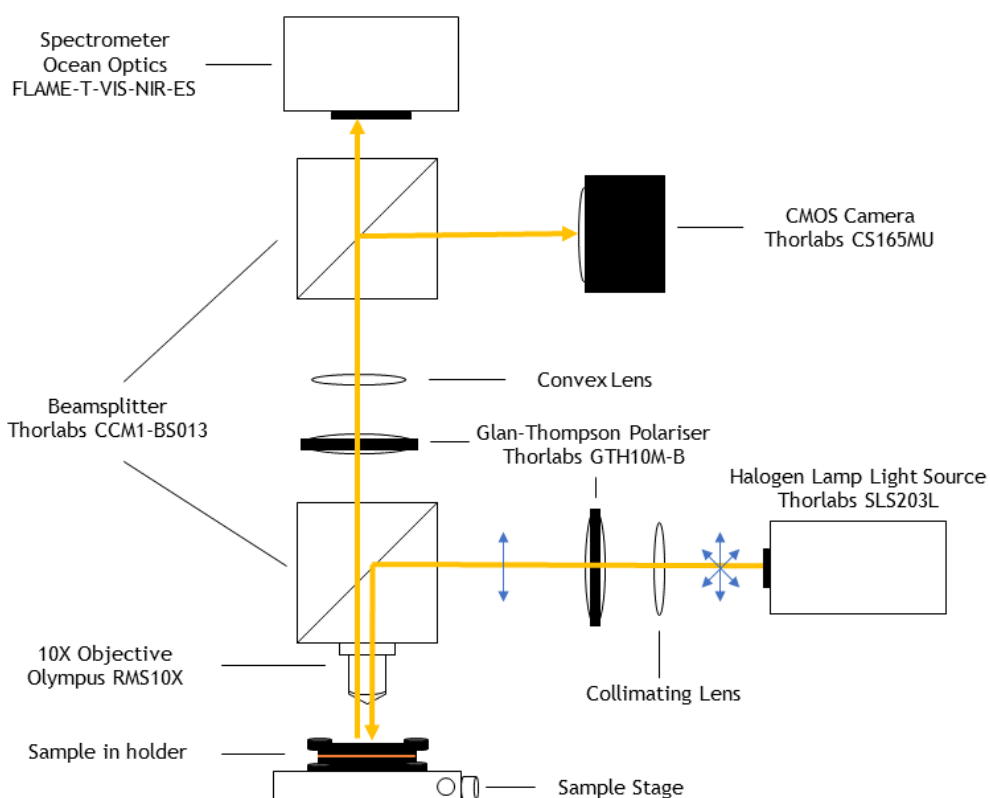


Figure 3.2: A schematic of the Stokes polarimeter used for reflectance and ORD measurements. The camera is used to align the sample and the analyser is rotated to obtain ORD data.

A 50 W halogen lamp produces unpolarised, broadband light that first passed through a Glan-Thompson polariser, making the light linearly polarised. A 50:50

beam splitter then directed light through a 10X objective and onto the sample stage. Reflected light was then returned through the beam splitter and through a second polariser (analyser) and beam splitter, the latter directing the light towards a CCD camera and spectrometer.

Intensity measurements were taken with the analyser at four angles: 0° , 45° , 90° and 135° . These intensities were then used to calculate the optical rotation of a sample across a wavelength range using the equation²:

$$\text{ORD} = \frac{1}{2} \tan^{-1} \frac{I_{45} - I_{135}}{I_0 - I_{90}} . \quad [3.2]$$

Relative reflectance (Rel. Ref.) measurements were also obtained by taking the ratio of the array reflectance intensity and the reflectance from the substrate where no nanostructures were present:

$$\text{Relative Reflectance} = \frac{\text{Nanostructure Reflectance}}{\text{Substrate Reflectance}} . \quad [3.3]$$

3.1.2.2 Photoluminescence Measurements

The silicon samples also underwent photoluminescence (PL) measurements when quantum dots were deposited on them. A schematic of this optical setup is shown in **figure 3.3**. Intensity measurements were taken with the analyser set to 0° , with a total of 1000 acquisitions and an acquisition time of 0.5 s.

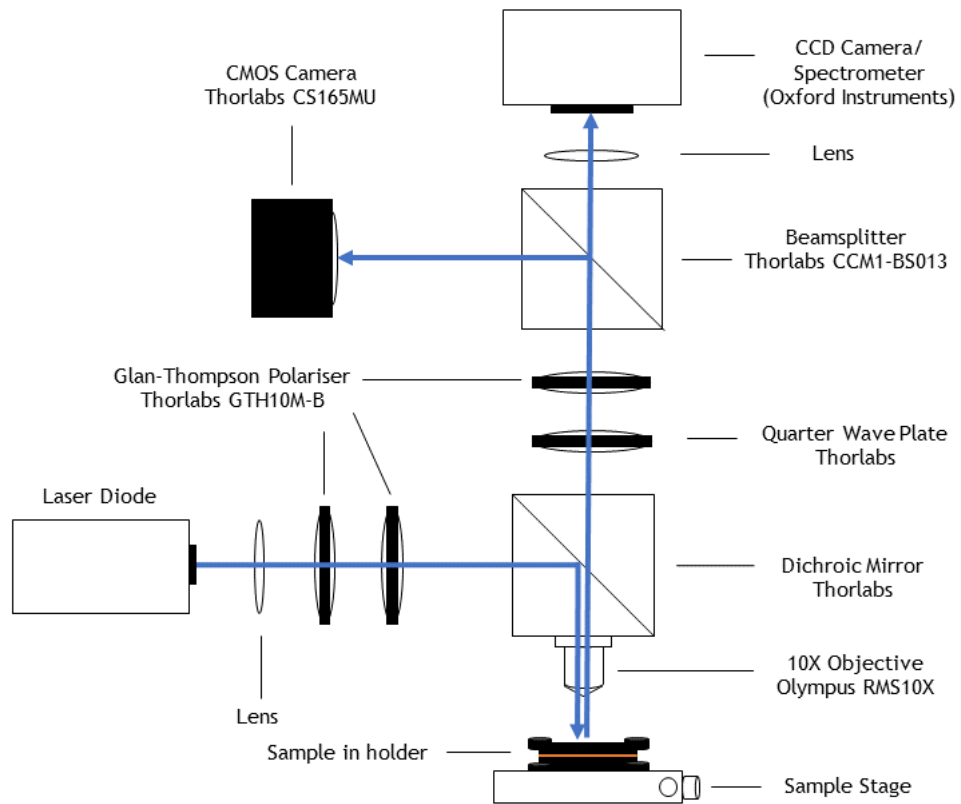


Figure 3.3: A schematic of the PL microscope used in experiment, operating with a 404 nm laser.

Mueller Matrix Polarimetry measurements were also taken for these samples, however, the optical setup for such instruments is more complex and require

further context.³ These measurements were performed externally at *Diamond Light Source Ltd.* and are discussed in greater detail in **Chapter 6**.

3.2 Numerical Simulations

In this work, the commercial finite element method (FEM) software *COMSOL Multiphysics Wave Optics Module* was used.⁴ This powerful software package allows for the solving of Maxwell's equations for customisable systems.⁵ This section will give a generalised description of the several components involved in creating a model in COMSOL, with more specific details relevant to each model type detailed in their respective chapters.

In FEM numerical simulations, approximate solutions to physical phenomena are calculated by the discretisation of the problem into solvable units.⁶ One method of discretisation is the meshing of the model into finite elements, typically taking the form of tetrahedra, cubes and triangles, which in general are suitable to contour most modelled geometries.⁷ Adjacent discretised elements meet at a points known as nodes, which act as a coordinate where the calculated solutions should converge. The solutions are calculated using numerical methods pertaining to partial differential equations and are solved within the regions of each meshing element.⁸

The user determines which variable they will alter and specifies the range and steps by which this is done, which in this case was the wavelength of incident light in steps of 1 nm. The polarisation state of the light can also be specified, as per equation [1.19]. For each wavelength, the expansive equation list is solved, including those detailed in **section 1.1**. Additional variables can be altered at each wavelength, such as polarisation state, however, the entire simulation will have to be rerun for each variable. Adding an extra variable will therefore double the original simulation time.

Meshing density can be varied, with smaller elements selected for regions that mesh smaller geometry features or that are expected to undergo large changes in field properties. Elsewhere, meshing can be reduced to lower computational demands. If more mesh elements are present, the simulation will require more computational resources and take more time to complete. It is therefore worthwhile to find the most efficient ranges of mesh sizes. This process is aided by the splitting of the model unit cell into several domains, shown in **figure 3.4a**. This refinement process typically involves running the simulation multiple times with different meshing values and identifying the fewest meshing elements above which the results do not vary by a significant amount, known as convergence.

Each of the models used in this work are based around a unit cell enclosed by periodic boundary conditions on the outer vertical faces and capped by perfectly matched layers (PMLs) on the top and bottom domain. The periodic boundary conditions require the solutions of opposite faces of surrounding boundaries to be equal, which models the fabricated sample arrays. PMLs are idealised domains that absorb all reflections from the remainder of the model.⁹ Input and output ports are assigned to the faces directly above/below the PMLs. The polarisation of incident light is described at the incident port. Reflectance and transmittance values are calculated at the ports and can be recalled with their respective variable names. The reflection is calculated from the ratio of light that leaves and returns to the input port, whilst transmission is obtained from the ratio of light that leaves the input port and that reaches the output port. As before, Rel. Ref. is calculated by performing a ratio between the reflectance intensities with and without a structure present.

Idealised geometries can be built in the COMSOL's own geometry builder or imported from external CAD sources. It is also possible to import geometries directly from AFM measurements, shown as part of **figure 3.4b**. It can be seen from the meshing of the two examples, that the AFM structure requires a denser meshing. Both were meshed using the same preset element size ranges, with the 'real' version resulting in the meshing requirements increasing by an order of magnitude. For this reason, the use of AFM based geometries in this work is limited due to the computational demands.

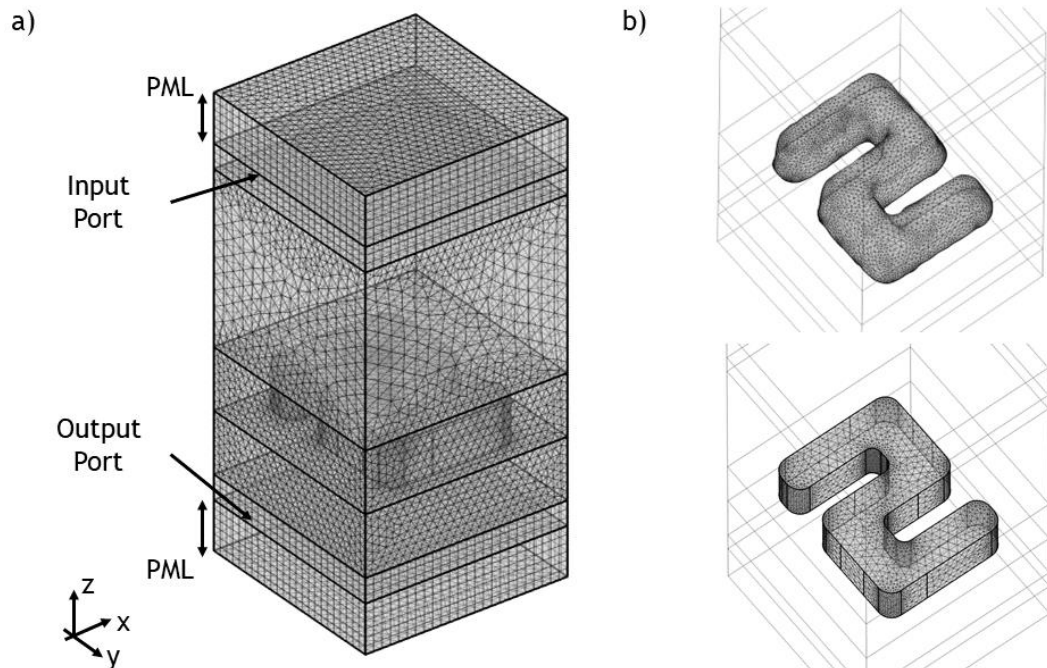


Figure 3.4: a) The meshed unit cell of the silicon model, with domain components labelled. b) The meshing of an AFM imported structure (top) and a COMSOL generated (idealised) structure (bottom) with the same preset element size.

Material parameters, such as permittivity and permeability functions, are assigned manually to their respective domains within the model, either by entering custom values or by using values from COMSOL's materials library. Once all materials are defined, the domains are meshed and the variables for the simulation are specified, the simulation is then ready to run. All simulations for this work were typically performed over 400 data points (wavelengths) per run, with the number of meshing elements at approximately 200,000. Under these conditions, the simulation could be expected to run between 8 - 24 hours, depending on the number of variables altered.

Upon completion of a simulation, COMSOL offers a wide range of postprocessing options, with the capability to analyse the distributions of most equation variables. The common examples used in this work relate to the electric and magnetic fields and the optical chirality density.

3.3 Conclusions

This chapter has discussed the sample preparation method prior to experiment. Descriptions of the optical setups were provided as well as the fundamental equations behind each measurement type, which includes CD, ORD and PL, although the theory of Mueller matrix polarimetry is reserved for a later chapter. Each sample used has nanopatterned arrays fabricated upon square quartz glass substrates. In each experiment, these samples are sealed within custom printed sample holders which allows for the addition of the chemical reagents necessary for each biomolecule deposition and measurement.

Throughout this work, experimental results are validated with numerical simulations. A general overview of the COMSOL FEM simulation strategy was provided, including details regarding the model setup that is consistent across both sample types, including meshing, variables and domain types.

3.4 References

1. Subadini, S., Hota, P. R., Behera, D. P. & Sahoo, H. Circular Dichroism Spectroscopy: Principle and Application. in (ed. Sahoo, H.) 19-33 (Springer Nature Singapore, 2022). doi:10.1007/978-981-16-4550-1_2.
2. Collett, E. *Field Guide to Polarization*. (SPIE Press, 2005).
3. Arteaga, O., Freudenthal, J., Wang, B. & Kahr, B. Mueller matrix polarimetry with four photoelastic modulators: theory and calibration. *Appl. Opt.* **51**, 6805-6817 (2012).
4. COMSOL. Wave Optics Module User's Guide. <https://doc.comsol.com/5.4/doc/com.comsol.help.woptics/WaveOpticsModuleUsersGuide.pdf> (2023).
5. Jackson, J. D. *Classical electrodynamics* . (1999).
6. Okamoto, K. Chapter 6 - Finite Element Method. in (ed. Okamoto, K. B. T. - F. of O. W. (Third E.) 271-338 (Academic Press, 2022). doi:<https://doi.org/10.1016/B978-0-12-815601-8.50006-9>.
7. Okereke, M. & Keates, S. *Finite Element Applications: A Practical Guide to the FEM Process* . (2018).
8. Jin, J.-M. *Theory and computation of electromagnetic fields* . (2015).
9. Pardo, D. *et al.* Chapter 7 - Absorbing boundary conditions. in (eds. Pardo, D. et al.) 219-246 (Elsevier, 2021). doi:<https://doi.org/10.1016/B978-0-12-821454-1.00015-7>.

Chapter 4: Chiral Plasmonic Detection of an Antibody-Antigen Complex

Plasmonic metamaterials are capable of producing strong, localised chiral near fields. They present a means to reduce the scale disparity between chiral molecules and the incident light, which as previously discussed, is a major contributor to the general weakness of traditional chiroptical detection methods. These fields, generated by optical excitation, can have greater chiral asymmetries than that of CPL. This can facilitate stronger interactions with chiral media (biomolecules), which is measurable in the far field through asymmetric responses of chiroptical measurements. This chapter seeks to explore how the chiral media interact with the fields produced by plasmonic gammadion structures, specifically, if the conformation of a deposited antibody-antigen complex has any influence.

The structural features of a gammadion allow them to generate unique spectra and support a variety of resonance modes with varying electromagnetic field distributions. Each of these resonances has different properties, particularly in the case of biomolecular interactions. A combination of experiment and numerical simulation reveals the source of each resonance, with two of the three examined having behaviour predominantly localised to the structures. The remaining resonance is found to be periodic, with strong fields linking adjacent structures within the arrays. All of these resonances exhibit chiral asymmetries, with LH and RH structures displaying equal and opposite behaviours, as would be expected of a chiral system. The presence of the antigen-antibody complex asymmetrically perturbs the field properties of the structures. The layer is deposited using both a disordered and ordered protocol. Both produce asymmetric changes in the optical responses of the gammadions, with the greatest changes occurring from the ordered deposition, which is attributed to the layer possessing birefringent character.

4.1 Introduction to Planar Chiral Metamaterials

Throughout the literature, chiral plasmonic nanostructures have been fabricated in a range of complexities; from intricate three-dimensional nano-helices¹ and nanostructure assemblies, to more fundamental objects such as discs and crosses.² They have drawn strong interest over recent years, particularly for nanochemistry³ and biosensing applications⁴, due to their ability to produce intense localised fields, the properties of which are highly controllable depending on the structures used and their environments.

4.1.1 Plasmonics

Metals are often described by the free electron gas model, in which an array of positive ions cores is surrounded by a sea of electrons moving between them. Upon exposure to an external electromagnetic field, the free electron gas can be displaced, and the electron plasma will oscillate about its equilibrium position, due to the restoring force from the positive nuclei. The oscillation occurs at what is known as the bulk plasma frequency, ω_p , given by⁵:

$$\omega_p = \sqrt{\frac{ne^2}{\epsilon_0 m}} . \quad [4.1]$$

Where n is the density of valence electrons, ϵ_0 the permittivity of free space, e the elementary charge and m the electron mass. Oscillations in the electrons occur in the presence of a time-varying field. When the frequency of the oscillating electrons matches the wavelength of the exciting light, coupling between the two generates surface plasmon polaritons (SPPs), which are quantised electromagnetic excitations that propagate along the interface between the metal and a dielectric. Plasmonic materials have historically been used decoratively due to their vibrant colours, famously in the Lycurgus cup.⁶ A more modern application relies on their sensing properties, in techniques such as surface plasmon resonance (SPR).⁷ Surface plasmonic modes are highly dependent on surface topology and can exist on a variety of complex surfaces.⁸ The SPP resonance frequency, ω_{SPP} , is given by⁹:

$$\omega_{SPP} = \frac{\omega_p}{\sqrt{1 + \epsilon_d}} . \quad [4.2]$$

Where ϵ_d is the relative permittivity of the dielectric. Whilst SPPs propagate along an interface such as a continuous film¹⁰, surface plasmon modes that do not propagate are known as localised surface plasmon resonances (LSPRs), which typically exist in isolated nanoparticles and nanostructure systems. Given that they are localised, they do not possess the phase matching requirements of their SPP counterparts, and as such can be excited from reflection alone¹¹. LSPRs provide intense regions of electric field at the surface of nanostructures, essentially confining the incident light. This offers a route to reduce the scale disparity that traditionally exists between light and analyte molecules, allowing them to interact more strongly.^{12,13} Due to the enhanced local fields, the dielectric environment surrounding the nanostructures can elicit significant changes to the resonance positions of the LSPRs. In the presence of an external dielectric layer such as a biomolecule, a response in the LSPR spectra will occur ($\Delta\lambda$), approximated by¹²:

$$\Delta\lambda = m\Delta n \left[1 - \exp\left(\frac{-2d}{l_d}\right) \right] . \quad [4.3]$$

Here, m is the bulk refractive index response, Δn is the change in effective refractive index caused by the dielectric layer, d is the layer thickness and l_d is the spatial evanescent decay of the local fields.¹⁴

4.1.2 Planar Chiral Metamaterial Sensing

The plasmonic nanostructures utilised in this chapter are known as gammadians. In free space, they belong to the C_{4h} point group, possessing four-fold rotational symmetry and a horizontal mirror plane. When placed on a substrate, their mirror symmetry is broken, making them chiral with a point group symmetry of C_4 .¹⁵ They have been used in previous investigations in periodic arrays and were found to display large levels of optical activity in the visible and near IR region of the spectrum¹³ and be capable of detecting chiral biomolecular materials¹².

The chiral sensitivity of the chiral metamaterials is characterised by their ability to produce asymmetric changes in the chiroptical properties of the enantiomorphous nanostructures. The CD is one such example in which these asymmetries, $\Delta\Delta\lambda$, have been seen to manifest. Changes in the spectral resonances have been parameterised previously as¹²:

$$\Delta\Delta\lambda = \Delta\lambda_{RH} - \Delta\lambda_{LH}. \quad [4.4]$$

In which $\Delta\lambda_{RH}$ and $\Delta\lambda_{LH}$ correspond to the change in resonance wavelength for the RH and LH structures, respectively.

The simplest model with which to explain how optical activity arises in metamaterials, is the Born-Kuhn coupled oscillator model.^{17,18} It provides an intuitive explanation of the optical activity that is exhibited by chiral systems and can be extended to more complicated designs. The model details the most fundamental system that can exhibit a chiroptical response, described by two vertically displaced coupled electrons of mass m , which undergo orthogonal harmonic oscillations under stimulation by an external light field, shown in **figure 4.1**. It builds from the Lorentz oscillator model, which describes an electron bound to the nucleus as a mass on a spring that oscillates in the presence of an applied electric field.¹⁹ A solitary electron is incapable of being chiral, however, the presence of an additional coupled electron introduces a handedness to the system, depending on whether the second electron is confined to move in the $+y$ or $-y$ direction. The upper and lower (displaced) electrons are confined to oscillate in orthogonal axes. When an incident LPL wave impinges on the upper electron, it causes it to oscillate in the y -axis. As the lower electron is coupled to it, it will itself oscillate in the x -axis. The centre of mass of the coupled system will thus vary from that of the y -direction, which amounts to a polarization rotation. The enantiomorphous nature of the system therefore results in differential responses to RCP and LCP light.²⁰

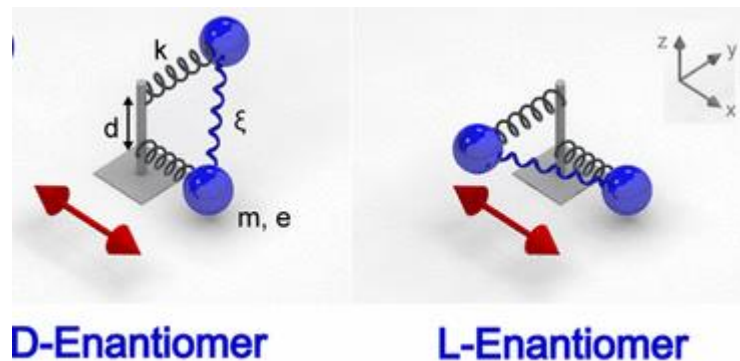


Figure 4.1: The coupled oscillator model of optical activity. This arrangement of coupled electrons (coupling constant ξ) of mass m , charge e and separation d , with confined oscillations (restoring constant k), creates two distinct enantiomeric states. Figure adapted from ²¹.

This model was extended to chiral plasmonic systems, which considers two identical 90° corner stacked nanorods, shown in **figure 4.2**.²¹ Incident light generates movement in the electron clouds of the rods, approximated by harmonic oscillation.²² A handedness is again intrinsic to the system depending on the direction the top rod is extended a quarter wavelength relative to the bottom rod, as is shown in **figure 4.2a**. Consequently, the state of the incident CPL will have a differential interaction with each of the rods. In each case, RCP or LCP light interacting with the D- or L-enantiomer will interact with the upper

rod in the same way. It is the interaction with the lower rod that will differ. For an RCP wave interacting with the D- enantiomer, **figure 4.2b**, the electric field vector will rotate and align with the lower nanorod. In this example, both nanorod's electron oscillations will be driven in phase. For an incident LCP wave the electric field vector anti-aligns with the lower rod as it counter-rotates with respect to the rod. The polarisation states of the rods can be visualised with a hybridisation diagram, **figure 4.2c**. The higher energy (antibonding) state will arise from the RCP case whilst the lower energy anti-aligned (bonding) state will result from the LCP wave, due to the dipoles induced in the rods. In the case of the L-enantiomer, the hybridized modes are reversed for incident RCP and LCP waves. The model assumes that the incident light has its polarization aligned with the upper rod and that the rods are displaced by a quarter wavelength.

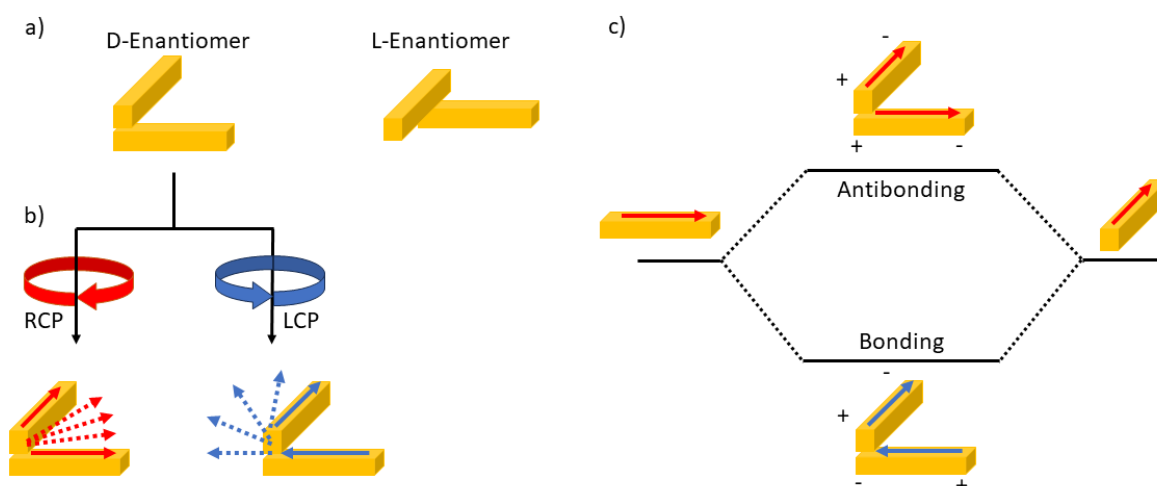


Figure 4.2: The plasmonic extension of the Born-Kuhn coupled oscillator model. a) The corner-stacked plasmonic nanorod arrangements produce distinct enantiomeric forms. b) Incident R-/L-CPL interacts differently between the enantiomers as the electric field vector rotates. c) The respective charge distributions in the stacked rods produces hybridized states. Figure adapted from reference ²¹.

Experimental and numerically simulated CD spectra were obtained by Yin *et al.* for the model, shown in **figure 4.3**, which confirms the existence of these hybridized modes. The transmission data for the D-enantiomer shows differences between the RCP and LCP waves. Similarly, the CD peaks were determined through the difference in transmitted RCP and LCP, $\Delta T = T_R - T_L$ and show equal and opposite behaviour. The D-enantiomer CD peak below 1300 nm (purple plot), takes a negative value due to the reduced transmittance of RCP compared to LCP. The lower resonance wavelength indicates a higher energy state, corresponding to the antibonding state of the hybridization model. This behaviour is then reversed for the post 1300 nm peak where the transmittance shows $T_{RCP} > T_{LCP}$, thus generating a positive CD value at a higher wavelength (lower energy), indicative of the lower energy bonding state. The plasmonic Born-Kuhn model helps provide an understanding as to how spectra obtained from different nanostructure geometries relate to their constituent parts for a range of material architectures, including nanoshells²³, dimers²⁴, metallic thin films and others²⁵.

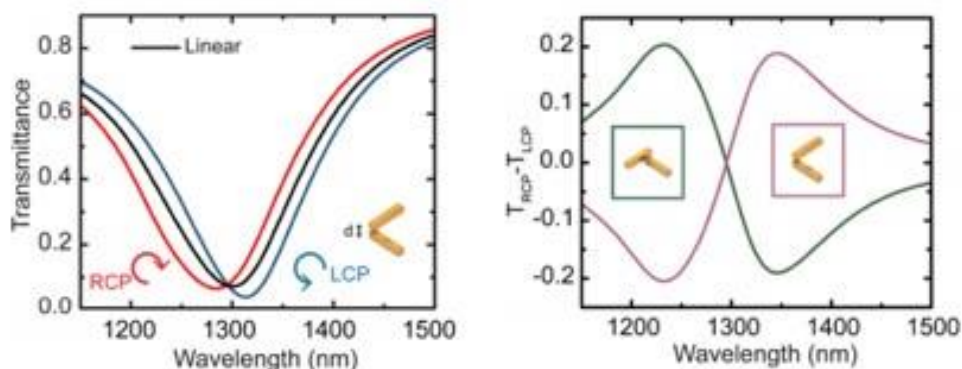


Figure 4.3: Transmittance (left) of a D-enantiomer when exposed to RCP, LCP and LPL. CD (right) spectra of the nanorods for the D- (purple) and L-enantiomer (green), forming mirror image bisignates. Figure adapted from reference ²¹.

There also exists the helical oscillator model for optical activity, which describes the preferential interaction of R- and LCPL with a chiral molecule based on the path the excited plasmons follow, depicted in **figure 4.4**. An achiral nanoparticle exposed to a LPL wave, **figure 4.4a**, will produce a localised surface plasmon, the electron cloud displacement for which is shown in blue. In the case of an incident CPL wave, the plasmons will follow a helical path, shown in **figure 4.4b**. If a chiral particle is present, the helical path of the plasmons will be better accommodated by one of the enantiomorphs, **figure 4.4c**, whose handedness coincides with the incident CPL, whilst the other presents a mismatch, **figure 4.4d**.^{13,26}

The two models can often be distinguished from their characteristic CD/ORD spectra. Coupled oscillator systems typically exhibit a bisignate CD spectrum, whilst helical oscillators display a bisignate ORD spectrum, which have been observed in shuriken nanostructures.²⁷ Bisignate line shapes appear as two adjacent, symmetric peaks of opposite sign. The helical oscillator model is more simplistic, taking into account only geometry. The couple oscillator offers a complex description that considers each transition (charge displacement) as a coupled oscillator which collectively represents the molecule, taking into account coupling between neighbouring oscillators.

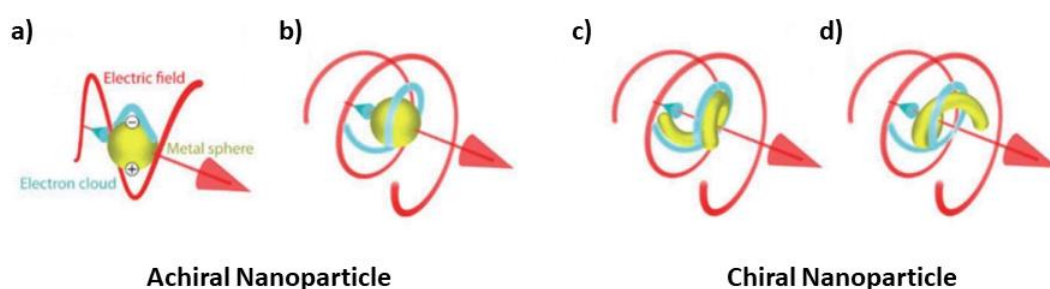


Figure 4.4: A visualisation of the helical oscillator model of optical activity. a) An achiral metal nanoparticle interacting with a LPL wave. b) An achiral particle interacting with CPL causes the plasmon to follow a helical path. c) A chiral nanoparticle interacting with CPL of the same handedness produces a strong chiroptical response as the particle can accommodate the helical plasmon. d) A chiral particle the opposite handedness interacting with the CPL wave produces a weaker response, due to a mismatch between the two. Figure adapted from ²⁶.

4.2 Methodology

4.2.1 Experimental Procedure

LH and RH gammadion arrays were fabricated as described in **section 2.2.1**. Streptavidin protein (*ThermoFisher*) was selected for experiments with these nanostructures as it could be used to form both structurally isotropic and anisotropic layers, referred to as non-specifically and specifically bound layers, respectively. Streptavidin protein was originally derived from the bacteria *Streptomyces avidinii* and has a tetrameric structure. It is widely used in biotechnology mainly due to its high affinity for biotin. For the non-specific case, the streptavidin was adsorbed directly onto the gold nanostructures which will occur in a range of orientations relative to the surface, characteristic of non-specific binding. The resultant biomolecular layer was therefore considered isotropic.

Specific binding was facilitated with biotin-PEG-thiol (*Polypure*) self-assembled monolayers (SAMs). The interaction between gold and the sulfhydryl/thiol group (SH) has been used extensively due to the strong interaction formed between them.²⁸⁻³¹ The thiol was dissolved in PBS 10X pH 7.4 buffer (*Gibco*) to a concentration of 60 μM . The SAM was left overnight to deposit on the gold nanostructures. Streptavidin diluted to a concentration of 2 μM was then deposited overnight. The interaction between biotin and streptavidin is well studied and known to form a strongly bound complex with a binding constant of (k_d) $\sim 10^{-14}\text{M}$.³² The four subunits of the streptavidin tetramer each possess a binding site for a biotin molecule. The interaction between the two chiral species allowed for the streptavidin to be bound to the nanostructures in a well-defined orientation³³ and was considered an anisotropic layer.

In addition to the deposition of streptavidin, the subsequent binding of an anti-streptavidin antibody (referred to as antistrep) was also investigated. The antibody is a polyclonal IgG antibody (*Sigma-Aldrich*) made to a concentration of 4 μM , which was deposited over a period of 2 hours. After the depositions of the streptavidin and antibody, the samples were rinsed in 0.1% NaOH/Tween and 0.05% NaOH/Tween respectively, to remove non-specifically bound species. Tween (*Sigma-Aldrich*) is a non-ionic detergent routinely used as a wash in biochemical processes.

Measurements were taken in a *JASCO J-810* spectropolarimeter, referred to in **section 3.1.2**. After the samples were left in protein solutions during the depositions, measurements were taken with the samples immersed in PBS replacement.

4.2.2 Simulation Procedure

Numerical simulations were used to investigate the effects of the isotropic and anisotropic depositions. The model used for the gammadion structure is shown in figure 4.5.

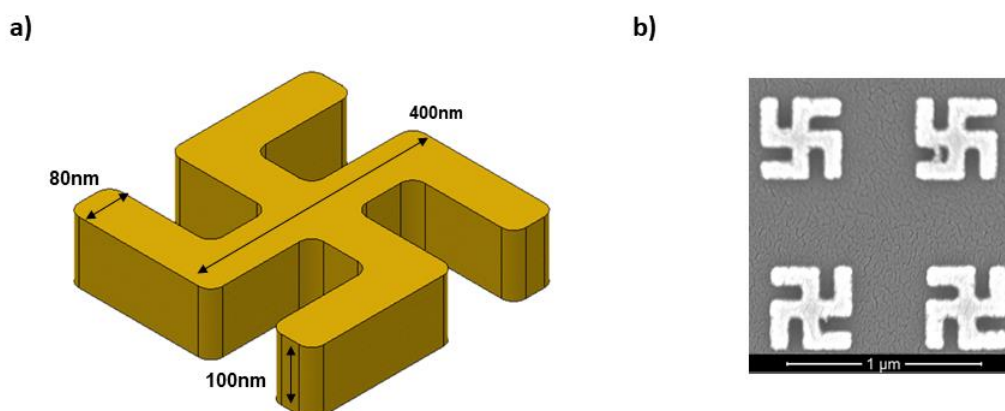


Figure 4.5: a) A visualisation of a RH gammadion, with the diameter 400nm, height 100nm and an arm width 80nm. b) SEM images of RH (top) and LH (bottom) nanostructures, upon which the model dimensions were based. Scale bar 1 μm.

The gammadion was placed in the middle of a block of height 1600 nm and width of 800 nm, as shown in figure 4.6.

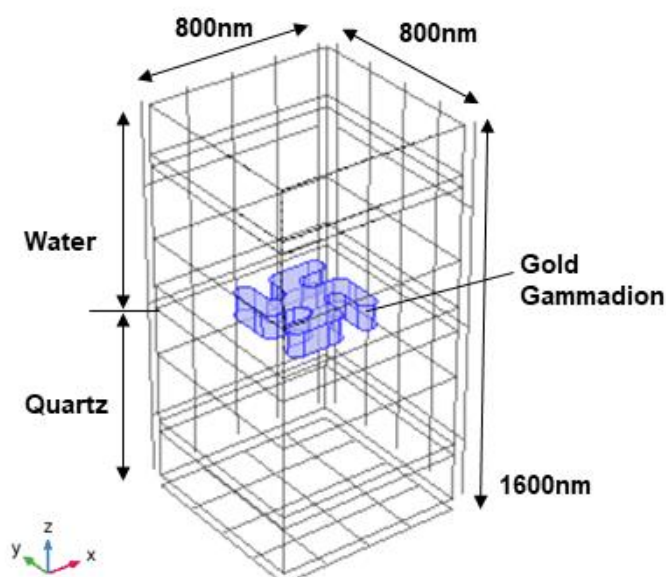


Figure 4.6: The periodic unit cell used in numerical simulation, with outer dimensions labelled. The gold gammadion (blue) is placed above quartz domains, with the remaining domains assigned as water.

To model the protein layers, a 20 nm external surface was generated on the outer faces of the gammadion, shown in figure 4.7a. The layer thickness was estimated from the approximate layer thicknesses of streptavidin and IgG antibody layers.^{34,35} This additional domain was split into discrete domains identified by the axis of their surface normal. The properties of these regions could be altered dependent on the type of deposition performed, visualised in figure 4.7b. In the case of modelling the isotropic (non-specific) deposition, the refractive index of the protein domains could be made uniform, with a refractive index value of

$n=1.4$. Diagonal elements of isotropic and anisotropic measurements are related by $n_{xx}^{iso} = \frac{1}{3} [n_{xx}^{ani} + n_{zz}^{ani}]$.¹⁰ Therefore, for the anisotropic (specific binding) model the discrete domains were assigned an anisotropic refractive index with a birefringence of 1.3/1.6 (equivalent to $n^{iso} = 1.4$), with the largest value corresponding to the axial component of the surface normal:

$$n_x^{aniso} = \begin{bmatrix} 1.6 & 0 & 0 \\ 0 & 1.3 & 0 \\ 0 & 0 & 1.3 \end{bmatrix}, n_y^{aniso} = \begin{bmatrix} 1.3 & 0 & 0 \\ 0 & 1.6 & 0 \\ 0 & 0 & 1.3 \end{bmatrix}, n_z^{aniso} = \begin{bmatrix} 1.3 & 0 & 0 \\ 0 & 1.3 & 0 \\ 0 & 0 & 1.6 \end{bmatrix}.$$

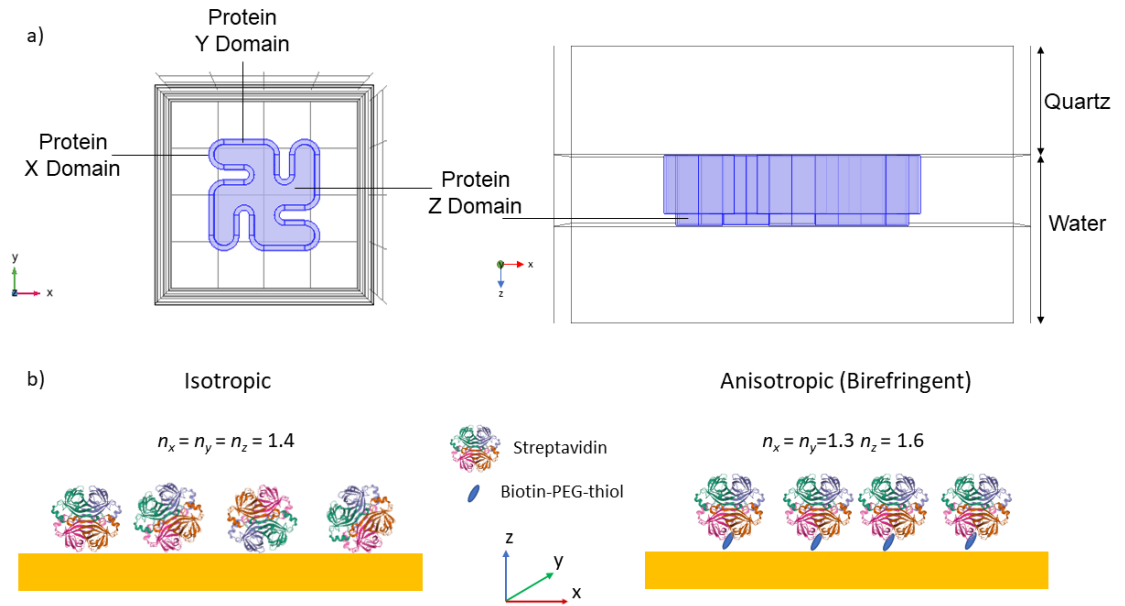


Figure 4.7: a) An idealised model of a LH gammadion with 20 nm external domains, which can be given a ξ value and an isotropic or anisotropic refractive index. b) A schematic (not to scale) illustrating the surface profile of streptavidin when non-specifically (isotropic) and specifically (anisotropic) bound to the gold structures.

In addition to modifying the refractive index values of the protein layers, they were made chiral. It was previously shown that Maxwell's equations must be modified to account for charges present in a system, giving rise to the displacement field, \mathbf{D} (equation 1.9) and magnetic field strength \mathbf{H} (equation 1.14). Similarly, chiral dielectric media can be modelled using the constitutive relations³⁶:

$$\mathbf{D} = \epsilon_0 \epsilon_r \mathbf{E} + i\xi \mathbf{B} \quad [4.5]$$

$$\mathbf{H} = \frac{\mathbf{B}}{\mu_0 \mu_r} + i\xi \mathbf{E}. \quad [4.6]$$

Where \mathbf{H} is the magnetic field, \mathbf{B} is the complex magnetic flux density and ξ is the chirality parameter. For this model, a ξ value of 5×10^{-4} was given to the external layer, based upon expected values for similar biomolecules.¹⁰

4.3 Results and Discussion – CD Spectra

4.3.1 Measured CD

To better understand the behaviour of the metamaterials and their interaction with the biomolecules being deposited, it is first important to determine the source of the spectral features produced by the gammadion samples. Previous studies with similar structures identified Bloch lattice modes in the spectra by varying the periodicity of the structures.³⁷ These mode assignments could be confirmed with the nanostructures fabricated in this work. To do this, the sample was given a gradual incline and tilted with respect to the incident light, the spectra for which are shown in **figure 4.8**.

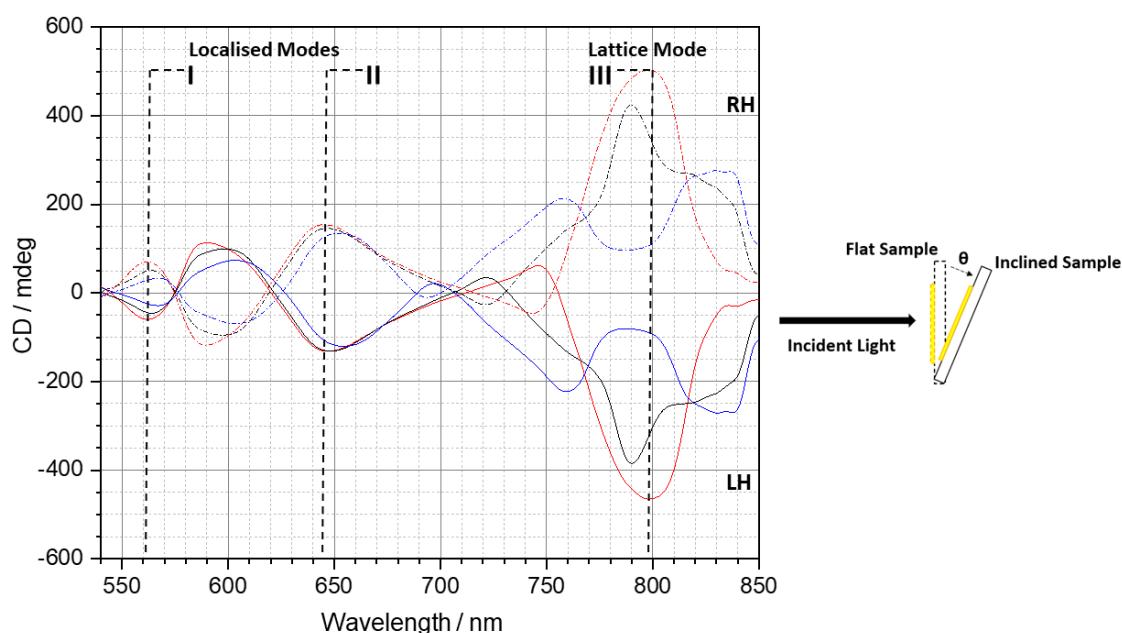


Figure 4.8: CD spectra for the LH (solid) and RH (dashed) samples in PBS, inclined at $\theta=0^\circ$ (red), 4° (black) and 10° (blue). Modes used for analysis are labelled as I, II and III.

Modes I, II and III were selected for examination based on previous work, as they displayed promising behaviour in terms of their ability for enhanced chiroptical detection.¹² As expected of enantiomorphic structures, the CD spectra are approximately equal and opposite. Resonance III occurs close to the 800nm periodicity of the structures and shows a strong dependence on the angle of incidence, indicating that it is a lattice (periodic) mode. The mode can be seen to gradually split as the incline is increased to 10° , due to the x- and y-axes (orthogonal to the propagation in the z-axis) no longer being equivalent relative to the incident light. Modes I and II are not significantly affected in comparison, indicating that these resonances are localised to the nanostructure. Numerical simulations were performed to further analyse the properties of the resonances through electric field analysis.

4.3.2 Simulated CD

The simulated CD spectra for enantiomeric nanostructures are shown in **figure 4.9**.

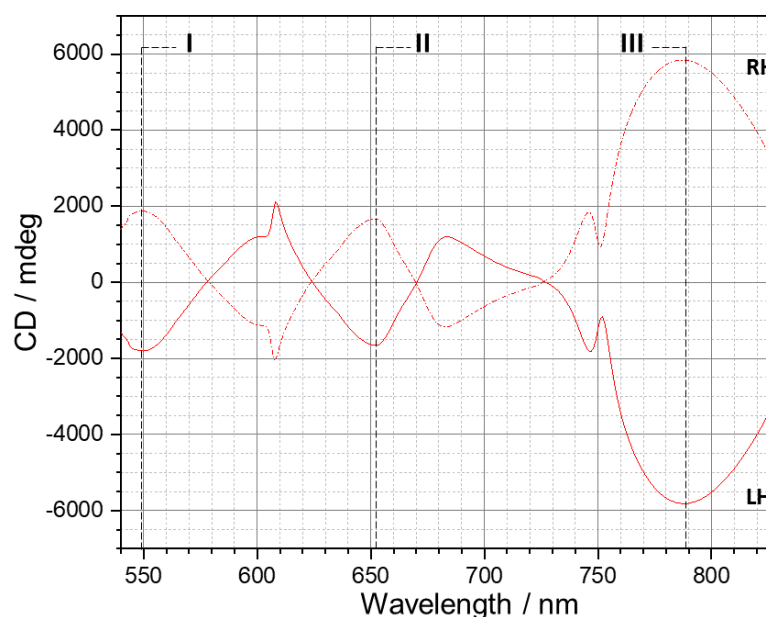


Figure 4.9: Simulated CD spectra for LH (solid) and RH (dashed) gammadion nanostructures in water, with no external layer present. Modes I, II and III are labelled.

The simulated spectra replicate the experimental data reasonably well, with the reproduction of the three labelled resonance modes. The magnitude of the simulated CD spectra are ≈ 1 order of magnitude greater than observed in experiment. This is attributed to the ‘perfect’ nature of the simulated models, in terms of structure quality and environment; in reality, experimental signals will suffer losses in signal quality due to fabrication and measurement limitations. This is also most likely the cause of the relatively sharp peak that occurs at ~ 610 nm which is not observed in experiment. It has previously been shown that spectra from large ensembles of nanostructures are essentially broadened due to averaging of the random defects that exist on each nanostructure, which can be mimicked with adjacent average smoothing of the spectra.³⁸

The field behaviour of the resonances provides a clearer indication as to their nature. As in previous studies^{12,39,40}, modes I, II and III have been selected for analysis. The electric field z-component (E_z) and optical chirality densities for LH and RH structures are shown in **figure 4.10**. With respect to the E_z plots, mode III shows strong field intensities occurring between adjacent structures, characteristic of a periodic resonance. The field intensities of modes I and II are more localised to the nanostructure. Mode I shows the most intense regions at the edges of arms, with less intense fields between the arms of the structures. Mode II shows similar behaviour, with even stronger field intensities at the ends of and between arms. As expected for enantiomeric structures with no external chiral influence, the field plots are mirror images of each other for RCP and LCP illumination. The optical chirality density plots also show behaviour characteristic of enantiomeric structures, in which their intensities are equal and opposite between opposing structures under different incident polarisations.

The origin of the localised modes can be understood from the Born-Kuhn (coupled oscillator) model for optical activity.^{17,21,41} Modes I and II arise from the out- and

in-phase combinations of the coupled oscillator system. The two orthogonal rods that together form an arm of the gammadion, can be approximated as two harmonic oscillators, capable of inductive and conductive coupling. Inductive coupling occurs between charge distributions (dipoles) between adjacent arm features, whilst conductive coupling refers to coupling of dipoles within the structures. The bisignate line shape of the CD spectra, of which there are two instances (below 625 nm and between 625 and 730 nm), are characteristic of a coupled oscillator.³⁹

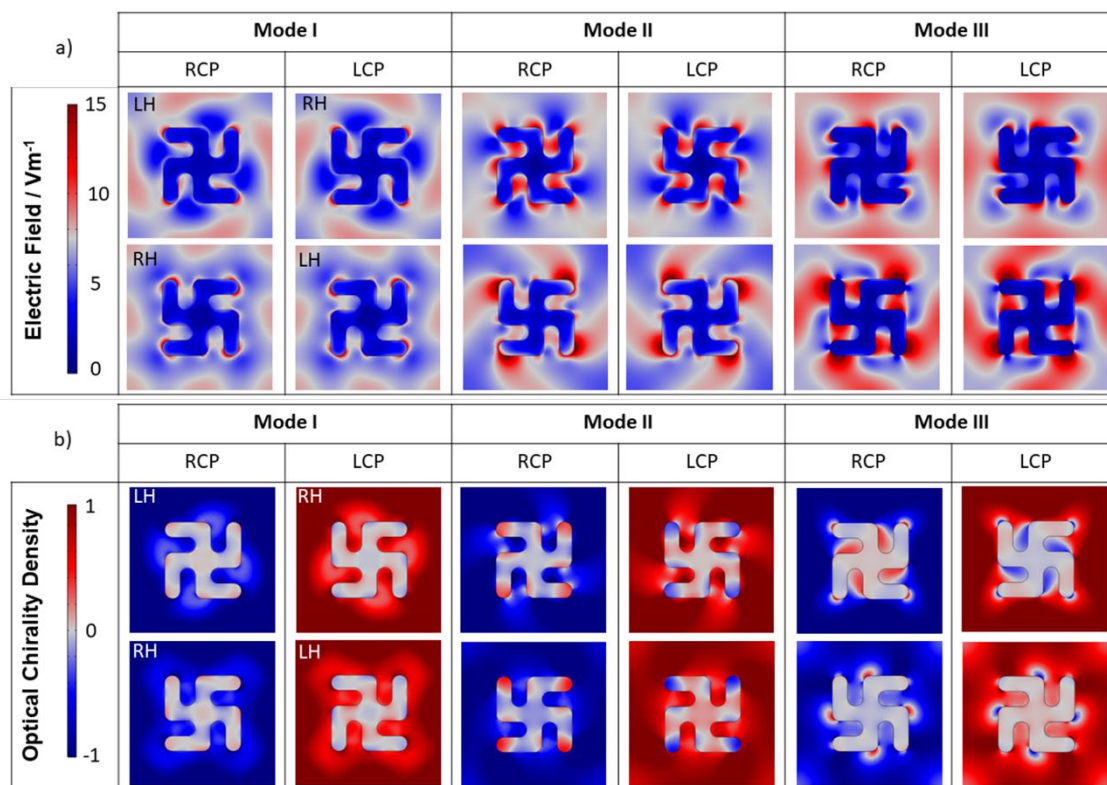


Figure 4.10: a) E_z plots for the 3 resonance modes of figure 4.8, for LH and RH structures, when exposed to RCP and LCP incident light. b) Optical chirality density plots for LH and RH structures for each mode. Each row includes symmetry equivalent pairs between the structure handedness and incident CPL. All field plots are taken from the midpoint of the structures. Optical chirality density plots are normalised to RCP.

4.4 Results and Discussion – Streptavidin Depositions

4.4.1 Isotropic Deposition

Experimental CD spectra were obtained for the sample with streptavidin non-specifically deposited on the sample, with no thiolated biotin present. **Figure 4.11** shows the spectral shifts relative to the PBS buffer post streptavidin and antistrep adsorption.

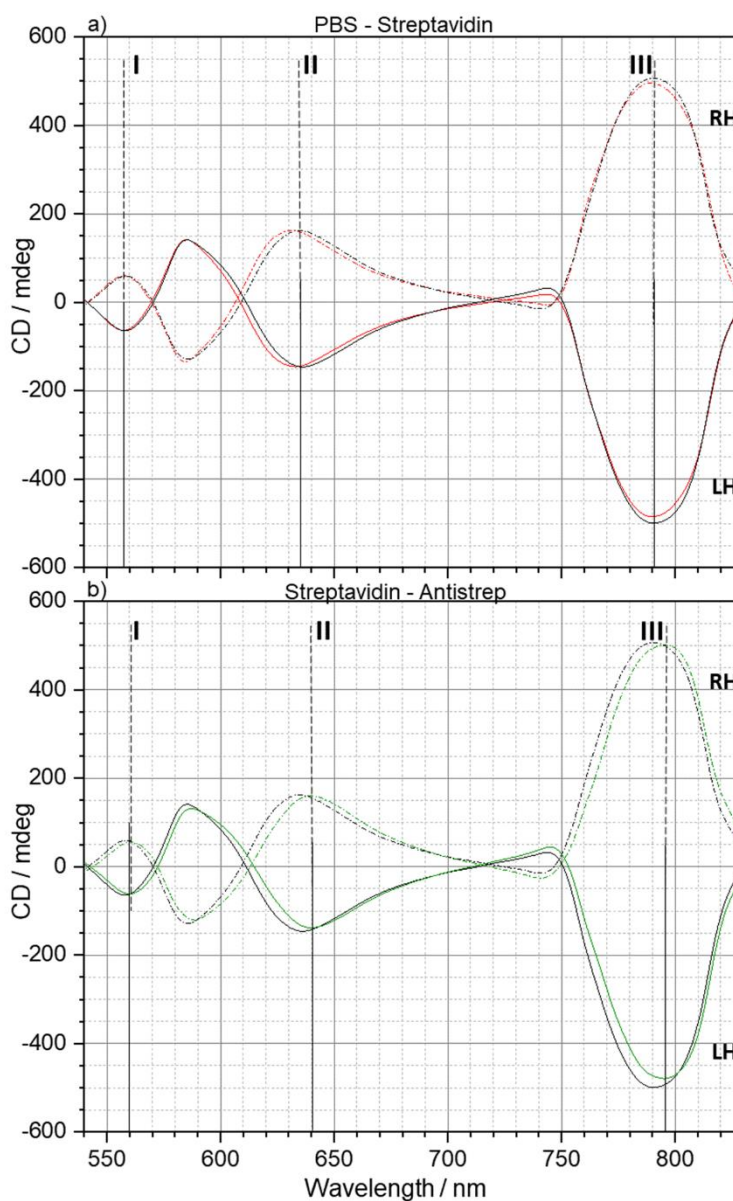


Figure 4.11: a) Experimental CD spectra collected in PBS buffer of LH (solid) and RH (dashed) samples (red), followed by the non-specific deposition of streptavidin (black). b) The subsequent deposition of antistrep (green) with respect to the streptavidin. The three modes used for measuring spectral shifts are highlighted with lines to aid the eye (LH solid and RH dashed).

As expected, the spectra show a redshift upon the addition of the streptavidin and antistrep, due to the increase in the local refractive index environment from the adsorption of the biomolecular species, as per **equation 4.3**. Analysis of the resonance shifts for the RH and LH spectra for both biomolecules reveal no measurable asymmetries, with $\Delta\Delta\lambda_{I,II,III} \approx 0$.

4.4.2 Anisotropic Deposition

Experimental CD spectra of the samples were obtained after functionalisation of the structures with the biotin SAMs and the subsequent depositions of the streptavidin and antistrep, shown in **figure 4.12**. The deposition of each species is again confirmed by the progressive redshifts in the spectra. Analysis of the shifts with respect to the resonances in PBS, reveal that there are $\Delta\Delta\lambda$ asymmetries in the resonance wavelength shifts. Biotin, itself a chiral molecule, produces a small, negative asymmetry in comparison to a larger and positive asymmetry for streptavidin. When streptavidin is added, the RH sample undergoes a greater wavelength shift than that of the LH, which is again seen with the binding of the antistrep, increasing the overall asymmetry observed from the spectra. In each case, it is resonant mode II that shows the largest asymmetries, followed by mode III and then mode I. The pattern and signs of the asymmetries agree with measurements adsorbed onto similar forms of gammadion nanostructures.¹² As in the study by Hendry *et al.*, asymmetries in the amplitudes of mode III are observed for the streptavidin and streptavidin-antistrep complex.

A further observation is the size of the average shifts of the samples being smaller when the biotin SAM is present. This can be rationalised by considering the greater distance the proteins are from the gold surface, and hence the local fields. It is also likely that there is a lower surface density of proteins, due to steric constraints, limiting the biotin-streptavidin interaction.

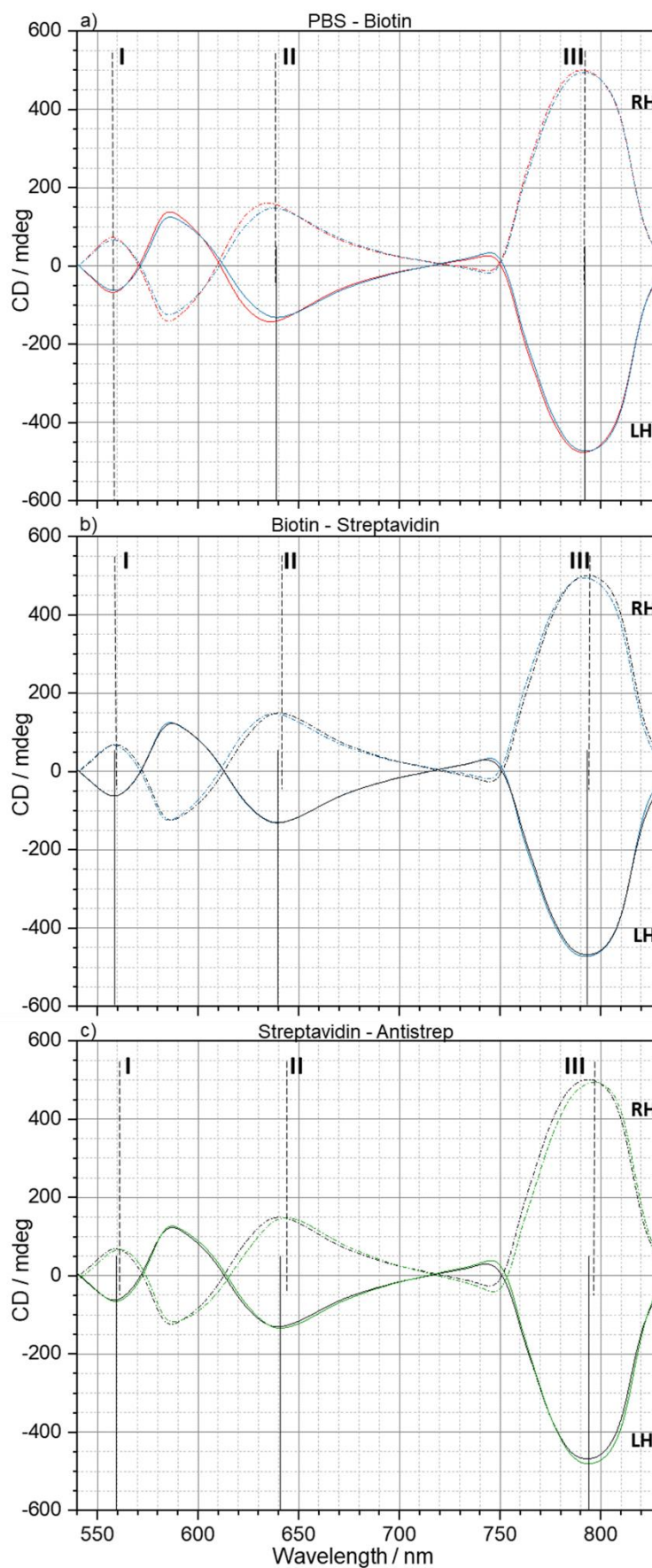


Figure 4.12: a) Experimental CD spectra collected in PBS buffer of LH (solid) and RH (dashed) samples (red), followed by the biotin SAM binding to the surface (blue). b) The subsequent deposition of streptavidin (black) and c) antistrep (green). The three modes used for measuring spectral shifts are highlighted with lines to aid the eye (LH solid and RH dashed).

4.4.3 Numerical Simulations

CD measurements were simulated with isotropic and anisotropic refractive index values assigned to 20 nm chiral layers that extended from the nanostructure's outer surface, shown in figures 4.13 and 4.14, respectively.

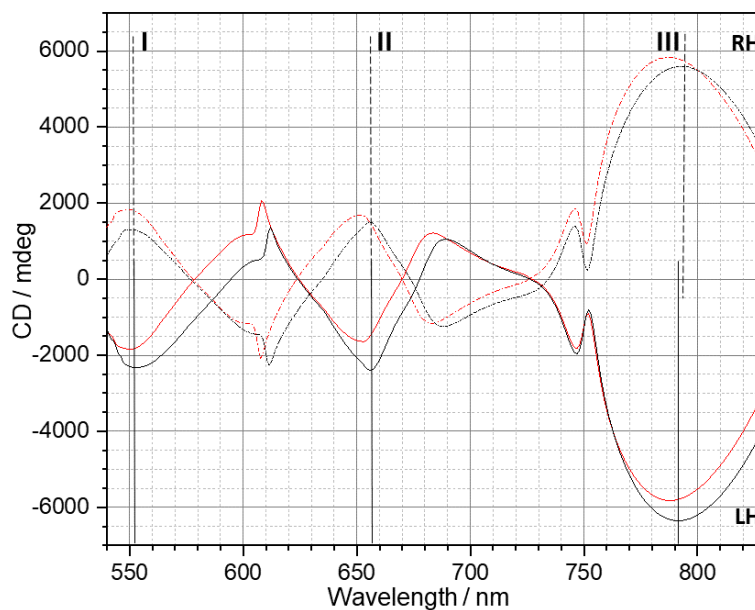


Figure 4.13: Simulated CD spectra in water of the gammadians (red) and with an isotropic external layer present (black) for LH (solid) and RH (dashed) structures.

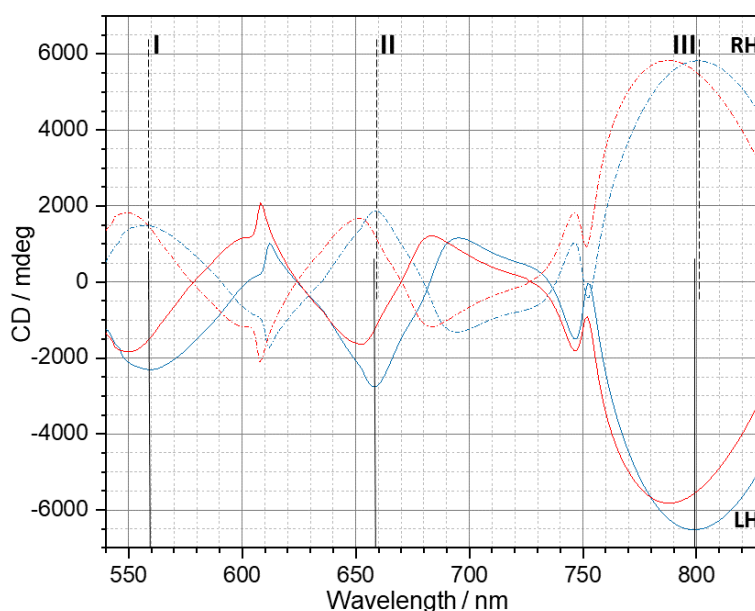


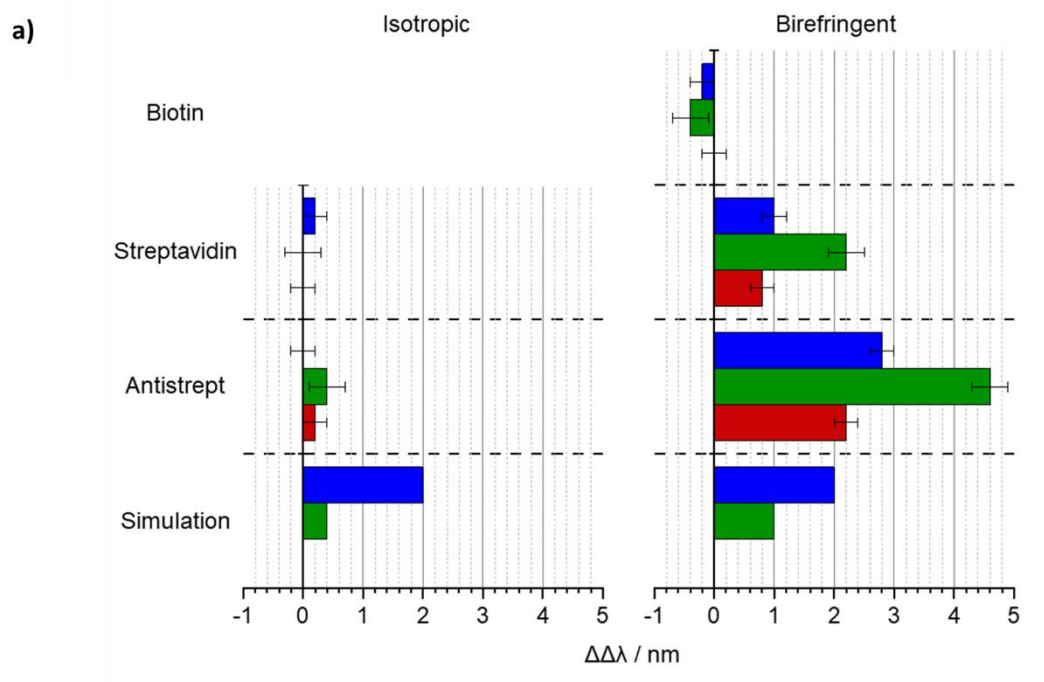
Figure 4.14: Simulated CD spectra in water of the gammadians (red) and with an anisotropic external layer present (blue) for LH (solid) and RH (dashed) structures.

A comparison of the $\Delta\lambda$ asymmetries produced from the two types of deposition performed experimentally and in numerical simulation are shown and tabulated in figure 4.15a,b. The isotropic layer simulation shows some disagreement with the experimental results, due to the asymmetry observed in mode III. In contrast, the anisotropic (birefringent) models provide better agreement with experiment,

with mode II showing a greater $\Delta\Delta\lambda$ asymmetry. There still remains some discrepancy in the birefringent simulation with respect to the experiment. Namely in the underestimation of the $\Delta\Delta\lambda$ values for modes I and II. This difference is attributed to the absence of surface roughness and structural defects in the models of the structures, compared to 'real' fabricated structures. It has been shown with similar gammadia, that the presence of structural irregularities generate near field hotspots on the structures, with the greatest effects occurring in the coupling between the arms, which are associated with the resonance of mode II.⁴² This suggests that the idealised structures used could underestimate the perturbations generated by an anisotropic chiral layer on mode II.

The results clearly indicate the dependence of the asymmetry on the level of anisotropy of the chiral layer. Chiral metamaterials have previously been shown to produce chiroptical responses due to differential coupling, brought about by the presence of a chiral media.^{10,22,39} It is therefore expected that the anisotropic arrangement of the chiral biomolecular layers alters the coupling between the arms of the nanostructures, which results in changes in the far field optical response. Therefore, it would be expected that the chiroptical response between the enantiomorphs corresponds to a significant differential in the near field properties of the structures between the arms.

Asymmetries obtained for control measurements for achiral solutions with respect to water, are shown in **figure 4.15c**. As expected of an achiral solution, there were no significant differences between the shifts of the LH and RH samples, with $\Delta\Delta\lambda \approx 0$ within experimental error. This indicates that the asymmetries are not inherent to the structures themselves.



b)

	$\Delta\Delta\lambda / \text{nm}$					
	Isotropic			Birefringent		
	Mode I	Mode II	Mode III	Mode I	Mode II	Mode III
Biotin	-	-	-	0	-0.4	-0.2
Streptavidin	0	0	0.2	0.8	2.2	1
Antistrep	0.2	0.4	0	2.2	4.6	2.8
Simulation	0	0.4	2	0	1	2

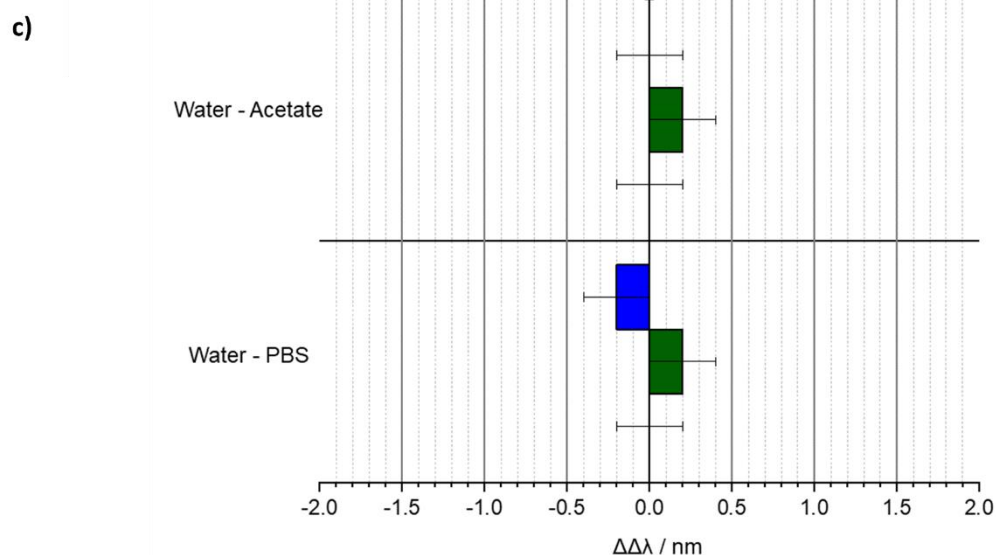


Figure 4.15: a) A comparison of the $\Delta\Delta\lambda$ asymmetry values for modes I (red), II (green), and III (blue) obtained from both experiment and simulation, for the isotropic and birefringent (anisotropic) layers. b) Tabulated $\Delta\Delta\lambda$ asymmetries. c) Asymmetries obtained for achiral reference solutions.

To validate the hypothesis that the anisotropic chiral layers cause differential changes in the near field properties of the LH and RH structures, the EM fields generated by the structures were analysed. **Figures 4.16** and **4.17** show the spatial distributions of E_z and optical chirality densities generated by incident RCP and LCP light, for mode II, respectively. **Figure 4.18** displays the averaged field intensities and optical chirality density values taken from regions between the arms of the gammadions, which appear as white blocks in the upper left plots of **figures 4.16** and **4.17**.

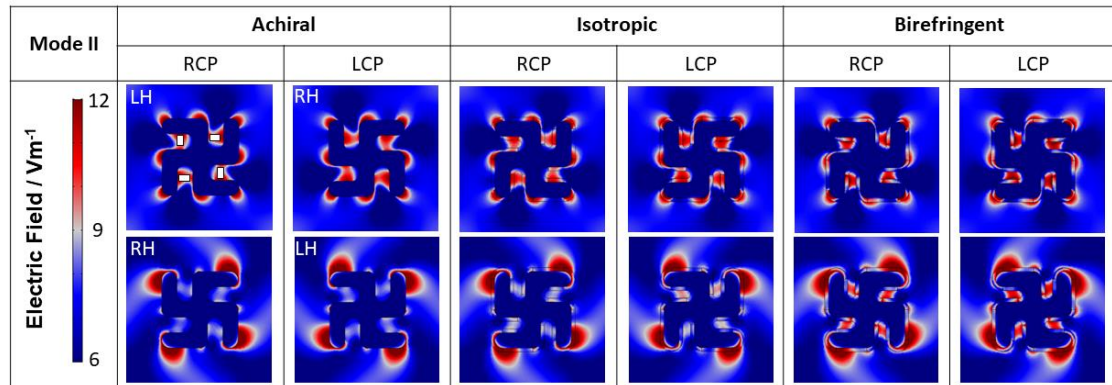


Figure 4.16: E_z plots for the achiral, isotropic and birefringent simulations at mode II. The white regions highlighted in achiral RCP / LH are used to calculate the average field intensities which are displayed in figure 4.17. Electric field values for the plots are between $6\text{-}12 \text{ Vm}^{-1}$ to improve image contrast between the arms. Each row includes symmetry equivalent pairs between the structure handedness and incident CPL. All field plots are taken from the midpoint of the structures.

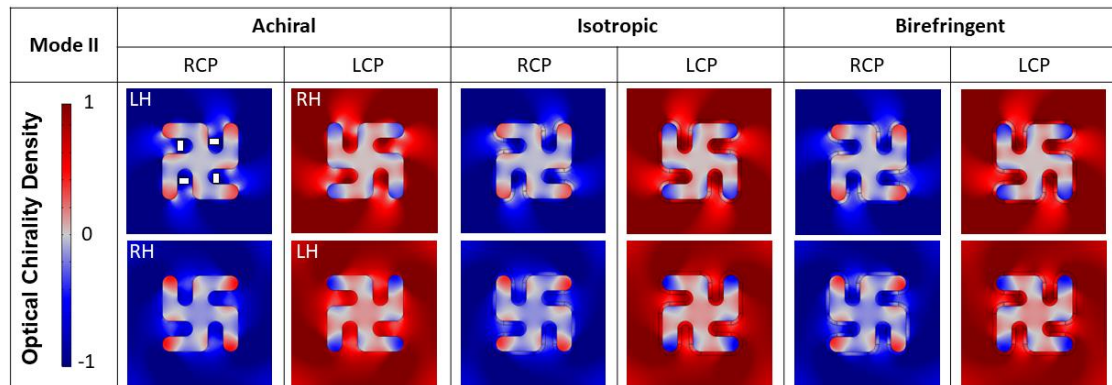


Figure 4.17: Optical chirality density plots for achiral, isotropic and birefringent simulations at mode II. As before, white regions highlighted in achiral RCP / LH were used for the intensity values in figure 4.17. Each row includes symmetry equivalent pairs between the structure handedness and incident CPL. All field plots are taken from the midpoint of the structures and are normalised against RCP.

In the presence of the achiral medium, the symmetry related combinations ($\text{RH/LCP} = \text{LH/RCP}$, $\text{RH/RCP} = \text{LH/LCP}$) are as expected, giving the same field intensities and equal but opposite optical chirality density maps. When the chiral dielectric layer is introduced, the symmetry relations are broken in both the electric field and chirality maps, such that $\text{RH/LCP} \neq \text{LH/RCP}$, $\text{RH/RCP} \neq \text{LH/LCP}$. Whilst this occurs for both the isotropic and birefringent chiral layers, it is found that the level of symmetry breaking with respect to the achiral case, is significantly greater for the birefringent example. The greater influence of the birefringent layers on the near fields of the structures suggest that they have the ability to act as an additional source/sink of optical chirality. Again, the idealised version of the structures underestimates the level of $\Delta\Delta\lambda$ asymmetry for resonances I and II. The presence of surface irregularities could potentially

produce stronger perturbations in the near field coupling between the arms of the structures.

Gammadion Handedness	Light Polarisation	Achiral		Isotropic		Birefringent	
		Electric Field / Vm^{-1}	Optical Chirality Density	Electric Field / Vm^{-1}	Optical Chirality Density	Electric Field / Vm^{-1}	Optical Chirality Density
LH	RCP	10.1	-0.7	10.1	-0.6	11.1	-0.7
RH	LCP	10.1	0.7	10.8	0.9	11.7	1.0
LH	LCP	8.3	0.5	9.2	0.7	10.8	0.8
RH	RCP	8.3	-0.5	8.7	-0.5	10.2	-0.7

Figure 4.18: Electric field and optical chirality density values compared for the three simulation types, each averaged from four equivalent areas (highlighted in figures 4.16 and 4.17 between the arms of the structures). The shaded rows denote one set of symmetry related pairs.

4.5 Conclusions

The source of optical resonances for enantiomeric plasmonic gammadions were identified through a combination of experiment and numerical simulations. The existence of a periodic lattice mode was confirmed by the splitting of the resonance upon inclination of the sample, with the increasing angle of incidence causing greater inequivalence in the x- and y-axes of the arrays. Given that no such effect was observed for the shorter wavelength resonances, they were predicted to be localised resonances which was confirmed through field plot analysis from the numerical simulations. The field intensities for these modes were seen to be highly localised around and between the arms of the nanostructures, in contrast to the periodic modes, where field intensities showed the strongest connections to adjacent structures.

Anisotropic and isotropic depositions of streptavidin and anti-streptavidin antibody were performed with and without the presence of a thiolated biotin SAM, respectively. Significant asymmetries were observed only when the gold nanostructures were functionalised with the biotin. Numerical simulations were performed utilising a 20 nm external layer on the outer faces of the structure, which were assigned an isotropic and anisotropic (birefringent) refractive index, to model the two types of deposition. There was reasonable agreement in the $\Delta\Delta\lambda$ asymmetries between experiment and simulation, however there was an underestimation in the simulated mode I and II values. With these resonances being attributed to coupling between gammadion arms, the underestimation was attributed to the idealised nature of the structures, as the structural imperfections not included in the model are understood to produce field hotspots.

Based on analysis of the local electric field and optical chirality density maps of the resonance with the greatest experimental asymmetry (mode II), it was shown that the presence of chiral layers produced asymmetric changes to the near field properties between LH and RH structures, with the greatest differences occurring for the chiral birefringent layers. The asymmetric behaviour exhibited by the CD spectra of the samples for anisotropic (birefringent) biomolecule deposition was therefore attributed to the birefringent layers acting as a further source/sink of optical chirality.

If the development of enhanced sensing devices based on chiral plasmonic nanostructures is to be realised, it is important that the mechanisms behind their operation are fully understood. There still remains a great deal to be discovered regarding these forms of materials, particularly as to how their local fields can be optimised for greater chiral asymmetries that will translate to the far field. However, this applies not only to their fabrication designs, but also to the techniques in which they are used. This chapter has shown that the conformation of analytes they are detecting, can have a significant influence on the sensing capabilities of the metamaterial platforms.

Whilst work will undoubtedly continue in the field of plasmonic sensing, other routes for novel devices are being explored to address limitations with plasmonic devices. One such platform is that of dielectrics, which will constitute the remainder of this thesis.

4.6 References

1. Kusters, D. *et al.* Core-Shell Plasmonic Nanohelices. *ACS Photonics* **4**, 1858-1863 (2017).
2. Collins, J. T. *et al.* Chirality and Chiroptical Effects in Metal Nanostructures: Fundamentals and Current Trends. *Adv. Opt. Mater.* **5**, (2017).
3. Wang, P. *et al.* Plasmonic Metamaterials for Nanochemistry and Sensing. *Acc. Chem. Res.* **52**, 3018-3028 (2019).
4. Lee, Y. Y., Kim, R. M., Im, S. W., Balamurugan, M. & Nam, K. T. Plasmonic metamaterials for chiral sensing applications. *Nanoscale* **12**, 58-66 (2020).
5. Kittel, C. *Introduction to solid state physics.* (John Wiley & Sons, 1996).
6. Freestone, I., Meeks, N., Sax, M. & Higgitt, C. *The Lycurgus Cup-A Roman Nanotechnology.* vol. 40 (2007).
7. Tang, Y., Zeng, X. & Liang, J. Surface Plasmon Resonance: An Introduction to a Surface Spectroscopy Technique. *J. Chem. Educ.* **87**, 742-746 (2010).
8. Maradudin, A. A., Sambles, R. & Barnes, W. L. *Modern plasmonics.* vol. 4;4.; (Elsevier, 2014).
9. Zhang, J., Zhang, L. & Xu, W. Surface plasmon polaritons: physics and applications. *J. Phys. D. Appl. Phys.* **45**, 113001 (2012).
10. Kelly, C. *et al.* Chiral Plasmonic Fields Probe Structural Order of Biointerfaces. *J. Am. Chem. Soc.* **140**, 8509-8517 (2018).
11. Maier, S. A. & SpringerLink (Online service). *Plasmonics: fundamentals and applications.* (Springer, 2007).
12. Hendry, E. *et al.* Ultrasensitive detection and characterization of biomolecules using superchiral fields. *Nat. Nanotechnol.* **5**, 783 (2010).
13. Valev, V. K., Baumberg, J. J., Sibilia, C. & Verbiest, T. Chirality and Chiroptical Effects in Plasmonic Nanostructures: Fundamentals, Recent Progress, and Outlook. *Adv. Mater.* **25**, 2517-2534 (2013).
14. Jung, L. S., Campbell, C. T., Chinowsky, T. M., Mar, M. N. & Yee, S. S. Quantitative Interpretation of the Response of Surface Plasmon Resonance Sensors to Adsorbed Films. *Langmuir* **14**, 5636-5648 (1998).
15. Arteaga, O. *et al.* Relation between 2D/3D chirality and the appearance of chiroptical effects in real nanostructures. *Opt. Express* **24**, 2242-2252 (2016).
16. Kuwata-Gonokami, M. *et al.* Giant Optical Activity in Quasi-Two-Dimensional Planar Nanostructures. *Phys. Rev. Lett.* **95**, 227401 (2005).
17. Born, M. Über die natürliche optische Aktivität von Flüssigkeiten und Gasen. *Phys. Z* **16**, 251-258 (1915).
18. Kuhn, W. Z. Quantitative Verhältnisse und Beziehungen bei der natürlichen optischen Aktivität. *Phys. Chem. B* **4**, 14-36 (1929).
19. Lorentz, H. A. The theory of electrons and its applications to the phenomena of light and radiant heat . (1952).
20. Barron, L. D. *Molecular Light Scattering and Optical Activity.* (Cambridge University Press, 2004). doi:10.1017/CBO9780511535468.
21. Yin, X., Schäferling, M., Metzger, B. & Giessen, H. Interpreting Chiral Nanophotonic Spectra: The Plasmonic Born-Kuhn Model. *Nano Lett.* **13**, 6238-6243 (2013).
22. Liu, N. & Giessen, H. Coupling Effects in Optical Metamaterials. *Angew. Chemie Int. Ed.* **49**, 9838-9852 (2010).
23. Prodan, E., Radloff, C., Halas, N. J. & Nordlander, P. A hybridization model for the plasmon response of complex nanostructures. *Science* **302**, 419-422 (2003).
24. Nordlander, P., Oubre, C., Prodan, E., Li, K. & Stockman, M. I. Plasmon Hybridization in Nanoparticle Dimers. *Nano Lett.* **4**, 899-903 (2004).
25. Halas, N. J., Lal, S., Chang, W.-S., Link, S. & Nordlander, P. Plasmons in strongly coupled

- metallic nanostructures. *Chem. Rev.* **111**, 3913-3961 (2011).
26. Valev, V. K. Chiral Nanomaterials and Chiral Light. *Opt. Photonics News* **27**, 34-41 (2016).
 27. Karimullah, A. S. *et al.* Disposable Plasmonics: Plastic Templated Plasmonic Metamaterials with Tunable Chirality. *Adv. Mater.* **27**, 5610-5616 (2015).
 28. Liu, Y. & Ozolins, V. Self-Assembled Monolayers on Au(111): Structure, Energetics, and Mechanism of Reconstruction Lifting. *J. Phys. Chem. C* **116**, 4738-4747 (2012).
 29. Love, J. C., Estroff, L. A., Kriebel, J. K., Nuzzo, R. G. & Whitesides, G. M. Self-Assembled Monolayers of Thiolates on Metals as a Form of Nanotechnology. *Chem. Rev.* **105**, 1103-1170 (2005).
 30. Häkkinen, H. The gold-sulfur interface at the nanoscale. *Nat. Chem.* **4**, 443 (2012).
 31. Vericat, C., Vela, M. E., Benitez, G., Carro, P. & Salvarezza, R. C. Self-assembled monolayers of thiols and dithiols on gold: new challenges for a well-known system. *Chem. Soc. Rev.* **39**, 1805-1834 (2010).
 32. CHAIET, L. & WOLF, F. J. THE PROPERTIES OF STREPTAVIDIN, A BIOTIN-BINDING PROTEIN PRODUCED BY STREPTOMYCETES. *Arch. Biochem. Biophys.* **106**, 1-5 (1964).
 33. Sheng, J. C.-C., De La Franier, B. & Thompson, M. Assembling Surface Linker Chemistry with Minimization of Non-Specific Adsorption on Biosensor Materials. *Mater. (Basel, Switzerland)* **14**, (2021).
 34. Hamming, P. H. E. & Huskens, J. Streptavidin Coverage on Biotinylated Surfaces. *ACS Appl. Mater. Interfaces* **13**, 58114-58123 (2021).
 35. Tan, Y. H. *et al.* A nanoengineering approach for investigation and regulation of protein immobilization. *ACS Nano* **2**, 2374-2384 (2008).
 36. Govorov, A. O. & Fan, Z. Theory of Chiral Plasmonic Nanostructures Comprising Metal Nanocrystals and Chiral Molecular Media. *ChemPhysChem* **13**, 2551-2560 (2012).
 37. Kravets, V. G., Kabashin, A. V, Barnes, W. L. & Grigorenko, A. N. Plasmonic Surface Lattice Resonances: A Review of Properties and Applications. *Chem. Rev.* **118**, 5912-5951 (2018).
 38. Ciraci, C. *et al.* Impact of Surface Roughness in Nanogap Plasmonic Systems. *ACS Photonics* **7**, 908-913 (2020).
 39. Phua, W. K., Hor, Y. L., Leong, E. S. P., Liu, Y. J. & Khoo, E. H. Study of Circular Dichroism Modes Through Decomposition of Planar Nanostructures. *Plasmonics* **11**, 449-457 (2016).
 40. Davis, M. S., Zhu, W., Lee, J. K., Lezec, H. J. & Agrawal, A. Microscopic origin of the chiroptical response of optical media. *Sci. Adv.* **5**, eaav8262 (2019).
 41. Hentschel, M., Schäferling, M., Duan, X., Giessen, H. & Liu, N. Chiral plasmonics. *Sci. Adv.* **3**, e1602735 (2017).
 42. Gilroy, C., Koyroysaltis-McQuire, D. J. P., Gadegaard, N., Karimullah, A. S. & Kadodwala, M. Superchiral hot-spots in "real" chiral plasmonic structures. *Mater. Adv.* **3**, 346-354 (2022).

Chapter 5: Stokes Polarimetry of S-shaped Silicon Nanostructures

In this chapter, the reflectance and ORD properties of four types of silicon nanoarray are investigated for samples of varying heights, between 160 and 240 nm. It is found that both properties undergo red shifting behaviour as the height of the silicon increases. The observed changes in their optical behaviour are examined through a numerical technique known as multipole decomposition. This method can identify whether a resonance is predominantly electric or magnetic in origin and if it has dipolar or quadrupolar character. Understanding resonances in this way is important for the control of sample properties and development of design principles for novel sensing technologies. The ability of dielectrics to produce multiple resonance types is of particular interest to chiral sensing, as the interference of electric and magnetic modes is fundamental to generating optical activity, as previously discussed.

It is shown that the reflectance resonances undergo a gradual increase in wavelength until a sudden and significant change in line shape occurs at 240 nm silicon height. These observations are shown to arise from two primary sources: the increased size of the scatterer in accordance with Mie theory and the generation of quadrupolar resonances at 240 nm silicon thickness. Similar behaviour occurs for the ORD spectra; however, the behaviour is shown to be non-reciprocal which violates the necessary conditions for true chirality. This begins an important discussion into the distinction between optical activity and birefringent effects, that is at times overlooked within the literature,.

5.1 Introduction to Silicon Based Metamaterials

Whilst plasmonic materials have shown a wide variety of interesting properties and practical uses in sensing, there exists a key drawback in their material characteristics. The primary limitation in this respect is their tendency for high optical losses, arising from high absorption coefficients, that ultimately lead to inefficient devices. Silicon, along with other dielectric materials, may provide a solution due to their high real- and low imaginary-parts of their refractive indices.

As with plasmonic devices, many different nanostructure designs have been investigated for dielectric platforms due to the flexibility in fabrication approaches.^{1,2} One such conformation that has previously been explored were asymmetric S-shaped structures.³ Diao *et al.* focussed on their electromagnetically induced transparency window that occurs in the near infrared range. Through numerical simulations they found that the structures could produce high quality factor resonances and that magnetic and electric moments could be generated within the materials. This investigation, however, did not consider any potential chiral response of the materials, which will now be examined in this work.

5.1.1 Light-Matter Interactions in Silicon

As discussed in the previous chapter, plasmons arise from the oscillation of free electrons at a metal-dielectric interface under the excitation of incident light. If

no free electrons exist, such as in a dielectric material like silicon, a different theoretical approach must be used to describe the light-matter interaction. Gustave Mie provided this framework, by first describing the optical behaviour of arbitrarily sized spherical homogeneous particles.⁴ Mie theory describes the scattering of light by these particles as a series of multipole contributions. Whilst Mie theory is an expansive and complex description, it can be simplified to provide an easier understanding of the origin of optical resonances. This is done by considering the sphere as an optical cavity. For a sphere of diameter d , Mie resonances will occur when the wavelength of the light inside the sphere is comparable to its diameter, $\lambda_p \approx d$. There can be a second resonance expected when the wavelength is approximately equal to $\lambda_p \approx d/2$. Higher multipole terms are expected to arise at lower wavelengths with lower intensity as scattering efficiency decreases. As light passes from a lower refractive index medium, n_m , to a higher index medium or particle, n , the wavelength of the light shortens by a factor $\frac{\lambda_m}{\lambda_p} \approx \frac{n}{n_m}$, shown in **figure 5.1**. The first Mie resonance will occur when $\lambda_p = \frac{\lambda_0}{n}$, where λ_0 is the vacuum wavelength.⁵

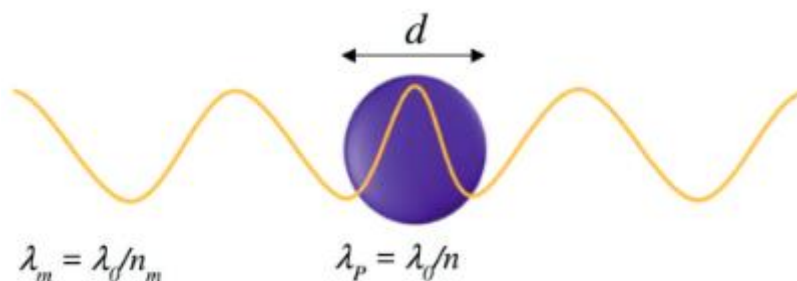


Figure 5.1: A visual representation of light passing through a higher index (spherical) cavity. Figure adapted from reference ⁵.

In silicon, the first dipolar resonance to occur is a magnetic one, in contrast to plasmonic materials which are of electric character. This occurs due to a key difference by the way in which electric currents behave in the material. Whilst electric dipoles are formed from the separation of a positive and negative region of charge, magnetic dipoles are formed from the closed circulations of electric current. In the absence of free charge carriers, circulating currents can be generated by displacement currents, which arise from a changing electric field within the material. As shown in **figure 5.2**, silicon produces circulating electric currents which support a magnetic field parallel to the incident electric field vector in the centre of the circulating region.⁶⁻⁹ The control of the magnetic resonances at visible frequencies has been demonstrated with spherical nanoparticles of different sizes, given their $d = \frac{\lambda_0}{n}$ dependence.^{10,11}

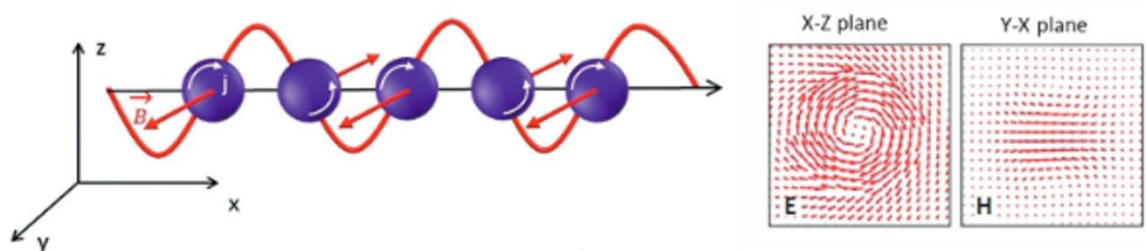


Figure 5.2: Incident EM radiation shown by its B-field vector (red) travelling in the x-axis, generates a circulating E field displayed in the leftmost arrow plot. The magnetic field arrow plot is shown in the orthogonal plane. Figure adapted from reference ⁵.

The differences in material excitation between metals and dielectrics can also be highlighted by the optical resonances they can support. Plasmonic dimers can produce a strongly coupled resonance with enhanced electric field ‘hotspots’ between particles when the incident light polarisation is aligned along the primary axis of the two metallic particles. Orthogonal polarisations on the other hand do not exhibit strong coupling, due to the misalignment of the material polarisation. High-index dielectric nanodimers, however, can produce strong coupling under both incident light polarisations. Light polarised along the primary axis of the dimer generate electric hotspots, whilst orthogonal polarisation produces magnetic hotspots as a consequence of the magnetic fields that arise from circulating E currents, visualised in **figure 5.3**.¹² Electric coupling is shown in red between dimers, whilst blue represents magnetic coupling. The dielectric dimer can support both under different excitation polarisations, whilst the metal dimer can only support electric coupling under one polarisation.

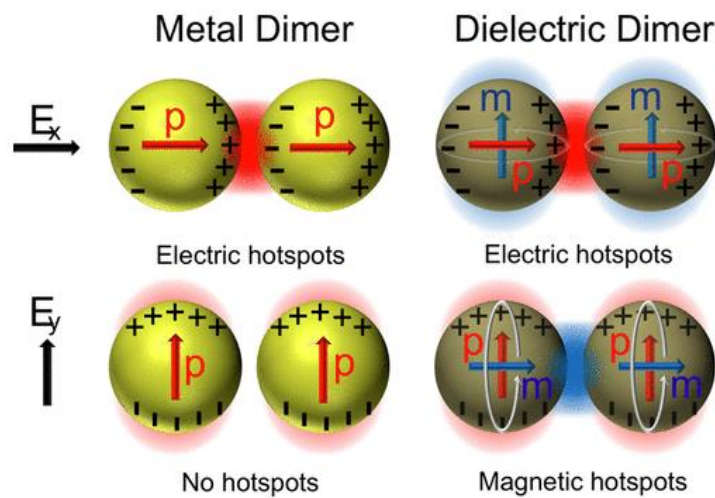


Figure 5.3: A comparison between metallic and dielectric dimers in terms of electric (p, red) and magnetic (m, blue) material polarisations and coupling, under E_x (top) and E_y (bottom) light polarisations. Figure adapted from ¹².

The ability of high-index nanoparticles to control light in the near-field has drawn interest due to their support of both magnetic and electric hotspots, which could prove advantageous in the enhancement of chiral fields, as they rely on the mutual interference of electric and magnetic dipole moments.¹³ The low optical losses compared to metallic platforms offer further incentive. All-dielectric metamaterials provide a means to achieve all four possible combinations of positive and negative permittivity and permeability, which opens them to a wide range of potential applications.¹⁴ This gives the freedom to access all possible material properties, as all natural materials occupy one quadrant. For instance, conventional metals are $\epsilon < 0$, $\mu > 0$, whilst water is a $\epsilon > 0$, $\mu > 0$ material. High-index dielectric metamaterials have so far been shown to be capable of chiroptical detection¹⁵, negative¹⁶ and zero-index materials¹⁷, magnetic mirrors¹⁸ and spectrally selective absorption in optoelectronic and solar cells¹⁹.

5.1.2 Birefringence and Chirality

Birefringence can be described as the orientation dependent difference in refractive index²⁰, and was first observed by Bartholin²¹ in calcite crystals. Optically isotropic materials will not exhibit birefringence due to light propagation

being uniform in all directions. Materials with inequivalent axes are classified as anisotropic, through which orthogonally polarised light will experience different paths, shown in **figure 5.4**. Incident light is split into two rays; the ordinary ray which travels at the same velocity uniformly throughout the crystal and the extraordinary ray that experiences a higher refractive index and travels a different path. There are several sources from which birefringence can arise, including material stress²² and the Faraday effect from external magnetic fields²³. As previously discussed, birefringence can occur with LPL (LB) and CPL (CB), with the latter providing a measure of a sample's optical rotation, detected through ORD.

Whilst optical rotation can often give an indication that a structure is chiral, this is not always the case. For a truly chiral response, the optical activity displayed by a structure should be reciprocal and invariant under any proper spatial rotation.²⁴⁻²⁶ If performing Stokes polarimetry on a birefringent medium LB can also contribute to optical rotation, however, this is not always decoupled from the CB. Conversely, a truly chiral structure such as a gammadion will yield the same resonant excitations independent of the incident polarisation.

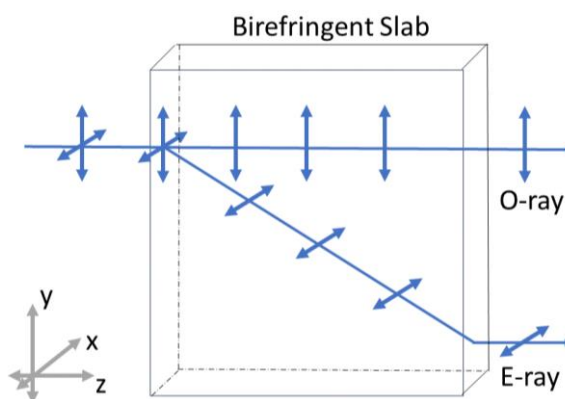


Figure 5.4: Orthogonally polarised components of the light incident on the birefringent slab experience different refractive indices. The ordinary ray (O-ray) experiences the same refractive index in every direction of the medium, whilst the extraordinary ray's (E-ray) velocity is dependent on propagation direction.

5.2 Methodology

5.2.1 Sample Design and Fabrication

Four distinct forms of nanoarray consisting of two enantiomorphous S-shaped structures were fabricated according to the process detailed in section 2.2.2. The arrays included those of entirely LH and RH structures, as well as two racemic versions that include both enantiomorphs. One racemic array, referred to as RA, contains alternating 19×19 regions of either LH or RH structures. The remaining array, referred to as RS, is formed from alternating individual LH and RH structures. The structure design and each array type can be seen in figure 5.5. Racemic arrays are of interest as they represent a means of halving fabrication demands if they are capable of enantiomeric discrimination, removing the need for separate LH and RH arrays. Racemic arrays will likely affect any periodic resonances generated by the structures, which is a further point of interest given the chiroptical properties of the gammadion periodic modes analysed previously.

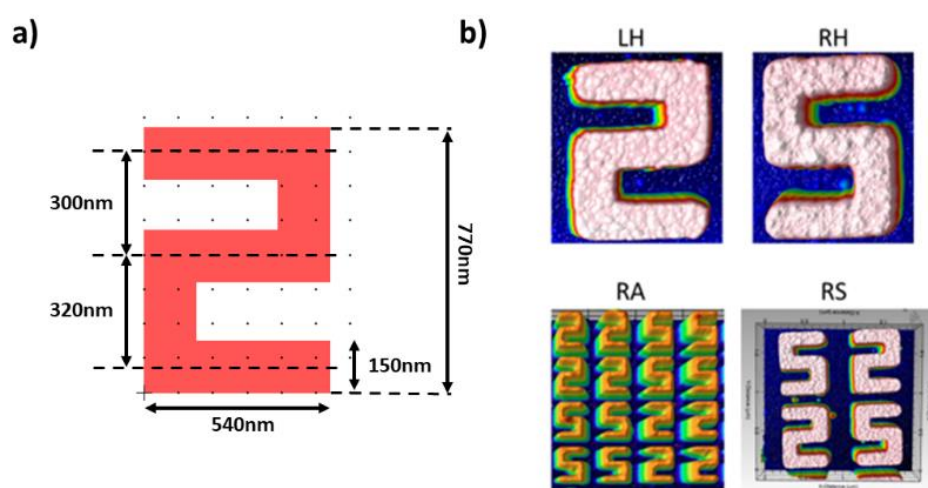


Figure 5.5: a) The L-Edit design file for a single LH S-structure, with dimensions labelled. Black dots represent $10 \mu\text{m}$ intervals. b) AFM images from each array type, the RA image is taken from where four of the 19×19 arrays meet.

There is an asymmetry in the design of the S structure, the distance between the centre of the middle arm and the centre of the top arm is 300 nm, whilst the equivalent distance between the middle and bottom arms is 320 nm. From the AFMs it is apparent that the fabricated structures do not perfectly resemble the design files, particularly with the separations between the arms, although there is still a clear asymmetry in the structures from the separation of the top and bottom arms with respect to the centre arm. Rounding of the structure's edges is also a noticeable difference when compared to the original design, all of which arise from limitations in the fabrication process. The LH, RH and RS images represent the repeating units within the arrays. The RA image shows a point at which four of the 19×19 LH and RH meet, which is in the centre of the image.

5.2.2 Simulation Procedure

Due to the nature of the arrays used with the fabricated samples, two distinct types of model setup were required. In the previous chapter, only LH and RH arrays were modelled, which is performed with a one-structured unit cell surrounded by

periodic boundary conditions. The racemic RS array, however, requires a new model, given that it includes four structures within its unit cell. Details of the modelling required for the structures are shown in **figure 5.6**. As the RA array unit cell includes four 19×19 sets of structures, it is unfeasible to simulate given the extreme computational demands required of such a large model and as such no simulations for this array are performed. Even the smallest RA unit cell possible would require 4×4 sets of structures, which would still place extreme demands on the computer.

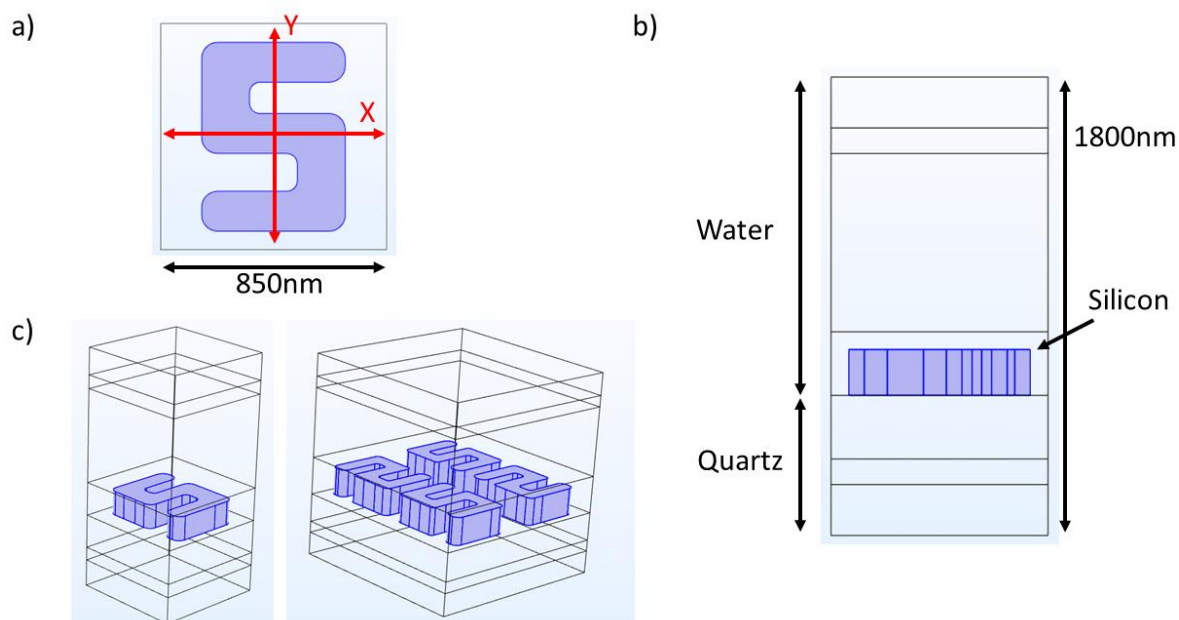


Figure 5.6: a) A top-down view a single RH idealised model of the silicon S structure, in a 850×850 nm unit cell of periodic boundary conditions. The two incident light polarisations used throughout this chapter are labelled with respect to the structure's orientation b) A side-on view of the model, with domain materials labelled. c) The two variations of models used single structures (left) and four structures (right).

Throughout the following results sections, references to x- and y-polarised incident light will be made. The orientation of the sample in this respect is shown in **figure 5.6a** and will be specified for each set of data. The idealised models that are also shown in this figure include filleted (rounded) edges that better represent the structures measured under AFM. Simulations are also performed on models imported from AFM measurements, the main difference between these and the idealised versions being the surface deformities of the AFM imports. The 4-structure simulations require significantly more computational memory due to the large increase in mesh elements, due to the four-fold increase in structures present. The unit cell size is doubled in the x- and y-axes, however the primary source of the increased meshing results from the presence of the extra structures.

5.2.3 Experimental Procedure

Experimental results detailed in this chapter are taken from the Stokes polarimeter described in **section 3.1.2.1**. Reflectance and ORD measurements were taken with the samples immersed in PBS buffer, illuminated under x- and y-polarised light. Prior to experimental measurements being taken, the sample heights were verified with a *Bruker Dektak Surface Profiler*, shown in **figure 5.7**.

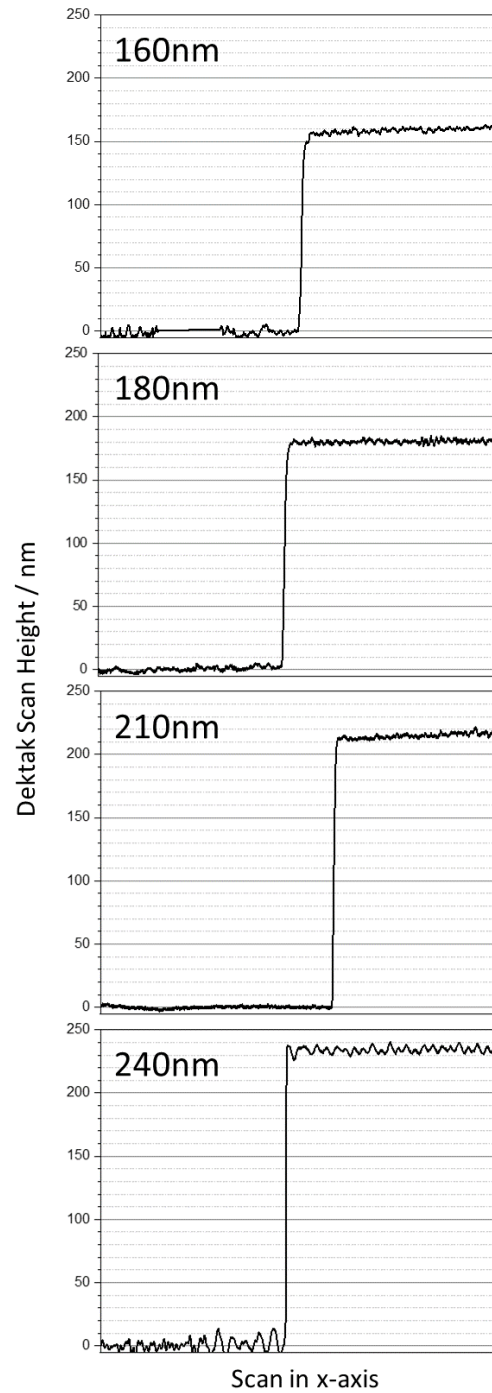


Figure 5.7: Dektak scan data for each of the four samples used in experiment. The profilometer tip scans across the sample's quartz glass substrate and onto the silicon array, measuring the step height between them.

5.3 Results and Discussion - Reflectance

5.3.1 Measured Reflectance

Reflectance spectra for each sample height and array type under the orthogonal incident light polarisations are displayed in **figure 5.8**. For y-polarised illumination of the 160-210 nm samples, the spectra display a characteristic double peak, consistent for all array types, which have been labelled as A and B. A red shift of this double peak is observed as the sample height is increased. At 210 nm silicon depth, peak A undergoes splitting and peak B significantly decreases in relative intensity. The thickest sample shows the greatest spectral change, with both the appearance of multiple peaks and a general broadening of the reflectance spectra across the measured wavelength range. The x-polarised data displays relatively little reflectance in comparison for the 160-210 nm heights, however, two peaks either side of a broader region of intensity can be seen to redshift with increasing sample height. Two of these features have been labelled as peaks D and E. As before, the spectra undergo a significant change in reflectance behaviour for the thickest sample.

The LH, RH and RA arrays all show very similar reflectance behaviour as would be expected. Variations between the spectra will arise from deformities and small differences intrinsic to the fabrication procedure. It is also likely that there are small misalignments in the measuring apparatus, which account for differences in peak heights, as arrays will receive slight differences in exposure to the incident light. The RS arrays differ slightly in terms of reflectance intensity and peak shape and display an additional peak, labelled C, for the 180 nm sample. Peak C occurs close to the 850 nm periodicity of the structures.

It is clear from both sets of data that incident polarisation has a strong effect on the reflectance, showing the nanostructures to be strongly birefringent. To understand the features and differences observed in the reflectance measurements, numerical simulations are required.

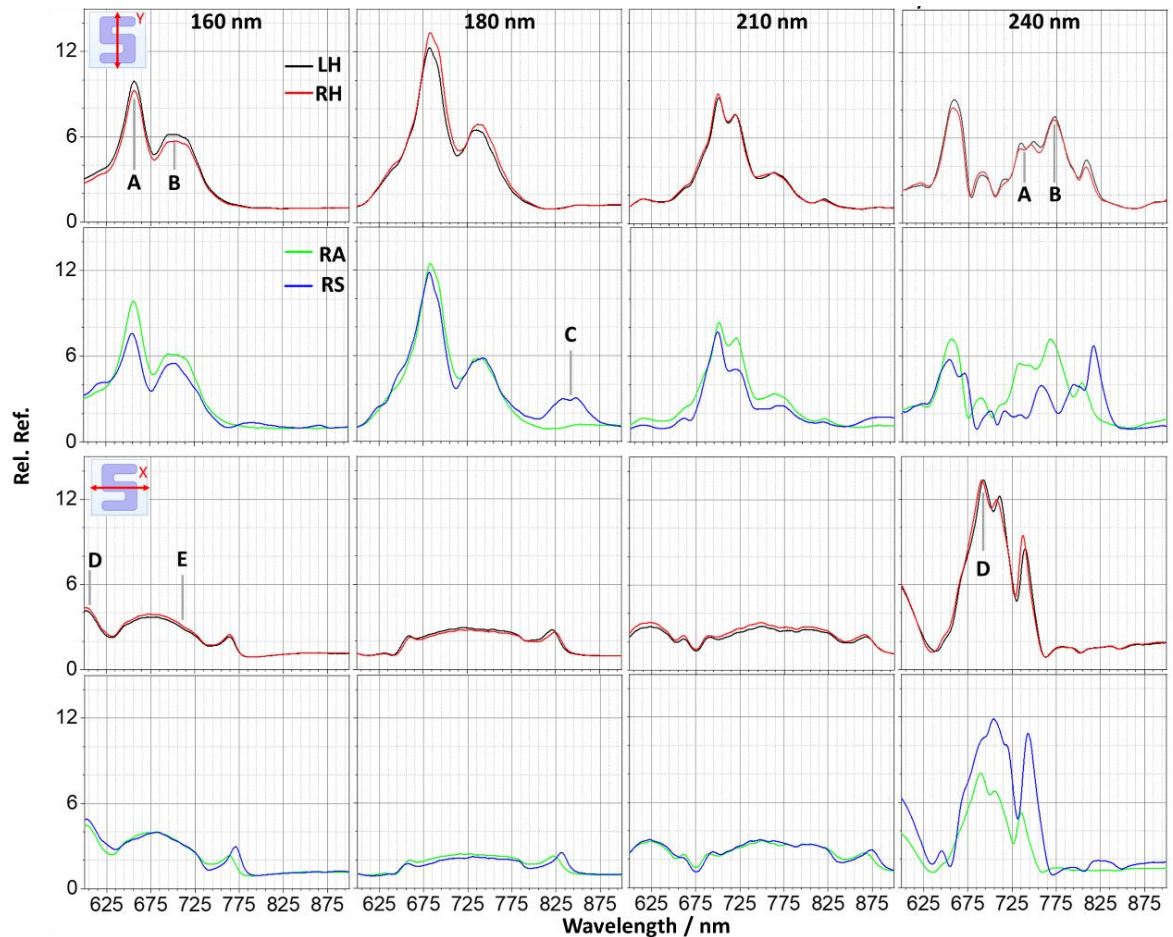


Figure 5.8: Experimental reflectance spectra for LH (black), RH (red), RA (green) and RS (blue) arrays at four different heights of silicon deposition under incident y- and x-polarised light (labelled in the left-most plots of the first and third rows). Peaks A and B represent the dominant feature of the y-polarised spectra, with the RS arrays also producing a peak close to the sample periodicity, labelled C. Peaks D and E occur for x-polarised spectra, representing a sharp peak prior to a broader one, respectively.

5.3.2 Simulated Reflectance

The LH and RH arrays were simulated using single structured unit cells, whilst RS arrays used 4-structure unit cells. The LH and RH arrays were also simulated using 4-structured unit cells to validate the use of the larger model. The reflectance spectra for RH and RS arrays for each sample thickness under y- and x-polarisations are shown in **figure 5.9**. As simulated LH and RH reflectance produces identical spectra, only the RH values are plotted.

For all cases with the simulated spectra, there is an order of magnitude difference between the experimental and simulated reflectance values. This is partly attributed to the structural heterogeneity (e.g. missing structures and contaminants) not accounted for in the ‘perfect’ model structures. The single structure simulations reproduce the experimental spectra reasonably well, qualitatively replicating both the line shape and its abrupt change between the 210 and 240 nm samples, for both polarisations. Under y-polarisation, the splitting of peak A at 210 nm silicon is observed. The 240 nm simulation reproduces the single peak below 700 nm as well as the general shape of the broader peak between 700 - 800 nm. The x-polarised spectra show the characteristic line shapes seen in experiment but exhibit an exaggeration in their intensities. This is most

apparent for the 210 nm sample with a continuous increase in intensity from ≥ 700 nm that is not observed experimentally.

The 4-structured RH and RS spectra show less agreement with the experiment in terms of the relative peak intensities and peak resolutions (such as lack of splitting for peak A for the 210 nm sample). This is likely due to the decreased meshing density per structure for the 4-structure unit cell, which leads to lower simulation accuracy. The 4-structured spectra do however generally display similar behaviour to the single structured models. Notably, the RS simulations do reproduce peak C for the 180 nm sample. The presence of a less intense instance of peak C is also observed for the shallowest sample, which is not seen experimentally.

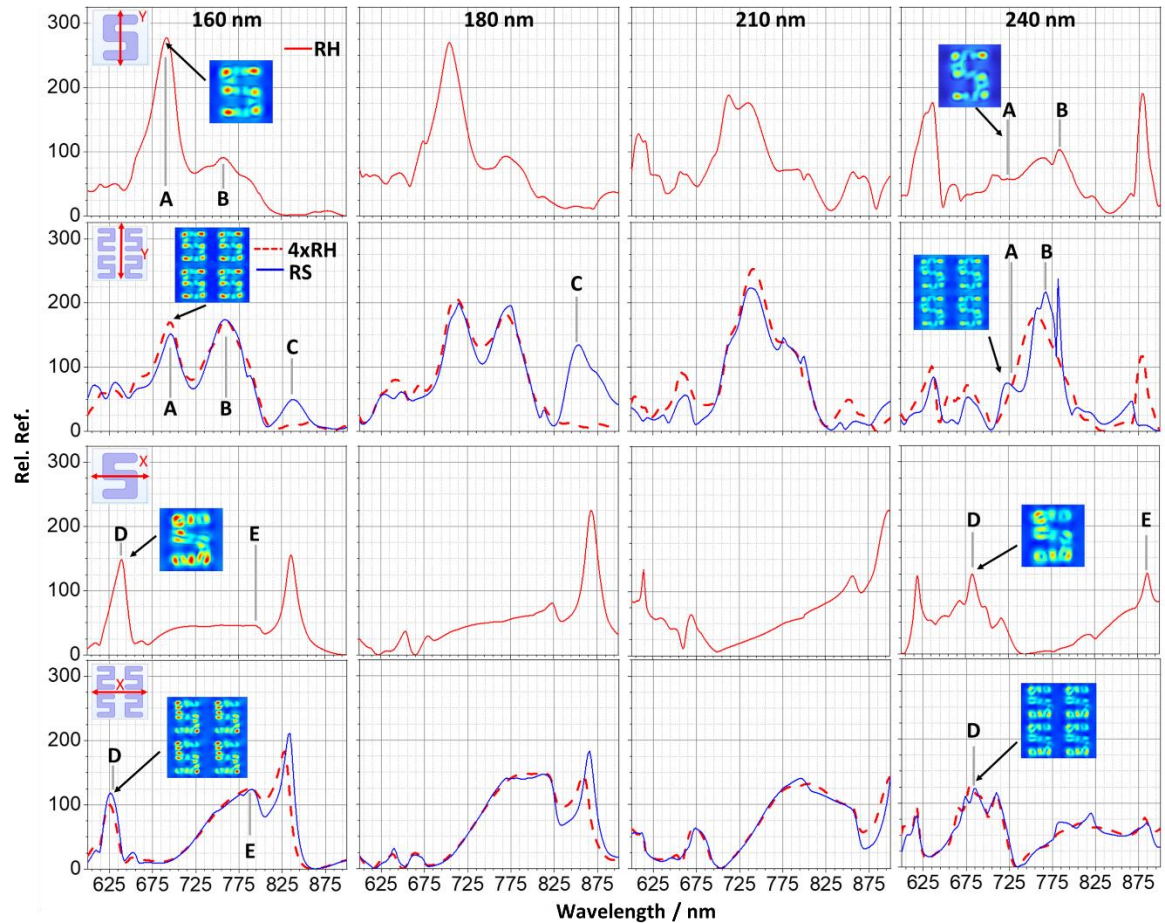


Figure 5.9: Simulated reflectance spectra for RH single structured models (red) and 4-structured RH (red dashed) and RS (blue) models, for each sample thickness under y- (left) and x-polarisations (right). Equivalent peaks of figure 5.8 are labelled A-E.

As is the case experimentally, the characteristic spectra for both polarisations show a progressive redshift with increasing silicon height. This behaviour is consistent with that expected from Mie theory, where resonances increase with scatterer diameter.^{5,10,14} The red shifting of the resonances can be confirmed and tracked across each sample depth by analysis of magnitudes of the electric ($|\mathbf{E}|$) and magnetic ($|\mathbf{H}|$) field distributions, shown in **figure 5.10**. Field magnitude plots can in some cases provide a clearer picture of electromagnetic field patterns, as they are time averaged. As LH and RH structures generate mirror equivalent fields, only the RH are shown.

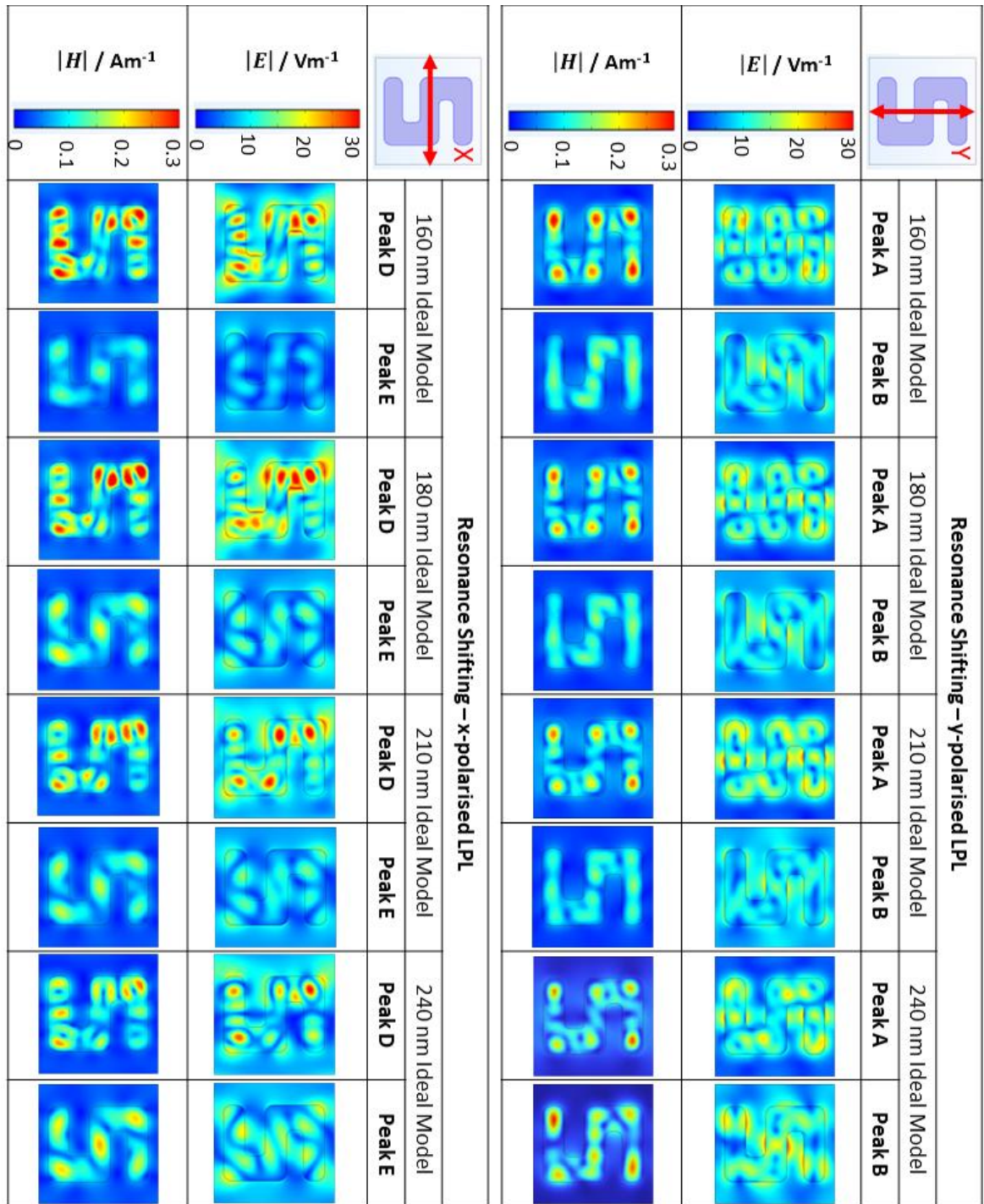


Figure 5.10: Distributions for the electric ($|E|$) and magnetic ($|H|$) field magnitudes plotted from single structure models, for equivalent resonances across all sample thicknesses under y- (top two rows) and x-polarisations (bottom two rows). Field plots here and subsequently are taken from the midpoint of the structures.

Although there are some variations in the field intensities, the general $|E|$ and $|H|$ distributions for each resonance peak are shown to persist across each sample thickness. For peak A, intense regions of $|E|$ at the ends of each arm form a ‘split ring’ shape (circular pattern with a gap on one side). The lower $|E|$ intensity in the centre of these rings corresponds to an intense region of $|H|$. The combination of strong $|E|$ and weaker $|H|$ (and vice versa) are common across each of the resonances. This field analysis confirms that the spectral peaks that red shift with increasing sample height are equivalent.

A common feature of the simulated spectra is the red shifting of resonances with respect to the experimental data. This is attributed to the lack of morphological flaws such as surface defects and wall sloping that result from the fabrication procedure. To verify this hypothesis, simulated spectra were obtained using an AFM imported 'real' model geometry. A comparison between experimental and simulated spectra using both the 'real' AFM model and idealised 'perfect' model are shown in **figure 5.11**.

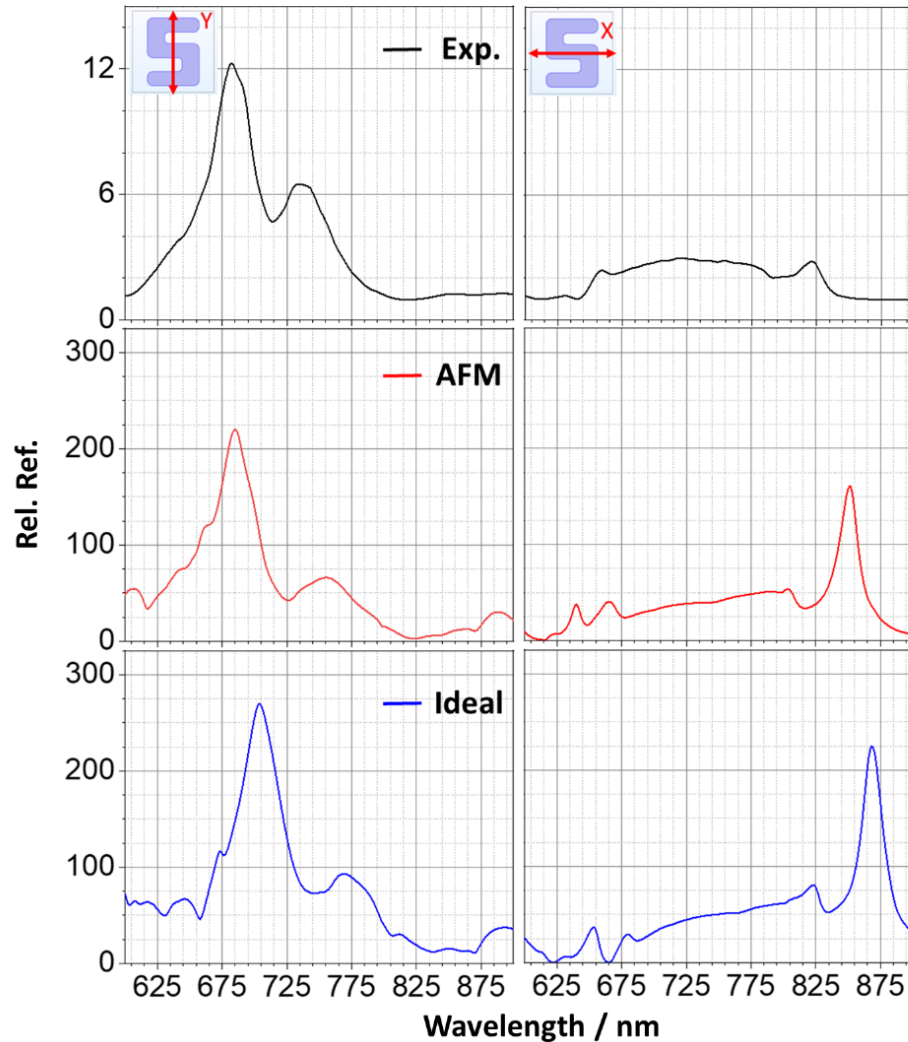


Figure 5.11: Reflectance comparison of y- (left) and x-polarised (right) illumination of a 180 nm sample between experiment (black), a 'real' AFM imported model (red) and the idealised model (blue).

It is clear that the AFM imported model produces spectra in better agreement with experiment. The typical ~ 20 nm red shift observed for idealised models is significantly reduced with the use of the 'real' AFM structure. The AFM model shows a general reduction in excess peaks and exaggerated peak intensities that occur for the idealised version. The idealised models are however used later to reduce the computational demand associated with the meshing of the AFM structures, which are significantly increased due to unsmooth surfaces. A comparison between the electric and magnetic field magnitudes was made, shown in **figures 5.12**, to further validate the spectra.

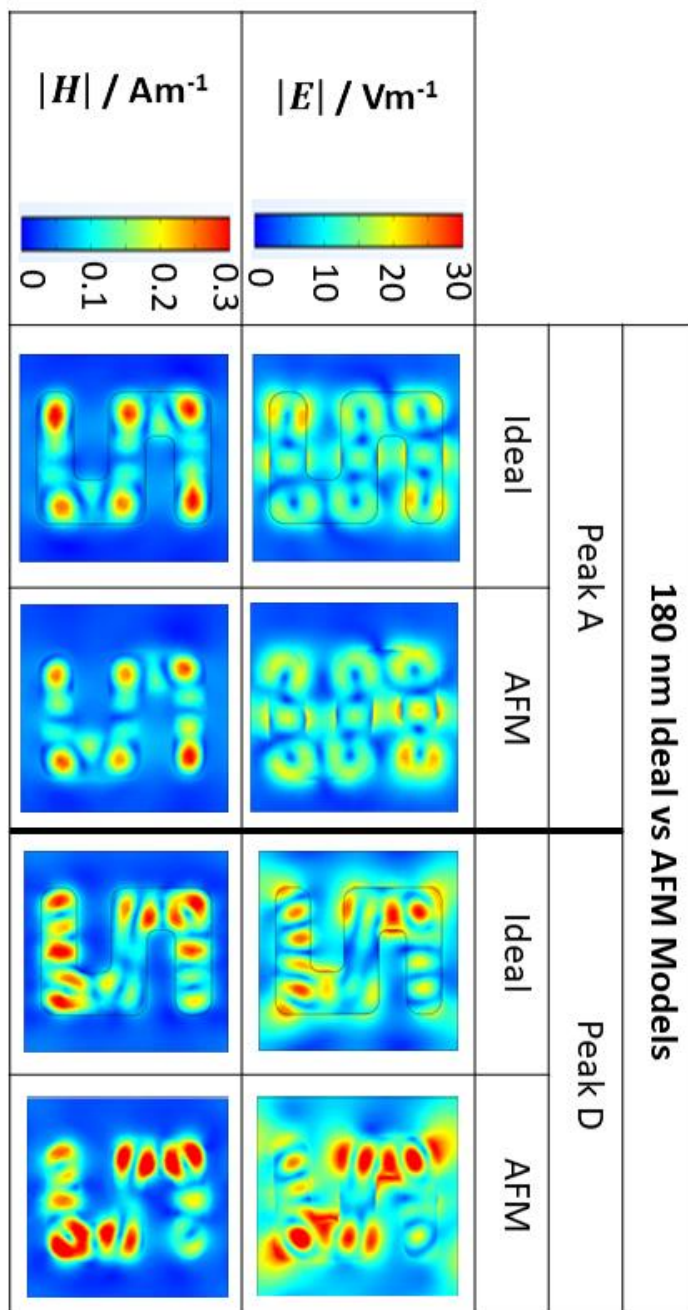


Figure 5.12: $|E|$ and $|H|$ field distributions for 180 nm ‘ideal and ‘real’ AFM structures for peaks A and D.

The field analysis confirms that there is good agreement between the AFM and ideal models. Equivalent resonances are identified, with the ideal resonances occurring at longer wavelengths. As expected, the AFM model produces stronger fields, or ‘hotspots’, around the edges of the arms due to the presence of structural imperfections, further highlighting the impact of the surface morphology.^{27,28}

EM field plots can be a useful tool for analysis of a resonance's origin, particularly in the case of a periodic mode. To investigate the origins of peak C, $|E|$ and $|H|$ distributions were compared between RH and RS simulations, shown in figure 5.13.

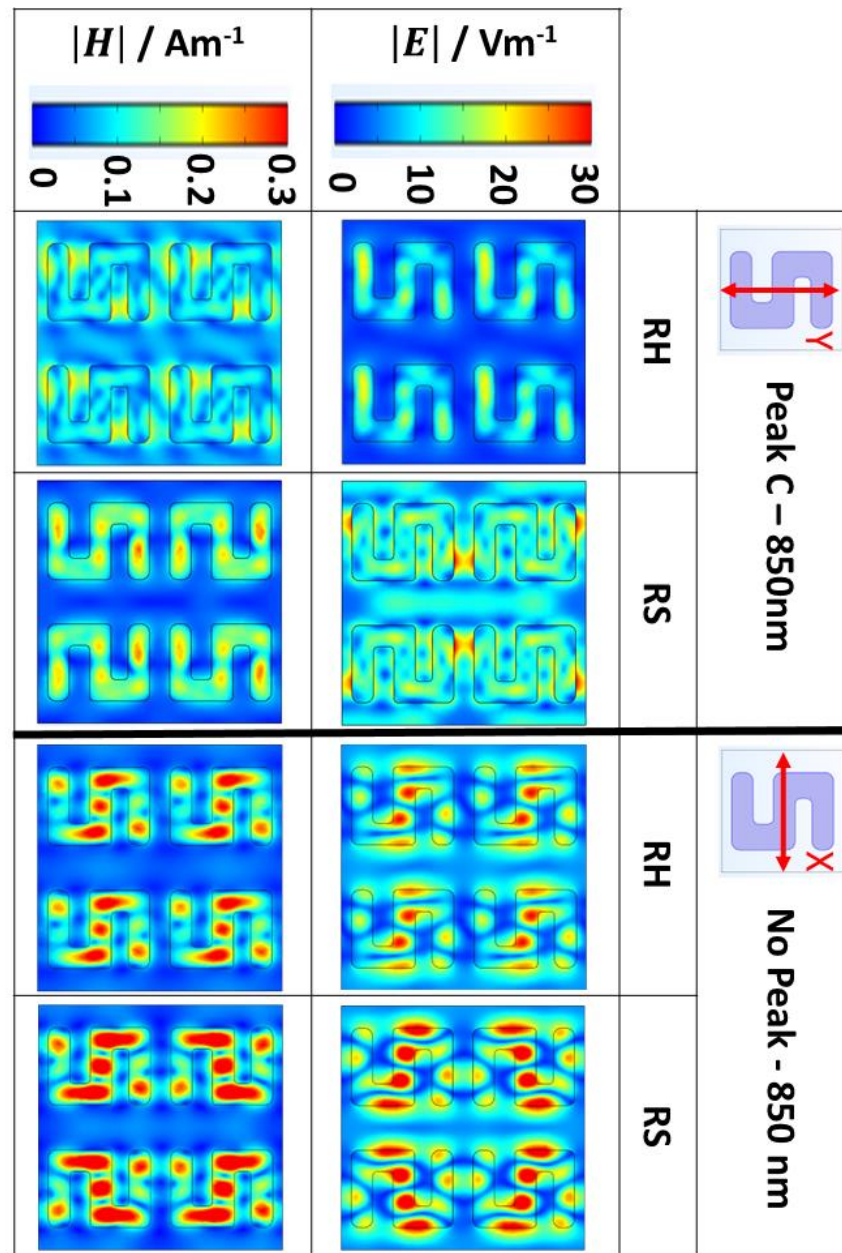


Figure 5.13: $|E|$ and $|H|$ field distributions for 180 nm 4-structured RH and RS arrays under y- and x-polarised excitation. Distributions give an indication of the degree to which resonances are localised or periodic.

Considering the $|E|$ distributions, peak C arises due to coupling between adjacent structures in the y-axis of the RS arrays when incident LPL is y-polarised. This occurs due to preferential alignment between the arms (and associated internal fields) of y-adjacent structures, allowing them to couple across the entire array. In an enantiomorphic array, the arms of adjacent structures are anti-aligned, preventing them from coupling and resulting in a lack of a resonance in the reflectance spectra. Under x-polarised light, there are no periodic resonances observed due to the much-reduced coupling that occurs between structures. The ability for coupling to occur in the x-axis is particularly limited, given the increased distance between the structures in this direction.

The lack of periodic resonances in the thicker samples can be understood by considering previous work on periodic resonances of silicon nanoarrays.²⁹ It was found that the resonances also underwent a redshift with increasing sample height, despite no changes to the periodicity of the arrays. These resonances are likely not observed in the thicker samples due to them shifting out of the measured range. The periodic resonances are more intense in the simulated data compared to experiment, likely due to the lack of structural imperfections. As such, the periodic resonance that occurs for the 160 nm simulation at ~835 nm (which is inherently less intense than that of the 180 nm sample) is not observed experimentally.

Whilst analysis of the structure's field plots can give some indication of what EM character a peak possesses, it is not possible to accurately determine the full nature of the resonance. In order to do so, a numerical method known as multipole decomposition was implemented within COMSOL.

5.3.3 Multipolar Decomposition

Mie theory can describe the scattering behaviour of nanoparticles at distances larger than the scatterer, through a superposition of electric fields created by multipole moments. The total scattered field at some point $\mathbf{E}(\mathbf{r})$, can be considered the sum of $\mathbf{E}_p + \mathbf{E}_m + \mathbf{E}_Q + \mathbf{E}_M$, where the \mathbf{E} terms represent the electric fields produced by the electric dipole \mathbf{p} , magnetic dipole \mathbf{m} , electric quadrupole \mathbf{Q} and magnetic quadrupole \mathbf{M} moments.^{11,30-33} The fields produced are calculated from the current densities, \mathbf{j} , produced within the material, as a result of external excitation from an applied EM wave:

$$\mathbf{j} = -i\omega\mathbf{P}. \quad [5.1]$$

Where the material polarisation \mathbf{P} , related to the applied field by:

$$\mathbf{P} = \varepsilon_0(\varepsilon_r - 1)\mathbf{E}. \quad [5.2]$$

Where ε_0 and ε_r are the vacuum and material permittivity, respectively. The field propagators which describe the electric field created by the scatterer at a given point can be used to calculate the fields generated by these moments, the derivations of which are beyond the scope of this work. Written in the far-field approximation and considering the first four multipole moments, the total scattered field can be given as¹¹:

$$\mathbf{E}(\mathbf{r}) = \frac{k_0^2 e^{ik_0 r}}{4\pi\varepsilon_0 r} \left([\mathbf{n} \times [\mathbf{p} \times \mathbf{n}]] + \frac{ik_0}{6} [\mathbf{n} \times [\mathbf{n} \times \mathbf{Q}\mathbf{n}]] + \frac{1}{c} [\mathbf{m} \times \mathbf{n}] + \frac{ik_0}{2c} [\mathbf{n} \times (\mathbf{M}\mathbf{n})] \right). \quad [5.3]$$

Here, k_0 is the wavenumber in vacuum, c the vacuum speed of light and \mathbf{n} the unit vector directed from the source to the observation point. The scattering power can then be calculated through Poynting's Theorem, such that³¹:

$$dP = \frac{1}{2} \sqrt{\frac{\varepsilon_0 \varepsilon_d}{\mu_0}} |\mathbf{E}|^2 r^2 d\Omega. \quad [5.4]$$

Where P is the scattering power, ε_d the permittivity of the dielectric, μ_0 the permeability of free space and $d\Omega$ the solid angle. Substituting $\mathbf{E}(\mathbf{r})$ into the Poynting equation yields³¹:

$$P \approx \frac{k_0^4}{12\pi\varepsilon_0^2 v_d \mu_0} |\mathbf{p}|^2 + \frac{k_0^4 \varepsilon_d}{12\pi\varepsilon_0 v_d} |\mathbf{m}|^2 + \frac{k_0^6 \varepsilon_d}{1440\pi\varepsilon_0^2 v_d \mu_0} |\mathbf{Q}|^2 + \frac{k_0^6 \varepsilon_d^2}{160\pi\varepsilon_0 v_d} |\mathbf{M}|^2. \quad [5.5]$$

With v_d the speed of light in the dielectric. The scattering power can then be used to calculate the scattering cross section, σ , by dividing it by the incident irradiance. Evlyukhin *et al.* have derived and implemented these equations for structures in a variety of shapes.^{31,33-35}

A comparison between the experimental reflectance, simulated reflectance and total multipole scattering power (calculated in COMSOL using equation [1.5]) of the 180 and 240 nm idealised nanostructures is shown in **figure 5.14**.

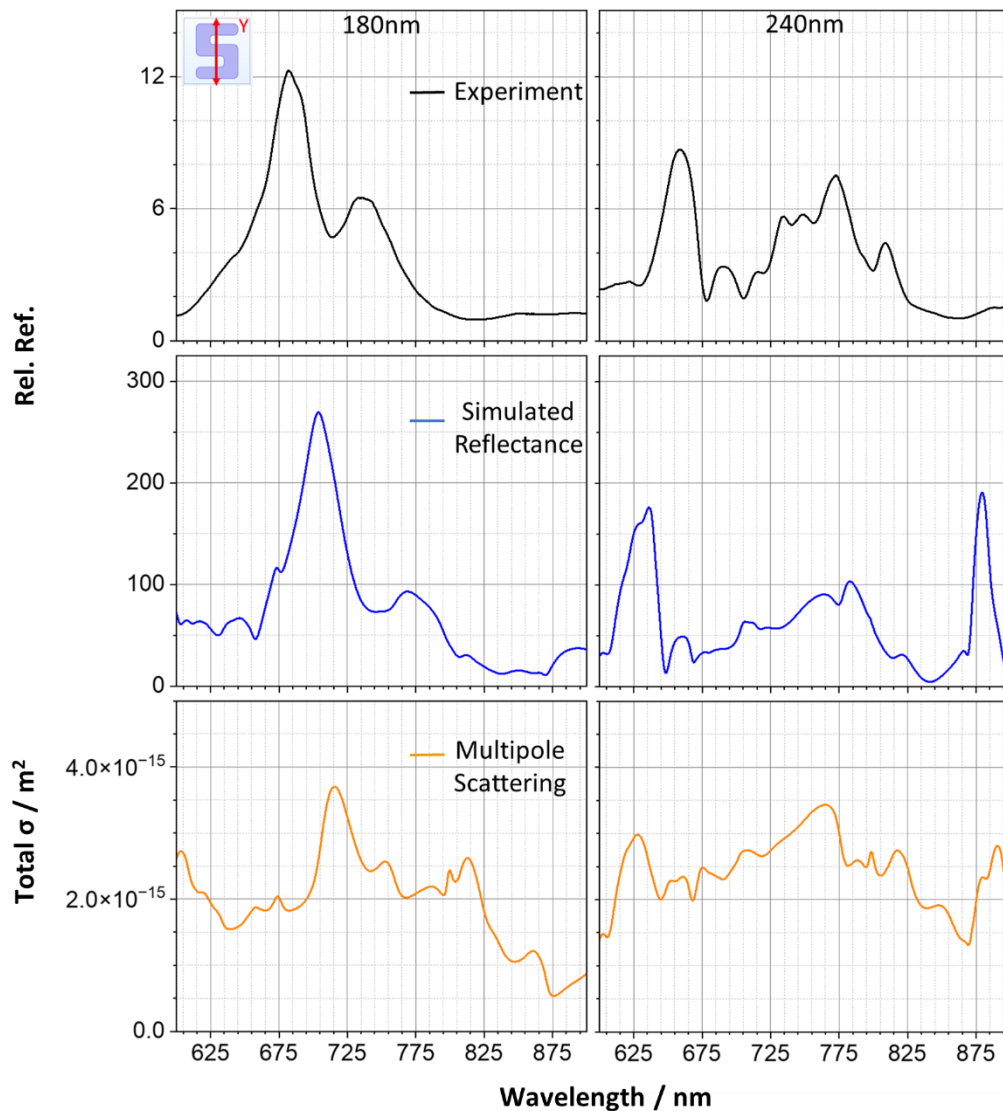


Figure 5.14: A comparison of the RH experimental reflectance (black), simulated reflectance (blue) and the total multipole scattering cross section (orange) for the 180 nm (left column) and 240 nm (right column) structures when illuminated with y-polarised incident light.

There is reasonable agreement between the three, with the 180 nm multipole scattering displaying the characteristic double peak, although it is narrower than in the other cases and there is also the emergence of an exaggerated peak between 800-820 nm. The multipole scattering spectra also displays a greater redshift than the simulated reflectance. Differences between the multipole scattering and simulated reflectance will arise primarily from how they are calculated. The simulated reflectance is measured at the input port of the model, providing a directionally dependent factor (as with an objective from experiment). In contrast, the scattering power is calculated in all directions, as no solid angle (equation [5.4]) was applied.

The 240 nm multipole scattering agrees qualitatively with experimental and simulated reflectance, where there are resonances present at 630 and 660 nm and a broader intensity between 700 and 800 nm. The relative intensity of these features, however, are not consistent with the other spectra.

The multipole scattering displayed in these figures is the sum of the four components, labelled as E_D (electric dipole), M_D (magnetic dipole), E_Q (electric quadrupole) and M_Q (magnetic quadrupole). By considering these elements individually, a multipole decomposition is performed, and the nature of the resonances can be revealed. **Figure 5.15** details the components of the total multipole scattering for the 180 nm sample.

It is evident that the characteristic double peak line shape originates predominantly from a magnetic dipole resonance, due to their similar shapes, with a significant electric quadrupolar contribution also present. This agrees with the resonance behaviour of silicon, where the magnetic dipole supports the electric quadrupole in the form of circulating electric currents, which show the characteristic ‘split-ring’ $|\mathbf{E}|$ field distributions shown previously. The peak between 800-820 nm appears to be exaggerated in the multipole scattering, which is determined to be of electric dipole nature. There is magnetic quadrupolar behaviour across most of wavelength range, although it appears to be a more dominant contribution at lower wavelengths where there is less of a contribution from the other multipoles.

Analysis of the 240 nm structure’s multipole decomposition, shown in **figure 5.16**, can help explain why there are such large differences in reflectance associated with an increase in silicon height. There is a general redshift for all peaks of the multipole contributions, as Mie theory predicts, where the resonance wavelength increases due to increased diameter of the scatterer. The magnetic dipole and quadrupole contributions continue to overlap but appear broader and smoother across their range. For these structures, the biggest change of the multipole components at the 240 nm depth occurs for the magnetic quadrupole. The contribution increases by almost double in the 620-680 nm range, which accounts for the two new peaks that are present in the reflectance spectra. It contributes to the broadening of the spectra between 700-800 nm and accounts for the additional peak at 880 nm seen in the simulated reflectance, which is much less intense in the experimental data.

The significant change in the reflectance spectra therefore arises from two main causes. One is the redshift of the resonances due to increased sample thickness as is predicted by Mie theory. The second, from the increase in magnetic quadrupolar contribution. This can be rationalised by considering the increased sample thickness allowing greater support of a the quadrupolar behaviour, as the magnetic fields are generated across the height of the sample.³⁴ The scattering decomposition results also agree with behaviour observed for silicon nanospheres, in which the presence of higher order multipoles increased with greater sample thicknesses.¹⁰

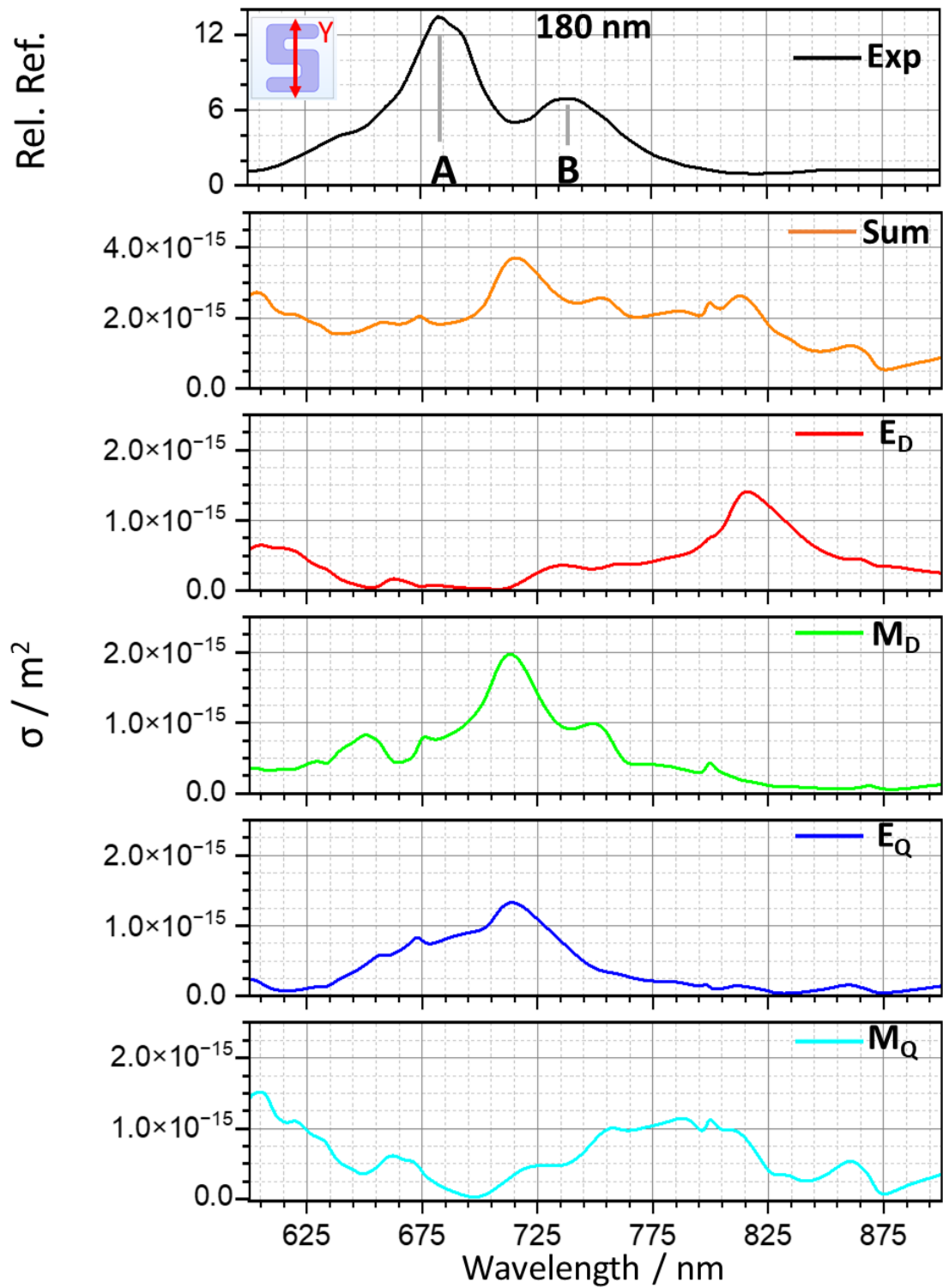


Figure 5.15: A comparison between experimental reflectance (black) and the simulated sum of the scattering cross section (orange) for the 180 nm structure under y-polarised illumination. The components include the E_D (red), M_D (green), E_Q (blue) and M_Q (cyan) contributions. Note that the scale of the sum plot is double that of the contributions.

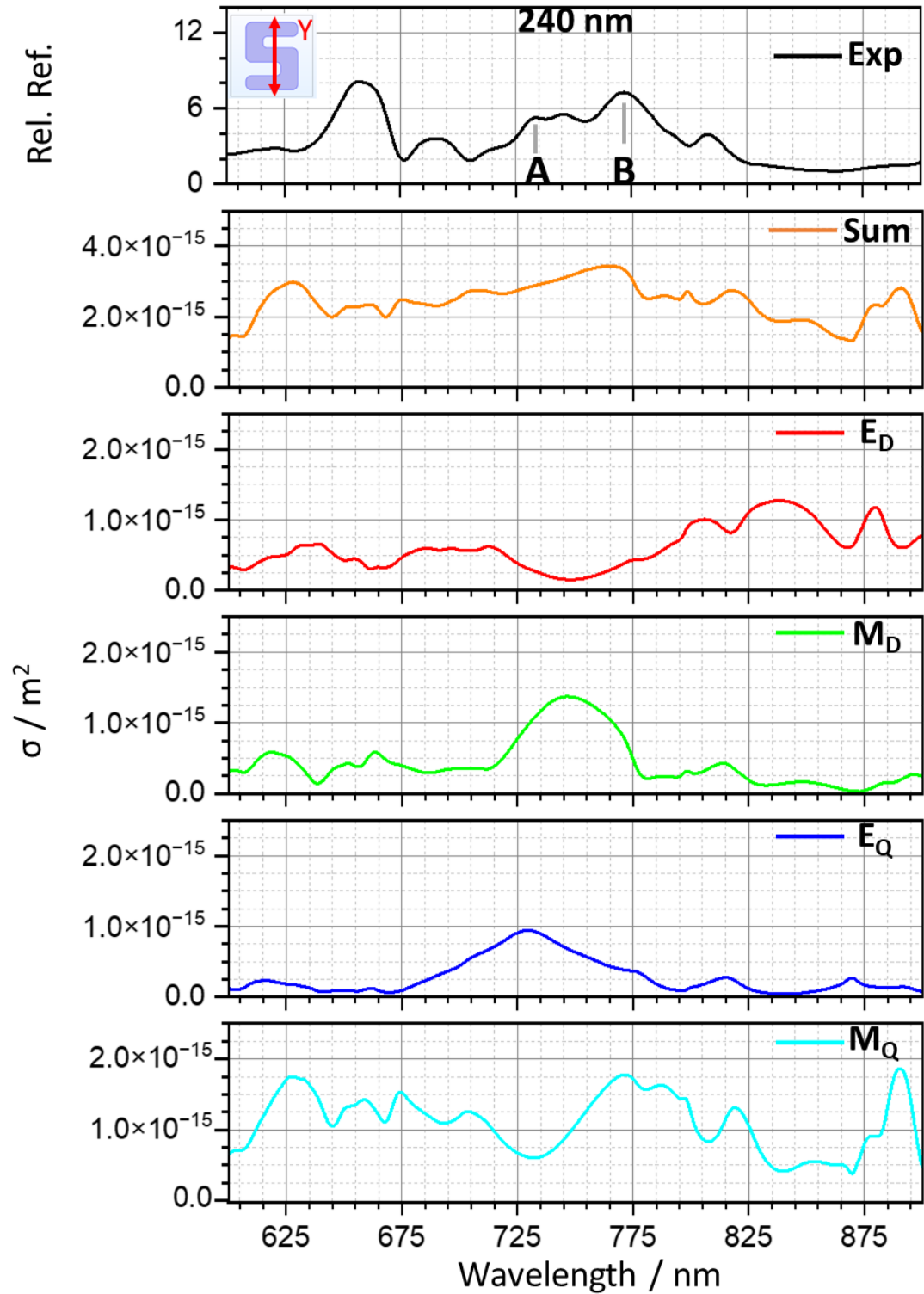


Figure 5.16: A comparison between experimental reflectance (black) and the simulated sum of the scattering power components (orange) for the 240 nm structure under y-polarised illumination. The components include the E_D (red), M_D (green), E_Q (blue) and M_Q (cyan) contributions.

Field analysis of the z-components of $|\mathbf{E}|$ (E_z) and $|\mathbf{H}|$ (H_z), shown in figure 5.17, can be used to support the multipole assignments from the decompositions. For the H_z of peak A, the field distributions are negative with inversion of the structure which indicates a degree of dipolar character. This distribution is consistent at both sample heights, with an increase in intensity for the 240 nm sample. The E_z pattern for peak A displays a more complex field arrangement in both planes, which suggest higher order multipole character. The appearance of an additional reflectance peak for the 240 nm sample is observed in experiment and replicated

in simulation at ~ 636 nm. Field analysis of this wavelength shows much more complex field patterns in both E_z and H_z , indicative of a higher order multipole contribution. In each case, the field behaviour is consistent with the multipole decomposition.

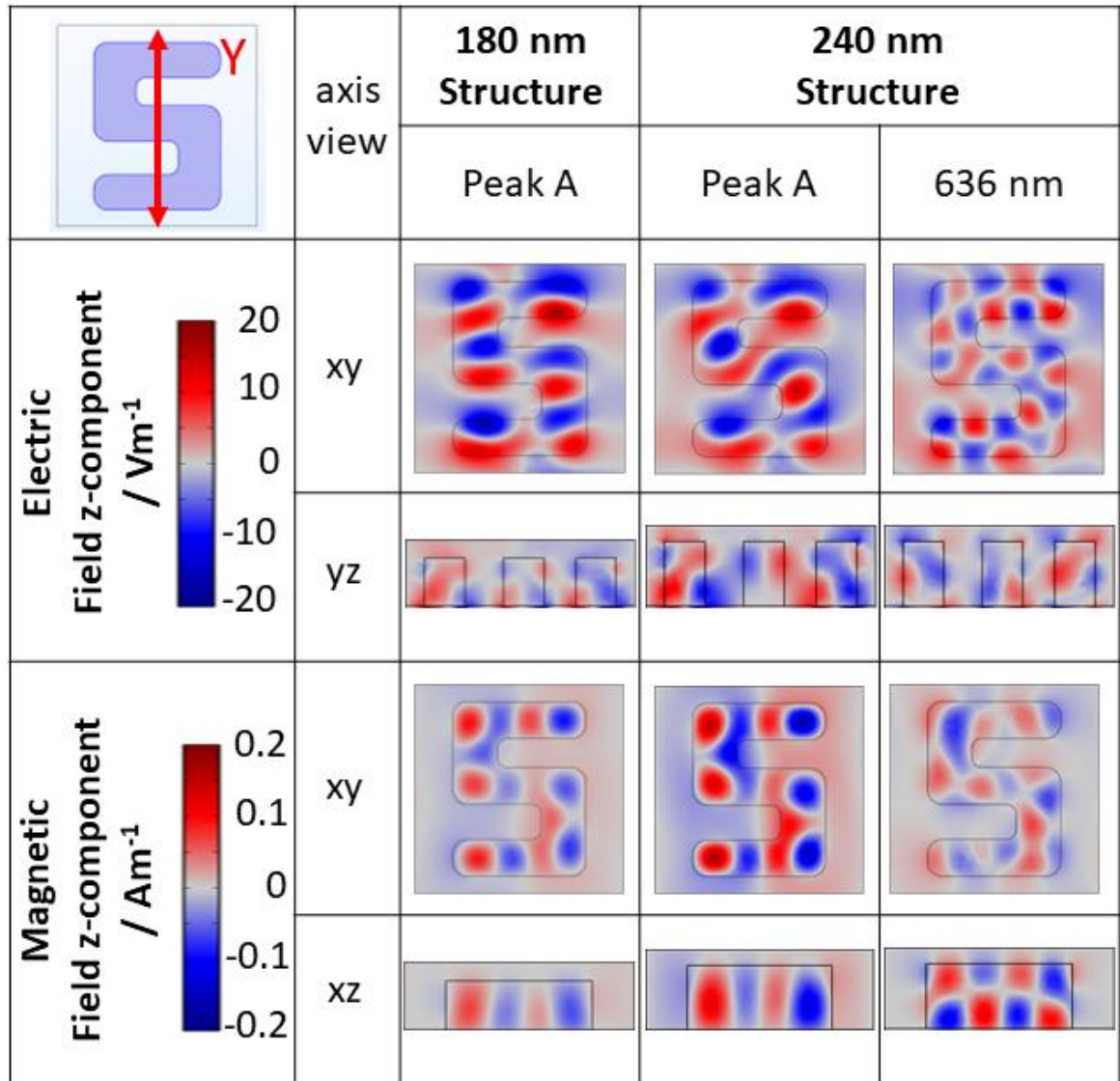


Figure 5.17: E_z and H_z distributions for select peaks under y-polarisation, viewed from different planes. x-y plane images are taken from the midpoint of the structures, whilst orthogonal planes dissect the centre of the unit cell.

Previous field distributions for $|\mathbf{E}|$ and $|\mathbf{H}|$ resembled those of circulating electric currents which were centred on the magnetic resonance, which is generated across the height of the silicon. This characteristic behaviour can be confirmed from field arrow plots, shown in **figure 5.18**. The electric field and current densities of peak A show a circulating pattern around the regions at which $|\mathbf{H}|$ is most intense. There is also significant coupling between the arms of the nanostructure. Peak B shows similar circulating patterns, albeit over broader regions.

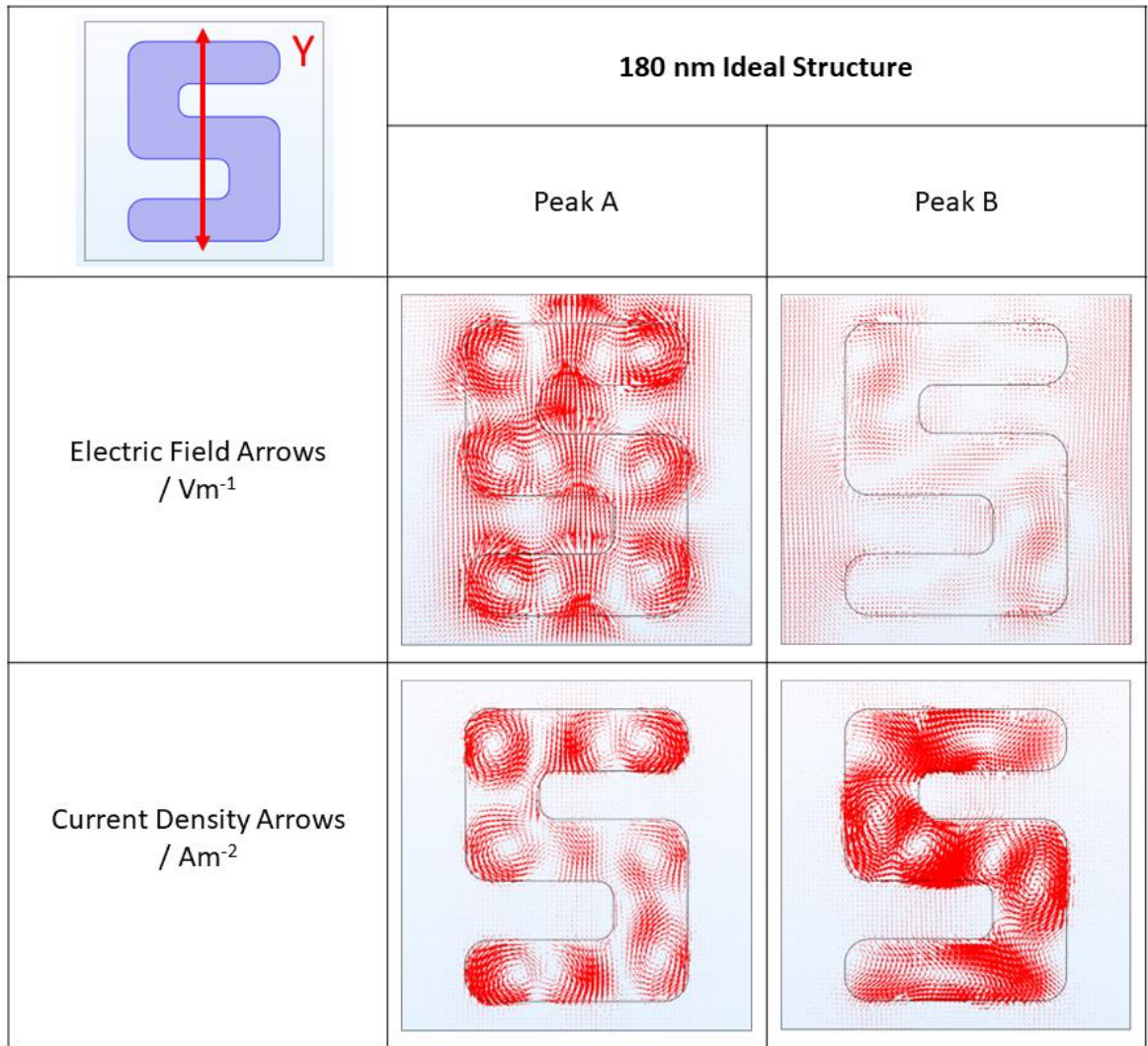


Figure 5.18: Electric field and current density arrow plots for peaks A and B of the 180 nm sample under y-polarised illumination. Arrow surfaces are taken at the midpoint of the structure.

Multipole decompositions were also performed for the structures when excited by x-polarised incident light. A comparison between the experimental and simulated spectra can be seen in **figure 5.19**. Beginning with the 180 nm sample, the multipole scattering shows some qualitative agreement with the other spectra due to the presence of peaks either side of a broad resonance that occurs between 680 nm and 800 nm. The relative size between peaks agrees more with the experimental intensity than that of the simulated reflectance. The 240 nm multipole scattering also displays some qualitative agreement with the other spectra, primarily with the intensity peak between 660-740 nm. The peak lacks the same features as the others, however, the overall change in spectral shape between sample heights provides reasonable agreement with experiment.

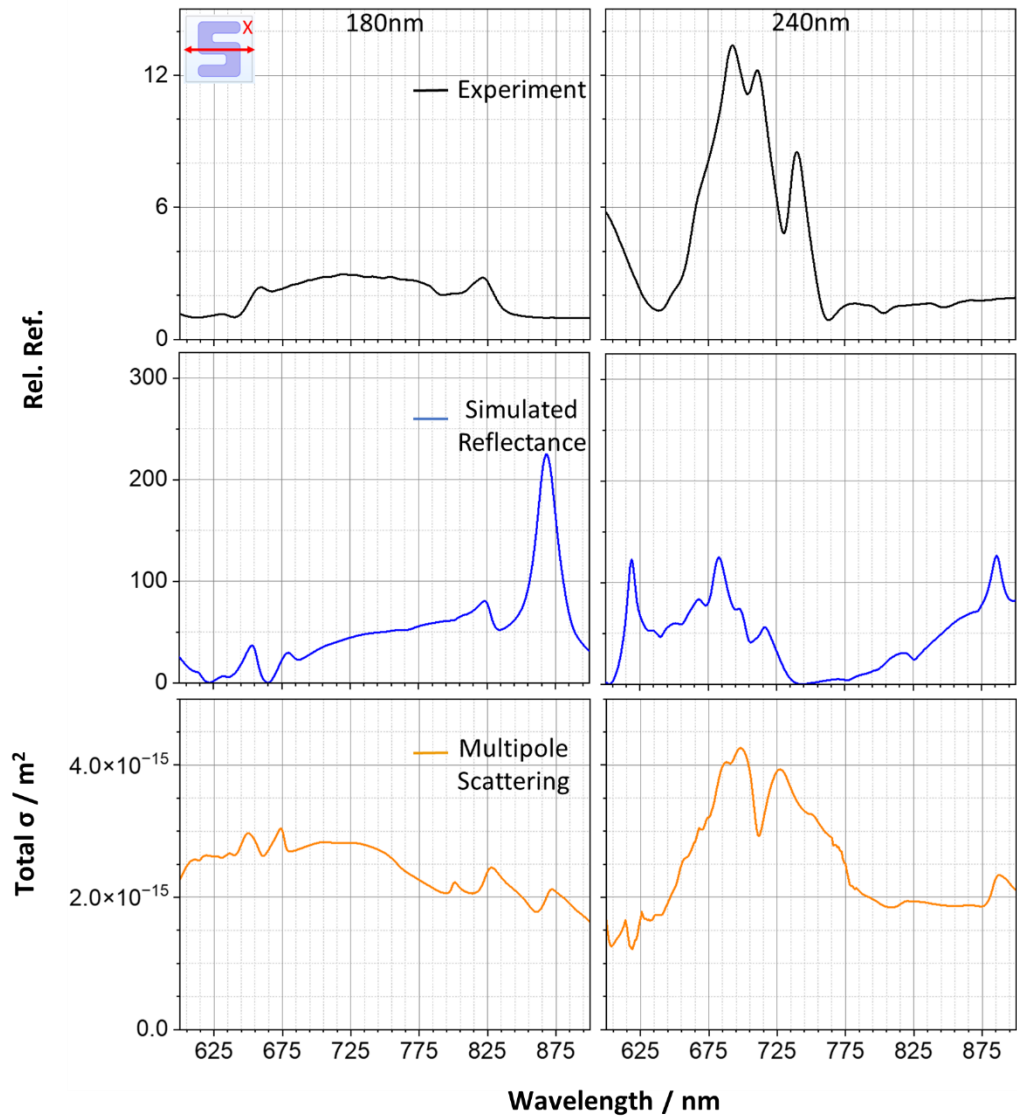


Figure 5.19: A comparison of the RH experimental reflectance (black), simulated reflectance (blue) and the total multipole scattering cross section (orange) for the 180 nm (left column) and 240 nm (right column) structures when illuminated with x-polarised incident light.

The full multipole decompositions for these spectra are shown in **figures 5.20** and **5.21**. In the case of the 180 nm structure, the primary contributions to the overall reflectance appear to arise from the magnetic dipole and quadrupole contributions. The electric dipole resonance shows little intensity across the entire range, whilst the electric quadrupolar contribution shows an intensity maximum that corresponds with that of the magnetic dipole, as was seen before, indicating the presence of circulating currents.

With the increase in silicon height, the total multipole scattering changes shape and increases in intensity around 700 nm, as is seen with the experimental reflectance. Like the previous polarised illumination, the increased sample thickness is accompanied by a significant increase in the magnetic quadrupolar contribution. At the 240 nm height, the magnetic quadrupole is by far the predominant contributor to the total scattering. Again, this behaviour supports the assertion that the magnetic quadrupole is better supported with increased sample thickness.³⁴

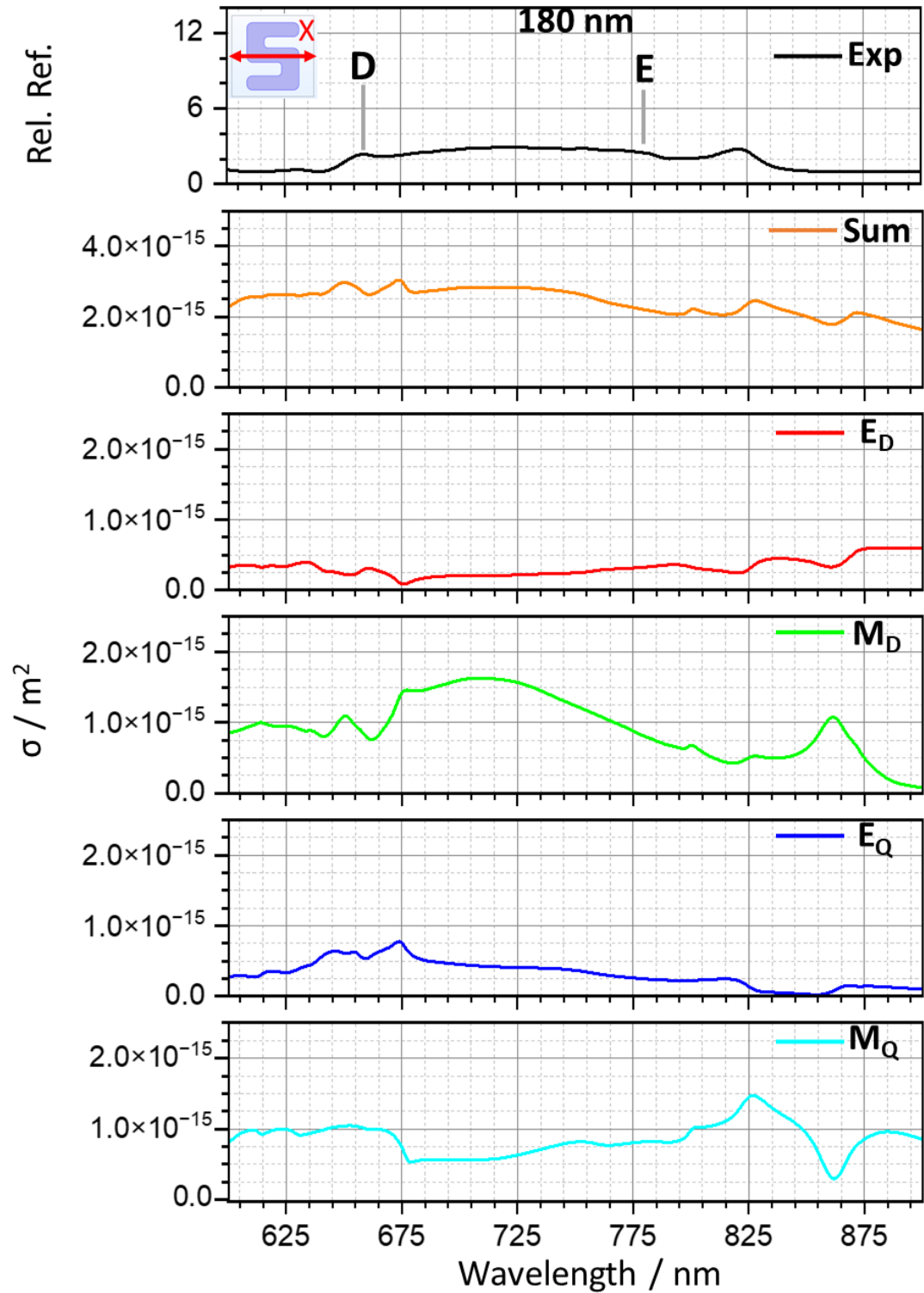


Figure 5.20: A comparison between experimental reflectance (black) and the simulated sum of the scattering cross section (orange) for the 180 nm structure under x-polarised illumination. The components include the E_D (red), M_D (green), E_Q (blue) and M_Q (cyan) contributions.

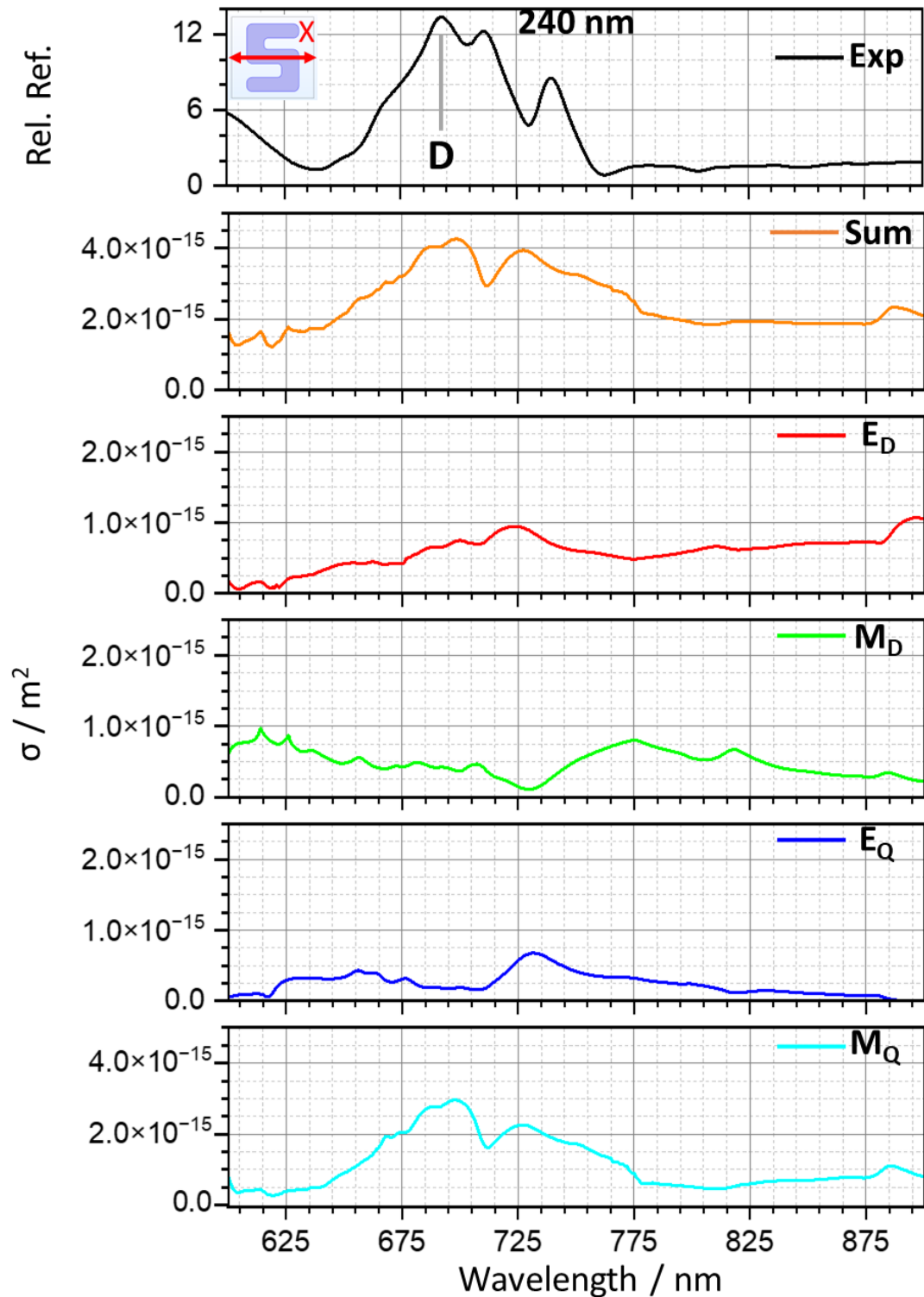


Figure 5.21: A comparison experimental reflectance (black) and the simulated sum of the scattering cross section (orange) for the 240 nm structure under x-polarised illumination. The components include the E_D (red), M_D (green), E_Q (blue) and M_Q (cyan) contributions. Note that the M_Q scale is double that of the other contributions.

Field plots were generated for the E_z and H_z of peak D, shown in **figure 5.22**. The field distributions for the 180 nm structure show a less distinct arrangement than in the y-polarised case, particularly for H_z . It is apparent that there are limitations

in using field analysis alone for the assignment of spectral character, highlighting the advantages of performing multipolar decompositions.

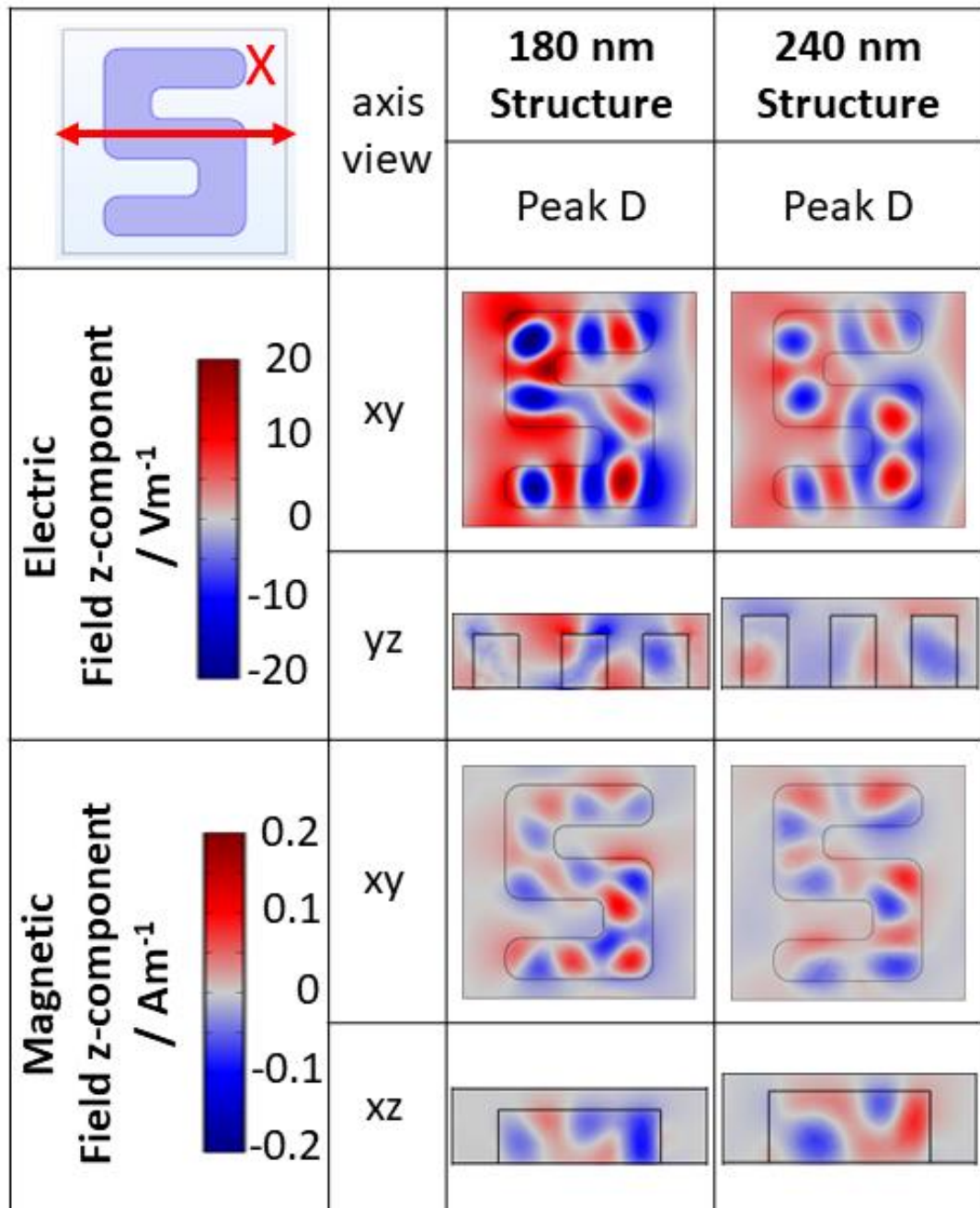


Figure 5.22: E_z and H_z distributions for select peaks under x-polarisation, viewed from different planes. x-y plane images are taken from the midpoint of the structures, whilst orthogonal planes dissect the centre of the unit cell.

As before, field arrow plots were obtained for the 180 nm sample, displayed in figure 5.23. For peak D, the circulating behaviour of the electric field is again observed around the regions at which $|\mathbf{H}|$ is most intense. This is less exaggerated for the material current density. Peak E does not show as great a presence of field arrows and material current densities due to the reduced intensity of this resonance. It is worth highlighting that the simulated reflectance resonance for peak D is exaggerated in relative intensity with respect to experiment, indicating that the intensities of both field and arrow plots will also be exaggerated.

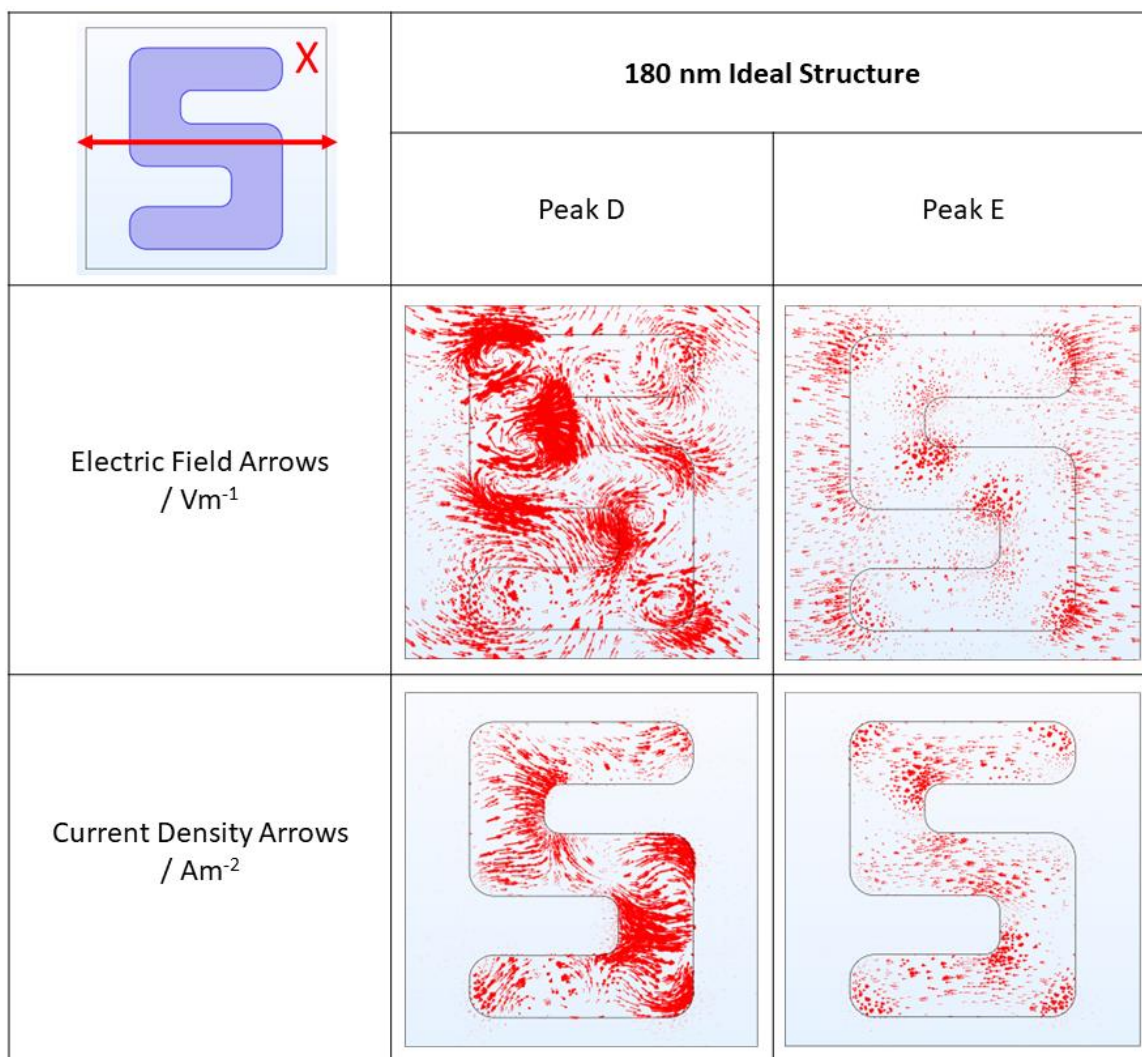


Figure 5.23: Electric field and current density arrow plots for peaks D and E of the 180 nm sample under x-polarised illumination.

5.3.4 Reflectance Summary

The silicon nanoarrays were observed to undergo gradual changes to their reflectance behaviour as the sample height was increased between 160 and 210 nm. At 240 nm the spectra changed more drastically, losing the characteristic double peak. This behaviour was rationalised using numerical simulations and a technique known as multipole decomposition. It was found that the double peak possessed magnetic dipole character, supported by an electric quadrupolar resonance. The redshift between 160 and 210 nm is characteristic of Mie scattering, where the scatterer diameter is proportional to the resonance wavelength. The sudden change in reflectance shape at 240 nm was found to occur from the generation of a magnetic quadrupolar resonance, which could only be supported at this silicon height given that the magnetic resonances exist across the z-axis of the structures, parallel to the incident light. Examination of field distributions supported these conclusions.

5.4. Results and Discussion - Optical Rotation

5.4.1 Measured ORD

In addition to the reflectance behaviour being studied, the ORD properties of the samples were also investigated. It was previously shown that the arrays of a given sample thickness yield similar reflectance spectra, the associated ORD spectra are shown in **figure 5.24**. As expected for enantiomorphic structures, they produce approximately equal and opposite ORD plots. The RA and RS arrays both differ, showing a lack of ORD signal which can be attributed to a net cancellation of LH and RH contributions. Under y- polarisation, there is a consistent ORD resonance that occurs at the lower wavelength shoulder of peak A. There is a resonance that occurs at the same wavelength for the x-polarised data, which takes a bisignate form. In both cases, the ORD resonance red shifts with the reflectance, for the 160-210 nm samples. As before, there is a significant change in signal for the 240 nm sample, which becomes very complex, with the presence of multiple smaller peaks between 600-800 nm, and a larger peak above 800 nm.

A significant feature of these spectra are the changes in shape and sign that occur between the two incident polarisations, highlighting the birefringent nature of the structures. Inequivalent axes of the structure produce differing resonances within the material when the incident polarisation changes. Such a change in the ORD spectra would not be expected of a truly chiral response, which should be both invariant under proper rotations and reciprocal.²⁵ To further probe this, the ORD of a 210 nm sample was measured with forwards and backwards illumination, shown in **figure 5.25**.

The reflectance and ORD data under forwards illumination is generally consistent with that of the previous 210 nm sample, with only small changes in line shape and intensities. When the sample is flipped to backwards illumination, the reflectance data shows a similar shape to the forwards illumination, for both x- and y-polarisations. The ORD, whilst showing similarities in shape and resonance position, shows a noticeable change in sign of the optical rotation. The non-reciprocity of the sample is therefore confirmed, indicating that the source of the optical rotation is not dominated by optical activity^{25,26,36}, but rather the birefringent nature of the samples.

The optical rotation associated with peak A occurs in the regions in which the M_D and E_Q multipole contributions are located, previously shown in **figure 5.15** and **5.16**. As this resonance can be shifted with the height of the silicon structures, these samples provide a degree of control over the optical rotatory properties of the sample, given that natural optical activity can stem from E_D - E_Q cross terms in anisotropic chiral.^{13,37,38}

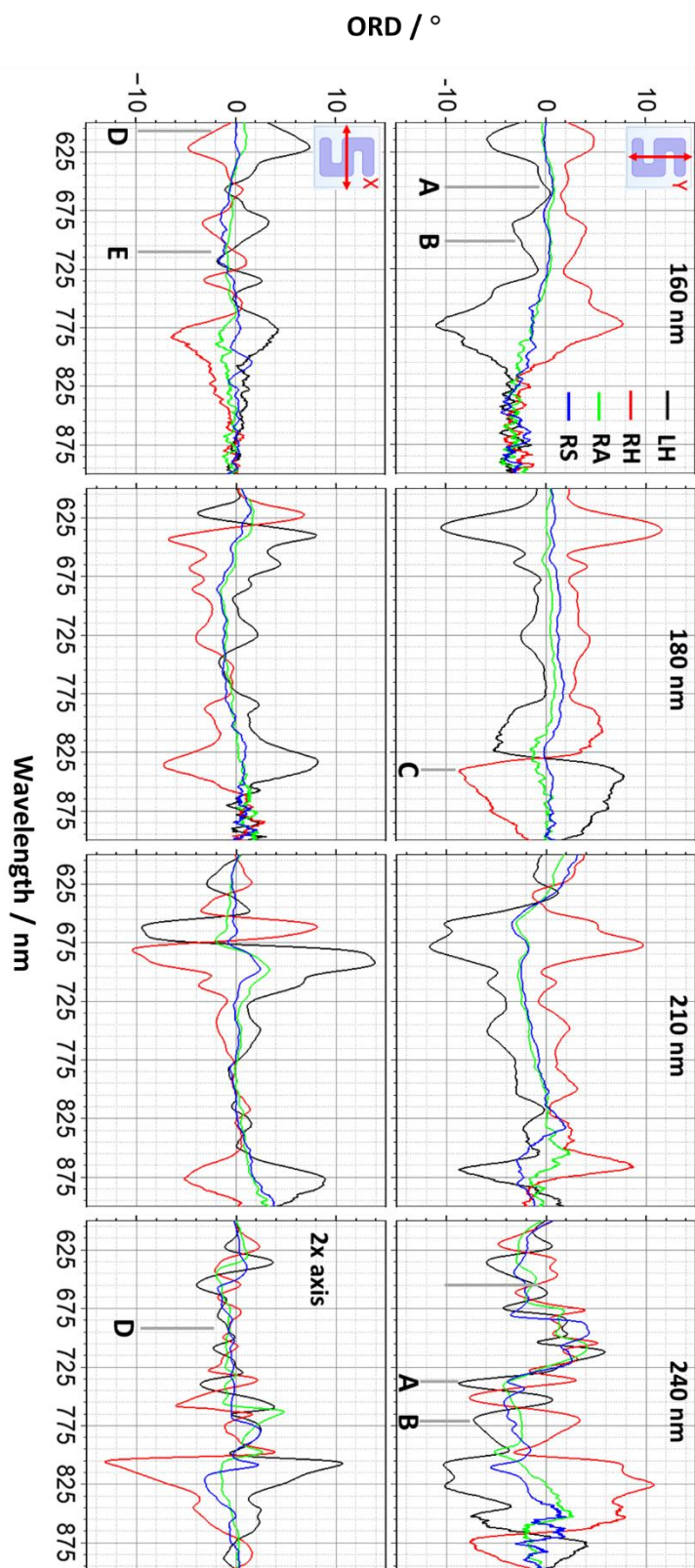


Figure 5.24: Experimental ORD under y- (top row) and x-polarisation (bottom row) for LH (black), RH (red), RA (green) and RS (blue) arrays for each sample thickness. Positions of experimental reflectance peaks A-E of figure 5.8 are labelled. Note that the x-polarised 240 nm ORD is on an increased scale.

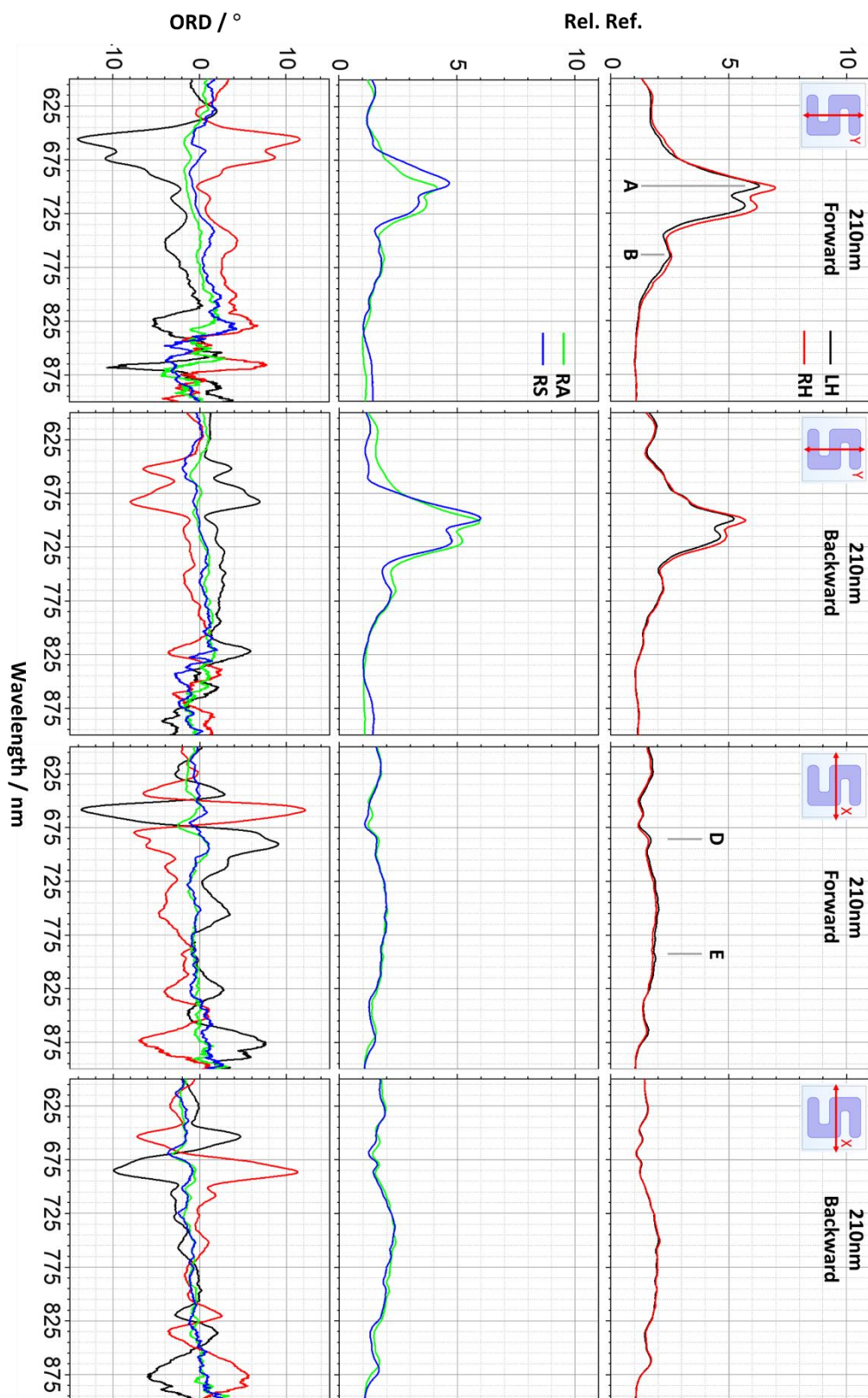


Figure 5.25: Reflectance and ORD measurements for each array of a 210 nm sample, for forwards and backwards x- and y-polarised illumination, with peaks labelled.

5.4.2 Simulated ORD

Numerical simulations of the sample CD were performed, which could be Kramers-Kronig (KK) transformed³⁹ to provide a comparison with experimental ORD data. The CD and KK transformed spectra are shown in **figure 5.26**.

Notably, the CD spectra show the greatest intensities at wavelengths below reflectance peak A for the 160-210 nm samples, whilst at 240 nm the largest peaks occur over a wider range from 675-825 nm. Although the simulated CD and corresponding KK transformed spectra show equal and opposite behaviour for LH/RH arrays and no significant signal for the RS array, it is clear that there is a discrepancy between the experimentally measured ORD and those obtained from the simulations (KK CD). This is due to the inherent difference in the two forms of measurement. Whilst the simulation measures the CD of the sample, the ORD measurements taken experimentally are shown to include non-chiroptical contributions from the birefringence, given that the ORD data is not reciprocal. Typical lab-based stokes polarimeters, such as the one used here, are incapable of decoupling chiroptical and birefringent (linear) effects. Linear optical properties, like linear birefringence or linear dichroism, can alter the polarisation state of the incident light, thus masking the true chiroptical ORD signal.^{26,40} In order to fully characterise the optical properties of a sample, a technique known as Mueller Matrix Polarimetry⁴¹ is required, which is performed in the following chapter.

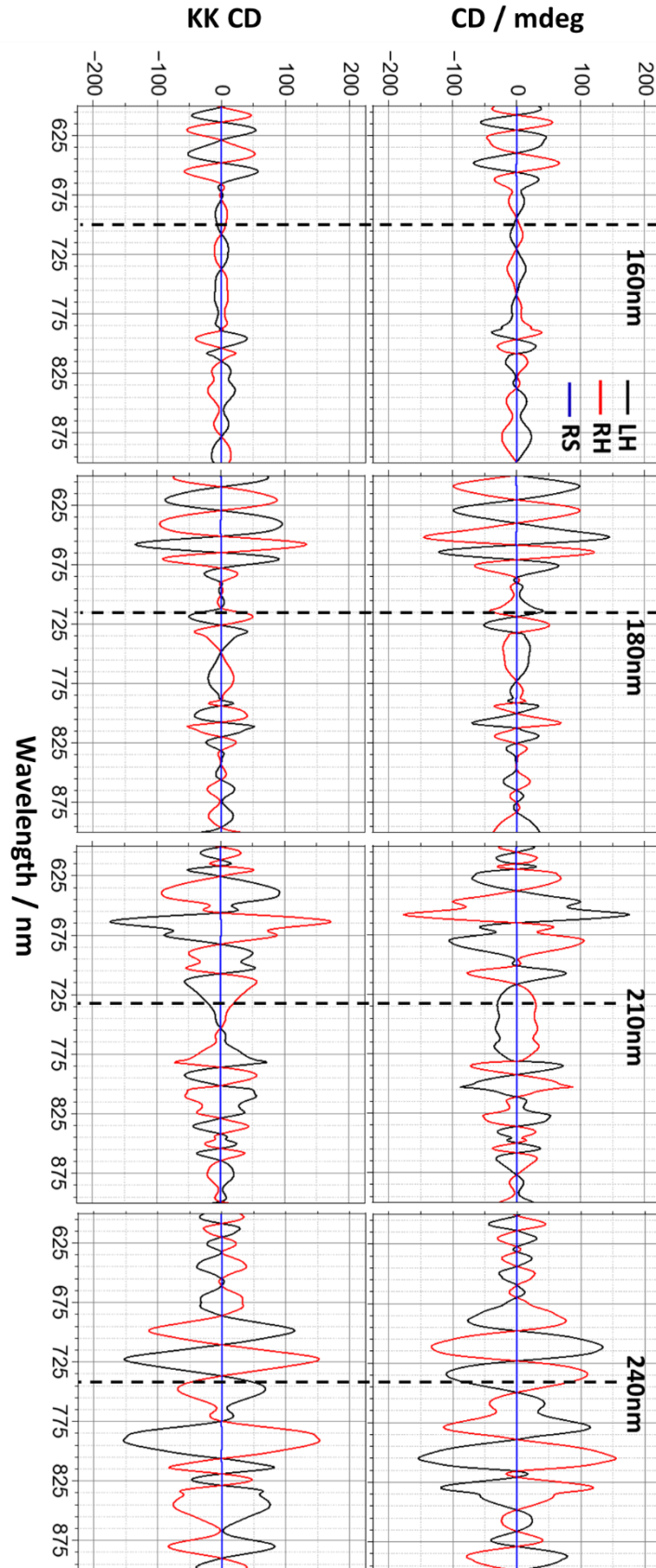


Figure 5.26: Simulated CD (top) and corresponding KK transformed CD (bottom) spectra of LH, RH and RS arrays for the four sample heights. Dashed lines correspond to Peak A of the simulated reflectance from figure 5.9.

5.4.3 Optical Chirality Density

To determine the potential for these structures to act as a chiral sensing platform, the chiral asymmetry of the near fields of the structures was analysed by calculating the volume averaged optical chirality density of the structure and surrounding volume, shown in **figure 5.27**. The spectra were obtained for LPL and normalised against RCP. As expected of enantiomorphic structures, the optical chirality values are equal and opposite, and the RS values are 0 due to the net contributions of the constituent structures. Whilst the ORD measurements were dominated by birefringent effects, the structures still exhibit chiroptical responses as evidenced by the volume averaged optical chirality density (and simulated CD measurements). Optical activity in isotropic chiral media stems from the interference between E_D and M_D cross terms.^{13,42} In anisotropic media, E_D and E_Q contributions can make significant contributions towards optical activity, particularly with metamaterials which can possess large field gradients which enhance their influence.^{37,38,43} This could explain the larger and more numerous peaks observed for y-polarised illumination, which generally possess stronger E_D , M_D and E_Q resonances than the x-polarised case.

To give an indication of the local distribution of the chiral fields, optical chirality density maps corresponding to peak A in the volume averaged optical chirality density (**figure 5.27** dashed lines) are shown in **figure 5.28**. The equal and opposite behaviour between enantiomorphs is again observed from the field distributions. The strongest regions of the chiral fields are highly localised within the structures, corresponding to the most intense EM fields shown previously. There are, however, relatively strong chiral fields that exist near the surface of the structures and between adjacent arms, particularly in the y-polarised case, which could potentially be exploited for chiral sensing. Optical chirality values exceeding values of 1 indicate chiral asymmetries greater than CPL, a property that is sometimes termed superchirality. The ability to manipulate the positions of the individual multipole contributions, simply by changing the height of the structures, indicates that the chiral response of the arrays can be controlled.

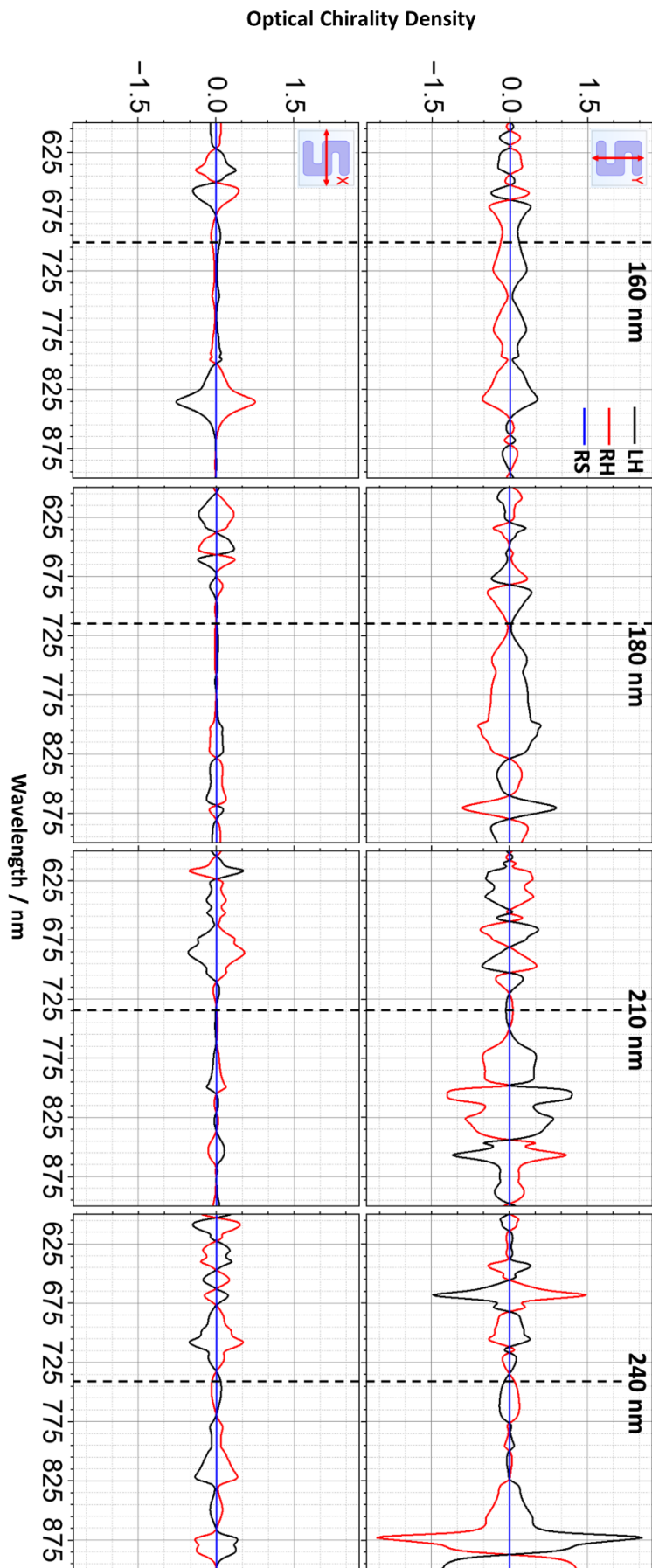


Figure 5.27: Volume averaged optical chirality density values for y- (top) and x-polarised (bottom) illumination of LH, RH and RS arrays for each sample thickness. Dashed lines correspond to peak A of simulated reflectance. Plots are normalised against RCP.

5.5 Conclusions

In this chapter the incident light polarisation and height dependent behaviour of the reflectance and ORD properties for enantiomorphic silicon nanostructured arrays, as well as the effects of racemic mixtures of the two, was investigated. Inequivalent spectra under orthogonal light polarisations indicate that the samples are strongly birefringent.

There were significant changes in the spectra observed as the height of the silicon structures increased from 160- 240 nm. This behaviour was determined to arise from two sources. First, it was shown that there is a progressive red shifting of the spectral resonances as sample height increases. This is the case for both x- and y-polarised excitation and agrees with Mie theory, which predicts an increase of resonance wavelength with increasing scatterer diameter. The resonances identified within the structures were consistent with other silicon nanoparticles, where a z-axis supported magnetic resonance is accompanied by circulating electric currents.

The second source of the changing behaviour was identified using the technique of multipole decomposition in numerical simulations. It was found that the 160-210 nm samples were dominated by a magnetic dipole and electric quadrupolar character, giving them a characteristic reflectance peak. At 240 nm, the sample underwent significant changes, attributed to a large increase in the presence of magnetic quadrupolar resonances. This was further justified by the increased sample height being able to better support magnetic modes³⁴, as they exist in the z-axis parallel to the incident light propagation. This suggests that the shallower samples do not have the space to establish this resonance. This occurs for both light polarisations, and findings were supported by field map analysis.

Further differences in the spectra, related to the RS racemic array were confirmed to arise from a periodic effect. Preferential alignment of the constituent nanostructures in the RS array, permits strong coupling between adjacent structures, which could not be supported by the enantiomorphic or RA racemic arrays. This behaviour was not observed for the x-polarised excitation, due to the greater distance between adjacent structures in this axis.

The LH and RH arrays were shown to produce equal and opposite ORD spectra for LH and RH arrays, which contributed to a net cancelation in optical rotation for both racemic arrays. The ORD spectra were observed to change under incident polarisation (equivalent to a 90° sample rotation) and a reversal in illumination direction. Such optical rotatory behaviour is inconsistent with natural optical activity and was therefore determined to be dominated by the sample's birefringence. As such, experimental ORD data was not replicated by numerical simulation, a result of the inherent differences in the measurement processes. Traditional lab-based Stokes polarimeters are often incapable of distinguishing between chiroptical and linear optical properties. The CD (and KK transformed) data measured via numerical simulation with CPL, was therefore inequivalent to the experimental ORD obtained with LPL.

The ability of the structures to support multiple resonances that can be tuned with respect to their height present a flexible means of developing potential devices. The strong optical rotational properties of the samples could find applications in optics as nano-waveplates, which can be manufactured to operate

at specific wavelength ranges. The structures were also shown to produce fields with enhanced chiral asymmetry, resonances which are also tuneable. Field distributions existing outside of the structures indicate their potential for enantiomeric sensing, which will be explored in a later chapter. There remains a question as to the source of the observed ORD spectra as it is not consistent with truly chiral behaviour, which will now be investigated through the more robust technique of Mueller matrix polarimetry.

5.6 References

1. Zograf, G. & Makarov, S. 3 - Dielectric materials. in *Nanophotonics* (eds. Shalin, A. S., Valero, A. C. & Miroshnichenko, A. B. T.-A.-D. N.) 49-69 (Elsevier, 2024). doi:<https://doi.org/10.1016/B978-0-32-395195-1.00008-9>.
2. Baranov, D. G. *et al.* All-dielectric nanophotonics: the quest for better materials and fabrication techniques. *Optica* **4**, 814-825 (2017).
3. Diao, J. *et al.* Analogue of Electromagnetically Induced Transparency in an S-Shaped All-Dielectric Metasurface. *IEEE Photonics J.* **11**, 1-10 (2019).
4. Mie, G. Beiträge zur Optik trüber Medien, speziell kolloidaler Metallösungen. *Ann. Phys.* **330**, 377-445 (1908).
5. De Marco, M. L. *et al.* Silicon-Based Dielectric Metamaterials: Focus on the Current Synthetic Challenges. *Angew. Chemie Int. Ed.* **57**, 4478-4498 (2018).
6. Liu, Q., Gross, S., Dekker, P., Withford, M. J. & Steel, M. J. Competition of Faraday rotation and birefringence in femtosecond laser direct written waveguides in magneto-optical glass. *Opt. Express* **22**, 28037-28051 (2014).
7. Reintjes, J. F. Nonlinear Optical Processes. in (ed. Meyers, R. A. B. T.-E. of P. S. and T. (Third E.)) 537-581 (Academic Press, 2003). doi:<https://doi.org/10.1016/B0-12-227410-5/00485-3>.
8. Ivchenko, E. L. B. T.-R. M. in M. S. and M. E. Optical properties of dielectrics and semiconductors. in (Elsevier, 2022). doi:<https://doi.org/10.1016/B978-0-323-90800-9.00009-3>.
9. Murai, S., Fujita, K. & Tanaka, K. Chapter 5.2 - New Glasses for Photonics. in (ed. Somiya, S. B. T.-H. of A. C. (Second E.)) 383-401 (Academic Press, 2013). doi:<https://doi.org/10.1016/B978-0-12-385469-8.00022-8>.
10. Kuznetsov, A. I., Miroshnichenko, A. E., Fu, Y. H., Zhang, J. & Luk'yanchuk, B. Magnetic light. *Sci. Rep.* **2**, 492 (2012).
11. Evlyukhin, A. B. *et al.* Demonstration of Magnetic Dipole Resonances of Dielectric Nanospheres in the Visible Region. *Nano Lett.* **12**, 3749-3755 (2012).
12. Bakker, R. M. *et al.* Magnetic and Electric Hotspots with Silicon Nanodimers. *Nano Lett.* **15**, 2137-2142 (2015).
13. Barron, L. D. *Molecular Light Scattering and Optical Activity*. (Cambridge University Press, 2004). doi:10.1017/CBO9780511535468.
14. Jahani, S. & Jacob, Z. All-dielectric metamaterials. *Nat. Nanotechnol.* **11**, 23-36 (2016).
15. García-Guirado, J., Svedendahl, M., Puigdollers, J. & Quidant, R. Enhanced Chiral Sensing with Dielectric Nanoresonators. *Nano Lett.* **20**, 585-591 (2020).
16. Huang, X., Lai, Y., Hang, Z. H., Zheng, H. & Chan, C. T. Dirac cones induced by accidental degeneracy in photonic crystals and zero-refractive-index materials. *Nat. Mater.* **10**, 582-586 (2011).
17. Moitra, P. *et al.* Realization of an all-dielectric zero-index optical metamaterial. *Nat. Photonics* **7**, 791-795 (2013).
18. Liu, S. *et al.* Optical magnetic mirrors without metals. *Optica* **1**, 250-256 (2014).
19. Kim, S. J., Fan, P., Kang, J.-H. & Brongersma, M. L. Creating semiconductor metafilms with designer absorption spectra. *Nat. Commun.* **6**, 7591 (2015).
20. Murphy, D. B., Spring, K. R., Fellers, T. J. & Davidson, M. J. Principles of Birefringence. *Olympus Microscopy Resource Centre* <https://www.microscopyu.com/techniques/polarized-light/principles-of-birefringence> (2023).

21. Bartholin, R. *Experimenta Crystalli Islandici disdiaclastici, quibus mira et insolita refractio detegitur*. (1669).
22. Slezák, O. *et al.* Thermal-stress-induced birefringence management of complex laser systems by means of polarimetry. *Sci. Rep.* **12**, 18334 (2022).
23. Mihailovic, P. & Petricevic, S. Fiber Optic Sensors Based on the Faraday Effect. *Sensors (Basel)*. **21**, (2021).
24. Barron, L. D. True and false chirality and parity violation. *Chem. Phys. Lett.* **123**, 423-427 (1986).
25. Barron, L. D. True and false chirality and absolute enantioselection. *Rend. Lincei* **24**, 179-189 (2013).
26. Arteaga, O. *et al.* Relation between 2D/3D chirality and the appearance of chiroptical effects in real nanostructures. *Opt. Express* **24**, 2242-2252 (2016).
27. Gilroy, C., Koyroytsaltis-McQuire, D. J. P., Gadegaard, N., Karimullah, A. S. & Kadodwala, M. Superchiral hot-spots in “real” chiral plasmonic structures. *Mater. Adv.* **3**, 346-354 (2022).
28. Lu, Y.-W., Li, L.-Y. & Liu, J.-F. Influence of Surface Roughness on Strong Light-Matter Interaction of a Quantum Emitter-Metallic Nanoparticle System. *Sci. Rep.* **8**, 7115 (2018).
29. Castellanos, G. W., Bai, P. & Gómez Rivas, J. Lattice resonances in dielectric metasurfaces. *J. Appl. Phys.* **125**, 213105 (2019).
30. Jackson, J. D. *Classical electrodynamics*. (1999).
31. Evlyukhin, A. B., Fischer, T., Reinhardt, C. & Chichkov, B. N. Optical theorem and multipole scattering of light by arbitrarily shaped nanoparticles. *Phys. Rev. B* **94**, 205434 (2016).
32. Evlyukhin, A. B., Reinhardt, C. & Chichkov, B. N. Multipole light scattering by nonspherical nanoparticles in the discrete dipole approximation. *Phys. Rev. B* **84**, 235429 (2011).
33. Evlyukhin, A. B., Reinhardt, C., Evlyukhin, E. & Chichkov, B. N. Multipole analysis of light scattering by arbitrary-shaped nanoparticles on a plane surface. *J. Opt. Soc. Am. B* **30**, 2589-2598 (2013).
34. Liu, C. *et al.* Characteristics of electric quadrupole and magnetic quadrupole coupling in a symmetric silicon structure. *New J. Phys.* **22**, 23018 (2020).
35. Evlyukhin, A. B. & Chichkov, B. N. Multipole decompositions for directional light scattering. *Phys. Rev. B* **100**, 125415 (2019).
36. Collins, J. T. *et al.* Chirality and Chiroptical Effects in Metal Nanostructures: Fundamentals and Current Trends. *Adv. Opt. Mater.* **5**, (2017).
37. Theron, I. P. & Cloete, J. H. The electric quadrupole contribution to the circular birefringence of nonmagnetic anisotropic chiral media: a circular waveguide experiment. *IEEE Trans. Microw. Theory Tech.* **44**, 1451-1459 (1996).
38. Tullius, R. *et al.* “Superchiral” Spectroscopy: Detection of Protein Higher Order Hierarchical Structure with Chiral Plasmonic Nanostructures. *J. Am. Chem. Soc.* **137**, 8380-8383 (2015).
39. Krueger, W. C. & Pschigoda, L. M. Circular dichromer calibration by Kramers-Kronig transform methods. *Anal. Chem.* **43**, 675-677 (1971).
40. Arteaga, O., Maoz, B. M., Nichols, S., Markovich, G. & Kahr, B. Complete polarimetry on the asymmetric transmission through subwavelength hole arrays. *Opt. Express* **22**, 13719-13732 (2014).
41. Arteaga, O. & Kahr, B. Mueller matrix polarimetry of bianisotropic materials [Invited]. *J. Opt. Soc. Am. B* **36**, F72-F83 (2019).

42. Hendry, E., Mikhaylovskiy, R. V, Barron, L. D., Kadodwala, M. & Davis, T. J. Chiral Electromagnetic Fields Generated by Arrays of Nanoslits. *Nano Lett.* **12**, 3640-3644 (2012).
43. Efrima, S. Raman optical activity of molecules adsorbed on metal surfaces: Theory. *J. Chem. Phys.* **83**, 1356-1362 (1985).

Chapter 6: Mueller Matrix Polarimetry of S-shaped Silicon Metamaterials

The silicon samples introduced in the previous chapter were shown to produce strong ORD signals which were non-reciprocal, indicating that they are, at least in part, from a non-chiral source. This chapter seeks to identify this source, using the technique of Mueller matrix polarimetry (MMP). Full MMP can provide a complete description of a sample's optical properties, and importantly, decouple the chiroptical and non-chiroptical effects of the samples. The symmetry of the matrices and resultant optical properties of the silicon arrays are also discussed.

The Stokes polarimeter used previously to obtain ORD measurements lacks the necessary components to generate or measure the light polarisation states required for full characterisation. This can present a problem when analysing the chiroptical properties of a material, as optical rotation from non-chiral sources contributes to the overall ORD measured. This identifies an important aspect that must be considered when characterising materials, especially those that are designed to be chiral. When examining structures that possess a degree of anisotropy one must be careful when assigning an ORD as chiral, which has at times been done erroneously throughout the literature. As is revealed in the following chapter, LB can provide a significant contribution to observed optical rotations. The numerical simulations presented in the previous chapter did not agree with the ORD measurements taken via Stokes polarimetry but are found to agree with MMP measurements. This confirms that a significant portion of the ORD stems from linear optical effects. Arteaga has performed full MMP with plasmonic gammadions, highlighting the significance in the difference between their C_4 symmetry and the C_1 symmetry of the silicon S-structures.

6.1 Introduction to Stokes and Mueller Matrix Polarimetry

The polarisation state of light can be described entirely by what are known as the four Stokes Parameters¹:

$$S_0 = \mathbf{E}_{0x}^2 + \mathbf{E}_{0y}^2 \quad [6.1]$$

$$S_1 = \mathbf{E}_{0x}^2 - \mathbf{E}_{0y}^2 \quad [6.2]$$

$$S_2 = 2\mathbf{E}_{0x}\mathbf{E}_{0y} \cos \delta \quad [6.3]$$

$$S_3 = 2\mathbf{E}_{0x}\mathbf{E}_{0y} \sin \delta. \quad [6.4]$$

Where the total intensity of the light, S_0 , is a sum of the other components:

$$S_0^2 = S_1^2 + S_2^2 + S_3^2. \quad [6.5]$$

δ is the phase difference $\delta_y - \delta_x$ and $\mathbf{E}_{0x,y}$ are the x- and y- electric field amplitudes of the total electric field \mathbf{E} :

$$\mathbf{E} = \mathbf{E}_0 e^{(ikz - i\omega t)}. \quad [6.6]$$

S_1 is the prevalence of x-polarised light over y-polarised light, S_2 gives the prevalence of +45° polarised light over -45° polarised light and S_3 describes the prevalence of RCP light over LCP light. Stokes parameters are often presented in the form of Stokes vectors:

$$\mathbf{S} = \begin{bmatrix} S_0 \\ S_1 \\ S_2 \\ S_3 \end{bmatrix} = \begin{bmatrix} \mathbf{E}_{0x}^2 + \mathbf{E}_{0y}^2 \\ \mathbf{E}_{0x}^2 - \mathbf{E}_{0y}^2 \\ 2\mathbf{E}_{0x}\mathbf{E}_{0y} \cos \delta \\ 2\mathbf{E}_{0x}\mathbf{E}_{0y} \sin \delta \end{bmatrix}. \quad [6.7]$$

The polarisation states of light can all be described by a Stokes vector, with incident intensity I_0 . For example:

$$\begin{array}{ll} \text{x-polarised light:} & I_0 \begin{bmatrix} 1 \\ 1 \\ 0 \\ 0 \end{bmatrix} & \text{y polarised light:} & I_0 \begin{bmatrix} 1 \\ -1 \\ 0 \\ 0 \end{bmatrix} \\ \\ \text{+45° polarised light:} & I_0 \begin{bmatrix} 1 \\ 0 \\ 1 \\ 0 \end{bmatrix} & \text{-45° polarised light:} & I_0 \begin{bmatrix} 1 \\ 0 \\ -1 \\ 0 \end{bmatrix} \\ \\ \text{RCP light:} & I_0 \begin{bmatrix} 1 \\ 0 \\ 0 \\ 1 \end{bmatrix} & \text{LCP light:} & I_0 \begin{bmatrix} 1 \\ 0 \\ 0 \\ -1 \end{bmatrix} \end{array}$$

A Stokes polarimeter is a device which allows for the determination of an incident light beam's polarisation state.² Stokes polarimeter systems can vary significantly by the individual components used as polarisation state generators and analysers, such as waveplates and retarders. Whilst individual optical properties can be calculated from the collection of the required Stokes vectors, optical set-ups generally lack all the required components to produce and measure each of the possible polarisation states of light. In order to provide a full description of a sample's interaction with incident light, MMP is required.

If the polarisation states (Stokes vectors) of light are known before and after its interaction with a sample or optical component, then a matrix responsible for the transformation between the states must exist. Such a transformation is represented by a Mueller Matrix, which is a 4 x 4 element matrix that fully describes a material's optical behaviour. The relationship between the input and output vectors can be described by:

$$\begin{bmatrix} S_0 \\ S_1 \\ S_2 \\ S_3 \end{bmatrix}_{\text{Output}} = \begin{bmatrix} M_{00} & M_{01} & M_{02} & M_{03} \\ M_{10} & M_{11} & M_{12} & M_{13} \\ M_{20} & M_{21} & M_{22} & M_{23} \\ M_{30} & M_{31} & M_{32} & M_{33} \end{bmatrix} \begin{bmatrix} S_0 \\ S_1 \\ S_2 \\ S_3 \end{bmatrix}_{\text{Input}}. \quad [6.8]$$

This representation aids in the interpretation of the Mueller matrix transformation. Some output polarisation is achieved by performing matrix multiplication between an optical component and the incident light (input Stokes vector). For example, the Mueller Matrix transformation for $+45^\circ$ LPL being converted to RCP light, would take the form:

$$\begin{bmatrix} 1 \\ 0 \\ 0 \\ -1 \end{bmatrix}_{\text{Output}} = \begin{bmatrix} 1 & 0 & 0 & 0 \\ 0 & 1 & 0 & 0 \\ 0 & 0 & 0 & 1 \\ 0 & 0 & -1 & 0 \end{bmatrix} \begin{bmatrix} 1 \\ 0 \\ 1 \\ 0 \end{bmatrix}_{\text{Input}} \quad [6.9]$$

This Mueller matrix therefore represents a quarter wave plate (with a vertical fast axis). Knowing the output Stokes vectors from multiple input Stokes vectors can therefore complete a Mueller matrix for an unknown material, revealing the ways in which the sample interacts with incident light. Each matrix element can be attributed to a characteristic property³:

$$\begin{bmatrix} T & -LD & -LD' & CD \\ -LD & T_L & CB & -LB' \\ -LD' & -CB & T_{L'} & LB \\ CD & LB' & -LB & T_C \end{bmatrix} \quad [M1]$$

Where T is transmission of unpolarised light and T_L , $T_{L'}$ and T_C represent the transmission for linear, linear $\pm 45^\circ$ polarised and circularly polarised incident light, respectively. For a depolarizing matrix, the values on the matrix diagonal will be less than 1, in which case the medium causes the incident light to reduce the degree to which it is polarised. Linear dichroism (LD), LB, CD and CB make up the remaining properties. Those with the ' notation relate to light linearly polarised at $\pm 45^\circ$. Again, LD and LB are described as the difference in absorption and refraction of orthogonally polarised light, respectively. Similarly, CD and CB are the difference in absorption and refraction of CPL.

The distribution of the optical effects within the matrix can be better understood by realising that each row of the matrix determines the overall outcome of a different Stokes parameter. Each column relates to a parameter affecting the incident form of light. For instance, the first row contributes to the total intensity S_0 , therefore S_0 is dependent on the dichroisms exhibited by the material. It follows that the prevalence of x-polarised light over y-polarised light, S_1 , is dependent on the LD of the total incident intensity, the transmission of the horizontally/vertically polarised light, the CB of the light linearly polarised at $\pm 45^\circ$ and the $\pm 45^\circ$ LB of CPL.⁴

Materials can be characterised, and their symmetry determined, by the symmetry of the elements in their Mueller matrices.^{5,6} Based on the arrangement of the elements and their values relative to one another, they can be defined as shown:

$$\begin{array}{l} \text{Isotropic - with rotational and mirror} \\ \text{symmetry} \end{array} \quad \begin{bmatrix} M_{00} & 0 & 0 & 0 \\ 0 & M_{11} & 0 & 0 \\ 0 & 0 & M_{22} & 0 \\ 0 & 0 & 0 & M_{33} \end{bmatrix} \quad [M2]$$

$$\begin{array}{l} \text{Biisotropic - with rotational symmetry} \end{array} \quad \begin{bmatrix} M_{00} & 0 & 0 & M_{03} \\ 0 & M_{11} & M_{12} & 0 \\ 0 & -M_{12} & M_{22} & 0 \\ M_{30} & 0 & 0 & M_{33} \end{bmatrix} \quad [M3]$$

$$\begin{array}{l} \text{Anisotropic - with mirror symmetry} \end{array} \quad \begin{bmatrix} M_{00} & M_{01} & M_{02} & M_{03} \\ M_{01} & M_{11} & M_{12} & M_{13} \\ M_{02} & M_{12} & M_{22} & M_{23} \\ -M_{03} & -M_{13} & -M_{23} & M_{33} \end{bmatrix} \quad [M4]$$

$$\begin{array}{l} \text{Bianisotropic - with no symmetry} \end{array} \quad \begin{bmatrix} M_{00} & M_{01} & M_{02} & M_{03} \\ M_{10} & M_{11} & M_{12} & M_{13} \\ M_{20} & M_{21} & M_{22} & M_{23} \\ M_{30} & M_{31} & M_{32} & M_{33} \end{bmatrix} \quad [M5]$$

Isotropic materials behave the same way no matter their orientation with respect to light propagation. Biisotropic materials are similar in that their properties are the same in all directions, however they interact differently with RCP and LCP waves. Anisotropic materials are those that have electromagnetic properties dependent on their orientation. Bianisotropic media are the most complex classification of materials, with directionally dependent magnetoelectric properties.⁷

6.2 Methodology

6.2.1 Experimental Procedure

The experimental data presented in this chapter was obtained at *Diamond Light Source UK* on the *B23 Beamline*. MMP was performed on silicon samples from the previous chapter, which were of 210 nm depth. Samples were sealed within the 3D-printed sample holders, as detailed in the **section 3.1**, at which point water was introduced to the holder cavity. The sample was then placed in the sample chamber of the polarimeter, a background is taken from the quartz substrate, to be subtracted from the measurements taken from the silicon arrays over a range of 500 - 700 nm.

MMP is a powerful method for providing a full analysis of a medium's interaction with different forms of incident light. A Mueller matrix polarimeter requires several different optical components in order to obtain all 16 elements of the Mueller matrix. To generate and measure the different polarisations of light, a combination of photoelastic modulators (PEMs) and polarisers are located on either side of the sample. Photoelastic materials exhibit birefringence when under mechanical stress, which can be controlled by a piezoelectric material. Compression or relaxation of the material dictates the lead or lag between orthogonal components of the light.^{8,9} Dual-PEMs allow for full MMP without reconfiguration of the optical components, **figure 6.1** shows the MMP setup at *Diamond*.¹⁰ The automated set up containing 4 PEMs removes the need for adjustment of optical components that can contribute to errors in measurements. Full MMP has the distinct advantage over standard Stokes polarimetry in its ability to decouple optical properties within the sample.

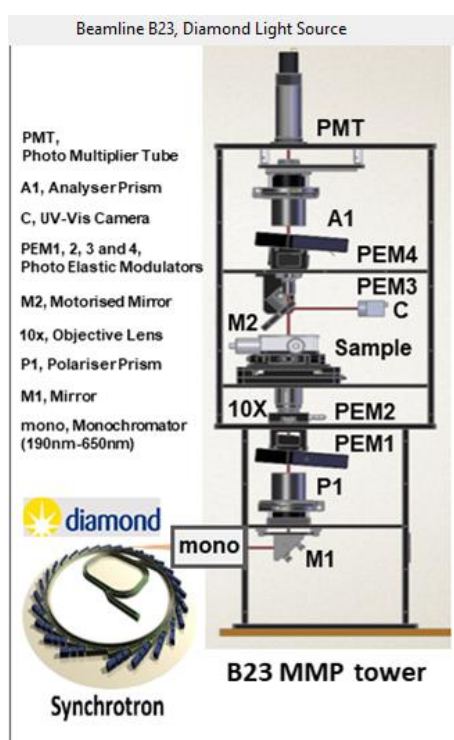


Figure 6.1: The optical components of the Mueller Matrix Polarimeter at *Diamond Light Source UK*, on the B23 beamline. Figure reproduced from ¹⁰.

6.2.2 Simulation Procedure

The simulations in this chapter include CD measurements made on a 210 nm sample, which used the same single and 4-structure models that were presented in chapter 5.

6.3 Results and Discussion

6.3.1 Mueller Matrix Symmetries of Silicon Nanoarrays

The 16 Mueller matrix elements obtained for LH and RH arrays in water are displayed in **figure 6.2**. The LH and RH elements are combined on the same plots to aid comparison, similarities and differences between symmetric elements are highlighted where the conditions of an anisotropic material ([M3]) are used to compare the symmetries of the elements.⁵ Green outlines indicate the element symmetries showing anisotropic character, whilst red indicates disagreement between them. A dashed line is visible on the main diagonal of the matrix to help visualise the symmetry pairs.

The isotropic and biisotropic categories can be ruled out immediately due to all elements of **figure 6.2** being non-zero. The remaining symmetry characterisations can be distinguished from elements on the antidiagonal of the matrix. For an anisotropic material, $M_{30} = -M_{03}$ and $M_{21} = M_{12}$. For the M_{30}/M_{03} pair, the mirrored behaviour is observed for the peak at ~680 nm, however, the intensities of these peaks are not consistent between the elements. Elsewhere, between 600-650 nm, the spectra are a different shape to each other. The peak that spans 550-600 nm for both elements do not display mirrored behaviour and are of the same sign. In the case of the M_{21}/M_{12} pair, the peaks between 650-700 nm share the same sign but differ in intensity and shape. The peaks that occur across ~600 nm and below show mirrored behaviour. Whilst the off-diagonal elements are more consistent with an anisotropic material, the observations from the antidiagonal indicate that the sample is bianisotropic.

A description of bianisotropic media can be obtained from the constitutive relations¹¹:

$$\mathbf{D} = \varepsilon_0 \mathbf{E} + \mathbf{P}_e \quad [6.10]$$

$$\mathbf{B} = \mu_0 \mathbf{H} + \mathbf{P}_m \quad [6.11]$$

Where \mathbf{D} is the displacement field, \mathbf{B} the magnetic flux density, \mathbf{E} the electric field, \mathbf{H} the magnetic field, ε_0 the vacuum electric permittivity and μ_0 the vacuum magnetic permeability. \mathbf{P}_e and \mathbf{P}_m represent the material electric and magnetic polarisation response, respectively, which can be written in terms of the material susceptibilities as^{11,12}:

$$\mathbf{P}_e = \varepsilon_0 \chi_{ee} \cdot \mathbf{E} + \sqrt{\varepsilon_0 \mu_0} \chi_{em} \cdot \mathbf{H} \quad [6.12]$$

$$\mathbf{P}_m = \sqrt{\varepsilon_0 \mu_0} \chi_{me} \cdot \mathbf{E} + \mu_0 \chi_{mm} \cdot \mathbf{H} \quad [6.13]$$

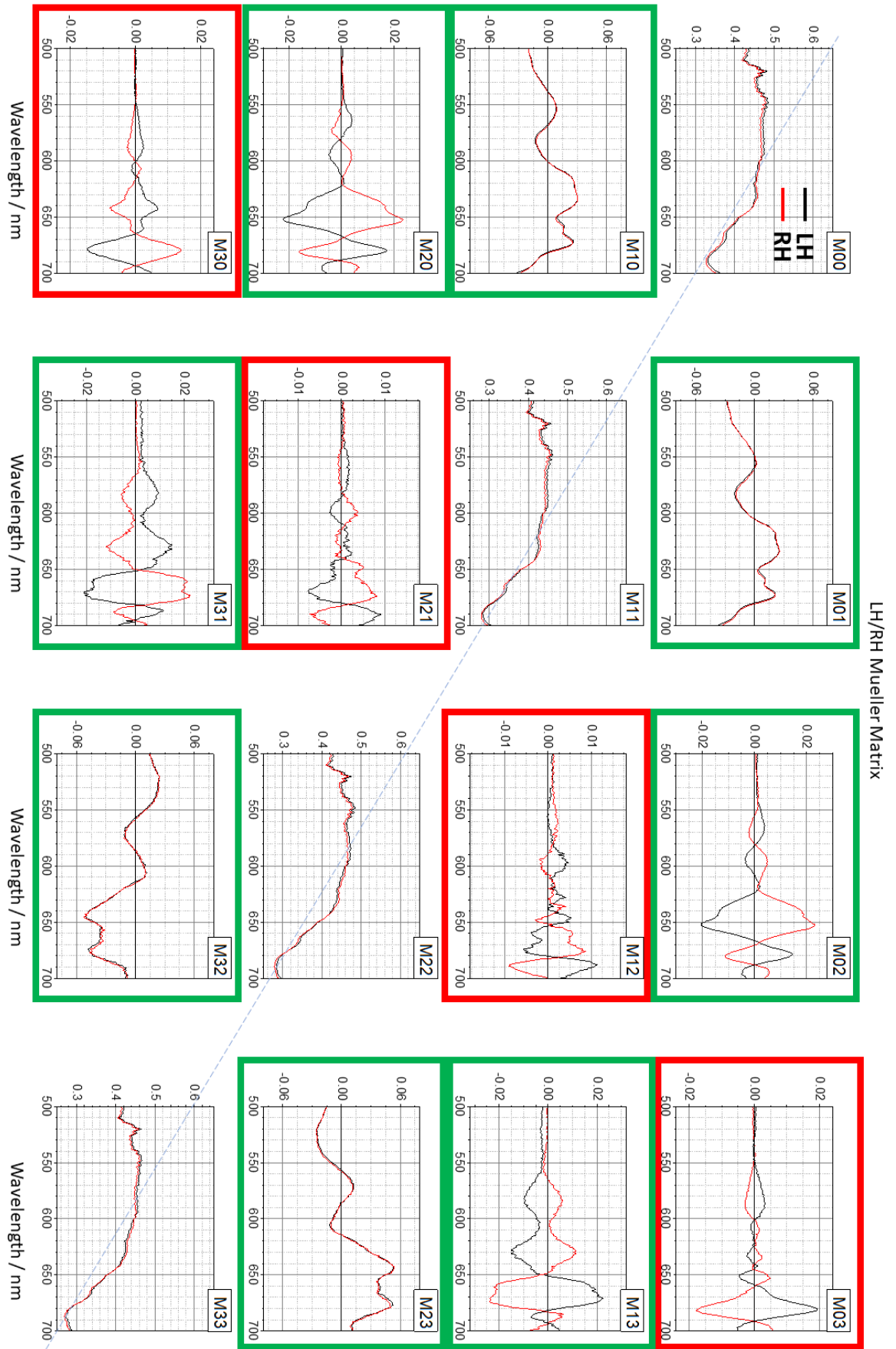


Figure 6.2: The 16 Mueller matrix elements for both the LH (black) and RH (red) arrays of a 210 nm sample immersed in water. The dashed blue line across the main diagonal is used to help visualise the symmetry plane between MMP element pairs, with green outlines representing predominant similarities between pairs and red showing stronger differences.

Where χ_{ee} , χ_{em} , χ_{me} and χ_{mm} the electric-electric, electric-magnetic, magnetic-electric and magnetic-magnetic susceptibility tensors, respectively. Therefore, combining these equations results in:

$$\mathbf{D} = \varepsilon_0(\mathbf{I} + \chi_{ee}) \cdot \mathbf{E} + \sqrt{\varepsilon_0\mu_0}\chi_{em} \cdot \mathbf{H} \quad [6.14]$$

$$\mathbf{B} = \sqrt{\varepsilon_0\mu_0}\chi_{me} \cdot \mathbf{E} + \mu_0(\mathbf{I} + \chi_{mm}) \cdot \mathbf{H}. \quad [6.15]$$

With unit tensor, \mathbf{I} . These terms can be simplified by defining the following:

$$\begin{bmatrix} \varepsilon & \xi \\ \zeta & \mu \end{bmatrix} = \begin{bmatrix} \varepsilon_0(\mathbf{I} + \chi_{ee}) & \sqrt{\varepsilon_0\mu_0}\chi_{em} \\ \sqrt{\varepsilon_0\mu_0}\chi_{me} & \mu_0(\mathbf{I} + \chi_{mm}) \end{bmatrix}. \quad [6.16]$$

This results in the conventional constitutive relations for bianisotropic materials¹³:

$$\mathbf{D} = \varepsilon\mathbf{E} + \xi\mathbf{H} \quad [6.17]$$

$$\mathbf{B} = \mu\mathbf{H} + \zeta\mathbf{E}. \quad [6.18]$$

With the ξ and ζ being the magnetoelectric coupling parameters. Bianisotropic materials can therefore be described as materials that acquire magnetic (electric) polarisation when excited by an external electric (magnetic) field.¹⁴ Such an assignment agrees with the results presented in **Chapter 5**, due to the incident electric field inducing an orthogonal magnetic response within the material.^{13,14} As was shown in the analysis of **figure 6.2**, the matrices do possess some anisotropic-like character. To explain this behaviour, it is necessary to consider the symmetry environment of the nanostructures.

A truly chiral structure such as the gammadions used in **Chapter 4**, possess four-fold rotational symmetry and exhibit CD that is invariant under rotation and time-inversion. It has been shown via MMP that these gammadion structures gain their optical activity through their placement on a substrate and the rounding of their edges.¹⁵ Therefore, an ideal gammadion suspended in a uniform medium will not exhibit optical activity due to the lack of a dissymmetric backing. The structures used in this work possess C_1 symmetry when placed on a substrate, the asymmetric spacing between the upper-middle bars and the middle-bottom bars removes any rotational symmetry (even spacing between the arms would make the structures C_2 symmetric). Again, a lack of mirror or rotational symmetry itself points to the material being bianisotropic based on the descriptions put forward by Arteaga in matrices [M2]-[M5], in which each matrix value is unique.⁵

As the presence of the quartz substrate and the structure's edge defects are the source of asymmetry, and changes to these factors will have an effect on the overall chirality of the sample. The asymmetry of the sample will decrease as the difference in the refractive indices of the two surrounding environments (below and surrounding the structure) becomes smaller¹⁵, depicted in **figure 6.3**. For example, if the structure were to be surrounded by air ($n=1$), the sample would belong to the C_1 point group. If the structures were to be surrounded entirely by

quartz, this would represent a uniform medium and essentially a free-floating structure. Under these conditions, the additional mirror symmetry plane would result in the sample belonging to the C_s point group. The measurements taken of the structures here, backed by quartz ($n=1.55$) and immersed in water ($n=1.33$), present an intermediate symmetry environment. The environment above the structures therefore acts as a symmetry perturbing variable, that is manifested in the Mueller matrix element symmetries which obtain a degree of anisotropic-like character.

As the overall symmetry of the surrounding environment becomes more symmetrical, the sample should exhibit a corresponding gradual reduction in optical activity. In a uniform environment, the defects would be the only source of symmetry breaking. A similar reduction in the optical activity would therefore be observed by the reduction in the rounding of the edges of the fabricated structures, i.e. if they were to become more idealised.¹⁵ Idealised planar structures would therefore be described as anisotropic due to the fact that they are achiral.⁵

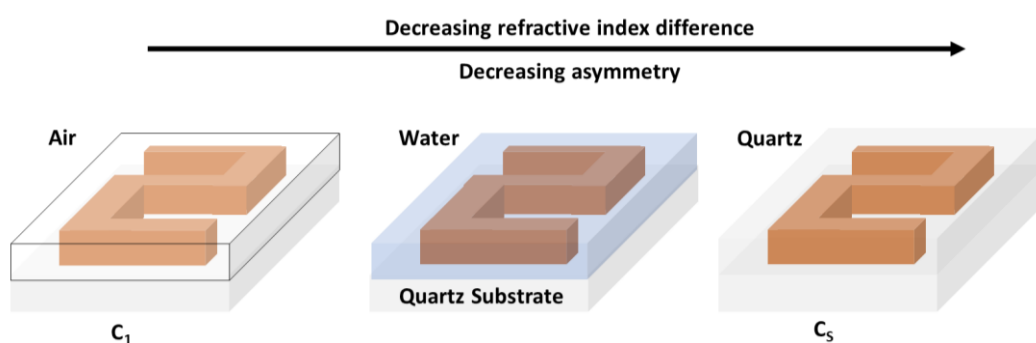


Figure 6.3: The overall symmetry of an idealised sample on the quartz substrate increases depending on the refractive index environment above the structure (relative to the substrate). The placement of the structure on the substrate is one of two major sources of dissymmetry of the structure.

Moving on to the racemic arrays, the RA and RS MMP element data is displayed in **figures 6.4** and **6.5**, respectively. As expected from the results in the previous chapter, there is a lack of CD and CB related signal ($[M_{11}]$ antidiagonal elements) in both arrays due to the cancelling of contributions from oppositely handed components of the arrays. This is also the case for the elements related to the LD' and LB' properties, as their LH/RH elements showed mirrored behaviour. The only elements to produce a significant signal are related to the LD and LB, elements M_{01} , M_{10} and M_{23} , M_{32} , respectively. As these elements show equivalent (rather than mirrored) behaviour for the LH/RH arrays, the racemic arrays maintain a signal. The signals measured for each of the elements of the RA array are found to be of the same form as those of the LH and RH structures, as was the case with their reflectance spectra.

The RS array's spectra deviate from the spectra of the other arrays for element pairs M_{01}/M_{10} and M_{23}/M_{32} . In both cases, the double peaks that appear for the RA array across ~ 650 nm instead form a single peak. This might be expected from the RS arrays, as they were found to differ the most from the other arrays in terms of their characteristic reflectance peaks (**figure 5.8**). Although there is a lack of signal in the antidiagonal elements, this only occurs due to the net contributions of the structures, which themselves are still bianisotropic.

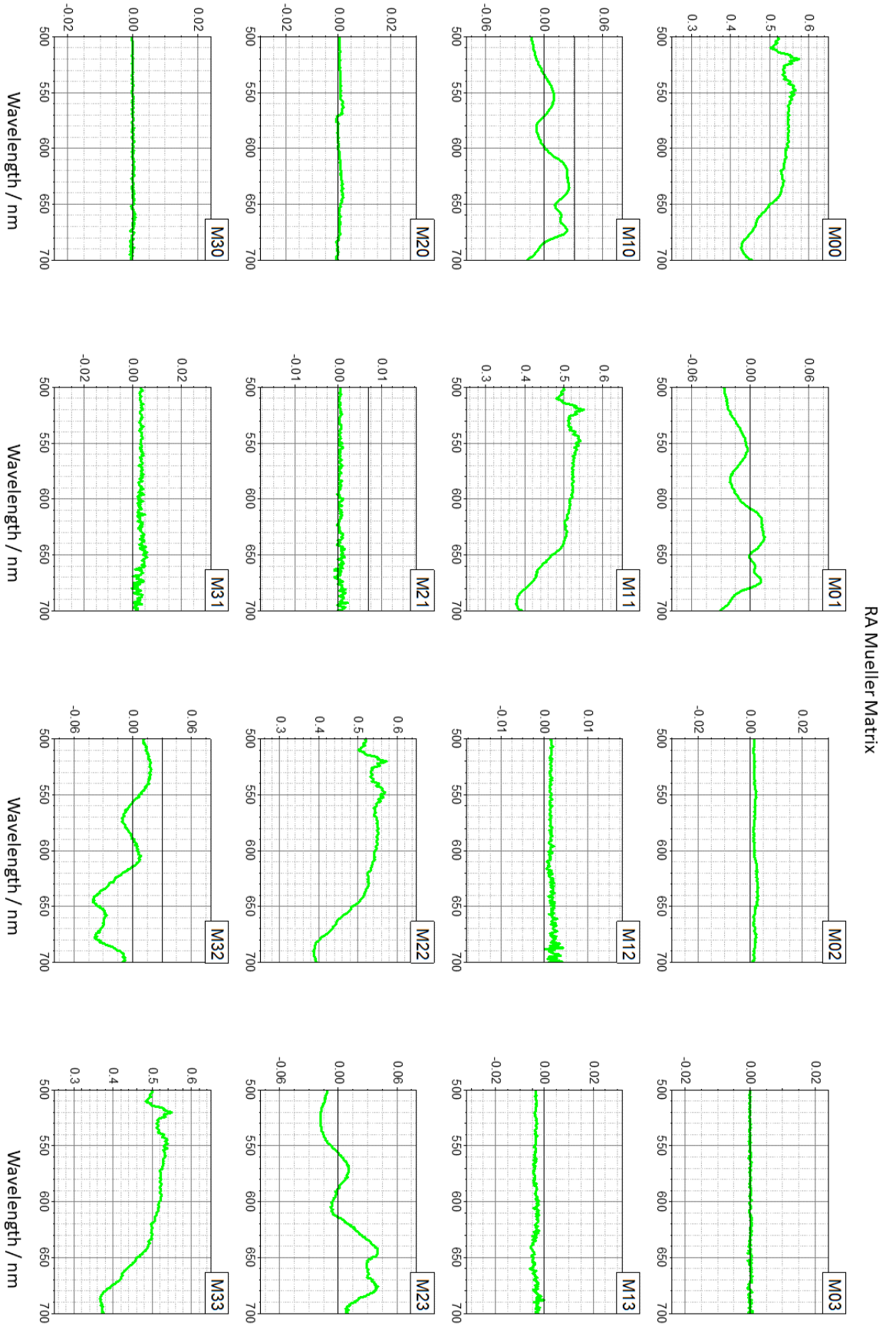


Figure 6.4: The 16 Mueller matrix elements for the RA array of a 210 nm sample immersed in water, for which only the LD and LB elements are non-zero.

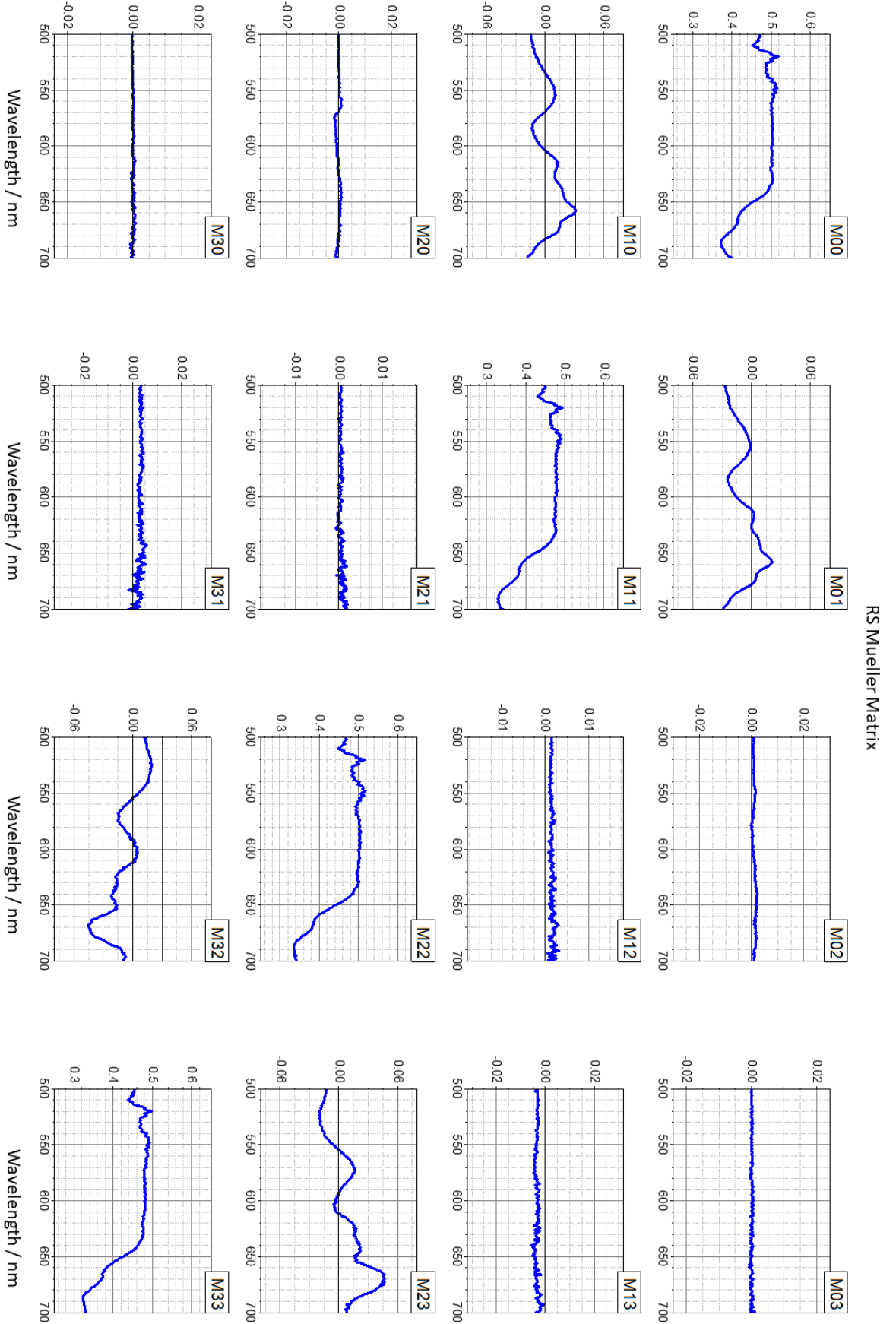


Figure 6.5: The 16 Mueller matrix elements for the RS array of a 210 nm sample immersed in water, where again, only the LD and LB elements are non-zero.

6.3.2 Optical Properties of Silicon Nanoarrays

Mueller matrix elements can be used to calculate several optical properties of a sample, relations which are shown in matrix [M1]. These include the CD, CB, LD, LB, LD', LB' and g-factor (described in equation [1.27]), which are shown for the LH/RH, RA and RS arrays in **figures 6.6, 6.7 and 6.8**, respectively. The software used as part of the MMP setup converts the individual elements into their respective properties.^{9,10,16}

The CD is obtained from the matrix elements $(M_{03}+M_{30})/2$. As expected for enantiomorphic structures, the CD spectra are approximately equal and opposite. This is also the case for the CB that was measured, which is calculated from the elements $(M_{12}-M_{21})/2$. The LD and LB plots, generated from elements $-(M_{01}+M_{10})/2$ and $(M_{32}+M_{23})/2$, respectively, show the most intense regions above 650 nm. This is again true for the LD' and LB' properties, calculated from $-(M_{02}+M_{20})/2$ and $(M_{13}+M_{31})/2$, however their maximum values are approximately half of those of the 0°/90° measurements.

From direct comparison between the individual properties, it is clear that the greatest contributions from the LB, LD, LB' and LD' are an order of magnitude larger than those of the CD and CB. As shown in **section 6.1**, the CPL related Stokes parameters will depend on the effects of linear birefringence at both 0°/90° and ±45°. ¹⁵ Therefore, the ORD derived CD spectra from the lab based Stokes polarimeters (**section 5.4.1**) may misrepresent the true CD of the sample by being unable to account for linear effects. It was shown in **section 5.4.1** that the ORD measurements were non-reciprocal, indicating a non-chiral response. This is validated by the strong linear effects observed in the MMP measurements. As the LB and LB' dominate, these act as the primary contributor to the optical rotation seen through the Stokes polarimetry performed in **chapter 5**. This emphasises the importance of full MMP, which prevents the misinterpretation of a sample's true optical activity. The presence of a weaker CD and CB signal indicate that the structures do still possess some level of chirality, due to the dissymmetry introduced by the substrate and fabrication defects. This is also reflected in the g-factor, g, which is commonly used to describe the optical properties of chiral materials.¹⁷ It is related to the absorption of RCP and LCP and therefore very closely resembles the CD plot.

The transmission elements are plotted for the LH array only, as there is no significant difference between the enantiomorphs. It is apparent that the total transmission, M_{00} , is greater than the other elements. As the elements M_{11} , M_{22} and M_{33} (the transmission for the 0°/90°, ±45° and CPL) are less than the total transmission intensity, this indicates that the Mueller matrix is depolarizing. A matrix is termed depolarizing if it produces partially polarised outgoing light from fully polarised input light⁵.

For the racemic arrays, the CD, CB, LD' and LB' yield no significant signal due to the overall cancellation of LH and RH components, as was seen for the individual matrix elements. The RA array's LD and LB both possess resonances that resemble the LH/RH arrays but have a reduced intensity for each peak. Consistent with previous observations, there are changes in spectral shape observed for the LD and LB properties of the RS array.

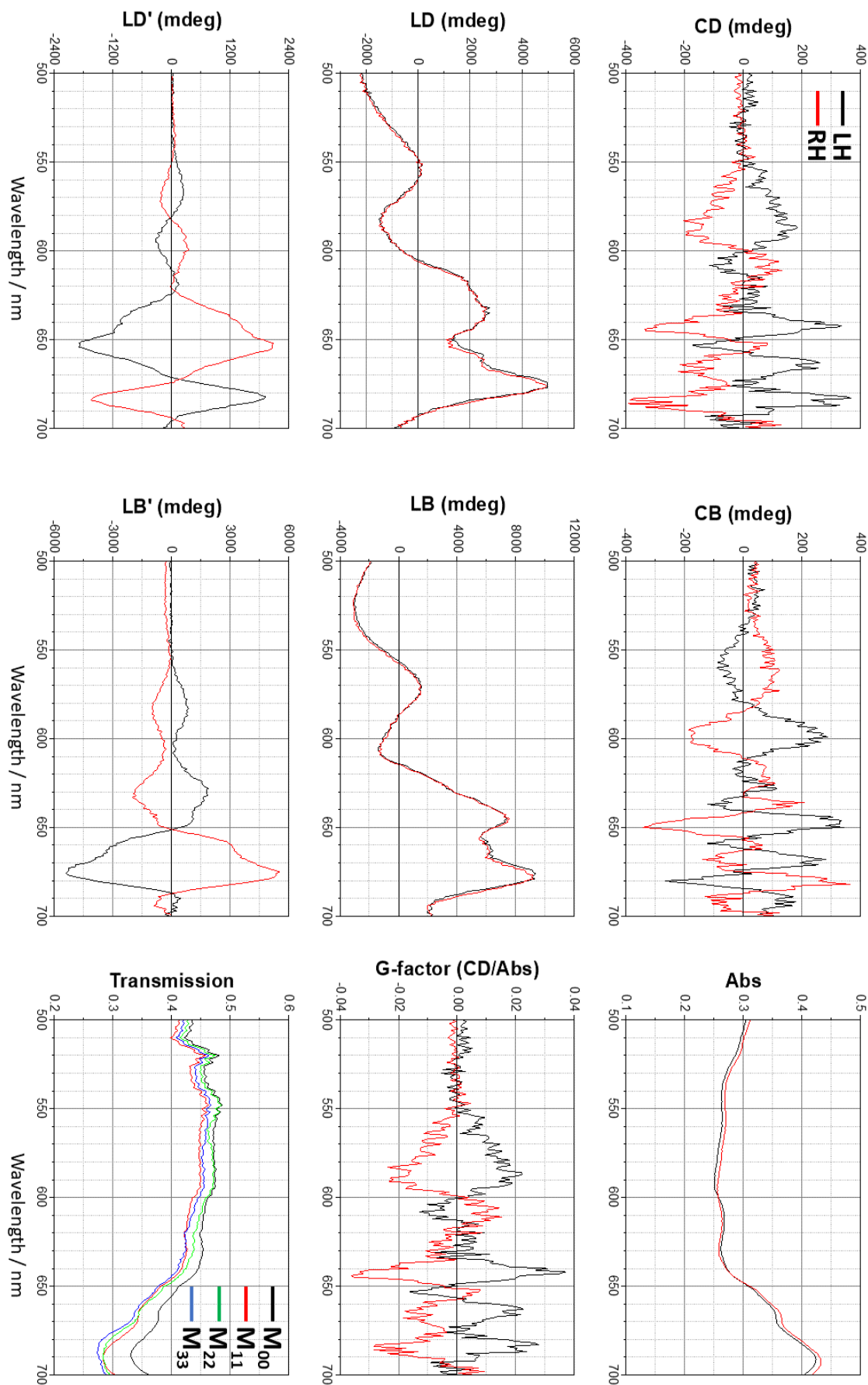


Figure 6.6: A comparison between the optical properties of the LH and RH arrays of a 210 nm sample immersed in water, based on MMP elements of figure 6.2.

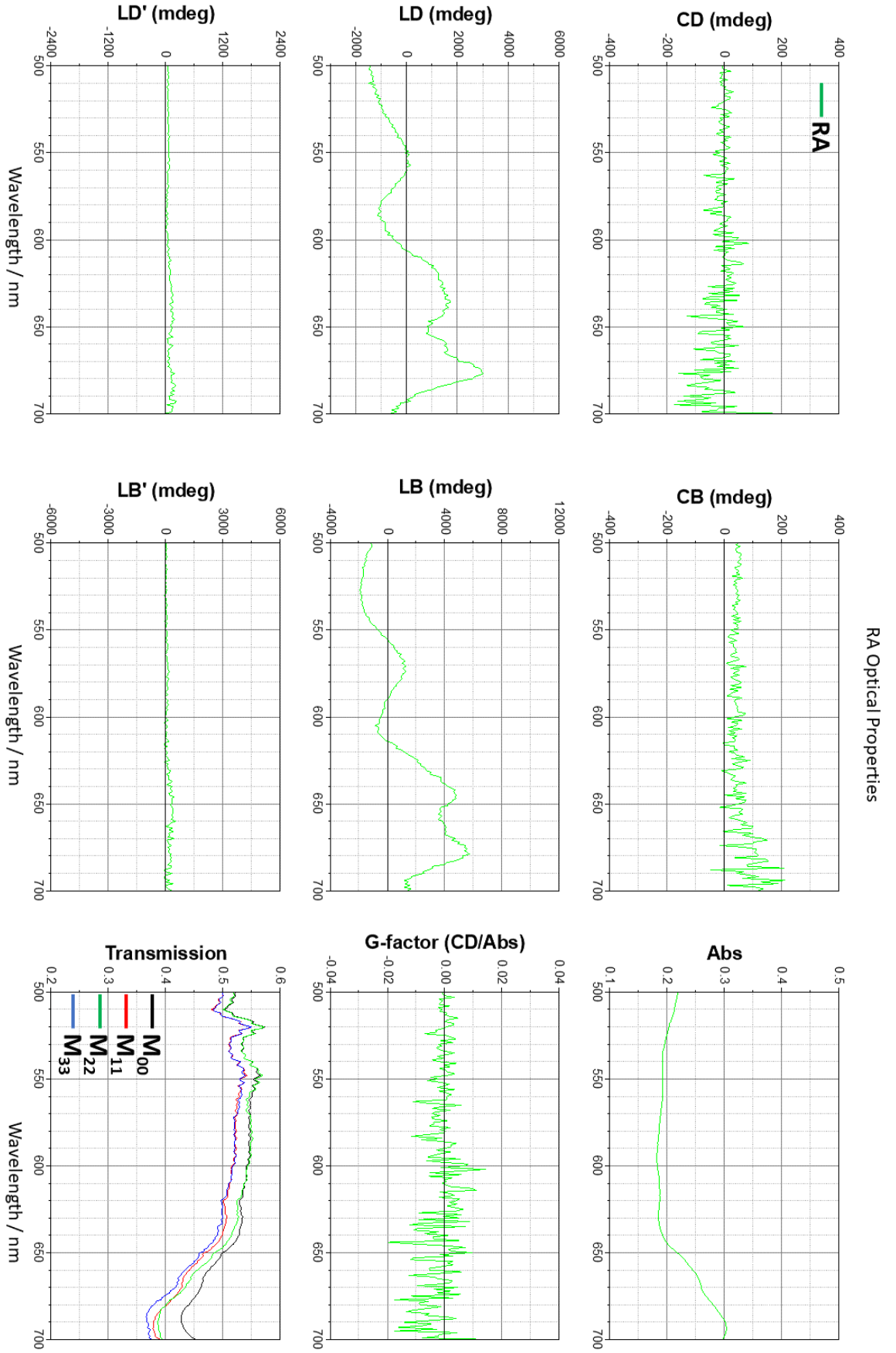
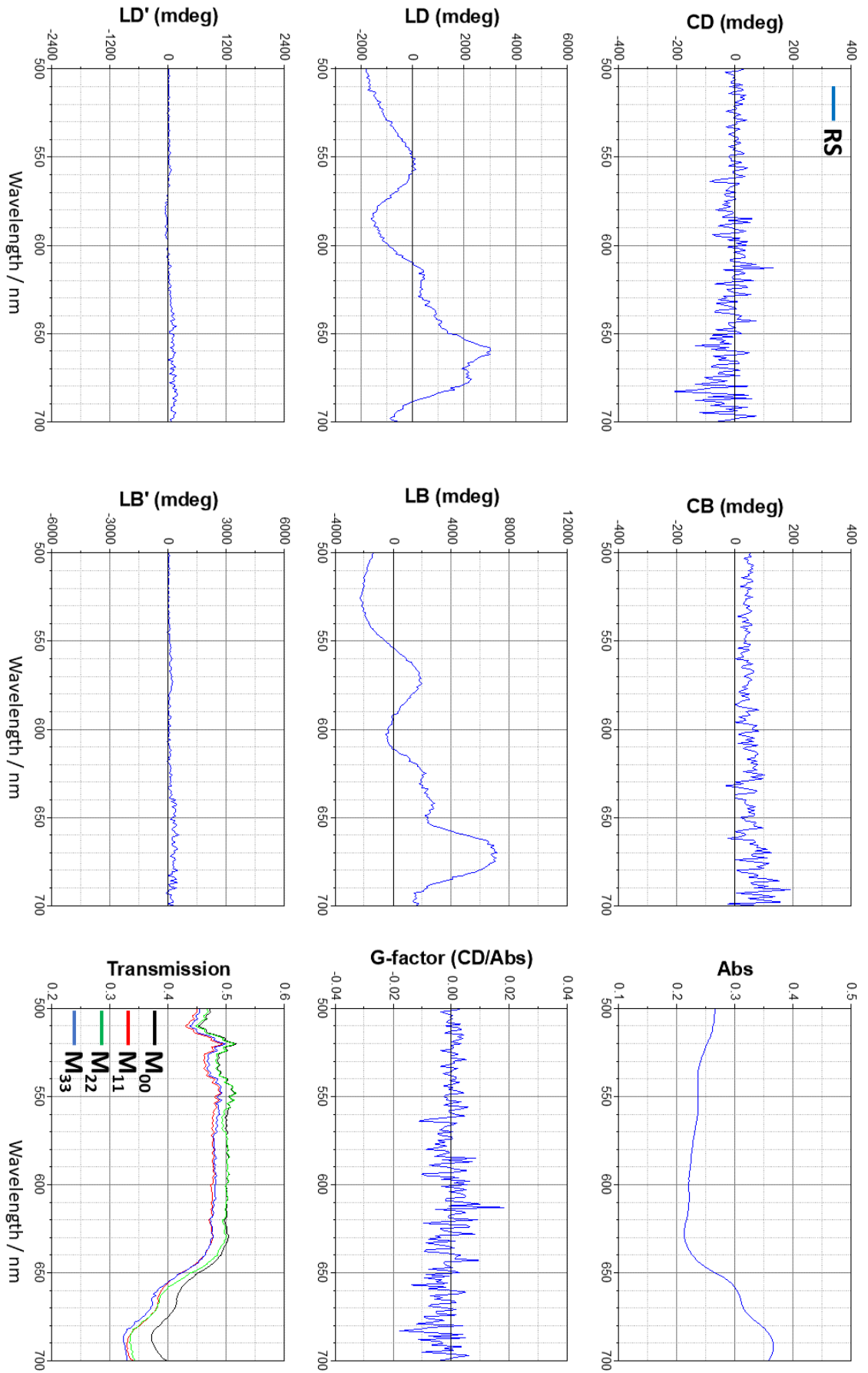


Figure 6.7: The optical properties of the RA array of a 210 nm sample immersed in water, based on MMP elements of figure 6.4.



RS Optical Properties

Figure 6.8: The optical properties of the RS array of a 210 nm sample immersed in water, based on the MMP elements of figure 6.5.

6.3.3 Numerical Simulations

As the traditional method of CD spectrometers measure the differential transmission of RCP and LCP, these measurements could be simulated using COMSOL. It was found in the previous chapter that the CD measurements from simulation did not resemble the ORD when KK transformed. This was attributed to inherent differences between the simulated CD (CPL) and experimental ORD (LPL) methods. The ORD data was also revealed to be dominated by the sample birefringence, which has been confirmed with MMP and the large LB and LB' effects measured. These optical properties will also alter the path of the CPL as it travels through the sample and contribute to the S_3 Stokes vectors, as measured with standard spectropolarimeters. A comparison between the simulated and MMP derived CD spectra is shown in **figure 6.9**. To aid comparison, the simulated spectra has been blue shifted by 25 nm to account for the typical red shift associated with the numerical (idealised) modelling and the MMP data has been smoothed.

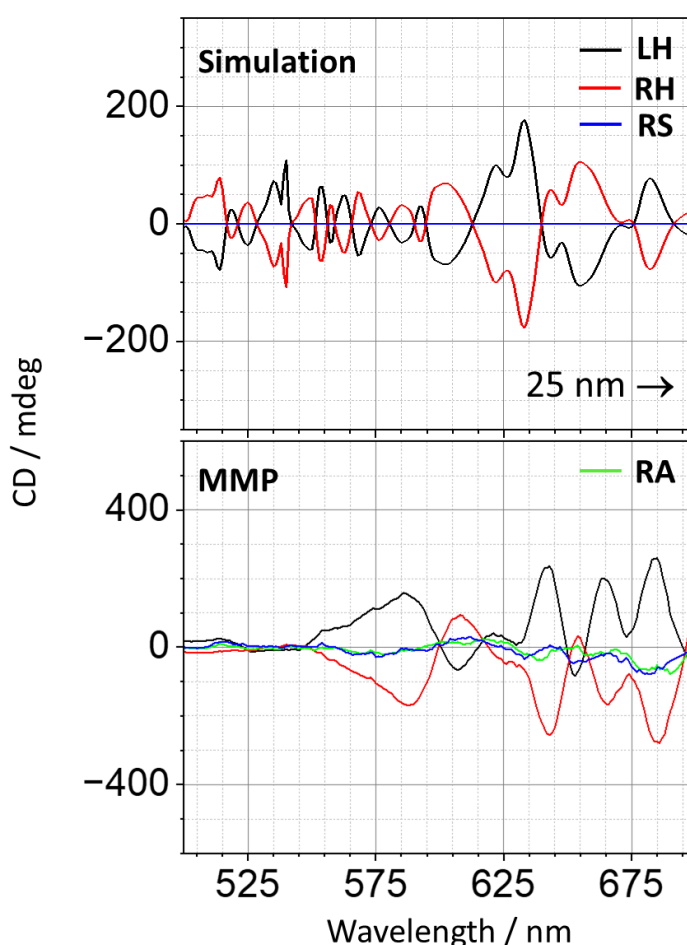


Figure 6.9: A comparison between the CD spectra obtained from simulation (top) and experimental MMP (bottom) for a 210 nm sample immersed in water. The simulated data is blue shifted 25 nm to account for the idealised model and aid comparison.

The MMP CD spectra provides better agreement with the experimentally measured CD in terms of spectral shape. As is typical of the idealistic structures in numerically simulated data, the spectra are more resolved and show numerous smaller resonances. Experimentally, between 645-695 nm, the LH/RH spectra diverge slightly and are off-centred, mimicked relatively closely by the RA/RS arrays. The LH/RH spectra would otherwise be expected to cross 0 mdeg around ~675 nm, in which case the simulation and experimental data show better

agreement. Lifting (lowering) of the RH (LH) experimental spectra at ~655 and ~675 nm would better replicate the double peaks present across this region in the simulations. At shorter wavelengths, the broad experimental peak across 575 nm appears as an oscillating feature in the simulation, which shows a positive (negative) mdeg bias for the LH (RH) array; broader averaging in this range would therefore improve the level of agreement.¹⁸

6.4 Conclusions

Results from **Chapter 5** revealed that the ORD signals of these silicon metamaterials, obtained through standard Stokes polarimetry measurements, were non-reciprocal. By performing full MMP, it has been shown here that the optical properties of the samples are dominated by linear effects, with the LB and LB' contributions an order of magnitude greater than those of CD or CB. This confirms that the non-reciprocal response observed previously are a result of the large linear contributions that alter the polarisation state of the light as it propagates through the material. This highlights the advantage of MMP over typical Stokes/CD spectrometers, in that MMP can decouple the individual optical properties of a medium and discriminate between true CD/CB and the effects of LB or LB'. These linear properties explain why the measured ORD measurements of the previous chapter were also not replicated by simulation.

Performing full MMP on a sample can also provide an insight into its symmetry properties. The symmetry of the antidiagonal Mueller matrix elements of the LH and RH arrays indicate the sample to be bianisotropic in nature. The refractive index environment above and below the structure can act as a symmetry perturbing factor in the overall Mueller matrix symmetry of the sample. Reducing the refractive index difference between the quartz substrate and the medium above it acts as a symmetry increasing perturbation, introducing more anisotropic-like character, which is reflected in the Mueller matrices.

The racemic arrays both showed no significant signals in their CD, CB, LD' or LB' or Mueller matrix elements pertaining to those optical properties. This is simply a result of the net cancellation of the LH and RH components of the RA and RS arrays. These arrays did provide a LD and LB signal given that the sign of these properties does not differ with the handedness of the structures.

Overall, the optical properties of this novel silicon metamaterial platform have been investigated using the comprehensive MMP technique. This casts further light on the fundamental behaviours and potential applications that these samples are capable of; their strong birefringence showing potential for tuneable waveplates and their chiroptical responses for chiroptical sensing. So far, these samples have only been exposed to water and buffer solutions, in the next chapter, biomolecules will be introduced to probe their interactions with the arrays.

6.5 References

1. Bohren, C. F. & Huffman, D. R. Electromagnetic Theory. in *Absorption and Scattering of Light by Small Particles* 12-56 (1998). doi:<https://doi.org/10.1002/9783527618156.ch2>.
2. Peinado, A., Lizana, A., Vidal, J., Lemmi, C. & Campos, J. Optimization and performance criteria of a Stokes polarimeter based on two variable retarders. *Opt. Express* **18**, 9815-9830 (2010).
3. Freudenthal, J. Intuitive interpretation of Mueller matrices of transmission. *HINDS Instruments* <https://www.hindsinstruments.com/wp-content/uploads/Intuitive-interpretation-of-Mueller-matrices-of-transmission-J-Freudenthal-January-18-2018.pdf> (2018).
4. Hilfiker, J. N., Hong, N. & Schoeche, S. Mueller matrix spectroscopic ellipsometry. **11**, 59-91 (2022).
5. Arteaga, O. & Kahr, B. Mueller matrix polarimetry of bianisotropic materials [Invited]. *J. Opt. Soc. Am. B* **36**, F72-F83 (2019).
6. Li, P., Tariq, A., He, H. & Ma, H. Characteristic Mueller matrices for direct assessment of the breaking of symmetries. *Opt. Lett.* **45**, 706-709 (2020).
7. Aladadi, Y. T. & Alkanhal, M. A. S. Classification and characterization of electromagnetic materials. *Sci. Rep.* **10**, 11406 (2020).
8. D Yang, J C Canit & E Gagnebet. Photoelastic modulator: polarization modulation and phase modulation. *J. Opt.* **26**, 151 (1995).
9. Arteaga, O., Freudenthal, J., Wang, B. & Kahr, B. Mueller matrix polarimetry with four photoelastic modulators: theory and calibration. *Appl. Opt.* **51**, 6805-6817 (2012).
10. Hussain, R., Jávorfí, T. & Siligardi, G. CD Imaging at High Spatial Resolution at Diamond B23 Beamline: Evolution and Applications. *Front. Chem.* **9**, (2021).
11. Caloz, C. & Sihvola, A. Electromagnetic Chirality, Part 2: The Macroscopic Perspective [Electromagnetic Perspectives]. *IEEE Antennas Propag. Mag.* **62**, 82-98 (2020).
12. Caloz, C. & Sihvola, A. Electromagnetic Chirality, Part 1: The Microscopic Perspective [Electromagnetic Perspectives]. *IEEE Antennas Propag. Mag.* **62**, 58-71 (2020).
13. Serdyukov, A. N., Semchenko, I. V, Tretyakov, S. A. & Sihvola, A. H. Electromagnetics of bi-anisotropic materials: Theory and applications. in (2001).
14. Asadchy, V. S., Díaz-Rubio, A. & Tretyakov, S. A. Bianisotropic metasurfaces: physics and applications. **7**, 1069-1094 (2018).
15. Arteaga, O. *et al.* Relation between 2D/3D chirality and the appearance of chiroptical effects in real nanostructures. *Opt. Express* **24**, 2242-2252 (2016).
16. Arwin, H. *et al.* Structural circular birefringence and dichroism quantified by differential decomposition of spectroscopic transmission Mueller matrices from *Cetonia aurata*. *Opt. Lett.* **41**, 3293-3296 (2016).
17. Tang, Y. & Cohen, A. E. Optical Chirality and Its Interaction with Matter. *Phys. Rev. Lett.* **104**, 163901 (2010).
18. Ciraci, C. *et al.* Impact of Surface Roughness in Nanogap Plasmonic Systems. *ACS Photonics* **7**, 908-913 (2020).

Chapter 7: Capacitive Sensing with Silicon Metamaterials

Previously, it was shown that gammadion structures were capable of biomolecule detection at resonances which generated near-field interactions between their arms. The gammadions exhibit a degree of inductive coupling, in which the fields generated in one part of the structure induce a response in a neighbouring part. The silicon structures of the preceding chapters were found to behave differently, with much of the electromagnetic excitation occurring within the structures. Several of their optical responses were measured and explained through Stokes polarimetry and MMP, which was done in the absence of biomolecular layers. In this chapter, the optical response of the silicon arrays in the presence of an antigen-antibody complex is investigated, with the effects of local charges explored through numerical simulation.

Whilst the asymmetries detected with the gammadions occurred due to the birefringence of the chiral biomolecular layers, it is the charge that is being investigated as the source of spectral changes with the silicon S-structures. Blue shifting effects are observed in the reflectance and MMP data of the samples in the presence of biomolecules which possess an overall molecular charge. These effects are not repeated in the presence of non-charged species.

To examine why this may be the case, approximations of charged external layers surrounding the structures are introduced to the numerical simulations. As the fields excited by the incident light are stored mostly within the structures, the changes brought about by the external charged layers are described as capacitive. The models provide some agreement in terms of spectral responses and changes to field properties, however, the simulations breakdown when x-polarised light is used. This indicates that further refinement of this model is needed.

The following results represent an initial attempt at validating the experimental results, using highly approximated and fundamental models. Had time not been a limitation, the simulation techniques might have been improved and refined to a greater degree. Regardless, the behaviours exhibited by the structures present an interesting area for further research.

7.1 Biosensing Platforms

7.1.1 Refractive Index Sensors

Refractive index (RI) based sensing is an established strategy for biosensors, with common platforms based on plasmonic metamaterials.^{1,2} They typically operate based on the spectral shifts of a nanomaterial's resonances, which arise due to the change in the local refractive index environment of the sample. As such, the sensitivity of a RI sensor is characterised by the spectral shift per RI unit (nm/RIU). One RI unit would be represented by a change from $n=1$ to $n=2$. The sensitivity of different sensing platforms varies drastically; plasmonic devices typically offer some of the best performances, with values in the range of ~ 1000 s nm/RIU.³ Although RI sensors can provide highly sensitive platforms, there are several drawbacks associated with their use. The high levels of optical losses associated

with plasmonic systems are a limiting factor in the efficiency of fabricated devices. In addition, RI sensors are typically sensitive to large volumes surrounding the nanostructures/ target molecules, leading to the potential masking of the desired signal. Dielectric materials offer an alternative, lack of Ohmic losses provide an avenue for spectrally sharper resonances and higher spatial localisation in sensing.

7.1.2 Capacitive Effects

Capacitors operate by storing electrical energy between conducting plates separated by a dielectric and are used in a multitude of electronic applications.⁴ Capacitance is defined as the ratio of the charge, Q , between the plates and the voltage, V , between them:

$$C = \frac{Q}{V}. \quad [7.1]$$

Capacitance has been utilised in biosensing as a sub-category of impedance biosensors, that measure changes in the local dielectric properties between the plates upon the binding of a target analyte. In the case of a parallel plate capacitor, the capacitance is dependent upon the surface area of the plates, A , their separation, d , and the dielectric response, ϵ_r ⁵:

$$C = \epsilon_0 \epsilon_r \frac{A}{d}. \quad [7.2]$$

Biosensing platforms that rely on capacitive effects that occur between components of nanostructures have also been explored.⁶ Split ring resonators (SRR) are an example of a highly tuneable metamaterial geometry that can induce a strong electromagnetic response between structural features. Such devices yield a resonance wavelength, λ , dependent on the capacitance and inductance, L , of the system⁸:

$$\lambda \approx 2\pi\sqrt{LC}. \quad [7.3]$$

The primary aspect of SRR devices is the local coupling that can occur between structural features of the nanostructures, which effects the respective resonance. They have been fabricated in a variety of forms, possessing concentric rings, S-shaped resonators⁹ and omega shaped rings¹⁰, shown in **figure 7.1**.¹¹ Each provide a means of producing a desired property based on the coupling that is supported by the geometries. The optical properties of the device are therefore dependent on several factors, including structure size, feature separation, inter-resonator separation and near-field EM interactions. Open-SRRs, **figure 7.1a**, operate through the coupling that occurs between the two rings as a result of the material currents of both rings. In the case of **figure 7.1b**, favourable overlap between inverted S-shaped nanowires separated by a substrate is used to engineer desired resonance frequencies. Single ring resonators, **figure 7.1c**, can also be used in arrays to form media with variable properties. In each case, changes in capacitance brought about by analytes can bring about a change to the resonances measured. Similarly, the silicon s-structures of this work are investigated in terms

of how the electromagnetic fields stored within them is altered in the presence of external charge, in the form of biomolecular layers.

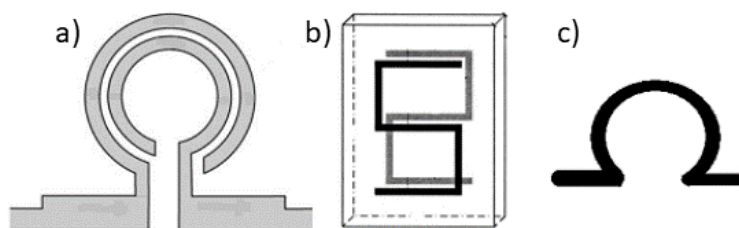


Figure 7.1: Examples of several SRR geometries. a) An open-SRR. b) Inverted S-shaped SRRs on opposite sides of a substrate. c) An omega SRR. Material currents and capacitive coupling differ due to the arrangement of the structural features. Figure adapted from reference ¹¹.

7.2 Methodology

7.2.1 Deposition Procedure

The experiments performed in this chapter required a multi-stage deposition of streptavidin, followed either by biotin or an anti-streptavidin antibody (again referred to as antistrep). A deposition strategy suitable for silicon substrates was utilised^{12,13}, a schematic for which is shown in **figure 7.2**. As per **section 3.1.1**, the different solutions were introduced to the sample holder cavity when required.

To begin, the sample was immersed in PBS buffer for at least 5 minutes, prior to the first species, poly-L-lysine (PLL), being deposited. The use of PLL as a pre-coating reagent for the adhesion of biomolecules and cells is a common protocol. It provides a well-anchored monolayer which can be rinsed extensively without a significant loss of coverage.^{14,15} The samples were left in the PLL for 15 minutes, which was sufficient for the positively charged PLL to bind to the silicon surface. Next, negatively charged glutaraldehyde was added and left for 45 minutes to bind to the positive PLL layer. At this stage, the streptavidin coated quantum dots (QDs) (Qdot™ Thermo Fisher) could be added for 30 minutes, which undergoes a cross-linking reaction with the glutaraldehyde.^{16,17} 40 mmol ethanolamine was then introduced, which acts as a capping layer to cover unbound glutaraldehyde sites and limit non-specific binding. After 20 minutes, the solution is replaced with PBS and measurements were performed. A final binding of either biotin or antistrep was performed, with these solutions being left for one hour to bind.

As a control, 2-Butanol was added to examine the effects of an uncharged environment around the unfunctionalized structures. Newly fabricated structures were used for each of these experiments.

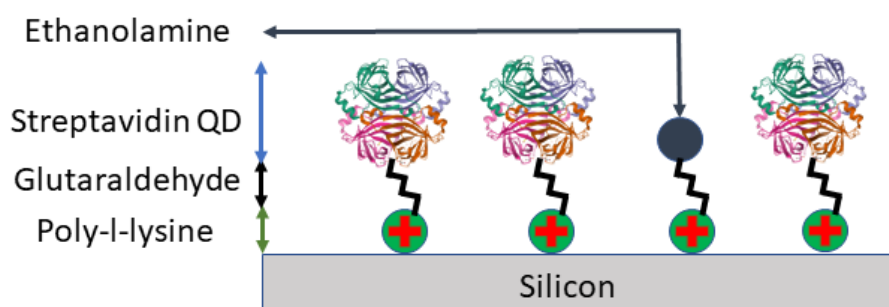


Figure 7.2: A schematic of the deposition process with labelled constituent layers. Positively charged poly-L-lysine binds to the silicon surface. Glutaraldehyde crosslinks between the lysine and the streptavidin coated QDs. Ethanolamine acts as a capping layer to limit nonspecific binding. The streptavidin coated QDs are then free to bind with additional species.

7.2.2 Spectra Collection

Reflectance measurements were acquired with the Stokes polarimeter detailed in **section 3.1.3.1** and MMP was also performed using the *Diamond Light Source Ltd.* polarimeter discussed in **chapter 6**. AFM measurements were also collected before and after each experiment, to ensure any spectral differences did not arise from morphological changes to the structures.

7.2.3 Simulation Procedure

In this chapter, two forms of model were used in numerical simulations. One form, shown in **figure 5.6a,b**, was used for simulations without the presence of proteins. The second form included 20 nm external layers on the outer faces of the S-structure's surface. This layer could be assigned an external polarisation, a refractive index and a chiral parameter (ξ) value to mimic the protein deposited around the structure. The model is described in greater detail in **section 7.4.2**.

7.3 Results and Discussion – Experimental

7.3.1 Butanol Measurements

Reflectance measurements were taken of the four unfunctionalized arrays of a ~210 nm sample immersed in racemic R,S-2-Butanol, which is composed of neutral molecules and has a refractive index of $n=1.397$.¹⁸ These spectra are shown in figure 7.3a-d. The presence of the higher refractive index solution, relative to PBS, produces a small redshift in the reflectance spectrum for each array. The tallest peak at ~700 nm (peak A) and peak at ~766 nm (peak B) shows a wavelength shift of ~+3 nm. Based on these spectral shifts, a shift per RIU can be calculated for the sample. A 3 nm shift and a refractive index change from 1.335¹⁹ to 1.397²⁰ constitutes a sensitivity value of ~48 nm/RIU. This value falls on the very low end of device sensitivity, with plasmonic SPR sensors capable of values in the several thousands.³ This indicates that these samples do not offer an effective platform for RI based sensing.

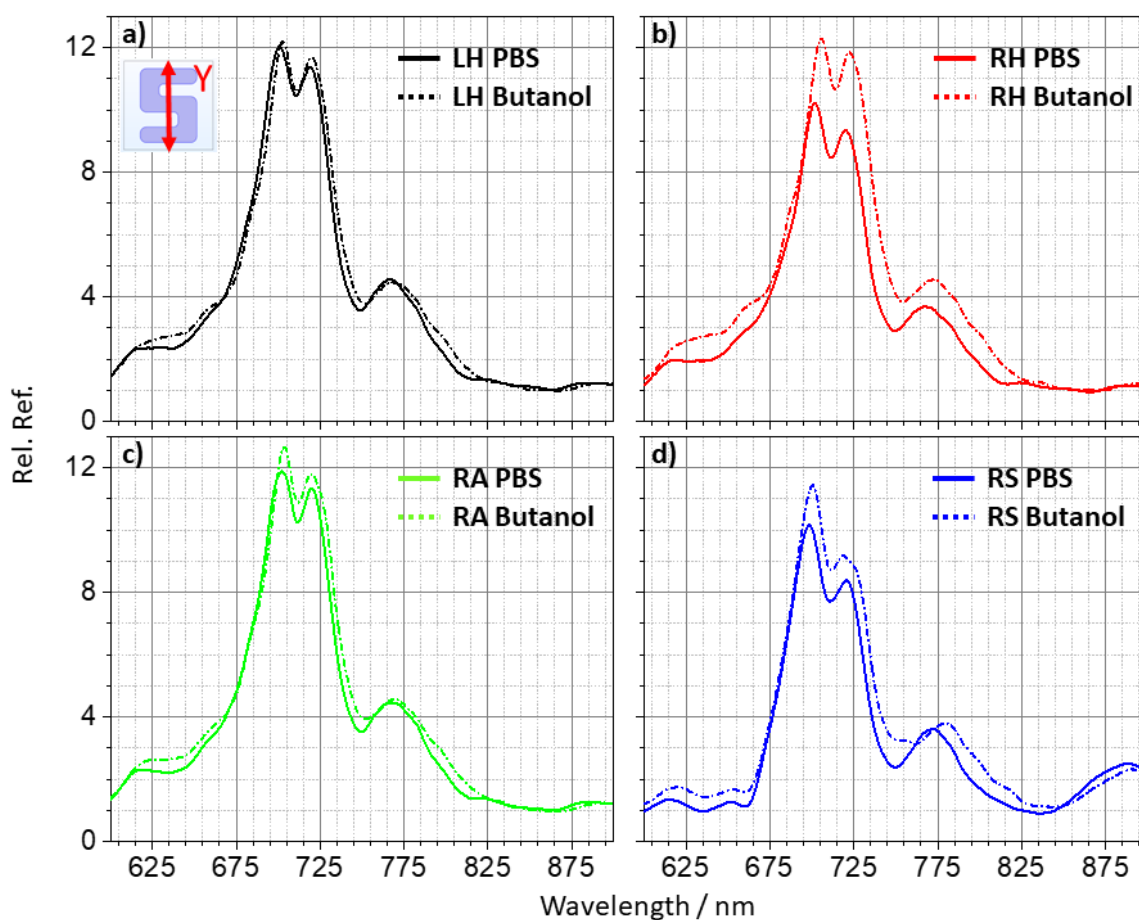


Figure 7.3: Y-polarised experimental reflectance data of a ~210 nm sample, obtained for a) LH b) RH c) RA and d) RS arrays immersed in PBS buffer (solid) and R,S-butanol (dashed).

7.3.2 Streptavidin Depositions

Streptavidin coated QDs were deposited on the structures using the multilayer process detailed in figure 7.2. The deposition of the streptavidin could be confirmed through photoluminescence measurements of the arrays, shown in figure 7.4a-d.

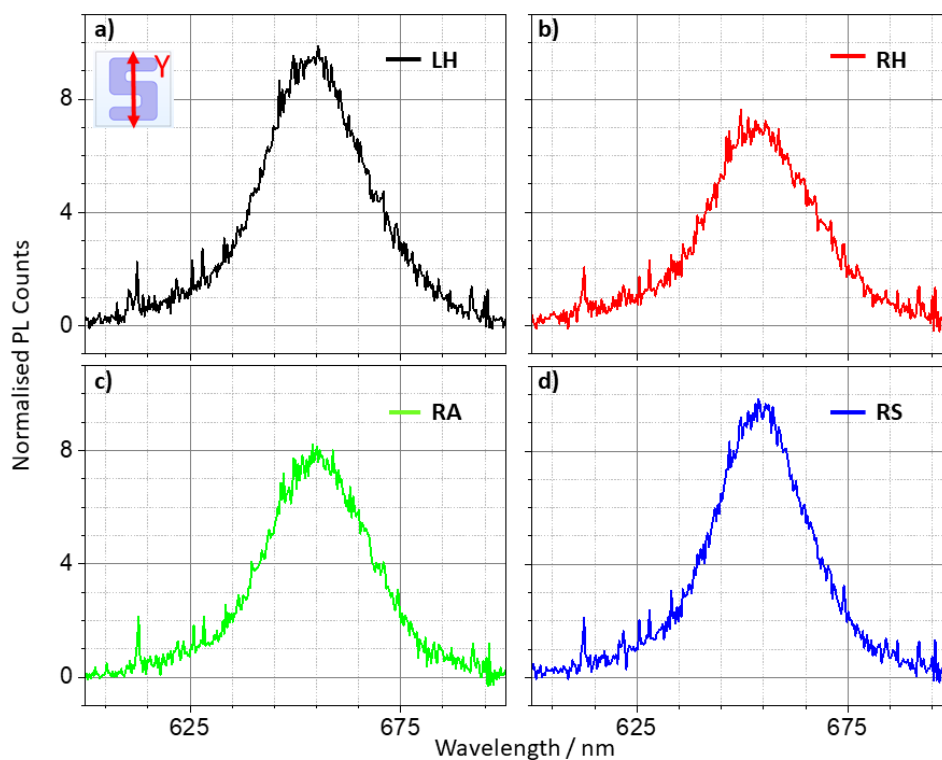


Figure 7.4: Photoluminescence signals obtained under y-incident polarisation for the streptavidin coated QDs on each array, excited at 404 nm. The signal is normalised against the number of acquisitions.

The QDs were manufactured to emit at 655 nm. The PL signals show a relatively consistent intensity between the arrays, centred across 655 nm, indicating that the deposition process provides a relatively consistent coverage of streptavidin. Two different samples were examined via Stokes polarimeter when deposited with the streptavidin coated QDs. An additional deposition layer was added in each case, one sample introduced to anti-streptavidin antibody solution and the other to biotin.

7.3.2.1 Streptavidin – Anti-streptavidin

A ~160 nm sample was used for the antistrep deposition, the reflectance measurements for which are shown in figure 7.5a-d. Upon deposition of streptavidin there is a significant change in the reflectance spectra, with a blue shift in the peak positions of peaks A and B (~ 655 and ~705 nm) and a decrease in the reflectance intensity. When the antistrep is added to the sample there is an additional smaller blue shift accompanied by an increase in the reflectance intensity.

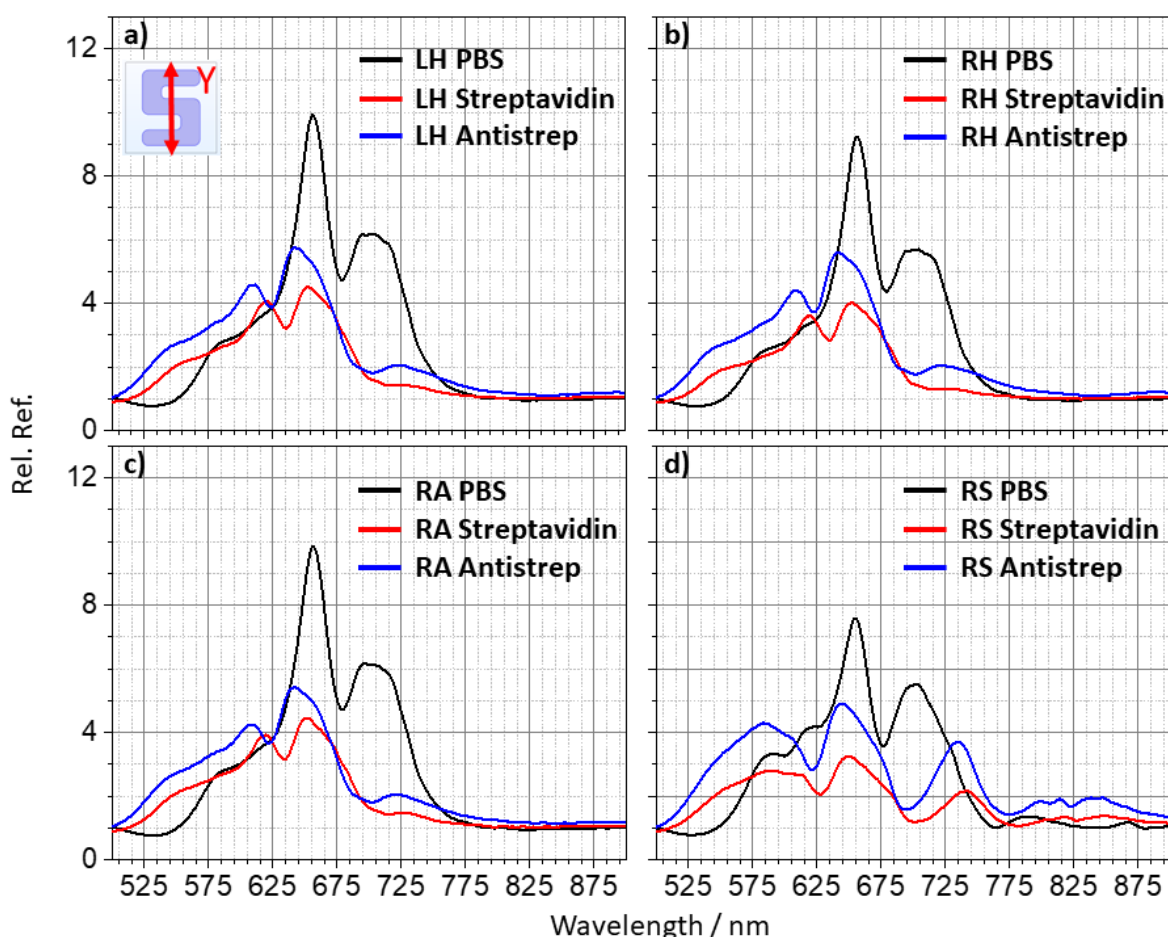


Figure 7.5: Experimental y-polarised reflectance spectra collected in PBS buffer for a) LH b) RH c) RA and d) RS arrays of a ~160 nm sample (black), followed by the depositions of streptavidin (red) and antistrep antibody (blue).

Although there is no detectable spectral asymmetry, the arrays appear capable of detecting the binding of the streptavidin and the antibody. Interestingly, the spectra undergo a blue shift, which is inconsistent with the typical red shifts of RI sensing.

AFM images were taken of the sample to examine their morphology before and after the experiments, displayed in **figure 7.6**. The metrology measurements show that there is no significant change in the height or shape of the structures, confirming that the spectral changes do not originate from differences in the sample morphology before and after the experiment. For brevity, these measurements are shown only for this sample, as each sample showed similar behaviour across each experiment. There is some sidewall sloping present in each measurement that is attributed to tip convolution; a common artifact of AFM measurements, due to sample-tip interference that prevents an accurate measurement of the true sidewall profile. The AFM measurements are performed on dried samples, conditions in which the deposited layer is expected to collapse, resulting in minimal changes to height measurements.

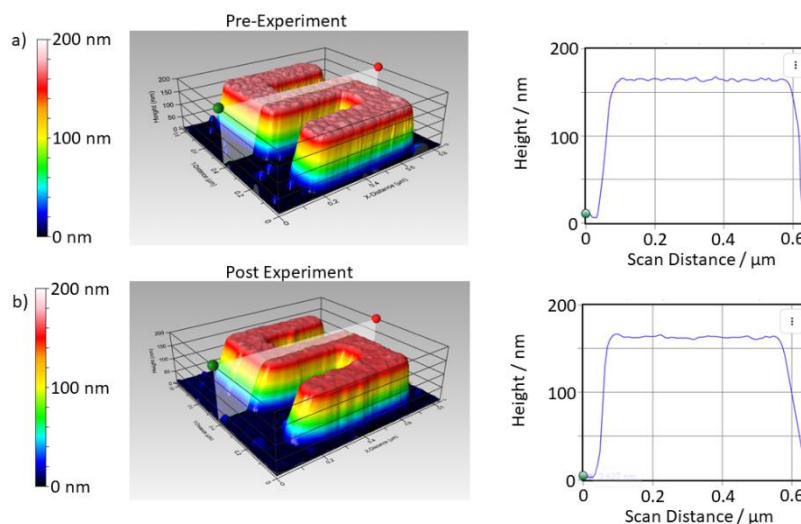


Figure 7.6: AFM data collected for the sample used in figure 7.5. a) AFM image (left panel) of a RH structure and the associated height profile (right panel) across the middle arm, of a pristine structure prior to any deposition. b) Equivalent data after experiment, following the deposition of antistrep onto the streptavidin functionalised surface.

7.3.2.2 Streptavidin – Biotin

The experiment was repeated with another sample of ~ 180 nm height, this time using biotin as the final binding species. The reflectance spectra for the arrays are displayed in **figure 7.7**. As before, a blue shift in the reflectance is observed when the streptavidin is added, with a decrease in the intensity of the spectra. Again, the addition of a streptavidin-binding species, biotin, produces a further blue shift in the reflectance.

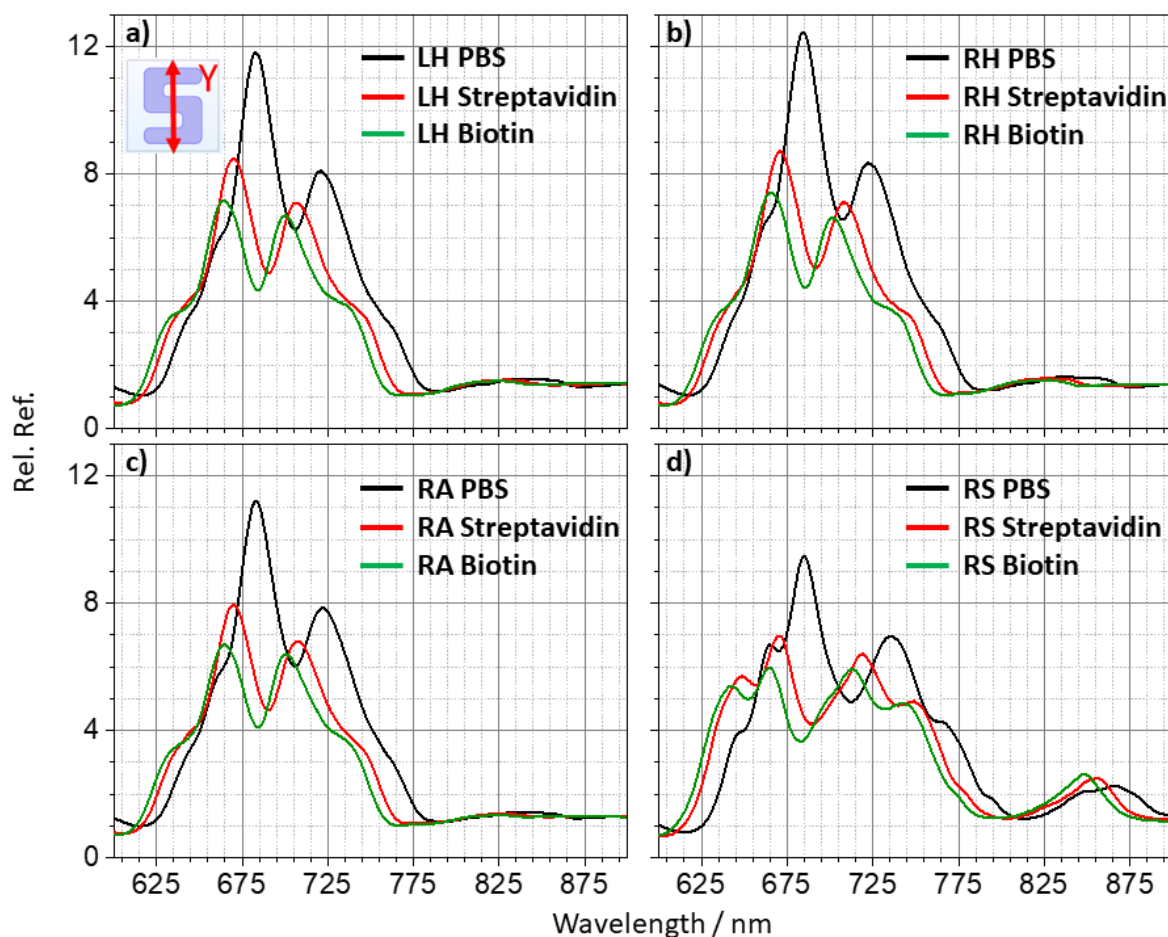


Figure 7.7: Experimental y-polarised reflectance spectra collected in PBS buffer for a) LH b) RH c) RA and d) RS arrays of a ~180 nm sample (black), followed by the depositions of streptavidin (red) and biotin (green).

In both cases of the streptavidin and subsequent biomolecule depositions, changes in the reflectance spectra are observed. Notably, the spectra undergo a blue shift, which contrasts the red shifting which is characteristic of RI sensing and is observed in the case of butanol. Given the lack of morphological changes observed for the samples, the source of the spectral changes in the presence of streptavidin is believed to arise from another source. A fundamental difference between butanol and the streptavidin lies in their charged states. Whilst the former is neutral, the latter possesses a slight negative charge at pH 7.4 given its slightly acidic isoelectric point. Charge has previously been shown to change the scattering properties of dielectric nanoparticles, causing an increase in their scattering frequency.²¹ The effects of the charged species from the biomolecule depositions are investigated with numerical simulations in **section 7.4**.

The blue shifting behaviour in the presence of biomolecules has so far been observed using stokes polarimetry. AFM measurements confirm that this is not due to changes in sample morphology. The biomolecules used possess an overall charge and the blue shifts do not occur in the presence of the uncharged butanol, suggesting that charge may contribute to the spectral changes. Before moving onto simulated results, MMP measurements were conducted with the streptavidin-antistrep complex to examine the influence they might have on the different optical properties measured by this technique.

7.3.3 MMP Measurements

The deposition process was repeated on a ~210 nm sample at the *B23 Beamline at Diamond Light Source Ltd.*, with antistrep being added to the streptavidin as the final step. The LD properties throughout the deposition of the LH and RH arrays are analysed in **figure 7.8a-c**, with asymmetries in the spectra parameterised through the LH:RH peak ratios for the peak maximums marked with a dashed line, tabulated in **7.8d**. The measurements in PBS produce similar spectra for the two array types as expected. With streptavidin present, there is an asymmetry in amplitudes of the peak, with the RH array showing less intensity at the analysed peak, now shifted to ~655 nm. The further addition of the antistrep results in a reduction in the peak asymmetry.

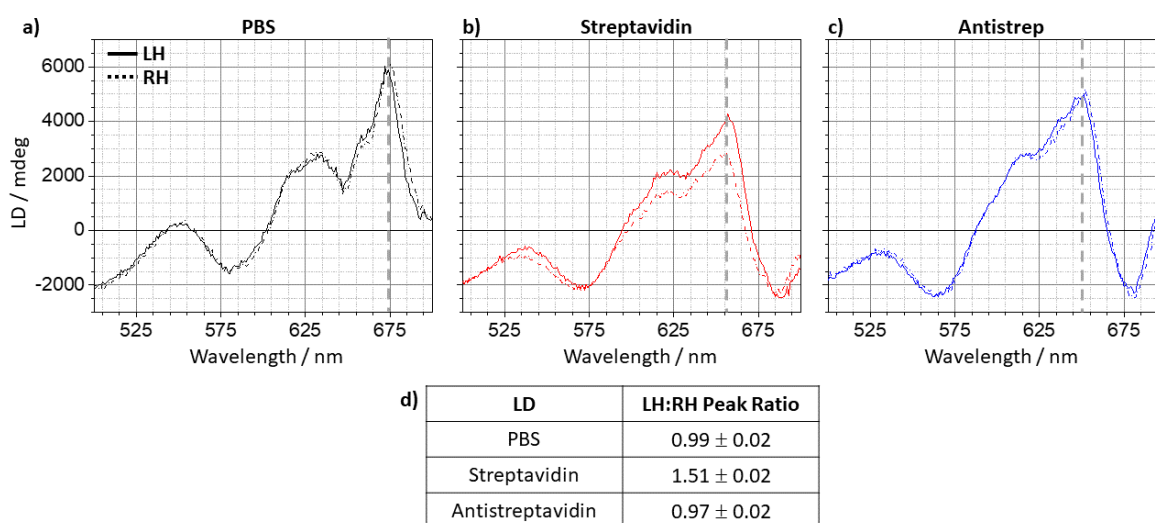


Figure 7.8: LD MMP data for the ~210 nm sample. LD spectra for LH (solid) and RH (dashed) structures collected in PBS buffer with a) no biomolecule present and with b) streptavidin and c) antistrep deposited. d) LH:RH peak ratios are calculated from the peaks marked by the dashed lines and are tabulated.

Similar analysis was performed for the LD' spectra, displayed in **figure 7.9a-d**. In the absence of any biomolecule, there is a near equal and opposite behaviour. For the (dashed line) resonance at ~679 nm, the ratios between the LH and RH arrays are found to be close to unity. As with the LD measurements, addition of streptavidin to the arrays generates an increased level of asymmetry in the spectra, with the amplitude of the resonance being greater for the LH structures. There is further similarity with the LD behaviour as the antistrep is deposited, with a reduction in the asymmetry of the peak ratio.

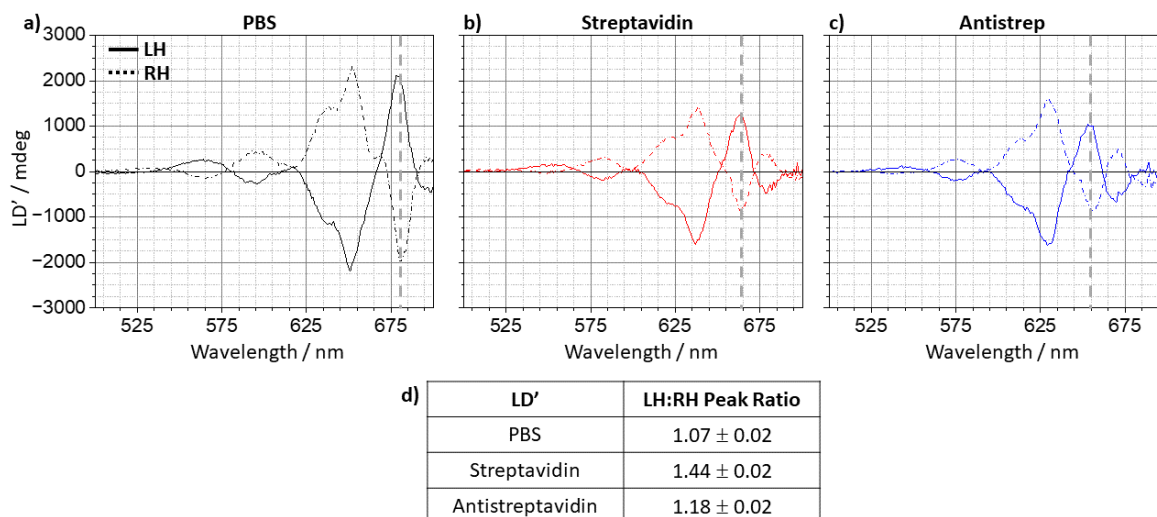


Figure 7.9: LD' MMP data for the ~ 210 nm sample. LD' spectra for LH (solid) and RH (dashed) structures collected in PBS buffer with a) no biomolecule present and with b) streptavidin and c) antistrep deposited. d) LH:RH peak magnitude ratios are calculated from the peaks marked by the dashed lines and are tabulated.

Finally, the CD data was analysed to determine if similar effects are observed in the chiroptical response of the samples. The MMP CD data for the sample is shown in figure 7.10a-d.

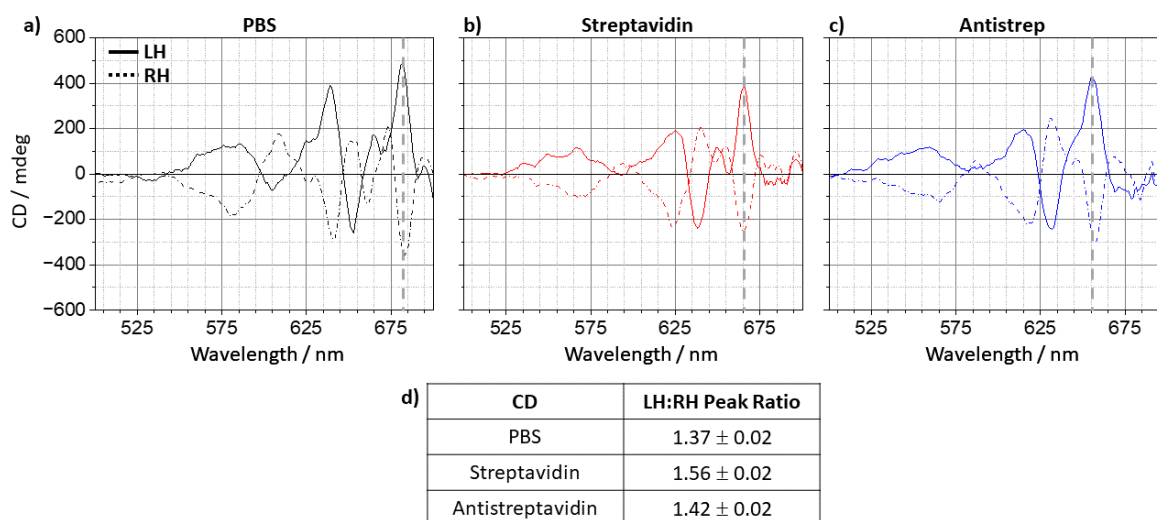


Figure 7.10: CD MMP data for the ~ 210 nm sample. CD spectra for LH (solid) and RH (dashed) structures collected in PBS buffer with a) no biomolecule present and with b) streptavidin and c) antistrep deposited. d) LH:RH peak magnitude ratios are calculated from the peaks marked by the dashed lines and are tabulated. The CD data is smoothed to aid analysis.

The CD data is smoothed due to the increased noise associated with the measurements, which are an order of magnitude smaller than the LD and LD' data. There still exists a similar pattern to the LD and LD' data, where the peak asymmetry increases with streptavidin and decreases when the antistrep is deposited.

The LD, LD' and CD data was also collected for the racemic arrays, which is presented in figure 7.11a-f. In each case, the racemic arrays show blue shifts in spectra when streptavidin and antistrep are added to the samples, again indicating that the racemic arrays are capable of detecting the analytes bound to the

surface. For a perfect racemic array, the LD' and CD spectra would give no signal due to the net contributions. If, however, the individual structures produce an asymmetric response, this would be expected to be reflected in the respective racemic spectra. For the LD' and CD racemic data, the signals generated are mostly positive above 625 nm. This agrees with the observations made for the enantiomorphic equivalents, in which the asymmetries in peak magnitudes (the LH:RH ratios) are positive due to the LH peak being greater than that of the RH.

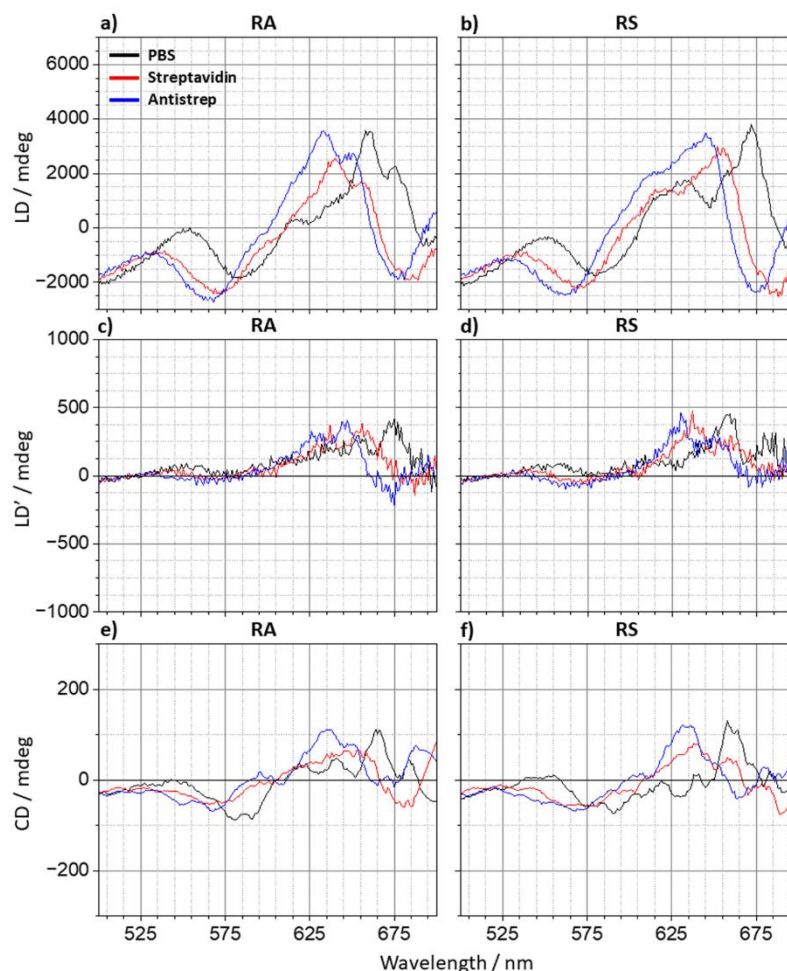


Figure 7.11: LD, LD' and CD MMP data for the racemic arrays of the ~ 210 nm sample. LD data for the a) RA and b) RS arrays is shown for the sample immersed in PBS with no biomolecule present (black) and with streptavidin (red) and antistrep (blue) deposited. Equivalent data is presented for c)-d) LD' and e)-f) CD. Note the scales for LD' and CD are reduced compared to the enantiomorphic data. The CD data is smoothed as before.

The blue shift observed through stokes polarimetry has been repeated with MMP measurements. In addition to the spectral blue shifts, asymmetries in the LD, LD' and CD data was observed. To probe this further, numerical simulations are required.

7.4 Results and Discussion – Numerical Simulations

7.4.1 Uncharged Layer Model

Modelling of the silicon structural arrays was performed extensively throughout **chapter 5**, which showed that the experimental reflectance behaviour could be reproduced reasonably well. The 2-butanol experiment shown in **figure 7.3** could be modelled simply by changing the refractive index of the domains above the structure and substrate, visualised in **figure 5.6b**. **Figure 7.12** shows the reflectance spectrum obtained for the modelling of butanol with a LH array, the response of the RH simulations is identical. The presence of the increased refractive index medium above the structures induces a small ~ 3 nm redshift in the simulated reflectance spectra, which agrees with the experimental spectral shifts. This supports the conclusion that these structures provide relatively poor refractive index sensitivity.

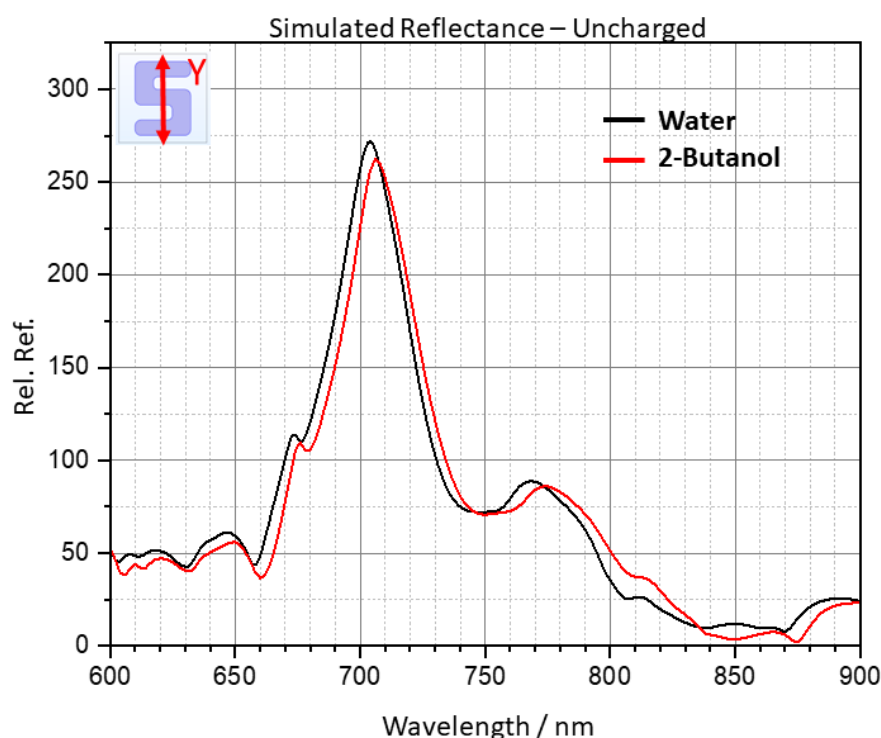


Figure 7.12: Simulated reflectance spectrum of an ideal 180 nm structure under y-polarised illumination, with media above the structure modelling water ($n=1.33$) and 2-butanol ($n=1.397$).

7.4.2 Charged Layer Model

Modelling of the biomolecular layer that was deposited on the substrates requires a different approach to simply changing the refractive index of the domains above the structure. To investigate whether the presence of charged biomolecular layers induces the effects seen in **section 7.3.2**, the model was adapted to include 20 nm domains around the outer edges of the nanostructure. The refractive index and ξ values were altered within these layers. Additionally, an external polarisation was assigned to model the charged biomolecular layers present during the deposition process. The model is relatively simplistic and considers the

external polarisation to arise from the deposited molecules in **figure 7.2**, approximated as a dipole layer extending from the negatively charged streptavidin, which has an isoelectric point of \sim pH 6.8, to the positively charged PLL bound directly to the surface. The polarisation magnitude (dipole moment per unit volume) was calculated by considering the streptavidin as a sphere with radius 10×10^{-9} m (half the width of the layer). The streptavidin coated QDs are quoted to range between \sim 15-20 nm in size.²² The dipole moment of the streptavidin was estimated to be 3.2×10^{-27} Cm, which is within the expected range of similar sized proteins.²³ This amounts to a polarisation of 8×10^{-4} Cm⁻², however, the value used in the simulations was 1×10^{-8} Cm⁻² to account for the layer being too idealised. The true value might be expected to be lower than the calculated value, given that the modelled layer around the structure is continuous and uniform, which does not reflect the true nature of a biomolecular layer, which will be much less dense due to steric constraints.

The external polarisation could be altered in each of the three axes and was made normal to each surface. As such, discontinuities in the polarisation direction exist due to the way in which the external domains were partitioned. This is visualised in **figure 7.13**, where the intersection between polarisation directions is shown. It is evident that there are regions of the structure, particularly in segments at the ends of each of the arms, where the polarisation direction is not perfectly normal to the surface.

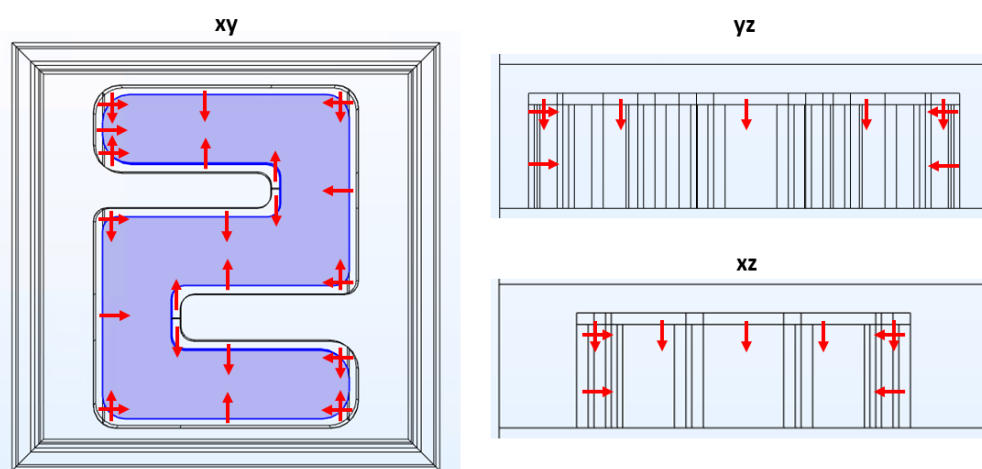


Figure 7.13: A depiction of the polarisation directions of the external layers in each of the three planes for a LH structure. The external layer is partitioned in each axis. Polarisation arrows are of arbitrary scale.

Properties of the layer were gradually introduced, beginning with refractive index ($n=1.4$), then ξ ($\pm 1.7 \times 10^{-4}$) and finally the polarisation, the reflectance spectra for each is shown in **figure 7.14**. When the layer is assigned a refractive index (and ξ value of 0), a small redshift in the spectra is observed which is similar to that produced in the presence of butanol (**figure 7.14**). Assigning a ξ value to the layer changes the reflectance behaviour slightly, with the two ξ spectra being very similar to the achiral data. In certain regions where there is less overlap between the three, such as \sim 685 nm, the 0 value lies between the two chiral values. This behaviour is reversed between the two enantiomorphs, indicating that the model is functioning correctly. The most pronounced effect occurs when the polarisation value is also added to the layer. There is a significant change in the

scattering behaviour of the structure, particularly with the increase in reflectance intensity at lower wavelengths, below ~ 700 nm, which provides qualitative agreement with experiment in which there is a blue shift upon deposition of the protein. As before, the different ξ values are equally distributed around the 0 value and are reversed between the LH and RH forms.

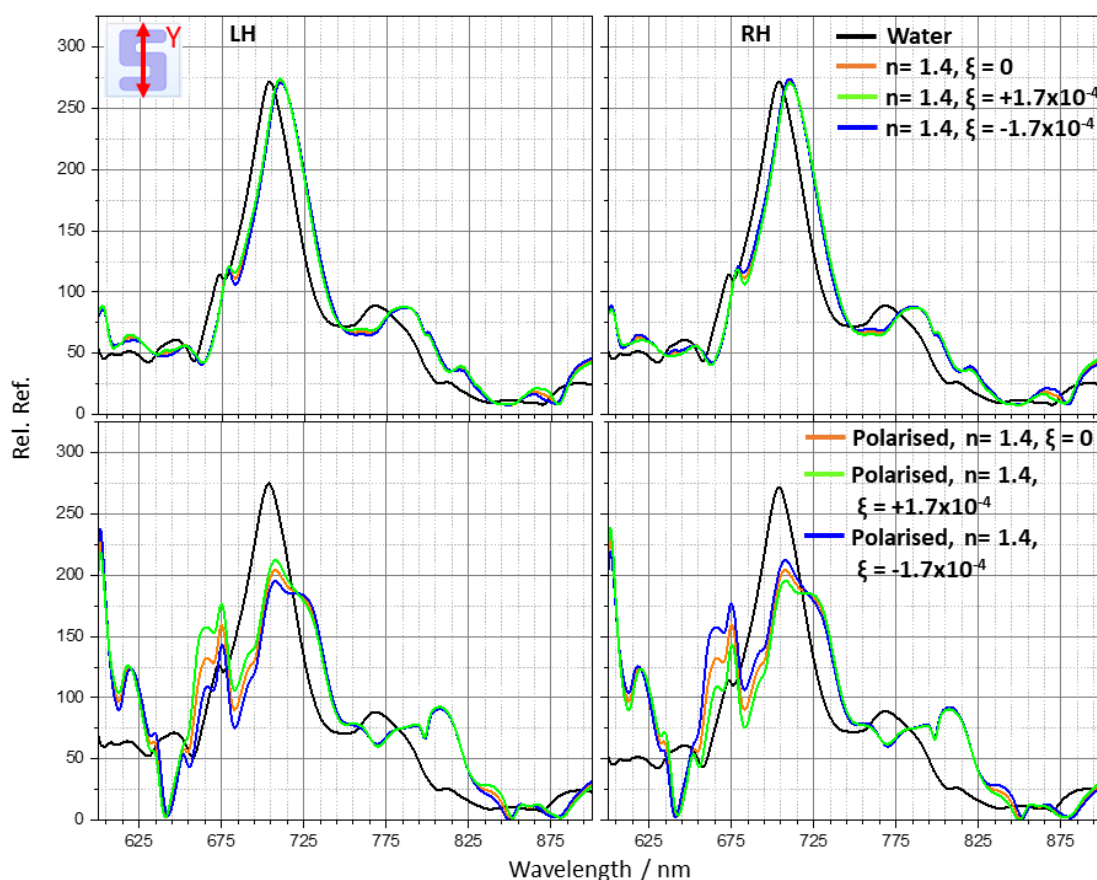


Figure 7.14: Simulated y-polarised reflectance spectra of ideal 180 nm LH (left) and RH (right) structures in water with external layer given a refractive index and chirality (top) and additional polarisation (bottom).

Equivalent measurements were performed with x-polarised incident light, shown in **figure 7.15**. However, it was found that the model broke down upon the implementation of the polarised layer, evidenced by the inequivalences in the LH and RH spectra.

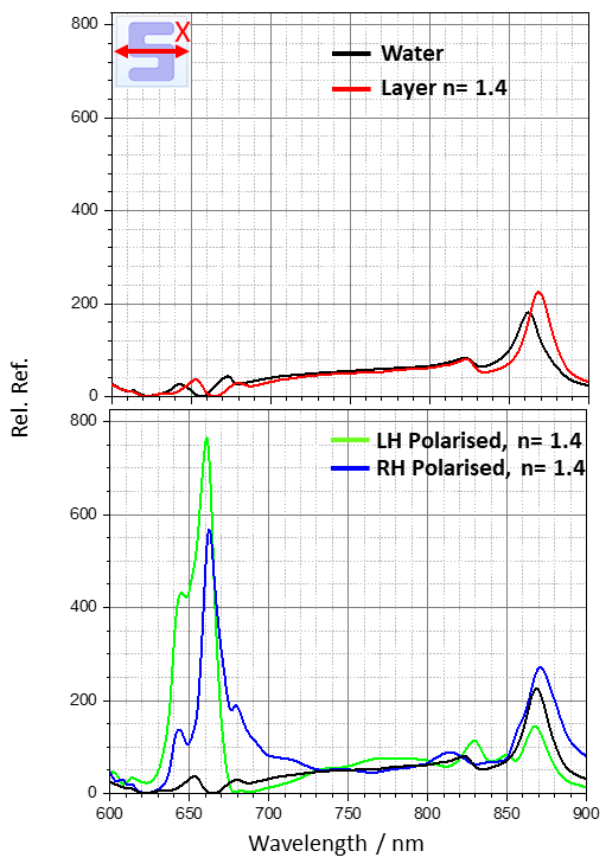


Figure 7.15: Simulated x-polarised reflectance spectra of ideal 180 nm structures in water (black) without (top) and with (bottom) a polarisation assigned to the external layer. LH (green) and RH (blue) data is shown when polarisation is present, which should be equivalent as the layer is achiral. Only LH data for water and the layer with no polarisation (red) is shown as the RH is identical.

7.4.3 Field Plots

Field plots generated from COMSOL were analysed to determine what effects the external polarisation had on the nanostructure's EM response. A comparison between the EM fields and optical chirality density maps with and without the charged layer for y-polarised illumination, are shown in **figure 7.16**. The introduction of the charged layer can be seen to have a strong effect on the field intensities both inside and between the arms of the structures. The relative intensities of each are increased in all the evaluated parameters.

For y-polarised illumination, the achiral polarised layer LH and RH plots show expected symmetric intensities and distributions, and the optical chirality density shows mirrored behaviour. This is reflected in the surface integrated values for $|E|$ and the optical chirality density (normalised against RCP) displayed beneath their respective maps. The symmetric fields between the structures are broken when a chirality is assigned to the layer. There is an increase in the field magnitude in the RH structure compared to the left. This is somewhat consistent with the LD and LD' data presented in **figures 7.8** and **7.9**. An asymmetry in the linear dichroisms would imply a difference in the absorption properties, which would be reflected in the local field magnitudes, which is observed in **figure 7.16**. The presence of the external polarised chiral layer appears to induce an asymmetric perturbation in the local fields stored within the structure. The experimental LD/LD' asymmetry reduces when the antistrep is deposited, suggesting that the charge distribution of the biomolecular layer changes in its presence, which can be rationalised given that the antibody itself is a charged species²⁴. There are also changes that occur in the optical chirality density values of the structures in the presence of the polarised layer, which enhances the chirality of the fields despite the layer itself being achiral. In the presence of the chiral layer, the enhancement is asymmetric, with a smaller increase in the overall value for the RH structure compared to that of the LH. This behaviour might be expected given the asymmetric behaviour displayed in the experimental CD response.

The structure's field response to the external layers could be considered a capacitive effect, due to their influence on the EM energy stored by the silicon at resonance. It should be noted that the polarised layer modelling was performed on a 180 nm sample, whilst the experimental MMP data was collected from a 210 nm sample. However, the respective regions from which the MMP effects and field analysis are performed (peak A shoulder) are equivalent.

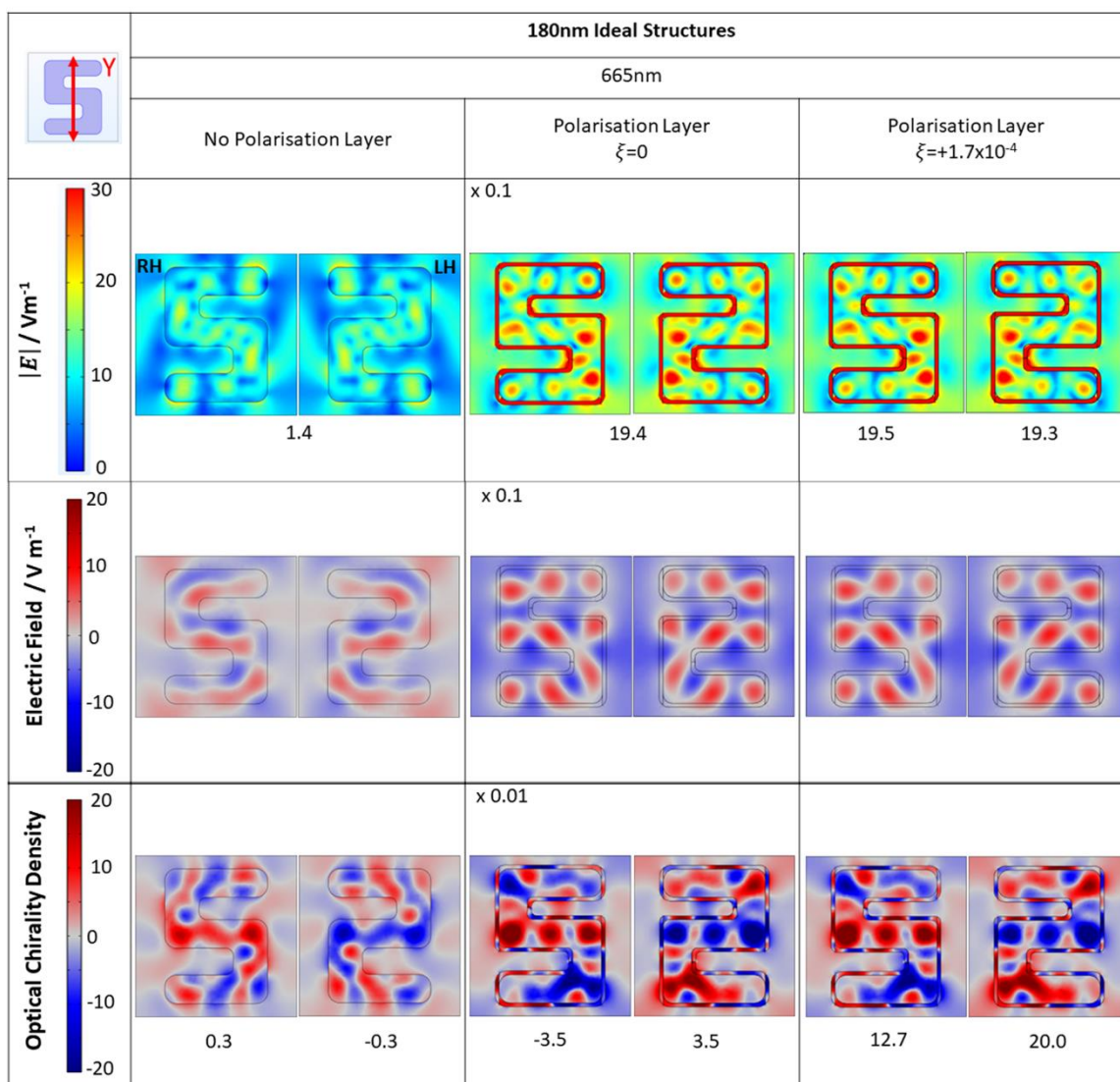


Figure 7.16: A comparison between the $|E|$ (top row), E_z (middle row) and optical chirality density (bottom row) plots for y-polarised illumination of a 180 nm structure without an external layer (left column), with an achiral polarised layer (middle column) and a chiral polarised layer (right column). Surface integrated values for the maps shown (taken from the midpoints of the structure) are labelled beneath the respective images. Scales for the polarised layers are altered, labelled in the top left corner of the middle column.

Equivalent analysis was performed for x-polarised incident light, shown in **figure 7.17**. The x-polarised reflectance in the absence of the polarised layer is consistent with the behaviour of enantiomorphic structures. When a polarisation is present, the $|E|$ values are not mirror symmetric images of one another, as would be expected due to the inequivalence of the LH and RH reflectance of **figure 7.15**. Similarly, the optical chirality density values are not equal and opposite. The breakdown of the model under this incident polarisation is unexpected given the consistency between enantiomorphs of the y-polarised simulations. It is believed that this arises from the simplicity of the model and the resultant discontinuities that exist between the layer domains, particularly in areas where adjacent layers (with orthogonal polarisations) meet, as was shown in **figure 7.13**. In order to fully investigate the array responses observed in the MMP measurements, the x-polarised data must also be considered as MMP measurements utilise two sets of orthogonal polarisation states ($0^\circ/90^\circ$ and $\pm 45^\circ$). The model will therefore require refinement if this is to be analysed further.

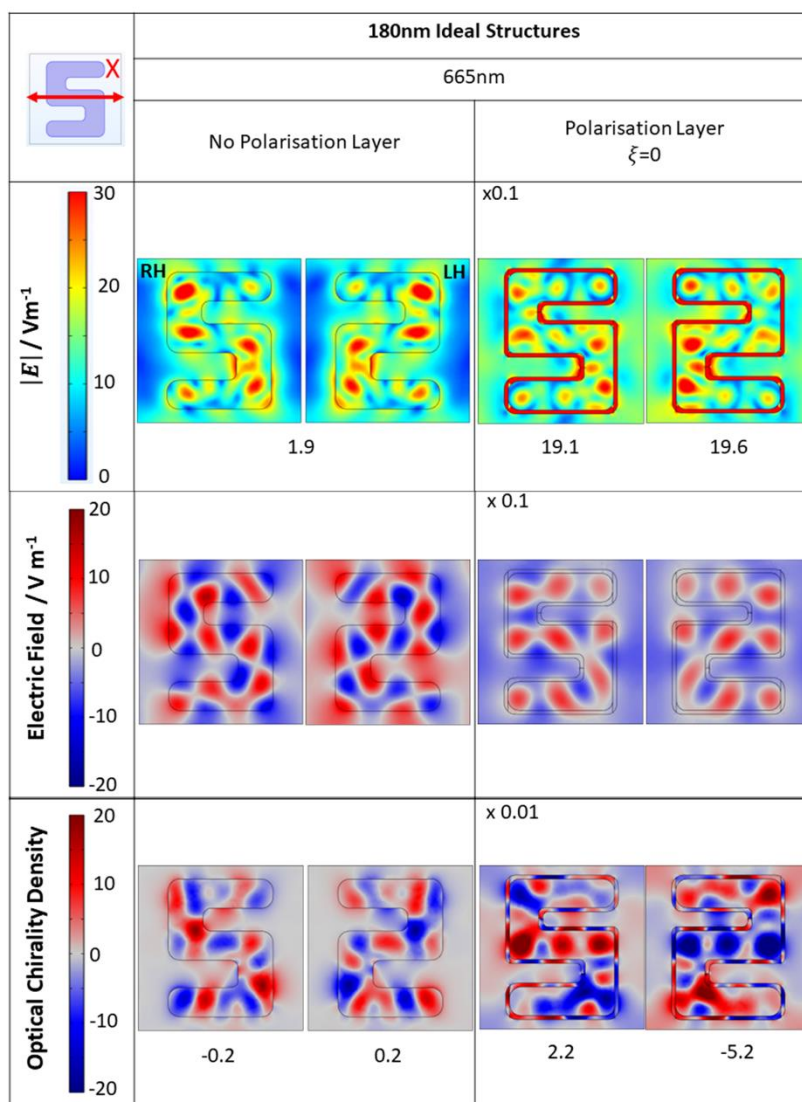


Figure 7.17: A comparison between the $|E|$ (top row), E_z (middle row) and optical chirality density (bottom row) plots for x-polarised illumination of a 180 nm structure without an external layer (left column) and with an achiral polarised layer (right column). Surface integrated values for the maps shown (taken from the midpoints of the structure) are labelled beneath the respective images. Scales for the polarised layer are altered, labelled in the top left corner of the right column.

Overall, the introduction of the external polarisation layer provides some qualitative agreement with experiment in terms of reproducing the reflectivity effects observed when the biomolecular layer is deposited. Analysis of the fields shows that there is a capacitive effect on the silicon structures, in which the internal fields are altered asymmetrically in the presence of a chiral polarised (charged) layer. The implementation of this layer requires improvement, particularly around its intersecting regions. The current design considered the computational requirements of modifying small regions of a thin layer, which requires a greater meshing density per unit volume, and was therefore simplified. It is also worth highlighting that there is currently no COMSOL module available which can specifically be used to model more complex biomolecular layers like the one deposited on these samples. The approximation of the layers is simplified for this reason. The dipole layer implemented for these simulations will therefore likely act as an exaggeration of the biomolecular layer. In addition to the exclusion of steric effects, the polarisation is also perfectly normal to the surface which is

not an accurate description of the biomolecular layer. In reality, the deposited biomolecules will be bound at random positions, with steric constraints limiting the deposition in certain regions. Furthermore, the charged state of the streptavidin QDs when deposited is not precisely known and becomes more complex when considering each QD can have 5-10 streptavidin molecules attached.

7.5 Conclusions

Common refractive index-based sensors are capable of sensitivities ranging from 100s-1000s of nm/RIU. The samples fabricated in this work were shown to provide a poor refractive index response, with a value of ~48 nm/RIU, when immersed in butanol. A similar lack of sensitivity was observed through numerical simulations. The deposition of streptavidin coated QDs was contrastingly found to generate a spectral blue shift experimentally, which was further increased by the subsequent binding of anti-streptavidin antibody or biotin. Numerical simulations were performed using an external polarised chiral layer, on the outer faces of the nanostructures, to determine if the experimentally observed effects were caused by a fundamental difference between the deposited biomolecules and butanol, that being their charged state. The simulated reflectance qualitatively replicated the increase in reflectance at lower wavelengths and a decrease in intensity of the original reflectance peak, however this was only the case for y-polarised incident light as the simplistic model broke down under orthogonal illumination.

Experimental MMP measurements were also performed on the sample with streptavidin coated QDs and antibody deposited. Asymmetries in the LH:RH peak ratios were observed for LD, LD' and CD measurements. Analysis of y-polarised field distributions revealed that the presence of the chiral charged layer asymmetrically perturbs the electric field intensities within the LH and RH structures. This capacitive effect, the changes to the stored EM energy within the structures, could potentially justify the behaviour observed from the linear dichroisms given that their properties are directly affected by the extinction properties of the structures. This could not however be confirmed due to the breakdown of the x-polarised simulations. Further refinement of the model is required to confirm the origins of the observed experimental results.

A key limitation of the model was the lack of a COMSOL module for modelling complex biomolecular layers. As such, the model used was unable to account for non-uniformity of the layers, steric effects, polarisations not being directly normal to the surface and local interference between biomolecules. Additional limitations arose from the simplistic approximation of the polarisation which was continuous across each layer sub domain. There were also interfaces between orthogonally polarised layers, which would create regions of unrealistic electromagnetic fields. Identifying ways to improve each of these factors would have been attempted had the ultimate limitation of time not been an issue, and therefore remain an interesting starting point for future work.

7.6 References

1. Hendry, E. *et al.* Ultrasensitive detection and characterization of biomolecules using superchiral fields. *Nat. Nanotechnol.* **5**, 783 (2010).
2. Karimullah, A. S. *et al.* Disposable Plasmonics: Plastic Templated Plasmonic Metamaterials with Tunable Chirality. *Adv. Mater.* **27**, 5610-5616 (2015).
3. White, I. M. & Fan, X. On the performance quantification of resonant refractive index sensors. *Opt. Express* **16**, 1020-1028 (2008).
4. Sun, J., Luo, B. & Li, H. A Review on the Conventional Capacitors, Supercapacitors, and Emerging Hybrid Ion Capacitors: Past, Present, and Future. *Adv. Energy Sustain. Res.* **3**, 2100191 (2022).
5. Ertürk, G. & Mattiasson, B. Capacitive Biosensors and Molecularly Imprinted Electrodes. *Sensors (Basel)*. **17**, (2017).
6. RoyChoudhury, S., Rawat, V., Jalal, A. H., Kale, S. N. & Bhansali, S. Recent advances in metamaterial split-ring-resonator circuits as biosensors and therapeutic agents. *Biosens. Bioelectron.* **86**, 595-608 (2016).
7. Jalil, M. E., Rahim, M. K. A., Samsuri, N. A. & Dewan, R. Flexible printed chipless RFID tag using metamaterial-split ring resonator. *Appl. Phys. A* **122**, 348 (2016).
8. Islam, M. R. *et al.* Metamaterial sensor based on rectangular enclosed adjacent triple circle split ring resonator with good quality factor for microwave sensing application. *Sci. Rep.* **12**, 6792 (2022).
9. Chen, H. *et al.* Left-handed materials composed of only S-shaped resonators. *Phys. Rev. E* **70**, 57605 (2004).
10. Tretyakov, S. A., Simovski, C. R. & Hudlička, M. Bianisotropic route to the realization and matching of backward-wave metamaterial slabs. *Phys. Rev. B* **75**, 153104 (2007).
11. Reddy, A. N. & Raghavan, S. Split ring resonator and its evolved structures over the past decade. in *2013 IEEE International Conference ON Emerging Trends in Computing, Communication and Nanotechnology (ICECCN)* 625-629 (2013). doi:10.1109/ICE-CCN.2013.6528575.
12. Mudraboyina, A. K. & Sabarinathan, J. Protein binding detection using on-chip silicon gratings. *Sensors (Basel)*. **11**, 11295-11304 (2011).
13. Duval, A. *et al.* Photonic crystal fiber based antibody detection. in *SENSORS, 2004 IEEE* 1222-1225 vol.3 (2004). doi:10.1109/ICSENS.2004.1426399.
14. Mazia, D., Schatten, G. & Sale, W. Adhesion of cells to surfaces coated with polylysine. Applications to electron microscopy. *J. Cell Biol.* **66**, 198-200 (1975).
15. Faussner, A., Deininger, M. M., Weber, C. & Steffens, S. Direct addition of polylysine or poly-ethylenimine to the medium: A simple alternative to plate pre-coating. *PLoS One* **17**, e0260173 (2022).
16. Hou, C., Zhang, L., Wang, Y. & Wang, Z. Synthesis and application of streptavidin functionalized organosilica microparticles. *J. Appl. Polym. Sci.* **132**, (2015).
17. Migneault, I., Dartiguenave, C., Bertrand, M. J. & Waldron, K. C. Glutaraldehyde: behavior in aqueous solution, reaction with proteins, and application to enzyme crosslinking. *Biotechniques* **37**, 790-802 (2004).
18. NIH. PubChem Compound Summary for CID 6568, 2-Butanol. (2023).
19. Advanced BioMatrix. Refractive Index and Total Solids of Extracellular Matrix (ECM) Solutions and Buffers. *Product Data Sheet* <https://advancedbiomatrix.com/Refractive-Index-and-Total-Solids-of>

- Extracellular Matrix (ECM) Solutions and Buffer.pdf (2023).
20. Santa Cruz Biotechnology. 2-Butanol (CAS 78-92-2). *Product Data Sheet*
[https://www.scbt.com/p/2-butanol-78-92-2#:~:text=Refractive Index %3A,%2FD1.397\(lit.\)](https://www.scbt.com/p/2-butanol-78-92-2#:~:text=Refractive Index %3A,%2FD1.397(lit.)) (2023).
 21. Gao, X., Xie, L. & Zhou, J. Active control of dielectric nanoparticle optical resonance through electrical charging. *Sci. Rep.* **12**, 10117 (2022).
 22. ThermoFisher Scientific. Qdot™ 655 streptavidin conjugate Product Overview.
<https://www.thermofisher.com/order/catalog/product/Q10123MP#:~:text=The Qdot™ streptavidin conjugate,class of streptavidin detection reagents.> (2023).
 23. Felder, C. E., Prilusky, J., Silman, I. & Sussman, J. L. A server and database for dipole moments of proteins. *Nucleic Acids Res.* **35**, W512-21 (2007).
 24. Yang, D., Kroe-Barrett, R., Singh, S. & Laue, T. IgG Charge: Practical and Biological Implications. *Antibodies (Basel, Switzerland)* **8**, (2019).

Chapter 8: Summary and Outlook

In this body of work, two forms of chiral metamaterial samples have been fabricated, characterised and used in optical measurements for biomolecular sensing. In **chapter 4**, the CD spectra of gold gammadion arrays were measured, and the sources of their resonances determined. The deposition of streptavidin with and without the presence of a biotin self-assembled monolayer showed that the sensing capabilities of the structures were strongly dependent on the anisotropy of the deposited biomolecular layers. Further study with these structures could involve the use of other thiolated biomolecule compounds to determine if similar effects could be observed. Research continues with plasmonic metamaterials to find the optimal structure format for enhanced detection and improve understanding of how chiral fields interact with matter.

In **chapters 5-7**, silicon S-shaped arrays were characterised using Stokes polarimetry and MMP. Through Stokes polarimetry and numerical simulations, the sources of reflectance and ORD resonances were identified using the numerical method of multipole decomposition. This technique was also used to rationalise the height dependence of the resonances. The importance of the full characterisation of low symmetry structures using MMP was highlighted, as the large optical rotation observed with ORD measurements were largely a result of the birefringence of the samples. The structures exhibited both bianisotropic and anisotropic behaviours over different wavelength ranges. Alterations to the design (symmetry) and surrounding media could be avenues for explaining this behaviour fully. Additional MMP measurements of the structures for each height would be of interest, in order to provide a complete characterisation of all of the samples described within this thesis.

Finally, in **chapter 7**, the biosensing capabilities of the silicon metasurfaces was investigated using a layered deposition process which bound streptavidin species to the structures. Changes to the reflectance behaviour were investigated using numerical simulations, which probed the effects of molecular charge on the optical response of the structures. There is further work required, most obviously with the numerical model used to represent the deposited biomolecules. Several aspects that could be improved were discussed, although the lack of a technique specific to the modelling of deposited protein layers is the main limiting factor.

The field of chiral nanophotonics is diverse, with plasmonic and dielectric platforms presenting only a fraction of the materials being utilised for modern applications. Since the completion of the work detailed in this thesis, the Kadodwala research group has gone on to look at different forms of chiral light, including Laguerre-Gaussian and optical angular momentum beams, and how they can alter the properties of 2D materials like graphene. This type of light-matter interaction is known as strain engineering and could lead to significant advances in electronics, with potential applications including reconfigurable electronic devices.

Metamaterials present one of the most exciting avenues for scientific research in the modern day. With such a wide scope of potential applications and the continuous advancements in fabrication technologies, the realisation of new structures is almost only limited by the imagination. The properties achievable with metamaterial platforms is a fascinating field, and hopefully, the small

glimpse of some of those properties presented in this thesis have been able to captivate some of that interest.